The Dissertation Committee for Hisanao Ouchi Certifies that this is the approved version of the following dissertation:

Development of Peridynamics-based Hydraulic Fracturing Model for Fracture Growth in Heterogeneous Reservoirs

Committee:

Mukul M. Sharma, Supervisor

Jon E. Olson

John T. Foster

David Nicolas Espinoza

Loukas F. Kallivokas

Development of Peridynamics-based Hydraulic Fracturing Model for Fracture Growth in Heterogeneous Reservoirs

by

Hisanao Ouchi, B.E.; M.E.

Dissertation

Presented to the Faculty of the Graduate School of

The University of Texas at Austin

In Partial Fulfillment

Of the Requirements

For the Degree of

Doctor of Philosophy

The University of Texas at Austin

May 2016

Dedication

To my wife and daughter for their sacrifice, endurance, and encouragement

Acknowledgements

I would like to sincerely gratitude to my supervisor Dr. Mukul M. Sharma for his guidance, patience, and support thorough my PhD study at the University of Texas at Austin. Despite his extreme busyness, he always made time for discussion and showed me the right direction. Without his insightful suggestions at the proper timings, I could not complete this research.

I would like to extend my deep appreciation to Dr. John T. Foster. He treated me as if I were his student. Through a lot of discussions with him, I gradually learnt more about peridynamics theory. I also would like to express my appreciation to my dissertation committee members: Dr. Jon E. Olson, Dr. D. Nicolas Espinoza, and Dr. Loukas F. Kallivokas for their time for reviewing my dissertation and for valuable comments.

I also want to express my sincere appreciation to Dr. Amit Katiyar. My research would never have been completed without collaboration and discussions with him. His words always encouraged me. I also want to express my gratitude to Jin Lee. I was really helped by her excellent administrative support and her kindness.

I would like to express my gratitude for the financial support from Japan Oil Engineering Co., Ltd. I am also grateful to my previous boss, Dr. Kurihara, for giving me the chance of studying at UT Austin.

I would like to thank all of my friends in our laboratory, especially, Dr. Jongsoo Hwang, Dongkeun Lee, Eric Briant, Weiwei Wu, Dr. Ripudaman Manchanda, Deepen Gala, Prateek Bhardwaj, Haotian Wang, Peng Zhang, Hanyi Wang, Shi Ting Yi, Shivam Agrawal, and Sho Hirose. Thanks to all of you, my student life at UT Austin was very happy. I could always keep my motivation during my PhD study.

Finally, I would like to thank my wife, Kanoko Ouchi, and my daughter, Moe Ouchi, for their sacrifice and dedication from the bottom of my heart.

Development of Peridynamics-based Hydraulic Fracturing Model for Fracture Growth in Heterogeneous Reservoirs

Hisanao Ouchi, Ph.D.

The University of Texas at Austin, 2016

Supervisor: Mukul M. Sharma

Oil and gas reservoirs are heterogeneous at different length scales. At the micro-scale mechanical property differences exist due to mineral grains of different composition and the distribution of organic material. At the centimeter or core scale, micro-cracks, sedimentary bedding planes, natural fractures, planes of weakness and faults exist. At the meter or log scale, larger scale bedding planes, fractures and faults are evident in most sedimentary rocks. All these heterogeneities contribute to the complexity in fracture geometry. However, very little research has been conducted on evaluating the effect of these heterogeneities on fracture propagation, primarily due to the absence of a numerical framework capable of incorporating such heterogeneities in fracture growth models.

In this dissertation we developed a novel method for simulating hydraulic fractures in heterogeneous reservoirs based on peridynamics and then utilized it to elucidate the complicated fracture propagation mechanisms in naturally fractured, heterogeneous reservoirs. Peridynamics is a recently developed continuum mechanics theory specially developed to account for discontinuities such as fractures. Its integral formulation

minimizes the impact of spatial derivatives in the stress balance equation making it particularly suitable for handling discontinuities in the domain.

No fluid flow formulation existed in the peridynamics framework since this theory had not been applied to fluid driven fracturing processes. In this dissertation, a new peridynamics fluid flow formulation for flow in a porous medium and inside a fracture was derived as a first step in the development of a peridynamics-based hydraulic fracturing model. In the subsequent section, a new peridynamics-based hydraulic fracturing model was developed by modifying the existing peridynamics formulation of solid mechanics and coupling it with the newly derived peridynamic fluid flow formulation. Finally, new shear failure criteria were introduced into the model for simulating interactions between hydraulic fractures (HF) and natural fractures (NF). This model can simulate non-planar, multiple fracture growth in arbitrarily heterogeneous reservoirs by solving fracture propagation, deformation, fracturing fluid pressure, and pore pressure simultaneously. The validity of the model was shown through comparing model results with analytical solutions (1-D consolidation problem, the KGD model, the PKN model, and the Sneddon solution) and experiments.

The 2-D and 3-D interactions behavior between a HF and a NF were investigated by using the newly developed peridynamics-based hydraulic fracturing model. The 2-D parametric study for the interaction between a HF and a NF revealed that, in addition to the well-known parameters (the principal stress difference, the approach angle, the fracture toughness of the rock, the fracture toughness of the natural fracture, and the shear failure criteria of the natural fracture), poroelastic effects also have a large influence on the interaction between a HF and a NF if leak-off is high. The 3-D interaction study elucidated that the height of the NF, the position of the NF, and the opening resistance of the NF have a huge impact on the three-dimensional interaction behavior between a HF and a NF.

The effects of different types of vertical heterogeneity on fracture propagation were systematically investigated by using domains of different length scales. This research clearly showed the mechanisms and the controlling factors of characteristic fracture propagation behaviors (“turning”, “kinking”, and “branching”) near the layer interface. In layered systems, the mechanical property contrast between layers, the dip angle and the stress contrast all play an important role in controlling the fracture trajectory. Each of these effects was investigated in detail. The effect of micro-scale heterogeneity (due to varying mineral composition) on fracture geometry was studied next. It was shown that even at the micro-scale, fracture geometry can be quite complex and is determined by the geometry and distribution of mineral grains and their mechanical properties.

TABLE OF CONTENTS

LIST OF TABLES

LIST OF FIGURES

CHAPTER1: INTRODUCTION

Shale gas reservoirs have heterogeneities at all length scales ranging from small scale (such as different mechanical properties of different mineral grains or micro cracks) to large scale (such as sedimentary layers or vertical/horizontal planes of weakness.) To design a hydraulic fracturing job properly, we have to understand how these heterogeneities affect fracture propagation. However, very few studies have been conducted that address these multi-scale heterogeneities. In this dissertation, we develop a novel mathematical approach to simulate the propagation of fluid driven fractures in porous media. This approach utilizes a non-local method, peridynamics, to simulate the interaction of fluid flow with solid mechanics and failure. We then utilize this method to analyze the effect of multi-scale heterogeneity on fracture propagation.

1.1 Background

Fig. 1.1 shows the natural gas production history and forecast in the U.S.. As shown in Fig. 1.1, the gas production from shale gas reservoirs has increased dramatically since 2008. In 2014, about 30% of gas in the U.S. was produced from shale gas/oil reservoirs. It is expected that by the end of 2040, about half of the dry gas production in the U.S. will come from shale reservoirs. Previously, the ultra-low permeability of shales (of the order of nano Darcy) prevented commercial gas production from shale reservoirs. However, the combination of two pre-existing technologies (horizontal drilling and hydraulic fracturing) changed the situation. By applying multi-stage hydraulic fracturing to horizontal wells, commercial gas production from shale gas reservoirs has been made possible. Shale

reservoirs are often highly fractured and heterogeneous. Many micro-seismic observations suggest there is a possibility that very complicated fracture networks are generated due to the interaction of hydraulic fractures with pre-existing natural fractures in shale gas reservoirs, which might result in better gas production. On the other hand, some production log data reveals that some of the fractures do not contribute to gas production at all when multiple fractures grow close to each other. This is caused by stress interference between fractures. However, none of the conventional hydraulic fracturing models can explain this phenomenon because they assume single planar fracture growth. A next generation numerical model which can fully explain this phenomenon is required for better design of hydraulic fracturing jobs.

Peridynamics is a recently developed continuum mechanics theory specially developed to account for discontinuities such as fractures. The theory has been well established for prediction of fracture propagation in solids [1-3] and the effectiveness of the theory has been fully demonstrated [4-9]. Application of this theory to hydraulic fracturing is promising. However, peridynamics does not have a fluid flow formulation. To apply peridynamics theory to hydraulic fracturing, we developed a peridynamics based fluid flow formulation first and established a framework to couple the fluid flow formulation with the existing solid mechanics formulation.

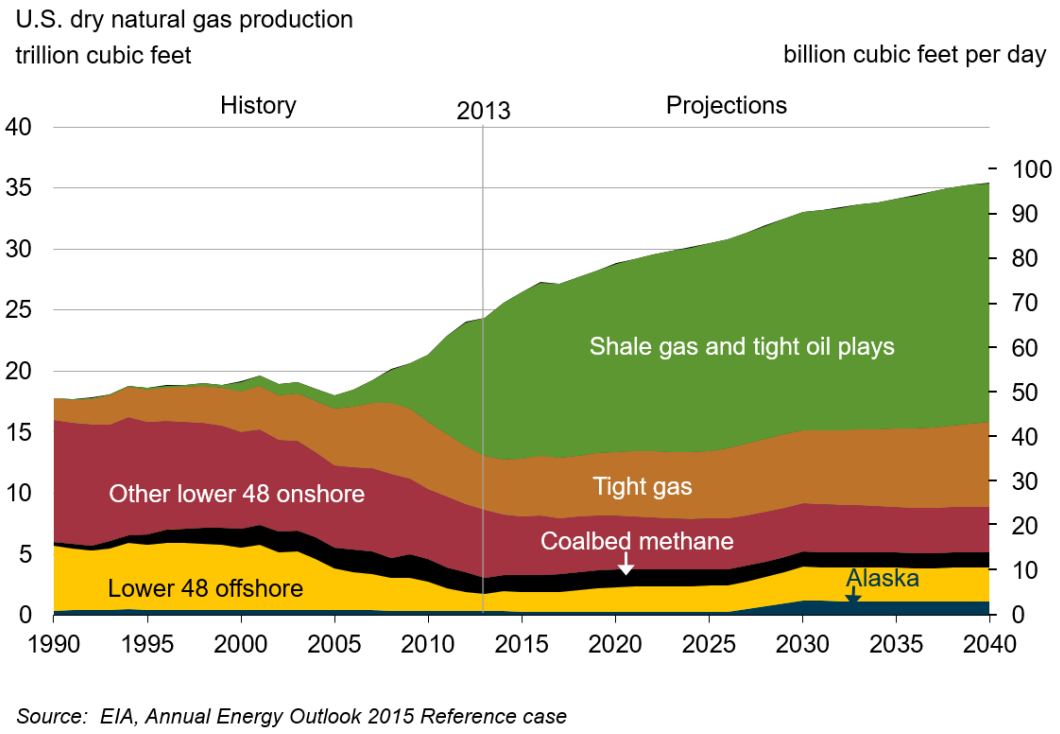

Fig. 1.1 U.S. natural gas production from different sources (http://www.eia.gov/forecasts/aeo/ppt/aeo2015_rolloutpres.pptx).

1.2 Objective of the research

The primary objective of this research is to develop a model to simulate the propagation of multiple, non-planar, fluid driven fractures in porous media and use it to elucidate the complicated fracture propagation mechanisms in naturally fractured, arbitrarily heterogeneous shale reservoirs. We have set three specific objectives for this research:

1. To derive a new peridynamics-based formulation for fluid flow in a porous medium and inside the fractures.

2. To develop a novel hydraulic fracturing model which can handle multiple, non-planar fracture propagation as well as porous flow in naturally fractured, arbitrarily heterogeneous and isotropic porous medium by coupling the new fluid flow formulation with the existing solid mechanics formulation.
3. To apply the model for understanding the complicated mechanisms involved in fracture propagation in naturally fractured, heterogeneous reservoirs.

1.3 Literature Review

1.3.1 HYDRAULIC FRACTURING MODELS

Hydraulic fracturing (HF) refers to fluid pressure induced deformation, damage and fracture propagation in a porous medium. It is an important technique for improving productivity in low permeability reservoirs. HF has been used in conventional oil and gas reservoirs since the 1940s [10]. In recent days, this process has become particularly important for the stimulation of unconventional hydrocarbon reservoirs. Since the development of HF techniques, modeling of HF has also been crucial for economic optimization of HF jobs. Various HF models have been developed over the past six decades. The characteristics of these models are reviewed here.

1.3.1.1 2-D analytical models (PKN and KGD model)

Khristianovitch-Geertsma-de Klerk (KGD) model [11, 12] and Perkins-Kern-Nordgren (PKN) model [13, 14] are the classic 2-D analytical models. Both these models

assume plane strain condition and elliptical crack growth to simplify the 3-D fracture propagation problem into a 2-D fracture propagation problem. The main difference between the models is the direction of plane strain assumption. The KGD model assumes plane strain condition in a horizontal cross section. As a result of this assumption, as shown in Fig. 1.2, fracture geometry in the KGD model assumes an elliptical shape in the horizontal plane and is independent of fracture length. This model is regarded as a good approximation when fracture height is more than fracture length.

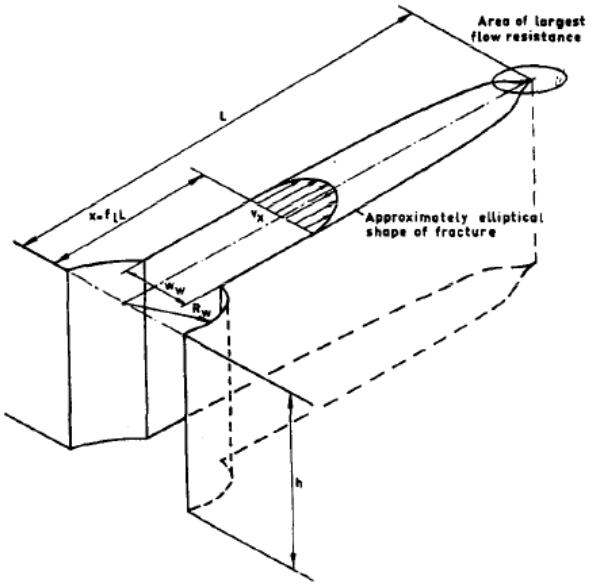

Fig 1.2 Schematic view of KGD model (from [12]).

On the other hand, the PKN model assumes a plane strain condition in vertical cross section. As shown in Fig. 1.3, fracture geometry shows an elliptical shape in the vertical plane and fracture width is not a direct function of fracture length. This assumption is a better approximation when the fracture is much longer than its height.

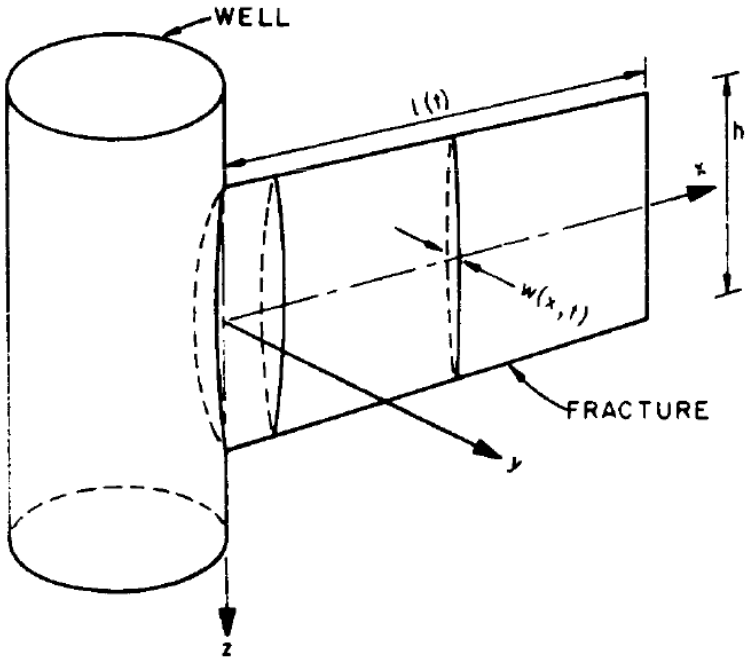

Fig 1.3 Schematic view of PKN model (from [14]).

Neither the KGD nor the PKN model are used in actual fracturing designs in recent days due to the difficulty of application to multi-layer problems. However, since they are valid under specific conditions, both the models still play an important role in model verification.

1.3.1.2 Pseudo 3-D and planar 3-D models

Following the 2-D analytical hydraulic fracturing models, conventional hydraulic fracturing models such as pseudo-three-dimensional (P3-D) models and plane three-dimensional (3-D) models have been developed. These models are both able to predict planar fracture growth in multiple layers based on the following assumptions.

- Reservoir deformation is solved under the framework of elastic theory (not assuming poroelastic effect and plasticity).
- Reservoir mechanical properties and fluid properties are homogeneous in the horizontal direction.
- Fracture geometry is planar.
- Fluid flow inside a fracture is modeled as flow in parallel slots combined with an analytical leak-off model.

These assumptions work well in conventional oil and gas reservoirs. The main difference between P3-D model and 3-D models is that the P3-D HF models can predict HF propagation in multiple layers with less computational effort based on some simplified assumptions.

The P3-D HF model was originally proposed by Simonson et al. [15] for fracture propagation in a three layer problem. Later several researchers [16-19] proposed different types of P3-D HF models which can simulate fracture height growth in multiple layers. They are typically categorized into two groups (cell-based models and lumped models) based on the way analytical relationship among width, height, and fracturing fluid pressure is assumed. In cell-based P3-D model, as shown in Fig. 1.4 [20], the fracture is divided into multiple cells along the fracture propagation direction. In each cell, fracture height and width are solved for independently under 2-D plane strain condition. On the other hand, as shown in Fig. 1.5 [20], in lumped P3-D model, the fracture is divided into an upper half and a lower half. In each half, fracture height, width and length are solved for assuming certain analytical relationships. They both, being comparatively fast, meet the need for engineering design and on-job evaluation in conventional oil and gas reservoirs.

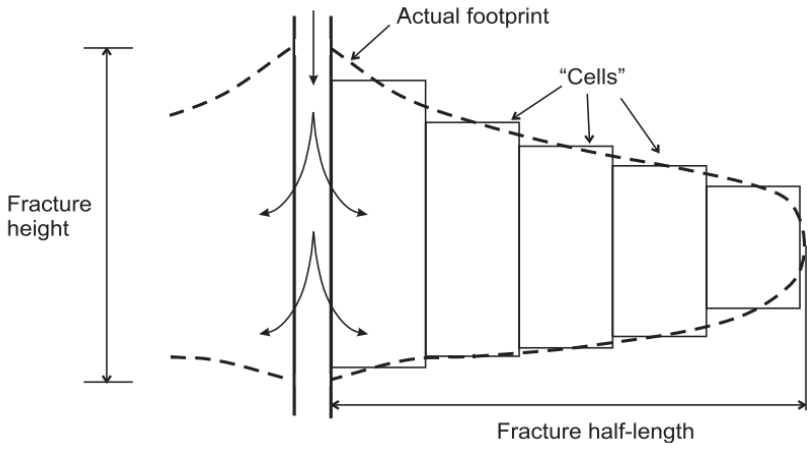

Fig. 1.4 Schematic view of cell-based P3-D model (taken from [20]).

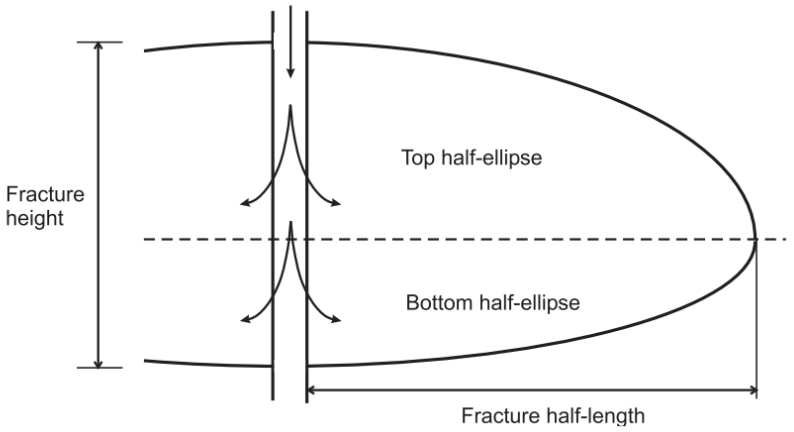

Fig. 1.5 Schematic view of cell-based P3-D model (taken from [20]).

The first plane 3-D model was presented by Clifton and Abou-Sayed [21]. In this model, the authors introduce a two-dimensional integral equation for normal stress over the fracture surface for calculating fracture surface displacement proposed by [22]. By combining this equation with 2-D fluid flow equations and crack opening criteria, the authors presented the framework of a three-dimensional hydraulic fracturing model.

Following this model, several authors [18, 23-25] presented 3-D models with different meshing approaches and different solution techniques for the two-dimensional integral equation of normal stress over the fracture surface. Although planar 3-D models substantially improve simulation predictions over P3-D models, they have not been commonly used in fracture design operations until recent years due to the associated computational expense.

1.3.1.3 Non-planar and multiple fracture models

In heterogeneous, anisotropic and highly fractured geologic settings such as shale oil and gas reservoirs, three-dimensional (3-D) fractures may initiate in a non-preferred direction, become non-planar and multi-stranded, interact with natural fractures, and compete with neighboring growing fractures [26-31]. The prediction of such a complex fracture geometry (i.e. length, width, and height) and a complex network is also becoming increasingly important for the design of hydraulic fracturing in unconventional reservoirs [32]. In recent years, several hydraulic fracturing models to simulate multiple non-planar hydraulic fracture growth and the interaction between hydraulic fractures and natural fractures have been proposed. Many of these models have been developed based on the displacement discontinuity (DD) method. Olson developed multiple hydraulic fracture propagation model based on two-dimensional displacement discontinuity (2-D DD) method and investigated the interaction between hydraulic fractures (HF) and natural fractures (NF) [33]. This model can incorporate the effect of fracture height to stress interference by applying height correction factor [34]. However, for avoiding numerical complexity, this model assumes a constant pressure inside fractures and does not couple with fluid flow in the fracture or matrix. Sesetty and Ghassemi also presented a model

based a 2-D DD method coupled with a fracturing fluid flow model and simulated complicated fracture geometries. They showed that the fracturing fluid pressure distribution affects the interaction between a HF and a NF [35]. McClure developed a model for simulating multiple fracture propagation and their interaction with complicated discrete fracture network based on 2-D DD method [36]. This model can simulate the interaction between HFs and hundreds of natural fractures in a practical computational time. However, all potential fracture propagation paths must be defined in advance. Weng et al. also developed a P-3D model to simulate multiple fracture growth in naturally fractured reservoirs by partially combining 2-D DD method [37]. Wu presented a hydraulic fracturing model for multiple fracture growth based on a simplified 3-D displacement discontinuity (S3-DDD) method [38]. This model can simulate stress interference among fractures more accurately than the 2-D DD method with height correction when multiple cracks grow simultaneously. The models based on the displacement discontinuity method described above simulate multiple fracture growth by assuming homogeneous property distribution in the horizontal direction. Hence, they are numerically efficient. However, they are not able to capture the effect of reservoir heterogeneity, poroelasticity on non-planar fracture growth.

Another approach to simulate complicated hydraulic fracture growth is the discrete element method (DEM). In this method, rock is modeled as a collection of particles connected to each other by joints called “bonds.” Bonds break when the applied force on a bond exceeds a predefined strength and this generates a micro-crack. Zhao et al. proposed a hydraulic fracturing model based on a two-dimensional discrete element method (2D DEM) and demonstrated that their model can reproduce the experiments of the interaction between a hydraulic fracture and a natural fracture [39]. Shimizu et al. developed a 2D DEM code and demonstrated that fracture geometry in unconsolidated sands was strongly

affected by the fracturing fluid viscosity [40]. DEM methods can reproduce complex fracture propagation behavior without using complicated constitutive laws. However, it is still limited by 2D plane strain conditions and is not suitable for field scale simulations since the model which is expressed as the aggregation of particles cannot represent actual field-scale porous media.

Complicated hydraulic fracture growth has also been modeled by using a finite element method (FEM) / finite volume method (FVM) coupled with a cohesive zone model (CZM). Yao et al. developed a hydraulic fracturing model based on FEM with CZM in ABACUS and showed that the model can reproduce the analytical solution better than the PKN model and the pseudo 3D model [41]. Later, Shin et al. investigated the simultaneous propagation of multiple fractures by using CZM in ABACUS [42], however, fracture geometry in this method is still limited to planar fractures. Manchanda [43] developed a hydraulic fracturing model based on FVM with CZM in OpenFOAM and demonstrated multiple non-planar fracture growth both in 2-D and 3-D. Although this model is still under development, this type of approach shows some degree of success in handling complicated fracture propagation.

Hydraulic fracturing has also been simulated using extended finite element methods (XFEM). Both Dahi Taleghani et al. and Keshavarzi et al. proposed hydraulic fracturing models based on XFEM and both of them investigated the interaction of hydraulic fracture with natural fracture [26, 44]. Haddad and Sepehrnoori [45] investigated 3-D multiple fracture growth in a single layer model by using XFEM-CZM model in ABACUS. XFEM allows a static mesh for a fracture and removes the need of re-meshing around the fracture. Hence, it is numerically much more efficient than conventional FEM. Application of XFEM to complicated hydraulic fracturing problems seems to be promising. However, the results presented so far are still limited to 2-D model or 3-D single layer model.

1.3.2 INTERACTION BETWEEN HYDRAULIC FRACTURE AND NATURAL FRACTURE

In many shale gas/oil fields, microseismic mapping techniques have shown the possibility of the growth of complex fracture networks and asymmetric fracture propagation due to the interaction of hydraulic fractures with natural fractures or other planes of weakness [28, 46]. To optimize the hydraulic fracturing jobs, many researchers have tried to elucidate the mechanism of the interaction between hydraulic fracture (HF) and natural fracture (NF) in different ways (experimental, analytical, and numerical).

1.3.2.1 Experimental and analytical studies

Several researchers have conducted experiments to investiagate the mechanism of interaction between a HF and a NF. Some of them developed analytical criteria for predicting the condition under which the HF crosses the NF.

Blanton et. al [47, 48] conducted experimental studies of the interaction between a HF and a NF by changing the principal stress difference and the angle of approach. They also derived analytical criteria for deciding the interaction behavior between the HF and the NF ("crossing" or "arresting") as a function of the principal stress difference and the approaching angle. These experiments and analytical solution show that the HF tends to turn along the NF under a low principal stress difference and low approach angle.

Wapinski and Teuful [27] conducted the same types of the experiments as Blanton et. al [47, 48] and obtained results consistent with Blanton et.al. They also analyzed the conditions under which dilatation or arresting (shear slip) will occur.

Zhou et. al [49] also studied the interaction between HF and NF through series of experiments, and concluded that shear strength of the NF is also an important parameter for the interaction between a HF and a NF (in addition to the principal stress difference and the approaching angle).

Renshaw and Pollard [50] developed an analytical criterion for deciding whether a HF crosses a NF or not when the angle of approach is 90 degree. They also demonstrated the validity of their model through a series of experiments. Later, Gu and Weng [51] extended their model to apply it to any angle of approach. The validity of the model was shown by comparing with the new experimental results and the existing experimental results by Gu et. al [52].

Cuprakov et. al [53] proposed a new analytical model for interaction between a HF and a NF. Based on the assumption that the fracture path at the intersection point of HF and NF is expressed as a constant slot, they analytically solved the stress distribution around the fracture and calculated fracture propagation by combining the stress solution with the energy criteria. They showed the validity of their model by comparing the model results with the experimental data and demonstrated that the interaction between the HF and the NF is also affected by flow rate, fracturing fluid viscosity, and fracture length in addition to the parameters already established such as principal stress difference and angle of approach.

1.3.2.2 Numerical studies

Several numerical investigations have been conducted for understanding the mechanism of the interaction between a HF and a NF.

Zhang and Jeffery [54] developed a 2-D hydraulic fracturing model for investigating interaction between a HF and a NF based on 2-D DD method. In this model, the NF is discretized into several elements. Then, the movement of the NF ("opening", "sticking", and "sliding") is calculated at each discretized element. The shear related movement such as "sticking" and "sliding" are evaluated based on the Coulomb frictional law in this model. In the later version of the model, their model is improved to handle a fracture re-initiation from the middle of the NF [55]. By using the model, they conducted a series of studies for investigating the effect of governing parameters on the interaction between HF and NF and analyzed the effect of "offsetting" on the fracturing fluid pressure [54-56].

Dahi-Taleghani and Olson [26, 57] developed a 2-D X-FEM based hydraulic fracturing model with a new crossing criteria for the interaction between HF and fully cemented NF based on the concept of energy release rate. In this model, the critical energy release rate G_c^{frac} is defined for the cemented NF. By comparing the normalized energy release rate of the NF (G / G_c^{frac}) with the normalized energy release rate of the intact rock (G / G_c^{rock}), the simulator can decide the fracture propagation path (the fracture propagation along the NF or fracture re-initiation from the NF). By using the model, they investigated the governing parameters for the interaction between the HF and the fully cemented NF. They also demonstrated that the fully cemented NF could be debonded before the HF reaches the NF due to stress interference from the HF.

Zhao et. al [39] developed a 2-D hydraulic fracturing simulator based on the commercial simulator PFC^{2D} where the discrete element method is applied. In this model, the simulation domain consists of multiple particles connected by the force of interaction called "bond". A NF is treated as a series of weaker bonds which have lower tensile strength and shear strength than the intact rock. Zhao et. al showed the validity of their

model by comparing their simulation results with the NF interaction experiment done by Zhou [49].

The approaches mentioned above successfully reproduce the complicated interaction behavior between a HF and a NF. However, the results of these models are limited to 2-D. In addition, due to the numerical expense, the application of these models to field scale hydraulic fracturing simulation is difficult.

Other types of numerical models have also been developed. They concentrate on investigating how complicated fracture networks are generated in a field scale domain by the interaction between HFs and NFs. However, for such large scale simulations, all such models adopt a certain simplifications such as an analytical criterion for the interaction between the HF and the NF or assuming pre-defined fracture propagation paths.

Olson [33] and Olson and Dahi-Taleghani [58] analyzed the interaction between multiple HFs and NFs by using a hydraulic fracturing model based on the 2-D DD method with the height correction factor (enhanced 2-D DD model). In this model, a constant pressure distribution is assumed inside the HFs. In addition, the HFs never cross the NFs. Under these assumption, they demonstrated that the propagation pattern of the HFs are highly affected by the magnitude of the net pressure.

Weng et. al [37] developed a pseudo-3D hydraulic fracturing model partially adopting the concept of the 2-D DD model [59] for multiple non-planar fracture growth. By using the model, they showed that a complicated fracture network can be generated by the interaction between the HFs and the NFs. However, in this model, the interaction between the HF and the NF is only evaluated at the intersection point by using the criterion proposed by Gu and Weng [51]. Therefore, once the HF is arrested by the NF, it always propagates until the end of the NF.

Wu [38] developed a hydraulic fracturing model based on the enhanced 2-D DD model coupled with fluid flow formulation. She investigated how a HF propagates after intersecting a NF by changing various parameters (length of NF, principal stress difference, angle of approach and configuration of the NF). Her model can select two crossing criteria (the Gu and Weng criterion [51] for un-cemented NF and Dahi-Taleghani's criterion for cemented NF [57]). However, both of them are evaluated only at the intersection point between the HF and the NF.

McClure [36] developed a hydraulic fracturing model for simulating large scale interaction between multiple HFs and hundreds of NFs based on 2-D DD method. In this model, the fracture propagation and the fracturing fluid flow formulation are fully coupled. By using this simulator, he investigated four different types of mechanism for the large scale interaction between the HFs and the NFs (pure opening, pure shear stimulation, mixed-mechanism stimulation, and primary fracturing with shear stimulation leak-off). Later, he extended the model from 2-D to 3-D [60] and demonstrated the interaction in 3-D domain. However, to achieve a practical calculation speed, all possible fracture propagation paths must be pre-defined in this model.

1.4 Outline of the dissertation

This dissertation is divided into seven chapters. Chapter 2 is an introduction of state-based peridynamics theory. Chapter 3 and Chapter 4 explain the derivation of the fluid flow formulation using peridynamics theory and the development of peridynamics-based hydraulic fracturing model respectively. Chapter 5 and Chapter 6 show the application of the model to investigate complicated fracture propagation behavior.

Chapter 2 introduces the basic theory behind the state-based peridynamics approach for solid mechanics. In this chapter, the definition of “states”, constitutive relations, and material failure models in peridynamics are explained.

Chapter 3 explains the derivation of a new state-based peridynamics formulation for a slightly compressive fluid in a porous medium followed by the verification of the formulation against 2-D analytical solutions.

Chapter 4 shows the development of a new peridynamics-based hydraulic fracturing model. An overview of our simulator’s numerical algorithm is presented, followed by our parallelization scheme. The verification of the hydraulic fracturing model against a 2-D analytical fracture propagation model and a 3-D analytical fracture propagation model are also shown in this chapter.

Chapter 5 introduces the preliminary shear failure model in the new hydraulic fracturing model for simulating the interaction between a hydraulic fracture (HF) and a natural fracture (NF) and shows the validity of our model by comparing with experimental results. The key parameters for the interaction in a 2-D domain are also investigated. Finally, the applicability of our hydraulic fracturing model to the 3-D interaction between HF and NF is demonstrated.

In Chapter 6, the effects of different types of vertical heterogeneity on fracture propagation are systematically investigated by using a different scale of model domains. The fracture propagation behavior near a layer interface, the mechanism of deciding the preferential fracture propagation side in the layers, the effect of small scale sub layers on fracture propagation, and the effect of micro-scale heterogeneity due to varying mineral composition are investigated in this chapter.

Finally, Chapter 7 presents the overall conclusions of this dissertation and makes recommendations for future work.

CHAPTER 2: REVIEW OF PERIDYNAMICS THEORY

2.1 Introduction

Peridynamics is a non-locally reformulated continuum formulation of the classical solid mechanics which is given by Equation (1.1)(2.1) [61].

$$\rho\ddot{\mathbf{u}} = \nabla\bullet\boldsymbol{\sigma} + \mathbf{b} \qquad (2.1)$$

Where,

$\mathbf{b}$	:	body force density	[N/m^3]
$\ddot{\mathbf{u}}$	:	acceleration	[m/s^2]
ρ	:	mass density	[kg/m^3]
$\boldsymbol{\sigma}$	:	Piola–Kirchoff stress tensor	[N/m^2]

In this theory, as shown in Fig. 2.1, material is assumed to be composed of material points of known mass and volume and every material point interacts with all the neighboring material points inside a nonlocal region, referred as a “horizon”, around it. Each interaction pair of a material point with its neighboring material point is referred as a “bond”. The main advantage of this method is the same integral based governing equation can be used for computing force at a material point both in the continuous and discontinuous medium. Since the special derivative is not used in peridynamics theory, the governing equation remains equally valid at the point of discontinuity, which makes it possible to overcome the limitations of the classical differential based theories for discontinuous medium. The peridynamic theory has been successfully applied to diverse

engineering problems [4, 62, 63] involving autonomous initiation, propagation, branching and coalescence of fractures in heterogeneous media.

2.2 State Based Peridynamics Theory

The original peridynamics formulation (2.2), which is called "bond-based peridynamics theory", was derived by Silling [61].

$$\rho_s \ddot{\mathbf{u}} = \int_{H_x} \mathbf{f}\left(\mathbf{u}(\mathbf{x}',t) - \mathbf{u}(\mathbf{x},t), \mathbf{x}' - \mathbf{x}\right) dV_{\mathbf{x}'} + \mathbf{b}(\mathbf{x},t) \qquad (2.2)$$

Where,

$\mathbf{f}$	:	pairwise force function	[N/m^6]
$H_{\mathbf{x}}$	:	neighborhood of $\mathbf{x}$	
$\mathbf{u}$	:	displacement vector field	[m]
$\ddot{\mathbf{u}}$	:	acceleration	[m/s^2]
$V_{\mathbf{x}'}$	:	differential volume of $\mathbf{x}'$	[m^3]
$\mathbf{x}$	:	material point	[m]
$\mathbf{x}'$	:	material point inside the horizon of $\mathbf{x}$	[m]
ρ_s	:	density of solid	[kg/m^3]

As shown in Fig. 2.2 (a), bond-based peridynamics formulation assumes the pairwise force interaction of the same magnitude in a bond, which results in the model limitation such as being only able to simulate an isotropic, linear, micro-elastic material which has Poisson's ratio of one-fourth. In order to overcome the limitations, Silling et al.

developed the state-based peridynamics theory by introducing a mathematical concept called “state”[2]. This concept allows to model materials with any Poisson’s ratio as well as applying any constitutive model in classical theory.

2.2.1 STATES

In the state-based peridynamic formulation, mathematical objects called peridynamic states have been introduced for convenience. Peridynamic states depend upon position and time, shown in square brackets, and operate on a vector, shown in angled brackets, connecting any two material points. Depending on whether the value of this operation is a scalar or vector, the state is called a scalar-state or a vector state respectively. To differentiate, peridynamic scalar states are denoted with non-bold face letters with an underline and peridynamic vector states are denoted with bold face letters with an underline. For instance, a vector state acting on a vector ξ is expressed as $\underline{\mathbf{A}}\left[\mathbf{x},t\right]\langle\boldsymbol{\xi}\rangle$ and a scalar state acting on a vector ξ is expressed as $\underline{a}\left[\mathbf{x},t\right]\langle\boldsymbol{\xi}\rangle$.The mathematical definition of these peridynamic states is provided wherever they have been used in this work.

2.2.2 REFERENCE AND DEFORMED CONFIGURATION

The reference position of material points $\mathbf{x}$ and $\mathbf{x}'$ in the reference configuration is given by the reference position vector state $\underline{\mathbf{X}}$ in state-based peridynamics theory.

$$\underline{\mathbf{X}}\langle\boldsymbol{\xi}\rangle = \mathbf{x}' - \mathbf{x} = \boldsymbol{\xi} \tag{2.3}$$

Where, ξ is a bond vector (unit: [m]). The relative position of the same material points in the deformed configuration is given by the deformed position vector state $\underline{\mathbf{Y}}$.

$$\underline{\mathbf{Y}}\langle\boldsymbol{\xi}\rangle = \mathbf{y}(\mathbf{x}') - \mathbf{y}(\mathbf{x}) = \boldsymbol{\xi} + \boldsymbol{\eta} \tag{2.4}$$

Where,

$\mathbf{y}$: deformed coordination [m]

$\boldsymbol{\eta}$: relative displacement ($= \mathbf{u}(\mathbf{x}') - \mathbf{u}(\mathbf{x})$) [m]

The relationship among those states and vectors is shown in Fig. 2.3. The bond length in the reference and the deformed configuration are given by the following scalar state respectively.

$$\underline{x}\langle\boldsymbol{\xi}\rangle = \|\boldsymbol{\xi}\| \tag{2.5}$$

$$\underline{y}\langle\boldsymbol{\xi}\rangle = \|\boldsymbol{\xi} + \boldsymbol{\eta}\| \tag{2.6}$$

2.2.3 STATE-BASED PERIDYNAMICS EQUATION OF MOTION

The generalized state-based peridynamics equation of motion is defined by the following formulation [2]. The detail of the derivation of Equation (2.7) is given in Appendix A.1.

$$\rho\ddot{u} = \int_{H_x} \left(\underline{T}[\mathbf{x}, t]\langle\boldsymbol{\xi}\rangle - \underline{T}[\mathbf{x}', t]\langle -\boldsymbol{\xi}\rangle\right) dV_{\mathbf{x}'} + b[\mathbf{x}] \tag{2.7}$$

Where,

$\underline{T}$: peridynamic force vector state [N/m^6]

$\boldsymbol{\xi}$: reference position vector ($= \mathbf{x}' - \mathbf{x}$) [m]

2.2.4 CONSTITUTIVE RELATION

The way how the peridynamic force vector state $\underline{\boldsymbol{T}}$ depends on deformed vector state $\underline{\mathbf{Y}}\langle\boldsymbol{\xi}\rangle$ is determined by the constitutive material model. If the force vector state has the same direction as the deformed vector state, as shown in Fig. 2.2 (b), the constituive model is called ordinary. The force vector state in the ordinaly material is given by the following formulation.

$$\underline{T}[\mathbf{x},t]\langle\boldsymbol{\xi}\rangle = \underline{t}[\mathbf{x},t]\langle\boldsymbol{\xi}\rangle \frac{\underline{\mathbf{Y}}\langle\boldsymbol{\xi}\rangle}{\left\|\underline{\mathbf{Y}}\langle\boldsymbol{\xi}\rangle\right\|} = \underline{t}[\mathbf{x},t]\langle\boldsymbol{\xi}\rangle \frac{\boldsymbol{\xi}+\boldsymbol{\eta}}{\left\|\boldsymbol{\xi}+\boldsymbol{\eta}\right\|} \tag{2.8}$$

Where, $\underline{t}$ is peridynamic force scalar state (unit: [N/m^6]). Liniear elastic material model mainly used in this research is included in the ordinary material group. The force scalar state $\underline{t}$ in the peridynamic liniear elastic is given by the following formulation. The datil of the derivation of Equation (2.9) is shown Appendix A2.

$$\underline{t}[\mathbf{x},t]\langle\boldsymbol{\xi}\rangle = \frac{3K\theta}{m}\underline{\omega}\underline{x}\langle\boldsymbol{\xi}\rangle + \frac{15G}{m}\underline{\omega}\underline{e}^{d}\langle\boldsymbol{\xi}\rangle \tag{2.9}$$

$$\underline{e}^{d}\langle\boldsymbol{\xi}\rangle = \underline{e}\langle\boldsymbol{\xi}\rangle - \frac{\theta}{3}\underline{x}\langle\boldsymbol{\xi}\rangle \tag{2.10}$$

Where,

$\underline{e}\langle\boldsymbol{\xi}\rangle$: elongation scalar state [m]

m : weighted volume [m^5]

G : shear modulus [Pa]

K : bulk modulus [Pa]

θ : dilatation

$\underline{\omega}$: influence function

The elongation scalar state, weighted volume, and dilatation are defined by the following formulations respectively.

$$\underline{e}\langle\boldsymbol{\xi}\rangle = \underline{y}\langle\boldsymbol{\xi}\rangle - \underline{x}\langle\boldsymbol{\xi}\rangle = \|\boldsymbol{\xi}+\boldsymbol{\eta}\| - \|\boldsymbol{\xi}\| \tag{2.11}$$

$$m = \underline{\omega}\underline{x}\langle\boldsymbol{\xi}\rangle \bullet \underline{x}\langle\boldsymbol{\xi}\rangle = \int_{H_x} \underline{\omega}\underline{x}\langle\boldsymbol{\xi}\rangle \underline{x}\langle\boldsymbol{\xi}\rangle \, dV_{\mathbf{x}'} \tag{2.12}$$

$$\theta = \frac{3}{m}\underline{\omega}\underline{x} \bullet \underline{e} = \frac{3}{m}\int_{H_x} \underline{\omega}\underline{x}\langle\boldsymbol{\xi}\rangle e\langle\boldsymbol{\xi}\rangle \, dV_{\mathbf{x}'} \tag{2.13}$$

For small deformation, θ is a measure of the volumetric strain. As highlighted by Silling et. al [2], for an isotropic deformation of the following form for all $\mathbf{x}$,

$$\underline{\mathbf{Y}} = (1+\varepsilon)\underline{\mathbf{X}} \tag{2.14}$$

If we assume constant $|\varepsilon| \ll 1$, θ is the exactly same as the trace of strain tensor ($\theta = 3\varepsilon$). In this research, we also examined the fracture propagation behavior in 2-D plain strain condition in addition to 3-D condition. If 2-D plain strain condition is assumed, the formulation (2.9), (2.12), and (2.13) change as follows,

$$\underline{t}[\mathbf{x},t]\langle\boldsymbol{\xi}\rangle = \frac{2K\theta}{m}\underline{\omega}\underline{x}\langle\boldsymbol{\xi}\rangle + \frac{8G}{m}\underline{\omega}\underline{e}^{d}\langle\boldsymbol{\xi}\rangle \tag{2.15}$$

$$m = \underline{\underline{\omega}}\underline{x}\langle\xi\rangle \bullet \underline{x}\langle\xi\rangle = \int_{H_x} \underline{\underline{\omega}}\underline{x}\langle\xi\rangle \underline{x}\langle\xi\rangle dA_{\mathbf{x}'} \tag{2.16}$$

$$\theta = \frac{3}{m}\underline{\underline{\omega}}\underline{x} \bullet \underline{e} = \frac{3}{m}\int_{H_x} \underline{\underline{\omega}}\underline{x}\langle\xi\rangle e\langle\xi\rangle dA_{\mathbf{x}'} \tag{2.17}$$

Where, $dA_{\mathbf{x}'}$ is differential area (unit: [m^2]).

2.2.4 MATERIAL FAILURE MODEL

In the state based peridynamics theory, two types of bond failure criteria are commonly used (critical strain criteria and critical energy criteria). In the simulator developed in this research, one of those criteria can be selected.

In the critical strain bond failure criteria, the failure of a bond is decided only by the strain of the bond defined below.

$$s = \frac{\underline{e}\langle\xi\rangle}{\underline{x}\langle\xi\rangle} = \frac{\|\xi + \eta\| - \|\xi\|}{\|\xi\|} \tag{2.18}$$

If a bond strain exceeds the yield value which is called critical strain s_c, the force scalar state of the bond becomes zero by multiplying the following boolean function. Note that critical strain s_c can be regarded as material property based on energy release rate and length scale.

$$\beta\langle\xi\rangle = \begin{cases} 0 & (s > s_c) \\ 1 & (otherwise) \end{cases} \tag{2.19}$$

Another approach is the energy based failure criteria proposed by Foster et.al [64]. In this criteria, the failure of a bond is decided based on the total energy density stored in

the bond. When the total energy density stored in a bond exceeds the predetermined critical energy density ω_c due to relative displacement of the associated material points, the bond breaks. As shown in Equation (2.20) and Fig. 2.4, the total energy density stored in a bond is obtained by the integration of the dot product of the force density vector acting on the bond and the relative displacement vector of the two material points ($\mathbf{x}$ and $\mathbf{x}'$) forming the bond. Note that, as shown in Equation (2.21), energy density stored in a bond must be evaluated in tensile condition.

$$\omega_{\xi} = \int_0^{\boldsymbol{\eta}\left(t_{final}\right)} \left\{ \underline{T}^{*}\left[\mathbf{x},t\right]\langle\boldsymbol{\xi}\rangle - \underline{T}^{*}\left[\mathbf{x}',t\right]\langle-\boldsymbol{\xi}\rangle \right\} \bullet d\boldsymbol{\eta} \tag{2.20}$$

$$\underline{T}^{*}\left[\mathbf{x},t\right]\langle\boldsymbol{\xi}\rangle - \underline{T}^{*}\left[\mathbf{x}',t\right]\langle-\boldsymbol{\xi}\rangle = \max\left(\underline{t}\left[\mathbf{x},t\right]\langle\boldsymbol{\xi}\rangle - \underline{t}\left[\mathbf{x}',t\right]\langle-\boldsymbol{\xi}\rangle, 0.0\right)\frac{\boldsymbol{\xi}+\boldsymbol{\eta}}{\left\|\boldsymbol{\xi}+\boldsymbol{\eta}\right\|} \tag{2.21}$$

Where, $\boldsymbol{\eta}\left(t_{final}\right)$ is the final scalar values of the relative displacement (unit: [m]). The peridynamic critical energy density ω_c in each bond is obtained by summing up the energy required to create unit fracture as a function of critical energy density and equating it to the energy release rate. As shown in Equation (2.22), energy release rate is given by integrating the energy to break all the bond connecting each point A along 0 <= z <= δ to point B in the spherical cap (a green region in Fig. 2.5) using the coordinate system centered at A.

$$\begin{aligned} G_c &= \int_0^{\delta}\int_0^{2\pi}\int_z^{\delta}\int_0^{\cos^{-1}\left(\frac{z}{\xi}\right)} \omega_c \xi^2 \sin\varphi \, d\varphi \, d\xi \, d\theta \, dz \\ &= \frac{\pi\delta^4}{4}\omega_c \end{aligned} \tag{2.22}$$

Where,

G_c : energy release rate [J/m^2]

ω_c : peridynamic critical energy density [J/m^6]

By solving Equation (2.22) for the critical energy density ω_c, we obtain

$$\omega_c = \frac{4G_c}{\pi\delta^4} \tag{2.23}$$

If fracture toughness K_{IC} is known, Equation (2.23) can be reformulated from the linear elastic fracture mechanics as follows,

$$\omega_c = \frac{4G_c}{\pi\delta^4} = \frac{4{K_{IC}}^2}{\pi\delta^4 E} \tag{2.24}$$

Where,

E : Young's modulus [Pa]

K_{IC} : fracture toughness [Pa/$\sqrt{m}$]

The relationship between ω_c and G_c in 2D is also derived by the following formulations.

$$\begin{aligned} G_c &= \int_0^{\delta}\int_z^{\delta}\int_{\sin^{-1}\left(\frac{z}{\xi}\right)}^{\pi-\sin^{-1}\left(\frac{z}{\xi}\right)} \omega_c \xi\, d\xi\, d\theta\, dz \\ &= \frac{4\delta^3}{9}\omega_c \end{aligned} \tag{2.25}$$

$$\omega_c = \frac{9G_c}{4\delta^3} \tag{2.26}$$

If 2D plain strain condition is assumed, Equation (2.26) is expressed by using fracture toughness as follows,

$$\omega_c = \frac{9G_c}{4\delta^3} = \frac{9K_{IC}{}^2\left(1-\nu^2\right)}{4\delta^3 E} \tag{2.27}$$

Where, ν is Poisson's ratio. The bond failure evaluated by the above criteria is numerically implemented through the multiplier for the influence function in the constitutive material model. Note that, in the case of multi material problem where two ends of the bond have the different material properties, the smaller critical energy density of the two different material is used as the critical energy density for the bond.

Force scalar state becomes zero in a broken bond by applying the following boolean function.

$$\beta\left\langle\boldsymbol{\xi}\right\rangle = \begin{cases} 0 & \left(\omega_{\boldsymbol{\xi}} > \omega_c\right) \\ 1 & \left(otherwise\right) \end{cases} \tag{2.28}$$

In a peridynamic formulation of solid mechanics, material failure is evaluated through a scalar filed referred as "damage" defined as the following function of broken bonds at a material point in its horizon.

$$d\left(\mathbf{x}\right) = 1 - \frac{\int_{H_{\mathbf{x}}} \beta\left\langle\boldsymbol{\xi}\right\rangle dV_{\mathbf{x}'}}{\int_{H_{\mathbf{x}}} dV_{\mathbf{x}'}} \tag{2.29}$$

Where, d is damage. Damage d at any point and time varies from 0 to 1, with 1 representing all the bonds attached to a point broken. Once bonds start to break and stop sustaining any tensile load, a softening material response results in leading to crack

nucleation. However, only above a critical damage value, when a certain number of bonds fail and coalesce onto a surface, fracture propagates.

2.2.5 PIORA-KIRCHHOFF STRESS TENSOR

In peridynamics simulation, the value of Piora-Kirchhoff stress tensor at the reference configuration is not directly evaluated. However, since stress is one of the most important measurable quantities in solid mechanics, the way how peridynamics force state relates the stress tensor is important to compare the simulation results with measured data. The relationship between Piora-Kirchhoff stress tensor and peridynamics vector force state is defined through the areal force density by the following formulation derived by Silling [61].

$$\boldsymbol{\sigma}\mathbf{n} = \tau(\mathbf{x},\mathbf{n}) = \int_{L}\int_{R^{+}} \left\{\underline{T}[\mathbf{x},t]\langle\boldsymbol{\xi}\rangle - \underline{T}[\mathbf{x}',t]\langle-\boldsymbol{\xi}\rangle\right\} dV_{\mathbf{x}'} d\hat{l} \tag{2.30}$$

Where,

$\mathbf{n}$: unit vector perpendicular to the given surface at $\mathbf{x}$ [m]

$\hat{l}$: distance from $\mathbf{x}$ parallel to $\mathbf{n}$

$\tau(\mathbf{x},\mathbf{n})$: areal force density [N/m]

In the above formulation, L and R^{+} are defined as follows (see also Fig. 2.6),

$$L = \left\{\hat{\mathbf{x}} \in B : \hat{\mathbf{x}} = \mathbf{x} - s\mathbf{n}, 0 \le s \le \infty\right\} \tag{2.31}$$

$$R^{+} = \left\{\mathbf{x}' \in R : (\mathbf{x}' - \mathbf{x}) \cdot \mathbf{n} \ge 0\right\}, \quad R^{-} = \left\{\mathbf{x}' \in R : (\mathbf{x}' - \mathbf{x}) \cdot \mathbf{n} \le 0\right\} \tag{2.32}$$

Piora-Kirchhoff stress tensor $\boldsymbol{\sigma}$ is gotten from the traction of the three independent surfaces which is calculated by Equation (2.30).

2.2.6 DISCRETIZATION

In order to solve the peridynamic equation of motion numerically, Equation (2.7) is discretized as follows,

$$\rho_s \frac{\left\{\left(y_i^{(n+1)} - y_i^{(n)}\right) - \left(y_i^{(n)} - y_i^{(n-1)}\right)\right\}}{\Delta t^2} = \sum_{j=1}^{N}\left\{T\left[\mathbf{x}_i, t\right]\left\langle \mathbf{x}_j - \mathbf{x}_i \right\rangle - T\left[\mathbf{x}_j, t\right]\left\langle \mathbf{x}_i - \mathbf{x}_j \right\rangle\right\} \Delta V_{\mathbf{x}'} \tag{2.33}$$

$$\begin{aligned} & T\left[\mathbf{x}_i, t\right]\left\langle \mathbf{x}_j - \mathbf{x}_i \right\rangle - T\left[\mathbf{x}_j, t\right]\left\langle \mathbf{x}_i - \mathbf{x}_j \right\rangle \\ & = \beta_{ij}\left[\left\{\left(3K - 5G\right)\left(\frac{\theta_i^{(n+1)}\omega_{ij}}{m_i} + \frac{\theta_j^{(n+1)}\omega_{ji}}{m_j}\right)\right\}\left\|\mathbf{x}_j - \mathbf{x}_i\right\| + 15G\left(\frac{\omega_{ij}}{m_i} + \frac{\omega_{ji}}{m_j}\right)e_{ij}^{(n+1)}\right]\frac{\left(\mathbf{y}_j^{(n+1)} - \mathbf{y}_i^{(n+1)}\right)}{\left\|\mathbf{y}_j^{(n+1)} - \mathbf{y}_i^{(n+1)}\right\|} \end{aligned} \tag{2.34}$$

$$m_i = \sum_{j=1}^{N} \underline{\omega}\underline{\xi}^2 \Delta V_{\mathbf{x}_J} = \sum_{j=1}^{N} \underline{\omega}\left\|\mathbf{y}_j^{(n+1)} - \mathbf{y}_i^{(n+1)}\right\|^2 \Delta V_{\mathbf{x}_J} \tag{2.35}$$

$$\theta_i = \frac{3}{m_i}\sum_{j=1}^{N} \beta_{ij}\underline{\omega}\underline{e}_{ij}^{(n+1)} \Delta V_{\mathbf{x}_j} = \frac{3}{m_i}\sum_{j=1}^{N} \omega_{ij}\left(\left\|\mathbf{y}_j^{(n+1)} - \mathbf{y}_i^{(n+1)}\right\| - \left\|\mathbf{x}_j - \mathbf{x}_i\right\|\right)\Delta V_{\mathbf{x}_j} \tag{2.36}$$

Where,

N : number of neighbors of element i

$(n+1)$: time step (n+1)

$\Delta V_{\mathbf{x}_j}$: volume of element j inside the horizon of element i [m^3]

β_{ij} : multiplier for bond ij (1.0: unbroken, 0.0: broken)

ω_{ij} : influence function for bond ij ($=\omega_{ji}$) (default value = $1/\xi$)

In the above formulations, the volumes of each element j are defined by the following formulation (see also Fig. 2.7) if the initial material point is allocated in the constant distance Cartesian coordinate.

$$\Delta V_{x_j} = \Delta l^3 \tag{2.37}$$

Where, Δl is minimum material points' distance (unit: [m]).

Although volumes of the most of the material points in a horizon are just expressed by Equation (2.37), volumes of some of the material points in a horizon are smaller than Equation (2.37) since they are not fully included, as shown in Fig. 2.8, inside the horizon. Hence, in order to improve the accuracy of the volume calculation, $\Delta V_{\mathbf{x}_j}$ is modified by the following volume modifier.

$$\chi\left(\mathbf{x}_j - \mathbf{x}_i\right) = \begin{Bmatrix} \dfrac{\delta - \left\|\mathbf{x}_j - \mathbf{x}_i\right\|}{2\Delta l} + \left(\dfrac{1}{2}\right) & \text{if } \delta - \Delta l \le \left\|\mathbf{x}_j - \mathbf{x}_i\right\| \le \delta \\ 1 & \text{if } \left\|\mathbf{x}_j - \mathbf{x}_i\right\| \le \delta - \Delta l \\ 0 & \text{otherwise} \end{Bmatrix} \tag{2.38}$$

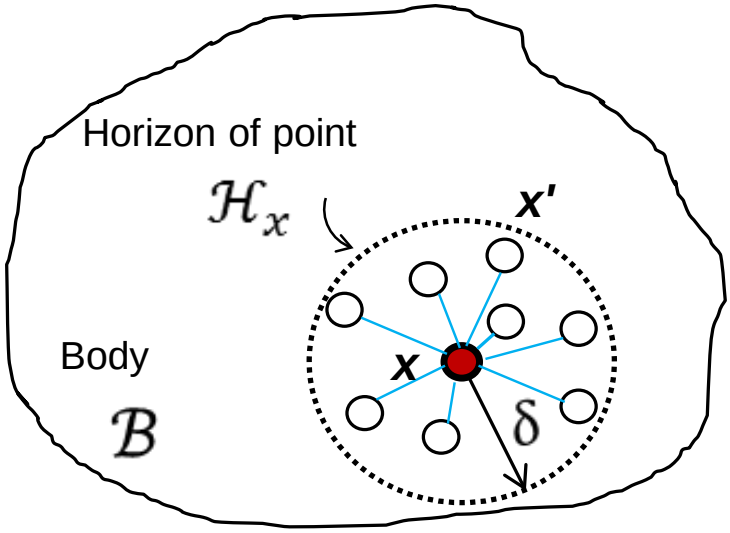

Fig. 2.1 Concept of horizon.

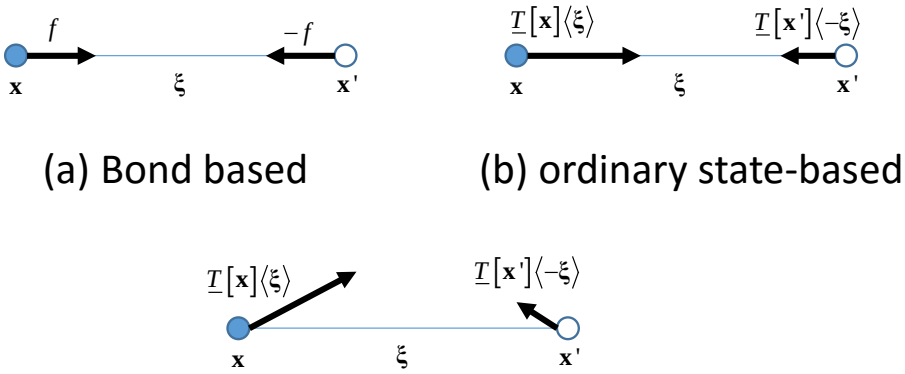

Fig. 2.2 Concepts of various states.

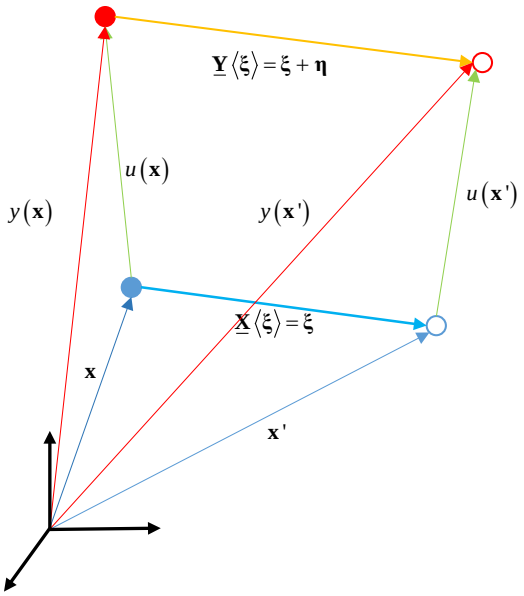

Fig. 2.3 The relationship among states and vectors.

$$w_\xi = \int_0^{\eta(t_{\text{final}})} \{\underline{\mathbf{T}}[\mathrm{x},t]\langle \mathrm{x}' - \mathrm{x}\rangle - \underline{\mathbf{T}}[\mathrm{x}',t]\langle \mathrm{x} - \mathrm{x}'\rangle\} \cdot d\eta$$

discretize

$$\omega_\xi = \sum_1^3 f_k \bullet d\eta_k$$

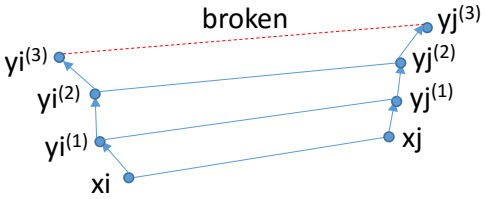

For example, the total energy density stored in the bond shown in the above figure until third steps is calculated by the following equation.

where,

$$f_k = T[x_i,t_k]\langle x_j - x_i\rangle - T[x_j,t_k]\langle x_i - x_j\rangle$$
$$= (3K-5G)\left(\frac{\theta_i^{(k)}\omega_i}{m_i} + \frac{\theta_j^{(k)}\omega_j}{m_j}\right)\|x_j - x_i\| + 15G\left(\frac{\omega_i}{m_i} + \frac{\omega_j}{m_j}\right)e^{(k)}$$

$$d\eta_1 = y_i^{(1)} - x_i + y_j^{(1)} - x_j$$
$$d\eta_2 = y_i^{(2)} - y_i^{(1)} + y_j^{(2)} - y_j^{(1)}$$
$$d\eta_3 = y_i^{(3)} - y_i^{(2)} + y_j^{(3)} - y_j^{(2)}$$

Fig. 2.4 Concept of total energy density.

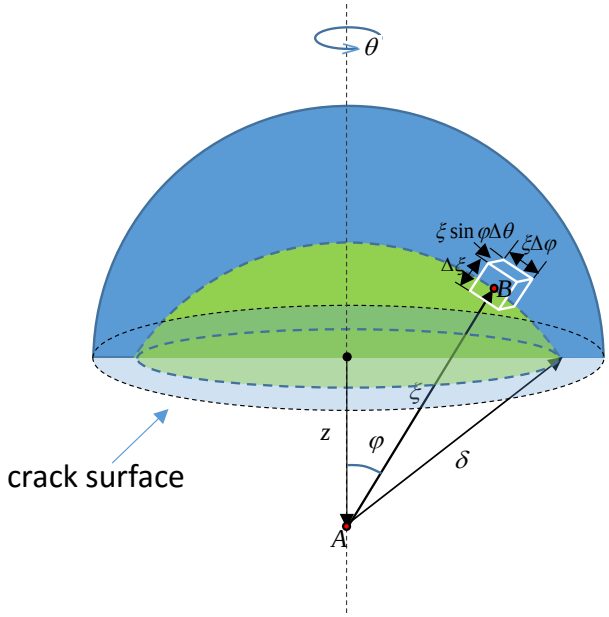

Fig. 2.5 Calculation of energy release late in peridynamics.

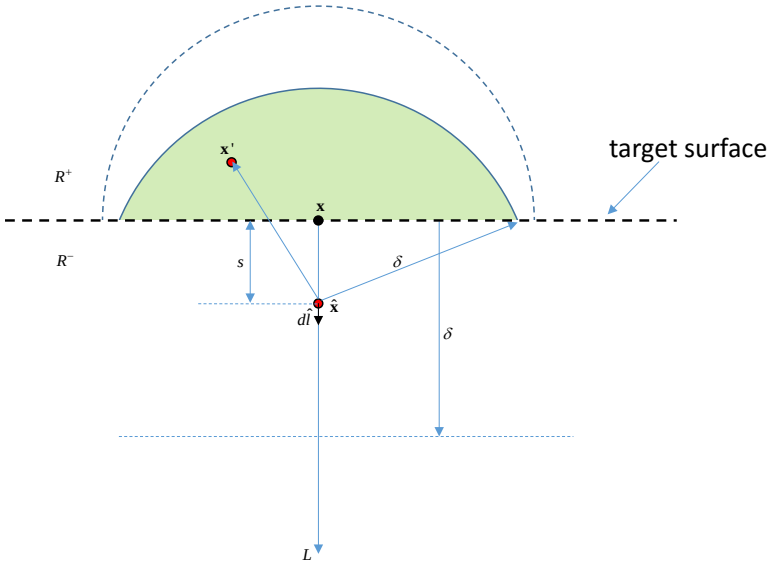

Fig. 2.6 Traction calculation in peridynamics.

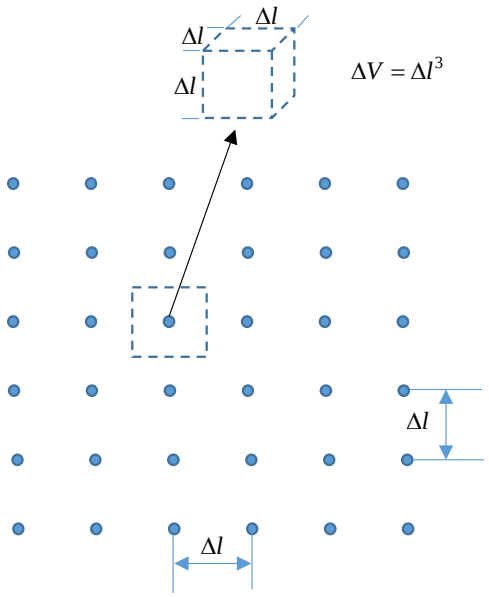

Fig. 2.7 Definition of elements.

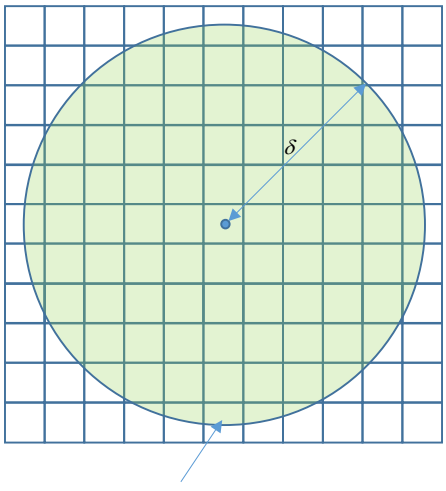

Fig. 2.8 Horizon covered area.

CHAPTER 3: DEVELOPMENT OF A PERIDYNAMICS-BASED POROUS FLOW MODEL

3.1 Introduction

Peridynamics is a recently developed continuum mechanics theory that is particularly suited to account for discontinuities such as fractures. The peridynamics theory for fracture propagation in purely elastic mechanics problems has been fully developed in the past and the effectiveness of the theory has been demonstrated [1, 2, 9]. However, a peridynamic theory for fluid flow in a porous medium and a fluid driven fracturing process has not been developed. In order to develop a peridynamics-based hydraulic fracturing model that can simulate multiple, non-planar and competing fractures, it is necessary to develop a peridynamic fluid flow formulation for flow in a porous medium and for flow inside a fracture and to couple those formulations with the peridynamics formulation for solid mechanics. In this chapter[1], as a first step in the development of a peridynamics-based hydraulic fracturing simulator, a general state-based peridynamics formulation for slightly compressive single phase flow in a heterogeneous porous medium is presented.

The porous flow formulation and fracturing fluid flow formulation are a general class of convection/diffusion equations in classical continuum theories. In these classical theories, the diffusion process is expressed as a result of a random walk of particles which result in Gaussian probability distribution. However, in complicated systems in nature, diffusion does not always follows the Gaussian statistics due to the heterogeneity of the porous medium such as pre-existing micro-cracks [65, 66]. Typically this anomalous

[1] This Chapter forms the basis of the following publication: Journal of Computational Physics: Katiyar, A., J. T. Foster, H. Ouchi, and M. M. Sharma, A peridynamic formulation of pressure driven convective fluid transport in porous media. 2014. 261: p. 209-229.

diffusion is simulated through continuous-time random walks [67, 68] or fractional dynamics [69]. However, another way to handle this anomalous diffusion is by using a non-local model. Several researchers have investigated non-local diffusion problems in peridynamics. Bobaru and Duagpanya [70, 71] presented a peridynamic diffusion formulation for the isotropic heat conduction problem by extending the original peridynamics formulation proposed by Silling [61]. Generic forms of peridynamic diffusion models have been extensively analyzed by Du et.al [72-74] and extended to model advection/diffusion problems. Later, Seleson et al. [75] proposed a useful constitutive model for the non-local diffusion problem and showed that the non-local model can preserve discontinuities across boundaries of different domains in a 1-D problem.

The work presented in this chapter uses the ideas first presented by Bobaru and Duangpanya [70, 71] and applies them to fluid flow and anisotropic diffusion in heterogeneous materials with applications to fluid flow in porous media (and fluid flow in fracture space through the lubrication approximation). First, a state-based peridynamic formulation for simulating convective transport of a slightly compressive fluid is derived based on a variational formulation of the classical theory. Our peridynamic flow formulation's non-local constitutive parameter is then related to the parameter of classical theory by deriving a relationship between them. This allows us to recover the isotropic model of Bobal and Duangpanya as a special case. Finally, we demonstrate the application of our model to simulate the well-known 5 spot well pattern problem as well as more complex problems with discontinuities (an impermeable area inside a simulation domain).

3.2 Mathematical model

As shown in Chapter 2, in a state-based peridynamics formulation, the peridynamic state of any given point in space is represented by a set of scalars or vector operators. The peridynamic state depends upon position and time and operates on a vector connecting any two material points. To distinguish these states, peridynamic scalar states are denoted with non-bold character, while peridynamic vector states are denoted with bold face letters with an underline (in this chapter and the previous chapter).

3.2.1 STATE-BASED PERIDYNAMIC FORMULATION FOR SINGLE-PHASE FLOW OF A LIQUID OF SMALL AND CONSTANT COMPRESSIBILITY THROUGH A POROUS MEDIUM

Here, we derive a state-based peridynamics formulation of single phase, slightly compressible fluid flow. Let a bond in some reference configuration occupy a region B. The mass conservation equation for single phase flow in a porous medium at position $\mathbf{x} \in B$ is given as,.

$$\frac{\partial\left(\rho[\mathbf{x},t]\phi[\mathbf{x},t]\right)}{\partial t} = -\nabla\cdot\left(\rho[\mathbf{x},t]\mathbf{u}[\mathbf{x},t]\right) + R[\mathbf{x},t] \qquad (3.1)$$

Where,

R	:	source/sink term	[kg/s]
t	:	time	[s]
$\mathbf{u}$	:	fluid velocity	[m/s]
$\mathbf{x}$	:	position vector	[m]

ϕ : porosity

ρ : fluid density [kg/m^3]

For a slightly compressible fluid, the fluid density at a fixed temperature is given by the following equation.

$$\rho[\mathbf{x}] = \rho_0 \left[1 + c\left(p[\mathbf{x}] - p_0[\mathbf{x}]\right)\right] \tag{3.2}$$

Where,

c : fluid compressibility [1/Pa]

p_0 : reference pressure [Pa]

ρ_0 : reference fluid density at pressure p_0 [kg/m^3]

The volumetric flux of fluid $\mathbf{u}$ can be obtained from Darcy's law,

$$\mathbf{u}[\mathbf{x}] = -\frac{1}{\mu}\mathbf{k}[\mathbf{x}]\nabla\Phi[\mathbf{x}] \tag{3.3}$$

Where,

$\mathbf{k}$: permeability tensor [m^2]

$\mathbf{u}$: fluid velocity [m/s]

Φ : fluid potential [Pa]

μ : fluid viscosity [Pa s]

The fluid potential is given as a function of pressure, density, and depth

$$\Phi[\mathbf{x}] = p[\mathbf{x}] + \rho[\mathbf{x}]\, g\, z[\mathbf{x}] \tag{3.4}$$

Where, g is the gravitational acceleration in m/s^2. Substituting Equation (3.3) into Equation (3.1) yields

$$\frac{\partial\left(\rho[\mathbf{x},t]\phi[\mathbf{x},t]\right)}{\partial t} = \nabla\cdot\left(\frac{\rho[\mathbf{x},t]}{\mu}\mathbf{k}[\mathbf{x}]\nabla\Phi[\mathbf{x}]\right) + R[\mathbf{x},t] \tag{3.5}$$

For the purpose of further analysis, we define

$$r[\mathbf{x}] = R[\mathbf{x}] - \frac{\partial\rho[\mathbf{x}]\phi[\mathbf{x}]}{\partial t} \tag{3.6}$$

From Equation (3.5) and (3.6), we obtain

$$\nabla\cdot\left(\frac{\rho[\mathbf{x},t]}{\mu}\mathbf{k}[\mathbf{x}]\nabla\Phi[\mathbf{x}]\right) + r[\mathbf{x}] = 0 \tag{3.7}$$

For the assumption of slightly compressible fluid, small pressure gradients and constant liquid viscosity, the above equation simplifies to the following form.

$$\nabla\cdot\left(\frac{\rho_0}{\mu}\mathbf{k}[\mathbf{x}]\nabla\Phi[\mathbf{x}]\right) + r[\mathbf{x}] = 0 \tag{3.8}$$

Now we multiply both side of Equation (3.8) by a virtual change in flow potential $\delta\Phi[\mathbf{x}]$ and integrate over body B.

$$\int_B \left[\nabla \cdot \left(\frac{\rho_0}{\mu} \mathbf{k}[\mathbf{x}] \nabla \Phi[\mathbf{x}] \right) \right] \delta\Phi[\mathbf{x}] dV_x + \int_B r[\mathbf{x}] \delta\Phi[\mathbf{x}] dV_x = 0 \qquad (3.9)$$

We integrate-by-parts the first term of Equation (3.9) to arrive at Equation (3.10). Here, we have assumed that the flow potential field is defined on the boundary and, therefore, the virtual variation of flow potential must vanish, i.e. $\delta\Phi[\mathbf{x}]\big|_{\partial B} = 0$.

$$\int_B \left[\nabla \delta\Phi[\mathbf{x}] \cdot \left(\frac{\rho_0}{\mu} \mathbf{k}[\mathbf{x}] \nabla \Phi[\mathbf{x}] \right) \right] dV_x - \int_B r[\mathbf{x}] \delta\Phi[\mathbf{x}] dV_x = 0 \qquad (3.10)$$

Equation (3.10) is the so called "weak" or variational form of Equation (3.5). Recognizing the first term in Equation (3.10) to be bilinear and symmetric due to $\mathbf{k}$ being symmetric, we can rewrite Equation (3.10) as the well-known "Variational problem"[76].

$$B[\delta\Phi[\mathbf{x}], \Phi[\mathbf{x}]] - l[\delta\Phi[\mathbf{x}]] = 0 \qquad (3.11)$$

Where,

$$B[\delta\Phi[\mathbf{x}], \Phi[\mathbf{x}]] = \int_B \left(\frac{\rho_0}{\mu} \mathbf{k}[\mathbf{x}] \nabla \Phi[\mathbf{x}] \right) \cdot \nabla \delta\Phi[\mathbf{x}] dV_x \qquad (3.12)$$

$$l[\delta\Phi[\mathbf{x}]] = \int_B r[\mathbf{x}] \delta\Phi[\mathbf{x}] dV_x \qquad (3.13)$$

It can be verified that the minimization of a quadratic functional, $\mathbf{I}[\mathbf{x}]$, is equivalent to the solution of the variational problem [76].

$$\delta I[\mathbf{x}] = B[\delta\Phi[\mathbf{x}], \Phi[\mathbf{x}]] - l[\delta\Phi[\mathbf{x}]] = 0 \tag{3.14}$$

Equation (3.14) is also written as Equation (3.15) where the symmetricity of B has been utilized in the second step.

$$\delta I[\mathbf{x}] = \frac{1}{2}\delta B[\Phi[\mathbf{x}], \Phi[\mathbf{x}]] - \delta l[\Phi[\mathbf{x}]] = \delta\left[\frac{1}{2}B[\Phi[\mathbf{x}], \Phi[\mathbf{x}]] - l[\Phi[\mathbf{x}]]\right] = 0 \tag{3.15}$$

Therefore, the quadratic functional can be inferred as follows.

$$I[\mathbf{x}] = \frac{1}{2}\int_B \nabla\Phi[\mathbf{x}] \cdot \left(\frac{\rho_0}{\mu}\mathbf{k}[\mathbf{x}]\nabla\Phi[\mathbf{x}]\right) dV_x - \int_B r[\mathbf{x}]\Phi[\mathbf{x}]\, dV_x \tag{3.16}$$

Equation (3.16) can also be written as Equation (3.17).

$$I[\mathbf{x}] = \int_B Z[\nabla\Phi[\mathbf{x}]] dV_x - \int_B r[\mathbf{x}]\Phi[\mathbf{x}]\, dV_x \tag{3.17}$$

Where,

$$Z[\nabla\Phi[\mathbf{x}]] = \frac{1}{2}\nabla\Phi[\mathbf{x}] \cdot \left(\frac{\rho_0}{\mu}\mathbf{k}[\mathbf{x}]\nabla\Phi[\mathbf{x}]\right) \tag{3.18}$$

At this step, we assume the peridynamic analogue of Equation (3.18) to develop a mathematical description of fluid flow in porous medium using the state-based peridynamic theory.

$$\hat{I}[\mathbf{x}] = \int_B \hat{Z}[\underline{\Phi}[\mathbf{x}]\langle\xi\rangle] dV_x - \int_B r[\mathbf{x}]\Phi[\mathbf{x}]\, dV_x \tag{3.19}$$

$$\underline{\Phi}[\mathbf{x}]\langle\xi\rangle = \Phi[\mathbf{x}'] - \Phi[\mathbf{x}] \tag{3.20}$$

Where, $\underline{\Phi}[\mathbf{x}]\langle\xi\rangle$ is peridynamic flow state (dimension: [Pa]). Here, $\mathbf{x}' \in B$ is separated from $\mathbf{x}$ by a finite distance. Bond $\xi = \mathbf{x}' - \mathbf{x}$ is analogous to a channel in Fig. 3.1. Angle brackets are used to distinguish the bond that a state operators on from spatial and temporal dependencies. The flow potential state maps a vector $\xi \in B$ onto the potential difference across the two end points of that vector or bond. Next we will proceed with taking the first variation of $\widehat{I}$, but briefly, let us return to a property of the Frechet derivative. If $\delta\underline{\Phi}$ is a virtual variation in $\underline{\Phi}$, then at any $\mathbf{x}$, the following formulation is valid.

$$\delta\hat{Z}\left[\underline{\Phi}[\mathbf{x}]\right] = \hat{Z}\left[\underline{\Phi}[\mathbf{x}] + \delta\underline{\Phi}[\mathbf{x}]\right] - \hat{Z}\left[\underline{\Phi}[\mathbf{x}]\right] = \underline{\nabla}\hat{Z}[\mathbf{x}] \bullet \delta\underline{\Phi}[\mathbf{x}] \qquad (3.21)$$

$$\delta\hat{Z}\left[\underline{\Phi}[\mathbf{x}]\right] = \int_B \underline{\nabla}\hat{Z}[\mathbf{x}]\langle\xi\rangle\,\delta\underline{\Phi}[\mathbf{x}]\langle\xi\rangle\,dV_{x'} \qquad (3.22)$$

Where, $\underline{\nabla}$ is Frechet differentiation.

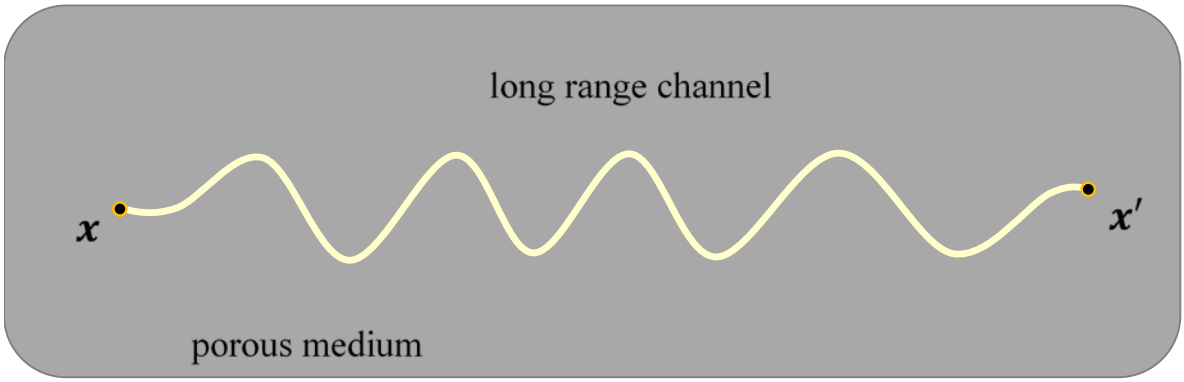

Fig. 3.1 Schematic of a long range flow channel connecting a material point $\mathbf{x}$ with its non-local neighboring material point $\mathbf{x}'$ in a porous medium[77].

In Equation (3.22), we have used the definition of the dot product of two states [2]. Now taking the first variation of $\widehat{\boldsymbol{I}}$ and using the property of the Frechet derivative in Equation (3.22), we have

$$\begin{aligned}\delta\hat{I}[\mathbf{x}] &= \int_B \delta\hat{Z}\left[\underline{\Phi}[\mathbf{x}]\right] dV_x - \int_B r[\mathbf{x}]\delta\Phi[\mathbf{x}]\, dV_x \\ &= \int_B\int_B \underline{\nabla}\hat{Z}[\mathbf{x}]\langle\xi\rangle\,\delta\Phi[\mathbf{x}']\, dV_{x'} dV_x - \int_B\int_B \underline{\nabla}\hat{Z}[\mathbf{x}]\langle\xi\rangle\,\delta\Phi[\mathbf{x}]\, dV_{x'} dV_x - \int_B r[\mathbf{x}]\delta\Phi[\mathbf{x}]\, dV_x\end{aligned}$$

(3.23)

Performing a change y variable $\mathbf{x}' \leftrightarrow \mathbf{x}$ in the first term and exchanging the order of integration we have

$$\begin{aligned}\delta\hat{I}[\mathbf{x}] &= \int_B\int_B \left(\underline{\nabla}\hat{Z}[\mathbf{x}']\langle -\xi\rangle - \underline{\nabla}\hat{Z}[\mathbf{x}]\langle\xi\rangle\right)\delta\Phi[\mathbf{x}]\, dV_{x'} dV_x - \int_B r[\mathbf{x}]\delta\Phi[\mathbf{x}]\, dV_x \\ &= \int_B\left(\int_B \left(-\underline{\nabla}\hat{Z}[\mathbf{x}]\langle\xi\rangle + \underline{\nabla}\hat{Z}[\mathbf{x}']\langle -\xi\rangle\right) dV_{x'} - r[\mathbf{x}]\right)\delta\Phi[\mathbf{x}]\, dV_x\end{aligned}$$

(3.24)

Finding the stationary value of the peridynamic flow potential functional by setting $\delta\hat{I}[\mathbf{x}] = 0$ and defining the mass flow state as $\underline{Q}[\mathbf{x}]\langle\xi\rangle = \underline{\nabla}\hat{z}[\mathbf{x}]\langle\xi\rangle$, we have

$$\int_B \left(\underline{Q}[\mathbf{x}]\langle\xi\rangle - \underline{Q}[\mathbf{x}']\langle -\xi\rangle\right) dV_{x'} + r[\mathbf{x}] = 0 \qquad (3.25)$$

The peridynamic mass flow state at $\mathbf{X}$ operating on a vector ξ maps the vector onto mass influx density in that bond. Replacing $r[\mathbf{x}]$ by $R[\mathbf{x}]$ and getting the accumulation term out, we finally have the state-based peridynamic form of Equation (3.5).

$$\frac{\partial}{\partial t}\left(\rho[\mathbf{x}]\phi[\mathbf{x}]\right) = \int_B \left(\underline{Q}[\mathbf{x}]\langle\xi\rangle - \underline{Q}[\mathbf{x}']\langle -\xi\rangle\right) dV_{x'} + R[\mathbf{x}] \tag{3.26}$$

This formulation makes no assumptions on the continuity of the potential field and can address flow driven by a larger non-local pressure difference.

Mass conservation over a body

Rewriting Equation (3.26) as Equation (3.27) and integrating both sides of the equation, we have Equation (3.28).

$$\frac{\partial}{\partial t}\left(\rho[\mathbf{x}]\phi[\mathbf{x}]\right) = \int_B \left(\underline{Q}[\mathbf{x}]\langle\mathbf{x}'-\mathbf{x}\rangle\right) dV_{x'} - \int_B \underline{Q}[\mathbf{x}']\langle\mathbf{x}-\mathbf{x}'\rangle\, dV_{x'} + R[\mathbf{x}] \tag{3.27}$$

$$\int_B \frac{\partial}{\partial t}\left(\rho[\mathbf{x}]\phi[\mathbf{x}]\right) dV_x = \int_B \int_B \underline{Q}[\mathbf{x}]\langle\mathbf{x}'-\mathbf{x}\rangle dV_{x'} dV_x - \int_B \int_B \underline{Q}[\mathbf{x}']\langle\mathbf{x}-\mathbf{x}'\rangle dV_{x'} dV_x + \int_B R[\mathbf{x}] dV_x \tag{3.28}$$

Performing a change of dummy variables $\mathbf{x}' \leftrightarrow \mathbf{x}$ in the second integral on the right hand side and exchanging the order of integration, we find the two integrals on the right hand side the same and we get,

$$\int_B \frac{\partial}{\partial t}\left(\rho[\mathbf{x}]\phi[\mathbf{x}]\right) dV_x = \int_B R[\mathbf{x}] dV_x \tag{3.29}$$

The equation above is the statement of the conservation of mass of any arbitrary bounded body, B.

Constitutive model

Here, we propose a constitutive model of the form [78, 79]

$$\underline{Q}\left[\mathbf{x}\right]\left\langle\boldsymbol{\xi}\right\rangle = \frac{\gamma}{2\mu}\underline{\omega}\left\langle\boldsymbol{\xi}\right\rangle\rho_0\frac{\boldsymbol{\xi}\mathbb{k}\left[\mathbf{x},\mathbf{x}'\right]\boldsymbol{\xi}}{\left\|\boldsymbol{\xi}\right\|^4}\left(\Phi\left[\mathbf{x}'\right]-\Phi\left[\mathbf{x}\right]\right) \tag{3.30}$$

Where,

$\mathbb{k}$: symmetric constitutive tensor [m^2]

γ : scaling factor depending on horizon δ and influence function $\underline{\omega}\left\langle\boldsymbol{\xi}\right\rangle$

In the above formulation, γ does not depend on the direction of the bond. Inside a non-local peridynamic region, the influence function provides an additional mechanism to modulate the non-local contribution in the computation of volume-dependent quantities [80]. The constitutive tensor $\mathbb{k}$ serves to define the physical setting being studied. To determine $\mathbb{k}$, we will seek to develop a relationship with the classical constitutive property $\mathbf{k}$. Substituting Equation (3.30) into Equation (3.26), we have,

$$\frac{\partial}{\partial t}\left(\rho\left[\mathbf{x}\right]\phi\left[\mathbf{x}\right]\right) = \frac{\gamma}{2}\int_B\frac{\rho_0}{\mu}\underline{\omega}\left\langle\boldsymbol{\xi}\right\rangle\frac{\boldsymbol{\xi}\left(\mathbb{k}\left[\mathbf{x},\mathbf{x}'\right]+\mathbb{k}\left[\mathbf{x}',\mathbf{x}\right]\right)\boldsymbol{\xi}}{\left\|\boldsymbol{\xi}\right\|^4}\left(\Phi\left[\mathbf{x}'\right]-\Phi\left[\mathbf{x}\right]\right)dV_{x'}+R\left[\mathbf{x}\right] \tag{3.31}$$

In order to derive the relationship between $\mathbb{k}$ and $\mathbf{k}$, following Seleson et al. [75], we assume the classical model and the peridynamic model are the same in the limit as the non-local region $H_x \notin B$ (please see Fig. 3.2) for which $\delta \to 0$.

$$\underline{Q}[\mathbf{x}]\langle\boldsymbol{\xi}\rangle = 0 \quad \forall\|\boldsymbol{\xi}\| > \delta \tag{3.32}$$

Only to make the connection to the local model, we assume continuously differentiable fields in $\mathbb{k}$ and $\boldsymbol{\phi}$ and use the following Taylor's expansions

$$\mathbb{k}[\mathbf{x},\mathbf{x}'] = \mathbb{k}[\mathbf{x},\mathbf{x}] + \boldsymbol{\xi}\nabla_2\mathbb{k}[\mathbf{x},\mathbf{x}] + \mathrm{O}\left(\|\boldsymbol{\xi}\|^2\right) \tag{3.33}$$

$$\mathbb{k}[\mathbf{x}',\mathbf{x}] = \mathbb{k}[\mathbf{x},\mathbf{x}] + \boldsymbol{\xi}\nabla_1\mathbb{k}[\mathbf{x},\mathbf{x}] + \mathrm{O}\left(\|\boldsymbol{\xi}\|^2\right) \tag{3.34}$$

$$\Phi[\mathbf{x}'] - \Phi[\mathbf{x}] = (\boldsymbol{\xi}\cdot\nabla)\Phi[\mathbf{x}] + \frac{1}{2}(\boldsymbol{\xi}\cdot\nabla)(\boldsymbol{\xi}\cdot\nabla)\Phi[\mathbf{x}] + \mathrm{O}\left(\|\boldsymbol{\xi}\|^3\right) \tag{3.35}$$

Here, ∇_1 and ∇_2 are gradient operators with respect to the functions' first and second arguments, respectively and they are related such that

$$\nabla\mathbb{k}[\mathbf{x},\mathbf{x}] = \nabla_1\mathbb{k}[\mathbf{x},\mathbf{x}] + \nabla_2\mathbb{k}[\mathbf{x},\mathbf{x}] \tag{3.36}$$

$$\begin{aligned}\frac{\partial}{\partial t}\left(\rho[\mathbf{x}]\phi[\mathbf{x}]\right) = \gamma\int_B \frac{\rho_0}{\mu}\underline{\omega}\langle\boldsymbol{\xi}\rangle \frac{\boldsymbol{\xi}\cdot\left(\mathbb{k}[\mathbf{x},\mathbf{x}] + \frac{1}{2}\boldsymbol{\xi}\cdot\nabla\mathbb{k}[\mathbf{x},\mathbf{x}] + \mathrm{O}\left(\|\boldsymbol{\xi}\|^2\right)\right)\cdot\boldsymbol{\xi}}{\|\boldsymbol{\xi}\|^4} \\ \times\left((\boldsymbol{\xi}\cdot\nabla)\Phi[\mathbf{x}] + \frac{1}{2}(\boldsymbol{\xi}\cdot\nabla)(\boldsymbol{\xi}\cdot\nabla)\Phi[\mathbf{x}] + \mathrm{O}\left(\|\boldsymbol{\xi}\|^3\right)\right)dV_{x'} + R[\mathbf{x}]\end{aligned} \tag{3.37}$$

Collecting terms,

$$\begin{aligned}
\frac{\partial}{\partial t}\left(\rho[\mathbf{x}]\phi[\mathbf{x}]\right) &= \gamma\int_B \frac{\rho_0}{\mu}\underline{\omega}\langle\boldsymbol{\xi}\rangle \frac{\xi_i\xi_m\mathbb{k}_{mn}\xi_n\xi_j\dfrac{\partial\Phi[\mathbf{x}]}{\partial x_i x_j}+\xi_i\xi_m\dfrac{\partial\mathbb{k}_{mn}}{\partial x_i}\xi_n\xi_j\dfrac{\partial\Phi[\mathbf{x}]}{\partial x_j}}{\|\boldsymbol{\xi}\|^4}dV_{x'}+\mathrm{O}\left(\delta^2\right)+R[\mathbf{x}] \\
&= \left[\gamma\int_{H_x}\frac{\rho_0}{\mu}\underline{\omega}\langle\boldsymbol{\xi}\rangle\frac{(\boldsymbol{\xi}\otimes\boldsymbol{\xi})\mathbb{k}(\boldsymbol{\xi}\otimes\boldsymbol{\xi})}{2\|\boldsymbol{\xi}\|^4}dV_{\xi}\right]:(\nabla\otimes\nabla)\Phi[\mathbf{x}] \\
&\quad+\nabla\cdot\left[\gamma\int_{H_x}\frac{\rho_0}{\mu}\underline{\omega}\langle\boldsymbol{\xi}\rangle\frac{(\boldsymbol{\xi}\otimes\boldsymbol{\xi})\mathbb{k}(\boldsymbol{\xi}\otimes\boldsymbol{\xi})}{2\|\boldsymbol{\xi}\|^4}dV_{\xi}\right]\cdot\nabla\Phi[\mathbf{x}]+\mathrm{O}\left(\delta^2\right)+R[\mathbf{x}] \\
&= \frac{\rho_0}{\mu}\mathbf{k}[\mathbf{x}]:(\nabla\otimes\nabla)\Phi[\mathbf{x}]+\frac{\rho_0}{\mu}\nabla\mathbf{k}[\mathbf{x}]\nabla\Phi[\mathbf{x}]+\mathrm{O}\left(\delta^2\right)+R[\mathbf{x}] \\
&= \nabla\cdot\left(\frac{\rho_0}{\mu}\mathbf{k}[\mathbf{x}]\nabla\Phi[\mathbf{x}]\right)+\mathrm{O}\left(\delta^2\right)+R[\mathbf{x}]
\end{aligned} \tag{3.38}$$

Where,

$$\mathbf{k}[\mathbf{x}] = \int_{H_x}\gamma\underline{\omega}\langle\boldsymbol{\xi}\rangle\frac{(\boldsymbol{\xi}\otimes\boldsymbol{\xi})\mathbb{k}(\boldsymbol{\xi}\otimes\boldsymbol{\xi})}{2\|\boldsymbol{\xi}\|^4}dV_{x'} \tag{3.39}$$

Allowing $\delta\to 0$, we recover Equation (3.5) from Equation (3.38). If we write Equation (3.39) in component form, we can establish a relationship between the non-local permeability tensor $\mathbb{k}$ and the local permeability tensor $\mathbf{k}$ through a judicious choice of constants γ.

$$k_{ij}[\mathbf{x}] = \gamma\mathbb{k}_{mn}\int_{H_x}\underline{\omega}\langle\boldsymbol{\xi}\rangle\frac{\xi_i\xi_n\xi_m\xi_j}{2\|\boldsymbol{\xi}\|^4}dV_{x'} \tag{3.40}$$

The relationship will be slightly different for problems in one, two, or three dimensions. Here, we will consider two dimensional and three dimensional cases. In the two

dimensional case, we will carry out the integral evaluation in polar coordinates with the following formulation,

$$\boldsymbol{\xi} = \begin{pmatrix} r\cos\theta \\ r\sin\theta \end{pmatrix} \tag{3.41}$$

In the three dimensional case, we will carry out the integral evaluation in polar coordinates with the following equation.

$$\boldsymbol{\xi} = \begin{pmatrix} r\sin\varphi\cos\theta \\ r\sin\varphi\sin\theta \\ r\cos\theta \end{pmatrix} \tag{3.42}$$

The choice of influence function will also affect the relation between $\mathbb{k}$ and $\mathbf{k}$ as shown the next section.

Relationship between $\mathbb{k}$ and $\mathbf{k}$ under different influence functions in 2 and 3 dimensions

Several examples of influence functions are presented below to demonstrate the relationship between the perdynamic permeability and the classical definition of the permeability tensor.

(a) $\underline{\omega}\langle\boldsymbol{\xi}\rangle = 1$, 2-dimensional problem

If $\underline{\omega}\langle\boldsymbol{\xi}\rangle = 1$ for 2-dimensional problems, the relationship between $\mathbb{k}$ and $\mathbf{k}$ is given as the following integral formulation of a circle of radius δ.

$$
\begin{aligned}
k_{ij} &= \gamma \mathbb{k}_{mn} \int_0^{2\pi} \int_0^{\delta} \frac{\xi_i \xi_n \xi_m \xi_j}{2r^4} r dr d\theta \\
&= \gamma \mathbb{k}_{mn} \left(\delta_{im}\delta_{nj} + \delta_{in}\delta_{mj} + \delta_{ij}\delta_{mn} \right) \frac{\pi\delta^2}{16}
\end{aligned}
\tag{3.43}
$$

The subscripted $\delta's$ are understood to be the Kronecker delta while the unscripted δ is the length-scale of non-locality. If we now choose $\gamma = \frac{8}{\pi\delta^2}$, we have an explicit relationship between $\mathbb{k}$ and $\mathbf{k}$, i.e.

$$
k_{ij} = \frac{1}{2}\left(\mathbb{k}_{ij} + \mathbb{k}_{ji} + \mathbb{k}_{kk}\delta_{ij} \right) \tag{3.44}
$$

Solving for $\mathbb{k}_{kk}$

$$
\mathbb{k}_{kk} = \frac{1}{2} k_{kk} \tag{3.45}
$$

Since $\mathbb{k}$ is symmetric, we can substitute Equation (3.45) into Equation (3.44) then solve for $\mathbb{k}_{ij}$

$$
\mathbb{k}_{ij} = k_{ij} - \frac{1}{4} k_{kk}\delta_{ij} \tag{3.46}
$$

Finally, we substitute Equation (3.45) and our choice of γ into the original proposed constitutive model (3.30) to obtain

$$
\underline{Q}\left[\mathbf{x}\right]\left\langle \boldsymbol{\xi} \right\rangle = \frac{\rho_0}{\mu} \frac{4}{\pi\delta^2} \frac{\boldsymbol{\xi}\left(\mathbf{k}\left[\mathbf{x}\right] - \frac{1}{4} tr\left(\mathbf{k}\left[\mathbf{x}\right] \right)\mathbf{I} \right)\boldsymbol{\xi}}{\left\| \boldsymbol{\xi} \right\|^4} \left(\Phi\left[\mathbf{x}'\right] - \Phi\left[\mathbf{x}\right] \right) \tag{3.47}
$$

$$-\underline{Q}[\mathbf{x}']\langle -\boldsymbol{\xi}\rangle = \frac{\rho_0}{\mu}\frac{4}{\pi\delta^2}\frac{\boldsymbol{\xi}\left(\mathbf{k}[\mathbf{x}'] - \frac{1}{4}tr\left(\mathbf{k}[\mathbf{x}']\right)\mathbf{I}\right)\boldsymbol{\xi}}{\|\boldsymbol{\xi}\|^4}\left(\Phi[\mathbf{x}'] - \Phi[\mathbf{x}]\right) \quad (3.48)$$

$$\frac{\partial}{\partial t}\left(\rho[\mathbf{x}]\phi[\mathbf{x}]\right) = \frac{8}{\pi\delta^2}\int_{H_x}\frac{\boldsymbol{\xi}\left(\mathbf{k}_m^a[\mathbf{x},\mathbf{x}'] - \frac{1}{4}tr\left(\mathbf{k}_m^a[\mathbf{x},\mathbf{x}']\right)\mathbf{I}\right)\boldsymbol{\xi}}{\|\boldsymbol{\xi}\|^4}\left(\Phi[\mathbf{x}'] - \Phi[\mathbf{x}]\right)dA_{x'} + R[\mathbf{x}] \quad (3.49)$$

Where, $\mathbf{k}_m^a[\mathbf{x},\mathbf{x}']$ is the arithmetic mean of the permeability at the two end points of the bond,

$$\mathbf{k}_m^a[\mathbf{x},\mathbf{x}'] = \left(\frac{\mathbf{k}[\mathbf{x}] + \mathbf{k}[\mathbf{x}']}{2}\right) \quad (3.50)$$

(b) $\underline{\omega}\langle\boldsymbol{\xi}\rangle = 1$ **in three dimensional problem**

Similarly, if $\underline{\omega}\langle\boldsymbol{\xi}\rangle = 1$ for three dimensional problems, the relationship between $\mathbb{k}$ and $\mathbf{k}$ is given as the following integral formulation of a sphere of radius, δ.

$$\begin{aligned} k_{ij} &= \gamma\mathbb{k}_{mn}\int_0^{2\pi}\int_0^{\pi}\int_0^{\delta}\frac{\xi_i\xi_n\xi_m\xi_j}{2r^4}r^2\sin\varphi dr d\varphi d\theta \\ &= \gamma\mathbb{k}_{mn}\left(\delta_{im}\delta_{nj} + \delta_{in}\delta_{mj} + \delta_{ij}\delta_{mn}\right)\frac{2\pi\delta^3}{45} \end{aligned} \quad (3.51)$$

If we choose, $\gamma = \frac{45}{4\pi\delta^3}$, we have the same explicit relationship between $\mathbb{k}$ and $\mathbf{k}$ as Equation (3.44). Hence by solving Equation (3.44) for $\mathbb{k}_{kk}$, we obtain

$$\mathbb{k}_{kk} = \frac{2}{5}\mathbf{k}_{kk} \quad (3.52)$$

Since $\mathbb{k}$ is symmetric, we can substitute Equation (3.52) into Equation (3.44) and solve for $\mathbb{k}_{ij}$.

$$\mathbb{k}_{ij} = \mathbf{k}_{ij} - \frac{1}{5}\mathbf{k}_{kk}\delta_{ij} \tag{3.53}$$

Finally we obtain the following equation by substituting Equation (3.53) and choose of γ into the original proposed constitutive model (3.30).

$$\frac{\partial}{\partial t}\left(\rho[\mathbf{x}]\phi[\mathbf{x}]\right) = \frac{45}{4\pi\delta^3}\int_{H_x}\frac{\xi\left(\mathbf{k}_m^a[\mathbf{x},\mathbf{x}'] - \frac{1}{5}tr\left(\mathbf{k}_m^a[\mathbf{x},\mathbf{x}']\right)\mathbf{I}\right)\xi}{\|\xi\|^4}\left(\Phi[\mathbf{x}'] - \Phi[\mathbf{x}]\right)dA_{x'} + R[\mathbf{x}] \tag{3.54}$$

(c) $\underline{\omega}\langle\boldsymbol{\xi}\rangle = 1 - \frac{r}{\delta}$ for a 2-dimensional problem

If $\underline{\omega}\langle\boldsymbol{\xi}\rangle = 1 - \frac{r}{\delta}$ for 2-dimensional problems, Equation (3.40) takes the following form.

$$\begin{aligned} k_{ij} &= \gamma\mathbb{k}_{mn}\int_0^{2\pi}\int_0^{\delta}\left(1-\frac{r}{\delta}\right)\frac{\xi_i\xi_n\xi_m\xi_j}{2r^4}rdrd\theta \\ &= \gamma\mathbb{k}_{mn}\left(\delta_{im}\delta_{nj} + \delta_{in}\delta_{mj} + \delta_{ij}\delta_{mn}\right)\frac{\pi\delta^2}{48} \end{aligned} \tag{3.55}$$

If we choose $\gamma = \frac{24}{\pi\delta^2}$, we can again relate $\mathbf{k}$ and $\mathbb{k}$ by Equation (3.36). Substituting Equation (3.36) and our choice of γ into the original proposed constitutive Equation (3.30) to obtain

$$\frac{\partial}{\partial t}\left(\rho[\mathbf{x}]\phi[\mathbf{x}]\right)=\frac{24}{\pi\delta^2}\int_{H_x}\left(1-\frac{r}{\delta}\right)\frac{\xi\left(\mathbf{k}_m^a[\mathbf{x},\mathbf{x}']-\frac{1}{4}tr\left(\mathbf{k}_m^a[\mathbf{x},\mathbf{x}']\right)\mathbf{I}\right)\xi}{\|\xi\|^4}\left(\Phi[\mathbf{x}']-\Phi[\mathbf{x}]\right)dA_{x'}+R[\mathbf{x}] \tag{3.56}$$

(d) $\underline{\omega}\langle\boldsymbol{\xi}\rangle=1-\frac{r}{\delta}$ for a 3-dimensional problem

If $\underline{\omega}\langle\boldsymbol{\xi}\rangle=1-\frac{r}{\delta}$ for 3-dimensional problems, Equation (3.40) takes the following form.

$$\begin{aligned}k_{ij}&=\gamma\mathbb{k}_{mn}\int_0^{2\pi}\int_0^{\pi}\int_0^{\delta}\left(1-\frac{r}{\delta}\right)\frac{\xi_i\xi_n\xi_m\xi_j}{2r^4}r^2\sin\varphi dr d\varphi d\theta\\&=\gamma\mathbb{k}_{mn}\left(\delta_{im}\delta_{nj}+\delta_{in}\delta_{mj}+\delta_{ij}\delta_{mn}\right)\frac{\pi\delta^3}{90}\end{aligned} \tag{3.57}$$

If we choose, $\gamma=\frac{45}{\pi\delta^3}$, we can relate $\mathbb{k}$ and $\mathbb{k}$ by Equation(3.53). Substituting Equation (3.53) and our choice of γ into the original proposed constitutive Equation (3.30) we obtain,

$$\frac{\partial}{\partial t}\left(\rho[\mathbf{x}]\phi[\mathbf{x}]\right)=\frac{45}{\pi\delta^3}\int_{H_x}\left(1-\frac{r}{\delta}\right)\frac{\xi\left(\mathbf{k}_m^a[\mathbf{x},\mathbf{x}']-\frac{1}{5}tr\left(\mathbf{k}_m^a[\mathbf{x},\mathbf{x}']\right)\mathbf{I}\right)\xi}{\|\xi\|^4}\left(\Phi[\mathbf{x}']-\Phi[\mathbf{x}]\right)dA_{x'}+R[\mathbf{x}] \tag{3.58}$$

(e) $\underline{\omega}\langle\boldsymbol{\xi}\rangle=\frac{1}{r}$ **for a 2-dimensional problem**

If $\underline{\omega}\langle\boldsymbol{\xi}\rangle=\frac{1}{r}$ for 2-dimensional problems, Equation (3.40) takes the following form.

$$k_{ij} = \gamma \mathbb{k}_{mn} \int_0^{2\pi} \int_0^{\delta} \left(1 - \frac{r}{\delta}\right) \frac{\xi_i \xi_n \xi_m \xi_j}{2r^4} r dr d\theta$$
$$= \gamma \mathbb{k}_{mn} \left(\delta_{im}\delta_{nj} + \delta_{in}\delta_{mj} + \delta_{ij}\delta_{mn}\right) \frac{\pi\delta}{8} \tag{3.59}$$

If we choose $\gamma = \frac{4}{\pi\delta}$, we can again relate $\mathbf{k}$ and $\mathbb{k}$ by Equation (3.36). Substituting Equation (3.36) and our choice of γ into the original proposed constitutive Equation (3.30) to obtain

$$\frac{\partial}{\partial t}\left(\rho[\mathbf{x}]\phi[\mathbf{x}]\right) = \frac{4}{\pi\delta} \int_{H_x} \frac{1}{r} \frac{\boldsymbol{\xi}\left(\mathbf{k}_m^a[\mathbf{x},\mathbf{x}'] - \frac{1}{4} tr\left(\mathbf{k}_m^a[\mathbf{x},\mathbf{x}']\right)\mathbf{I}\right)\boldsymbol{\xi}}{\|\boldsymbol{\xi}\|^4} \left(\Phi[\mathbf{x}'] - \Phi[\mathbf{x}]\right) dA_{x'} + R[\mathbf{x}] \tag{3.60}$$

(f) $\underline{\omega}\langle\boldsymbol{\xi}\rangle = \frac{1}{r}$ **for a 3-dimensional problem**

If $\underline{\omega}\langle\boldsymbol{\xi}\rangle = \frac{1}{r}$ for 3-dimensional problems, Equation (3.40) takes the following form,

$$k_{ij} = \gamma \mathbb{k}_{mn} \int_0^{2\pi} \int_0^{\pi} \int_0^{\delta} \frac{1}{r} \frac{\xi_i \xi_n \xi_m \xi_j}{2r^4} r^2 \sin\varphi dr d\varphi d\theta$$
$$= \gamma \mathbb{k}_{mn} \left(\delta_{im}\delta_{nj} + \delta_{in}\delta_{mj} + \delta_{ij}\delta_{mn}\right) \frac{\pi\delta^2}{15} \tag{3.61}$$

If we choose, $\gamma = \frac{15}{2\pi\delta^2}$, we can relate $\mathbf{k}$ and $\mathbb{k}$ by Equation(3.53). Substituting Equation (3.53) and our (3.54)choice of γ into the original proposed constitutive Equation (3.30) to obtain

$$\frac{\partial}{\partial t}\left(\rho[\mathbf{x}]\phi[\mathbf{x}]\right)=\frac{15}{2\pi\delta^2}\int_{H_x}\frac{1}{r}\frac{\xi\left(\mathbf{k}_m^a[\mathbf{x},\mathbf{x}']-\frac{1}{5}tr\left(\mathbf{k}_m^a[\mathbf{x},\mathbf{x}']\right)\mathbf{I}\right)\xi}{\|\xi\|^4}\left(\Phi[\mathbf{x}']-\Phi[\mathbf{x}]\right)dA_{x'}+R[\mathbf{x}] \qquad (3.62)$$

The relationships between $\mathbf{k}$ and $\mathbb{k}$ for different $\underline{\omega}\langle\xi\rangle$ in 2 and 3 dimensions derived above are summarized in Table 3.1.

3.2.1.1 Simplified forms of mass conservation equation

Here, we simplify Equation (3.48), (3.54), (3.56), (3.58), (3.60) and (3.62) for some special cases. In the simplified cases, we replace $R[\mathbf{x}]$ with $\rho[\mathbf{x}]I_v[\mathbf{x}]$ whenever necessary (Here, $I_v[\mathbf{x}]$ is the volumetric fluid injection rate).

Table 3.1 Summary of the relationship between non-local permeability tensor and local permeability tensor.

Influence function	Relation between $\mathbf{k}$ and $\mathbb{k}$ in 2D	γ in 2D	Relation between $\mathbf{k}$ and $\mathbb{k}$ in 3D	γ in 3D
$\underline{\omega}\langle\xi\rangle=1$	$\mathbb{k}_{ij}=\mathbf{k}_{ij}-\frac{1}{4}\mathbf{k}_{kk}\delta_{ij}$	$\frac{8}{\pi\delta^2}$	$\mathbb{k}_{ij}=\mathbf{k}_{ij}-\frac{1}{5}\mathbf{k}_{kk}\delta_{ij}$	$\frac{45}{4\pi\delta^3}$
$\underline{\omega}\langle\xi\rangle=1-\frac{r}{\delta}$		$\frac{24}{\pi\delta^2}$		$\frac{45}{\pi\delta^3}$
$\underline{\omega}\langle\xi\rangle=\frac{1}{r}$		$\frac{4}{\pi\delta}$		$\frac{15}{2\pi\delta^2}$

(a) Homogeneous and isotropic permeability

If we assume homogeneous and isotropic permeability in two dimension, the local permeability is simplified as follows,

$$\mathbf{k}\left[\mathbf{x}\right]=\mathbf{k}\left[\mathbf{x}'\right]=k\mathbf{I} \tag{3.63}$$

$$\mathbf{k}_m^a\left[\mathbf{x},\mathbf{x}'\right]=k\mathbf{I} \tag{3.64}$$

$$\mathbf{k}_m^a\left[\mathbf{x},\mathbf{x}'\right]-\frac{1}{4}tr\left(\mathbf{k}_m^a\left[\mathbf{x},\mathbf{x}'\right]\right)\mathbf{I}=\frac{k}{2}\mathbf{I} \tag{3.65}$$

Substituting Equation (3.65) into Equation (3.46) and (3.53), we have the simplified permeability form in 2-D and 3-D respectively.

$$\frac{\boldsymbol{\xi}\left(\mathbf{k}_m^a\left[\mathbf{x},\mathbf{x}'\right]-\frac{1}{4}tr\left(\mathbf{k}_m^a\left[\mathbf{x},\mathbf{x}'\right]\right)\mathbf{I}\right)\boldsymbol{\xi}}{\left\|\boldsymbol{\xi}\right\|^2}=\frac{k}{2} \tag{3.66}$$

Substituting Equation (3.66) in Equation (3.48), (3.56), and (3.60), we obtain the final mass conservation equation in two dimensions for the three influence functions respectively.

For $\underline{\omega}\left\langle\boldsymbol{\xi}\right\rangle=1$ in 2-D

$$\frac{\partial}{\partial t}\left(\rho\left[\mathbf{x}\right]\phi\left[\mathbf{x}\right]\right)=\frac{4k}{\pi\delta^2}\int_{H_x}\frac{\rho}{\mu}\frac{\left(\Phi\left[\mathbf{x}'\right]-\Phi\left[\mathbf{x}\right]\right)}{\left\|\boldsymbol{\xi}\right\|^2}dA_{x'}+R\left[\mathbf{x}\right] \tag{3.67}$$

For $\underline{\omega}\left\langle\boldsymbol{\xi}\right\rangle=1-\frac{r}{\delta}$ in 2-D

$$\frac{\partial}{\partial t}\left(\rho\left[\mathbf{x}\right]\phi\left[\mathbf{x}\right]\right)=\frac{12k}{\pi\delta^2}\int_{H_x}\left(1-\frac{r}{\delta}\right)\frac{\rho}{\mu}\frac{\left(\Phi\left[\mathbf{x}'\right]-\Phi\left[\mathbf{x}\right]\right)}{\left\|\boldsymbol{\xi}\right\|^2}dA_{x'}+R\left[\mathbf{x}\right] \tag{3.68}$$

For $\underline{\omega}\langle\boldsymbol{\xi}\rangle = \frac{1}{r}$ in 2-D

$$\frac{\partial}{\partial t}\left(\rho[\mathbf{x}]\phi[\mathbf{x}]\right) = \frac{2k}{\pi\delta}\int_{H_x}\frac{1}{r}\frac{\rho}{\mu}\frac{\left(\Phi[\mathbf{x}']-\Phi[\mathbf{x}]\right)}{\|\boldsymbol{\xi}\|^2}dA_{x'} + R[\mathbf{x}] \tag{3.69}$$

Similarly, if we assume homogeneous and isotropic permeability in three dimensions, the permeability formulation is simplified as follows,

$$\frac{\boldsymbol{\xi}\left(\mathbf{k}_m^a[\mathbf{x},\mathbf{x}'] - \frac{1}{5}tr\left(\mathbf{k}_m^a[\mathbf{x},\mathbf{x}']\right)\mathbf{I}\right)\boldsymbol{\xi}}{\|\boldsymbol{\xi}\|^2} = \frac{2k}{5} \tag{3.70}$$

Substituting Equation (3.70) in Equation (3.54), (3.58), and (3.62), we obtain the final mass conservation equation in three dimensions for the three influence functions respectively.

For $\underline{\omega}\langle\boldsymbol{\xi}\rangle = 1$ in 3D

$$\frac{\partial}{\partial t}\left(\rho[\mathbf{x}]\phi[\mathbf{x}]\right) = \frac{9k}{2\pi\delta^3}\int_{H_x}\frac{\rho}{\mu}\frac{\left(\Phi[\mathbf{x}']-\Phi[\mathbf{x}]\right)}{\|\boldsymbol{\xi}\|^2}dV_{x'} + R[\mathbf{x}] \tag{3.71}$$

For $\underline{\omega}\langle\boldsymbol{\xi}\rangle = 1-\frac{r}{\delta}$ in 3D

$$\frac{\partial}{\partial t}\left(\rho[\mathbf{x}]\phi[\mathbf{x}]\right) = \frac{18k}{\pi\delta^3}\int_{H_x}\left(1-\frac{r}{\delta}\right)\frac{\rho}{\mu}\frac{\left(\Phi[\mathbf{x}']-\Phi[\mathbf{x}]\right)}{\|\boldsymbol{\xi}\|^2}dV_{x'} + R[\mathbf{x}] \tag{3.72}$$

For $\underline{\omega}\langle\boldsymbol{\xi}\rangle = \frac{1}{r}$ in 3D

$$\frac{\partial}{\partial t}\left(\rho[\mathbf{x}]\phi[\mathbf{x}]\right) = \frac{3k}{\pi\delta^2}\int_{H_x}\frac{1}{r}\frac{\rho}{\mu}\frac{\left(\Phi[\mathbf{x}']-\Phi[\mathbf{x}]\right)}{\|\boldsymbol{\xi}\|^2}dV_{x'} + R[\mathbf{x}] \tag{3.73}$$

(b) Homogeneous and isotropic permeability, isotropic constant porosity medium, and neglecting gravity $\left(\Phi[\mathbf{x}] = p[\mathbf{x}]\right)$.

Using Equation (3.67) for $\underline{\omega}\langle\boldsymbol{\xi}\rangle = 1$, the governing equation becomes

$$\frac{\partial p[\mathbf{x}]}{\partial t} = \frac{k}{\phi\mu c}\left[\frac{4}{\pi\delta^2}\int_{H_x}\frac{\left(p[\mathbf{x}'] - p[\mathbf{x}]\right)}{\|\boldsymbol{\xi}\|^2}dA_{x'}\right] + \frac{I_v[\mathbf{x}]}{c\phi} \tag{3.74}$$

The equivalent form of Equation (3.74) in the classical theory is the following. Please note that the flow for this case is at steady state.

$$\frac{\partial p[\mathbf{x}]}{\partial t} = \frac{k}{\phi\mu c}\nabla^2 p[\mathbf{x}] + \frac{I_v[\mathbf{x}]}{c\phi} = 0 \tag{3.75}$$

(c) Homogeneous and isotropic permeability, isotropic constant porosity medium, incompressible fluid (ρ constant), and neglecting gravity $\left(\Phi[\mathbf{x}] = p[\mathbf{x}]\right)$.

Using Equation (3.67) for $\underline{\omega}\langle\boldsymbol{\xi}\rangle = 1$, the governing equation becomes

$$\frac{k}{\mu}\left[\frac{4}{\pi\delta^2}\int_{H_x}\frac{\left(p[\mathbf{x}'] - p[\mathbf{x}]\right)}{\|\boldsymbol{\xi}\|^2}dA_{x'}\right] + I_v[\mathbf{x}] = 0 \tag{3.76}$$

The equivalent form of Equation (3.76) in the classical theory is the following. Please note that the flow for this case is at steady state.

$$\frac{k}{\mu}\nabla^2 p[\mathbf{x}] + I_v[\mathbf{x}] = 0 \tag{3.77}$$

(d) constant porosity medium, incompressible fluid, and neglecting gravity $\left(\Phi[\mathbf{x}] = p[\mathbf{x}]\right)$

Using Equation (3.67) for $\underline{\omega}\langle\boldsymbol{\xi}\rangle = 1$, the governing equation becomes

$$\frac{8}{\mu\pi\delta^2}\int_{H_x}\frac{\boldsymbol{\xi}\left(\mathbf{k}_m^a[\mathbf{x},\mathbf{x}'] - \frac{1}{4}tr\left(\mathbf{k}_m^a[\mathbf{x},\mathbf{x}']\right)\mathbf{I}\right)\boldsymbol{\xi}}{\|\boldsymbol{\xi}\|^2}\left(p[\mathbf{x}'] - p[\mathbf{x}]\right)dA_{x'} + I_v[\mathbf{x}] = 0 \tag{3.78}$$

The equivalent form of Equation (3.78) in the classical theory is the following.

$$\nabla\cdot\left(\frac{\mathbf{k}[\mathbf{x}]}{\mu}\nabla p[\mathbf{x}]\right) + I_v[\mathbf{x}] = 0 \tag{3.79}$$

3.2.1.2 Peridynamic potential gradient and volume flux

To determine the peridynamic volumetric flux, we first obtained the peridynamic pressure gradient at any node $\mathbf{x}$ from kinematic and internal state quantities, i.e. $\underline{\phi}$ available to us in the peridynamic formulation. We use Taylor series expansion of flow potential $\Phi[\mathbf{x}']$ about the point $\mathbf{x}$ as in Equation (3.35) and we get

$$\underline{\Phi}[\mathbf{x}]\langle\boldsymbol{\xi}\rangle = \Phi[\mathbf{x}'] - \Phi[\mathbf{x}] = (\boldsymbol{\xi}\cdot\nabla)\Phi[\mathbf{x}] + \mathrm{O}\left(\|\boldsymbol{\xi}\|^2\right) \tag{3.80}$$

We define the approximate peridynamic potential gradient $\overline{\nabla}\overline{\Phi} \equiv \nabla\Phi$, using the least squares weighted residual technique such that $\left(\overline{\nabla}\overline{\Phi}\right)\cdot\boldsymbol{\xi}$ gives the best approximation to $\underline{\Phi}\langle\boldsymbol{\xi}\rangle$ in a weighted L2 norm.

$$\frac{\partial}{\partial\left(\overline{\nabla}\overline{\Phi}\right)}\int_{H_x}\underline{\omega}\langle\boldsymbol{\xi}\rangle\left(\underline{\Phi}[\mathbf{x}]\langle\boldsymbol{\xi}\rangle - \overline{\nabla}\overline{\Phi}\cdot\boldsymbol{\xi}\right)^2 dV_{x'} = 0 \tag{3.81}$$

Carrying out the derivative evaluation on a component-by-component basis, we have

$$\frac{\partial}{\partial\left(\bar{\nabla}\bar{\Phi}\right)}\int_{H_x}\underline{\omega}\langle\boldsymbol{\xi}\rangle\left(\underline{\Phi}[\mathbf{x}]\langle\boldsymbol{\xi}\rangle-\bar{\nabla}\bar{\Phi}_j\xi_j\right)^2 dV_{x'}=0 \tag{3.82}$$

$$\int_{Hx}\underline{\omega}\langle\boldsymbol{\xi}\rangle\underline{\Phi}[\mathbf{x}]\langle\boldsymbol{\xi}\rangle\xi_i dV_{x'}-\bar{\nabla}\bar{\Phi}_j\cdot\int_{Hx}\underline{\omega}\langle\boldsymbol{\xi}\rangle\xi_j\xi_i dV_{x'}=0 \tag{3.83}$$

Now solving for $\bar{\nabla}\bar{\Phi}_J$

$$\bar{\nabla}\bar{\Phi}_j=\int_{H_x}\underline{\omega}\langle\boldsymbol{\xi}\rangle\underline{\Phi}[\mathbf{x}]\langle\boldsymbol{\xi}\rangle\xi_i dV_{x'}\left(\int_{H_x}\underline{\omega}\langle\boldsymbol{\xi}\rangle\xi_j\xi_i dV_{x'}\right)^{-1} \tag{3.84}$$

or in vector form

$$\bar{\nabla}\bar{\Phi}=\int_{H_x}\underline{\omega}\langle\boldsymbol{\xi}\rangle\underline{\Phi}[\mathbf{x}]\langle\boldsymbol{\xi}\rangle\xi_i dV_{x'}\left(\int_{H_x}\underline{\omega}\langle\boldsymbol{\xi}\rangle\boldsymbol{\xi}\otimes\boldsymbol{\xi}dV_{x'}\right)^{-1} \tag{3.85}$$

Recognizing the second term in the parenthesis as a shape tensor of [2] and borrowing the notation from the same, we can write this more compactly as follows.

$$\bar{\nabla}\bar{\Phi}=\left(\underline{\omega}\underline{\Phi}\bullet\underline{\mathbf{X}}\right)\mathbf{M}^{-1} \tag{3.86}$$

As a double check, we can show that this approximate potential gradient is linearly consistent, i.e. the gradient operator can reproduce a homogeneous gradient of any linear potential

$$\begin{aligned}\bar{\nabla}\bar{\Phi}_i&=\left(\int_{H_x}\underline{\omega}\langle\boldsymbol{\xi}\rangle\underline{\Phi}[\mathbf{x}]\langle\boldsymbol{\xi}\rangle\xi_i dV_{x'}\right)M_{ij}{}^{-1}\\&=\left(\int_{H_x}\underline{\omega}\langle\boldsymbol{\xi}\rangle\left(\nabla\Phi_n\xi_n\right)\xi_j dV_{x'}\right)M_{ij}{}^{-1}\\&=\nabla\Phi_n\left(\int_{H_x}\underline{\omega}\langle\boldsymbol{\xi}\rangle\xi_n\xi_j dV_{x'}\right)M_{ij}{}^{-1}=\nabla\Phi_n\left(M_{nj}\right)M_{ji}{}^{-1}=\nabla\Phi_n\delta_{ni}=\nabla\Phi_i\end{aligned}$$

(3.87)

We propose the following relation to obtain the peridynamic volumetric flux,

$$\bar{\mathbf{u}}[\mathbf{x}] = -\frac{1}{\mu}\left(\underline{k}\underline{\omega}\underline{\Phi} \bullet \underline{\mathbf{x}}\right)\mathbf{M}^{-1} \tag{3.88}$$

Where,

$$\underline{k}[\mathbf{x}]\langle\xi\rangle = \frac{\xi \mathbf{k}_m^a[\mathbf{x}, \mathbf{x}']\xi}{\|\xi\|^2} \tag{3.89}$$

Here, we use the formally derived non-local peridynamic potential gradient equation and modify it to obtain a relation of the peridynamic volumetric flux. For this, we multiply the potential difference in the peridynamic potential gradient equation with the component of permeability in that bond calculated based on the average of the permeability at the two end points of that bond and divide the same by fluid viscosity. We numerically verified that our volumetric flux formulation matches exactly with the classical volumetric flux relation ($\bar{\mathbf{u}}[\mathbf{x}] = -\frac{1}{\mu}\mathbf{k}[\mathbf{x}]\bar{\nabla}\bar{\Phi}[\mathbf{x}]$) for a homogeneous isotropic medium.

3.2.1.3 Imposing boundary conditions

Boundary conditions or surface constraints are required to provide the complete description and yield a specific solution of a boundary value problem comprising partial differential equations in the classical local conservation model. However, in the non-local peridynamic theory, the requirement of boundary conditions does not mathematically emerge[61]. A non-local peridynamic formulation, therefore, utilizes volumetric constraints instead of surface constraints in an equivalent boundary value problem [73]. These volume constraints can be implemented in a non-local region along the boundary constraining the solution in a non-zero volume.

(a) Imposing the non-local Dirichlet boundary condition

In solid mechanics, the peridynamic analogue of the Dirichlet (displacement) boundary condition is the displacement loading condition [61] in which the integral term of the governing equation is evaluated for the known displacements in the non-local boundary region of finite thickness δ under the surface. In a peridynamic formulation of transient heat conduction, Bobaru and Duangpanya [71] applied the Dirichlet boundary conditions directly at the boundary nodes only and found the solutions away from the boundary region to be identical to that when boundary conditions were applied in the non-local region of thickness δ. Therefore, the non-local Dirichlet boundary condition for the convective mass transport problem can be applied directly at the boundary nodes and as the horizon size approaches zero, the non-local Dirichlet boundary condition will converge to the local one.

(b) Imposing the non-local Neumann boundary condition

In solid mechanics, the external forces can be applied through the loading force density term in the governing equation. Such a condition is called force loading condition [61]. Similarly for the present flow problem, we can apply the boundary mass flux as the mass source density at the boundary nodes. In Section 3.3.1.3, we show that such a mass source density can be distributed to several nodes inside the horizon of the boundary node. The Neumann boundary condition can also be applied through equating the known potential gradient or volumetric flux to their peridynamic equivalent given in equation (3.86) and (3.88). These equations provide additional relations among boundary nodes and the nodes inside the horizon of boundary nodes with boundary information included.

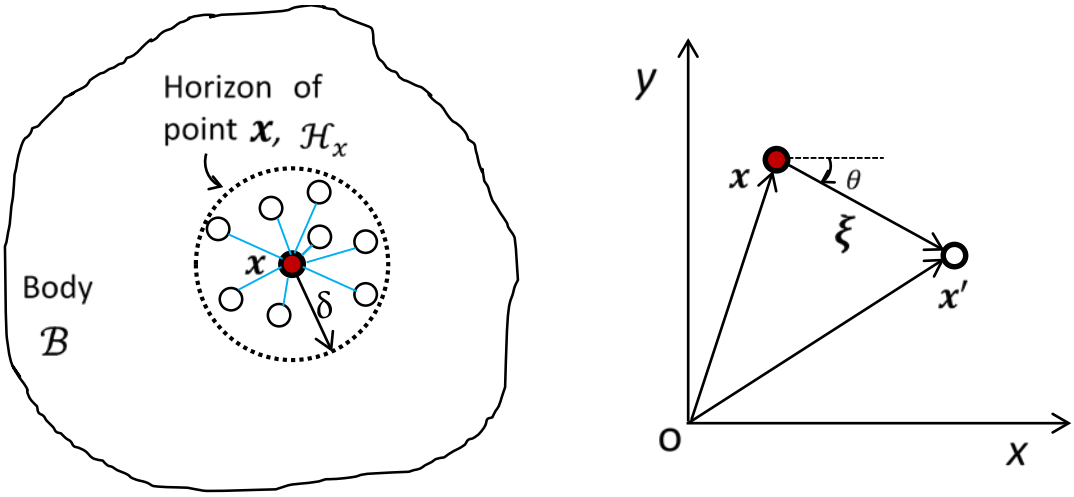

Fig. 3.2 Left: Schematic of a peridynamic material point $\mathbf{x}$ and connected flow bonds in its horizon; Right: Schematic of a flow bond between a material point $\mathbf{x}$ with its non-local neighboring material point $\mathbf{x}'$ in 2D [77].

3.2.2 BOND-BASED PERIDYNAMIC FORMULATION OF SINGLE-PHASE FLOW OF A LIQUID OF SMALL AND CONSTANT COMPRESSIBILITY THROUGH POROUS MEDIUM

Let B again represent a three-dimensional continuum region composed of material points of fixed mass and volume (Fig.3.2). The flow potential difference at the two end points of a bond is assumed to cause the fluid to flow only along the bond. Thus the fluid transport in a bond is independent of any other intersecting or nonintersecting bond or points in between. The volumetric flux of fluid flow in the bond is obtained from Darcy's law for low Reynolds number laminar flow as:

$$\mathbf{u}_b\left[\mathbf{x},\mathbf{x}'\right] = -\frac{k_b\left[\mathbf{x},\mathbf{x}'\right]}{\mu}\left(\frac{\Phi\left[\mathbf{x}'\right]-\Phi\left[\mathbf{x}\right]}{\left\|\boldsymbol{\xi}\right\|}\right)\mathbf{e}\left[\mathbf{x},\mathbf{x}'\right] \tag{3.90}$$

$$\mathbf{e}\left[\mathbf{x},\mathbf{x}'\right] = \frac{\boldsymbol{\xi}}{\left\|\boldsymbol{\xi}\right\|} \tag{3.91}$$

Where,

$k_b\left[\mathbf{x},\mathbf{x}'\right]$: scalar permeability of the flow bond [m^2]

Equation (3.90) is a simplification of Equation (3.3) for one dimensional flow due to a linear potential gradient in the direction of a bond vector with $k_b\left[\mathbf{x},\mathbf{x}'\right]$ being the permeability in the same direction. The mass flux along the flow bond is obtained from the product of fluid density in the bond, $\rho\left[\mathbf{x},\mathbf{x}'\right]$ and the volumetric flux, $\mathbf{u}_b\left[\mathbf{x},\mathbf{x}'\right]$ from Equation (3.90).

$$q_b\left[\mathbf{x},\mathbf{x}'\right] = -\rho\left[\mathbf{x},\mathbf{x}'\right]\frac{k_b\left[\mathbf{x},\mathbf{x}'\right]}{\mu}\left(\frac{\Phi\left[\mathbf{x}'\right]-\Phi\left[\mathbf{x}\right]}{\left\|\boldsymbol{\xi}\right\|}\right)\mathbf{e}\left[\mathbf{x},\mathbf{x}'\right] \tag{3.92}$$

The mass conservation equation for the bond is written below by equating the rate of accumulation of fluid mass in the bond per unit bond volume to the summation of the net inflow of fluid in bond per unit bond volume and mass generation per unit bond volume,

$$\frac{\partial}{\partial t}\left(\rho\left[\mathbf{x},\mathbf{x}'\right]\phi_{b\left[\mathbf{x},\mathbf{x}'\right]}\right) = \frac{q_b\left[\mathbf{x},\mathbf{x}'\right]\cdot\left(-A_b e\left[\mathbf{x},\mathbf{x}'\right]\right)}{A_b\left\|\boldsymbol{\xi}\right\|} + R_b\left[\mathbf{x},\mathbf{x}'\right] \tag{3.93}$$

or

$$\frac{\partial}{\partial t}\left(\rho\left[\mathbf{x},\mathbf{x}'\right]\phi_{b\left[\mathbf{x},\mathbf{x}'\right]}\right) = \frac{k_b\left[\mathbf{x},\mathbf{x}'\right]}{\mu}\rho\left[\mathbf{x},\mathbf{x}'\right]\frac{\Phi\left[\mathbf{x}'\right]-\Phi\left[\mathbf{x}\right]}{\left\|\boldsymbol{\xi}\right\|^2} + R_b\left[\mathbf{x},\mathbf{x}'\right] \tag{3.94}$$

Where,

A_b : cross sectional area of the flow bond [m^2]

$\phi_b[\mathbf{x},\mathbf{x}']$: porosity of the porous-flow bond

To obtain the mass conservation equation for point $\mathbf{x}$, we integrate Equation (3.94) over the horizon of $\mathbf{x}$,

$$\int_{Hx} \frac{\partial}{\partial t}\left(\rho[\mathbf{x},\mathbf{x}']\phi_b[\mathbf{x},\mathbf{x}']\right)dV_{x'} = \int_{Hx} k_b[\mathbf{x},\mathbf{x}']\frac{\rho[\mathbf{x},\mathbf{x}']}{\mu}\frac{\Phi[\mathbf{x}']-\Phi[\mathbf{x}]}{\|\boldsymbol{\xi}\|^2}dV_{x'} + \int_{Hx} R_b[\mathbf{x},\mathbf{x}']dV_{x'} \tag{3.95}$$

Next, we assume the bulk fluid density at point $\mathbf{x}$ to be given by the average of the fluid densities in all the porous-flow bonds attached to $\mathbf{x}$ in its horizon H_x .

$$\int_{Hx} \rho[\mathbf{x},\mathbf{x}']\phi_b[\mathbf{x},\mathbf{x}']dV_{x'} = \rho[\mathbf{x}]\phi[\mathbf{x}]V_x \tag{3.96}$$

Where,

V_x : the volume of the horizon of point $\mathbf{x}$

Similarly, the mass source term at the point $\mathbf{x}$ is obtained by the average of the same in all the porous-flow bonds attached to $\mathbf{x}$ in its horizon H_x.

$$\int_{Hx} R_b[\mathbf{x},\mathbf{x}']dV_{x'} = R[\mathbf{x}]V_x \tag{3.97}$$

From Equation (3.95), (3.96), and (3.97), we obtain the mass conservation equation for any material point $\mathbf{x}$.

$$\frac{\partial}{\partial t}\left(\rho[\mathbf{x}]\phi[\mathbf{x}]\right) = \int_{Hx} k[\mathbf{x},\mathbf{x}']\frac{\rho[\mathbf{x},\mathbf{x}']}{\mu}\frac{\Phi[\mathbf{x}']-\Phi[\mathbf{x}]}{\|\boldsymbol{\xi}\|^2}dV_{x'} + R[\mathbf{x}] \qquad (3.98)$$

$$k[\mathbf{x},\mathbf{x}'] = k_b[\mathbf{x},\mathbf{x}']/V_x \qquad (3.99)$$

Where,

$k[\mathbf{x},\mathbf{x}']$: the micro-permeability function of a bond $\boldsymbol{\xi}$ [1/m]

For the derivation above, we follow the approach of Bobaru and Duangpanya [71]. For simplicity, we consider the transport of an incompressible fluid in a two-dimensional homogeneous and isotropic porous medium. We also impose a match in the peridynamic mass flux and the classical mass flux for a linear variation in flow potential, under steady state condition. Here, we assume a linear variation in flow potential of the following form where C and Φ_0 are constants.

$$\Phi[\mathbf{x}] = Cx + \Phi_0 \qquad (3.100)$$

For a homogeneous and isotropic, two-dimensional porous medium, the material permeability tensor in Equation (3.3) becomes,

$$\mathbf{k} = \begin{pmatrix} k & 0 \\ 0 & k \end{pmatrix} \qquad (3.101)$$

From the classical theory, the mass flux at point $\mathbf{x}$ through the product of fluid density and volumetric flux is given by

$$q_{classical}\left[\mathbf{x}\right] = -\frac{k}{\mu}\rho\left[\mathbf{x}\right]C\mathbf{i} \tag{3.102}$$

Where,

$\mathbf{i}$: the unit vector in the x direction

Following the definition of Bobaru and Duangpanya [71], the peridynamic mass flux at any point $\mathbf{x}$ is given as,

$$q_{peridynamics}\left[\mathbf{x}\right] = -\frac{\rho\left[\mathbf{x}\right]}{\mu}\int_{Hx^+}\omega k_b\left[\mathbf{x},\mathbf{x}'\right]\frac{\Phi\left[\mathbf{x}'\right]-\Phi\left[\mathbf{x}\right]}{\left\|\boldsymbol{\xi}\right\|}e\left[\mathbf{x},\mathbf{x}'\right]dA_{x'} \tag{3.103}$$

Where,

H_x^+ : the particular area in the horizon of point $\mathbf{x}$ with neighboring points of higher flow potential than that at $\mathbf{x}$

ω : influence function

Here, we have also assumed $\rho\left[\mathbf{x},\mathbf{x}'\right]\to\rho\left[\mathbf{x}\right]$ in the limit of peridynamic horizon, $\delta\to 0$ to match the peridynamic flux with local flux from the classical continuum theory. By equating the flux from Equation (3.102) and (3.103) and replacing $e\left[\mathbf{x},\mathbf{x}'\right]=\left(\mathbf{i}\cos\theta+\mathbf{j}\sin\theta\right)$, we obtain the following formulation.

$$\int_{Hx^+}\omega k_b\left[\mathbf{x},\mathbf{x}'\right]\frac{\Phi\left[\mathbf{x}'\right]-\Phi\left[\mathbf{x}\right]}{\left\|\boldsymbol{\xi}\right\|}\left(\mathbf{i}\cos\theta+\mathbf{j}\sin\theta\right)dA_{x'} = kC\mathbf{i} \tag{3.104}$$

As shown in Equation (3.100), since there is no potential variation in the y direction, Realizing $\Phi\left(x'\right)-\Phi\left(x\right)=C\left\|\boldsymbol{\xi}\right\|\cos\theta$, Equation (3.104) reduces to the following form,

$$\int_{-\frac{\pi}{2}}^{\frac{\pi}{2}}\int_{0}^{\delta}\omega k_b\left[\mathbf{x},\mathbf{x}'\right]\cos^2\theta r dr d\theta = k \tag{3.105}$$

Equation (3.105) can be solved for $k_b\left[\mathbf{x},\mathbf{x}'\right]$ depending on the form of influence function as follows,

For $\omega = 1$

$$\frac{\partial}{\partial t}\left(\rho\left[\mathbf{x}\right]\phi\left[\mathbf{x}\right]\right) = \int_{Hx}\frac{\rho\left[\mathbf{x},\mathbf{x}'\right]}{\mu}\frac{4k}{\pi\delta^2}\frac{\Phi\left[\mathbf{x}'\right]-\Phi\left[\mathbf{x}\right]}{\left\|\boldsymbol{\xi}\right\|^2}dA_{x'} + R\left[\mathbf{x}\right] \tag{3.106}$$

For $\omega = 1-\frac{r}{\delta}$

$$\frac{\partial}{\partial t}\left(\rho\left[\mathbf{x}\right]\phi\left[\mathbf{x}\right]\right) = \int_{Hx}\frac{\rho\left[\mathbf{x},\mathbf{x}'\right]}{\mu}\frac{12k}{\pi\delta^2}\left(1-\frac{r}{\delta}\right)\frac{\Phi\left[\mathbf{x}'\right]-\Phi\left[\mathbf{x}\right]}{\left\|\boldsymbol{\xi}\right\|^2}dA_{x'} + R\left[\mathbf{x}\right] \tag{3.107}$$

For $\omega = 1-\frac{r}{\delta}$

$$\frac{\partial}{\partial t}\left(\rho\left[\mathbf{x}\right]\phi\left[\mathbf{x}\right]\right) = \int_{Hx}\frac{\rho\left[\mathbf{x},\mathbf{x}'\right]}{\mu}\frac{2k}{\pi\delta}\frac{1}{r}\frac{\Phi\left[\mathbf{x}'\right]-\Phi\left[\mathbf{x}\right]}{\left\|\boldsymbol{\xi}\right\|^2}dA_{x'} + R\left[\mathbf{x}\right] \tag{3.108}$$

As shown above, Equation (3.98), for the case of a single-phase fluid flowing in a two-dimensional homogeneous and isotropic porous medium, reduces to the formulations for a constant and linearly varying micro-permeability function respectively. These final equations obtained from a bond-based peridynamic model are exactly the same as those

obtained using a special case of the state-based formulation expressed in Equation (3.67), (3.68), and (3.69) when we realize the fluid density in a bond is the reference density. Although the three dimensional bond-based peridynamic model is not derived in this chapter, for the case of a single-phase fluid flowing in a three dimensional homogeneous and isotropic porous medium, Equation (3.98) also reduces to exactly the same formulations as those obtained using a special case of the state-based formulation expressed in Equation (3.71), (3.72), and (3.73).

3.3 Results and discussion

To validate the state-based peridynamic formulation of porous flow, we choose to solve a classical two-dimensional flow problem, a confined five-spot pattern where each fluid injection and production point is assumed to act as a point source and sink (negative source) respectively. In this injection pattern, four point sources are located at the corner of a square and the point sink sits in the center as shown in Fig. 3.3. In Fig 3.3, we plot a representative fluid pressure fluid pressure distribution and constant pressure (isopotential) lines for a confined five-spot pattern problem. The five-spot pattern is said to be balanced as the amount of fluid injected simultaneously through the four injection points is the same as the fluid removed from the central point-sink. There is no flow normal to the boundary of this balanced pattern. To minimize the computational time, we considered the smallest representable unit where there is only one positive point source (injector) and one negative point source (producer) (the smallest representative square unit of $L \times L$ in Fig. 3.3).

3.3.1 CASE1

For demonstration, we solve the five-spot pattern problem for the case in 3.2.1.4 (d) (homogeneous and isotropic constant porosity medium neglecting gravity in two dimensions). The simulation patterns are summarized as following: the smallest representative length $L = 400m$, fluid viscosity $\mu = 10^{-3}\ Pa\ s$, medium permeability $k = 10^{-13}\ m^2$, and injector's and producer's volumetric source $\dot{Q}_{n_i} = \pm 10^{-3}\ m^3 s^{-1}$ respectively. Neglecting gravity, the analytical steady-state solution of fluid pressure and volumetric flux due to an arbitrary point source i of net volume source $\dot{Q}_{n_i}$ at (x_i, y_i) in a porous medium of unit height is given by the following formulation [81].

$$p_i(x,y) = -\frac{\dot{Q}_{n_i}\mu}{4\pi k}\ln\left[(x-x_i)^2 + (y-y_i)^2\right] + C_i \qquad (3.109)$$

Where,

C_i : arbitrary constant assumed zero in this case

From the principle of superposition, fluid pressure and the volumetric flux due to N point sources and sinks is given by the following formulation [81]

$$p(x,y) = \sum_{i=1}^{N} p_i(x,y) = -\frac{\mu}{4\pi k}\sum_{i=1}^{N}\dot{Q}_{ni}\ln\left[(x-x_i)^2 + (y-y_i)^2\right] \qquad (3.110)$$

$$u(x,y) = -\frac{k}{\mu}\sum_{i=1}^{N}\mathbf{i}\frac{\partial p_i}{\partial x} + \mathbf{j}\frac{\partial p_i}{\partial y} = \frac{1}{2\pi}\sum_{i=1}^{N}\frac{\dot{Q}_{n_i}\left[\mathbf{i}(x-x_i) + \mathbf{j}(y-y_i)\right]}{(x-x_i)^2 + (y-y_i)^2} \qquad (3.111)$$

Where,

i : the unit vector in the Cartesian x coordinate direction

$\mathbf{j}$: the unit vector in the Cartesian y coordinate direction

The balanced five-spot pattern is obtained by considering several sources in the repeating pattern resulting in no-flow across the symmetry boundaries.

3.3.1.1 Numerical discretization

We use uniform discretization of grid spacing $\Delta x = \Delta y = L / n$ for the two-dimensional square domain where computational nodes, or collection points, are placed at the center of the square cells of length $\Delta x = \Delta y = L / n$. Each node is assigned an area equal to the square cell $\left(\Delta x^2\right)$. No node is placed on the boundary as two of the corners of the square domain have point source specified and the pressure there would asymptotically approach infinity. Bobaru and Duangpanya [71] have reported that for fine enough discretization, this approach would provide the same results as when the nodes are also placed at the boundaries and corners and the boundary and corner nodes have area different than those inside the domain. A mid-point numerical integration is used to convert the governing integral Equation (3.76) for a node $\mathbf{x}_i$ into coupled algebraic equations involving neighbor nodes $\mathbf{x}_n$ inside the horizon of the node $\mathbf{x}_i$

$$\frac{4k}{\pi\mu\delta^2}\sum_n \frac{p\left(\mathbf{x}_n\right)-p\left(\mathbf{x}_i\right)}{\left\|\boldsymbol{\xi}\right\|^2} A_{x_n} + l_v\left[\mathbf{x}_i\right] = 0 \qquad (3.112)$$

Where,

$A_{\mathbf{x}_n}$: the area of the neighbor node $\mathbf{x}_n$ inside the horizon of $\mathbf{x}_i$ [m^2]

Note that while approximating the integral with a summation, the contribution from the node area $A_{\mathbf{x}_i}$ is omitted since it does not exist. For a neighbor node whose square area

is completely inside the horizon of the node $\mathbf{x}_i$, $A_{\mathbf{x}_n} = \Delta x^2$. For nodes whose area is intersected by the horizon boundary, we have used the algorithm of Bobaru and Duangpanya [71] to calculate $A_{\mathbf{x}_n}$ .Note that the coefficient matrix for unknown fluid pressure in Equation (3.112) is singular which does not allow a unique solution of the system of equations. Also note that the analytical solution is symmetric about the diagonal line across which the two opposite sources have been placed. We, therefore, fixed the fluid pressure at one end of this diagonal line (left-top node) to zero making it the reference pressure in the domain. This makes the coefficient matrix nonsingular and a solution can be obtained. This steady state solution has also been verified with the solution from the corresponding transient problem with the same initial condition $(p = 0)$.

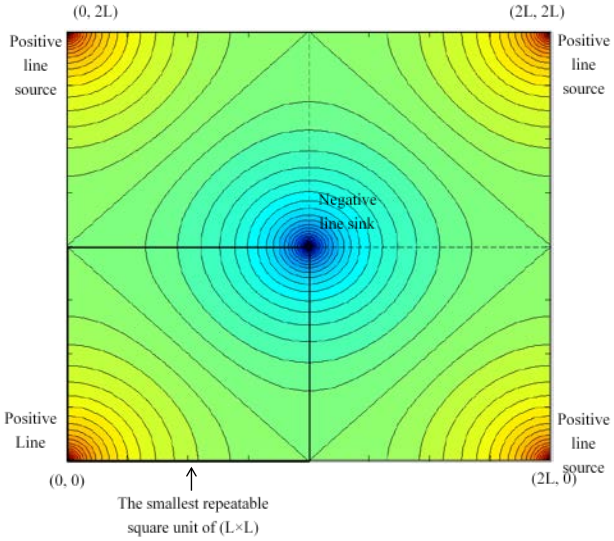

Fig. 3.3 Representative isopotentials for a confined five-spot well pattern. The square region of length L highlighted by the dark solid line in left-bottom is the smallest repeatable unit considered for computations. [77].

3.3.1.2 Imposing no-flow boundary condition

One way of imposing the no-flow boundary condition would be through imposing the non-local Neumann boundary condition. However, since the potential gradient across the no-flow boundary is zero, it was easier to impose it through creating ghost nodes outside the domain boundary. These ghost nodes are mirror images of the nodes near the domain boundary as the mirror plane. Thus across the domain boundary in the normal direction, the flow potential at any distance from the domain boundary is the same, resulting in local flow potential gradient becoming zero and the peridynamic potential gradient being approximately zero. Had the boundary nodes been on the domain boundary, the peridynamic potential gradient would also be zero. Due to the creation of ghost nodes outside the domain boundary in the region of thickness, δ, all the nodes in the domain have the same horizon size, otherwise the horizon of the nodes at and near boundaries would be smaller.

3.3.1.3 Applying the point source and sink

The peridynamic formulation, being non-local, utilizes volume constraints instead of boundary conditions used in local models [75]**.** The volume constraints are specified in a region of characteristic length scale δ, the peridynamic horizon. To numerically simulate porous flow due to a point source with net injection or production rate using classical theory, specifying the source term at just one node might be sufficient. However, doing the same in a non-local peridynamic formulation results in an over-prediction of the pressure at the source nodes i.e. $\left(\frac{\Delta x}{2}, \frac{\Delta y}{2}\right)$ and $\left(L-\frac{\Delta x}{2}, L-\frac{\Delta y}{2}\right)$ in the smallest repeatable unit. The larger is the peridynamic horizon, the larger is the over-prediction.

Introducing the volumetric source as a volume constraint in peridynamic formulation requires specifying it to all the nodes inside the horizon area (or volume) of the source node in the considered tow-dimensional (or three-dimensional) problem. However, specifying the source term in the complete horizon area through some form of numerical smoothing results in an under prediction of the source node pressure in comparison to the analytical solution (not shown here for brevity). Note that the non-local peridynamic formulation is never guaranteed to match with the solution of an equivalent local model (nor should it be expected to); it can only approach the local solution as the peridynamic horizon goes to zero. Therefore, specifying the source term in the complete horizon of the source node does provide an acceptable non-local peridynamic solution. However, we understand that there could be a length scale "λ" $\left(\frac{\Delta x}{2} < \lambda < \delta\right)$ such that the peridynamic solution of the source nodes' pressure can be closely matched with that from an equivalent local model. For redistributing the volumetric source term at $\mathbf{x}\left(I_v\left[\mathbf{x}\right]\right)$ over a distance λ, the net injection rate is assumed to be given by the following formulation.

$$\dot{Q}_n = \int_0^{\lambda}\int_0^{2\pi} l_v\left[r\right] r dr d\theta \tag{3.113}$$

Where, r is the radial distance of a neighbor node from the point source (dimension: [m]). We assume $I_v\left[r\right] = C\left[1+\cos\left(\frac{\pi r}{\lambda}\right)\right]$ and putting it back in Equation (3.113) and solving for C in terms of $\dot{Q}_n$ gives the following relationship.

$$I_v\left[r\right] = \frac{\pi \dot{Q}_n}{\lambda^2\left(\pi^2-4\right)}\left[1+\cos\left(\frac{\pi r}{\lambda}\right)\right] \tag{3.114}$$

The integral in Equation (3.113) is approximated numerically using the mid-point integration technique and we define a normalized volumetric source as follows,

$$Normalized\ volumetric\ source = \frac{\sum_{p} l_v\left[\mathbf{x}_p\right] A_p}{\dot{Q}_n} \tag{3.115}$$

Where, p represents only those nodes around source points for which distance from the point source, $r \le \lambda$.

Next, we define the relative difference to compare peridynamic solution with the analytical solution:

$$\mathrm{Re}\, l_{diff} = \frac{\left\| p_{analytical} - p_{peridynamics} \right\|^2}{\left\| p_{analytical} \right\|^2} \tag{3.116}$$

Fig. 3.4 shows the smoothing length $\frac{\lambda}{\Delta x}$ for different horizon size $\delta = m\Delta x$ vs. the relative difference. As shown in Fig. 3.4, the optimized smooth length which minimize the relative difference varies with horizon size. As shown in the inset of Fig. 3.4, the relationship between optimized smooth length and horizon size is given by the following formulation gotten through the simple linear regression.

$$\lambda = 0.385\delta + 1.2925\Delta x \tag{3.117}$$

The significance of source distribution is shown in Fig. 3.5 (a) where the variation of the relative difference in fluid pressure with m for the cases with smoothing and the case without smoothing are compared. As discussed above, the larger the horizon size, the larger the relative difference we observe for the cases without smoothing. However, for the cases

with optimized smoothing length, the relative error is much smaller than for cases without smoothing and does not increase with horizon size. In Fig 3.5 (b), we also compare pressure at the source node for the two cases. The pressure in the optimized smoothing length cases is closer to the analytical solution as the horizon size increases, while the pressure in the cases without smoothing show a huge separation from the analytical solution as horizon size increases.

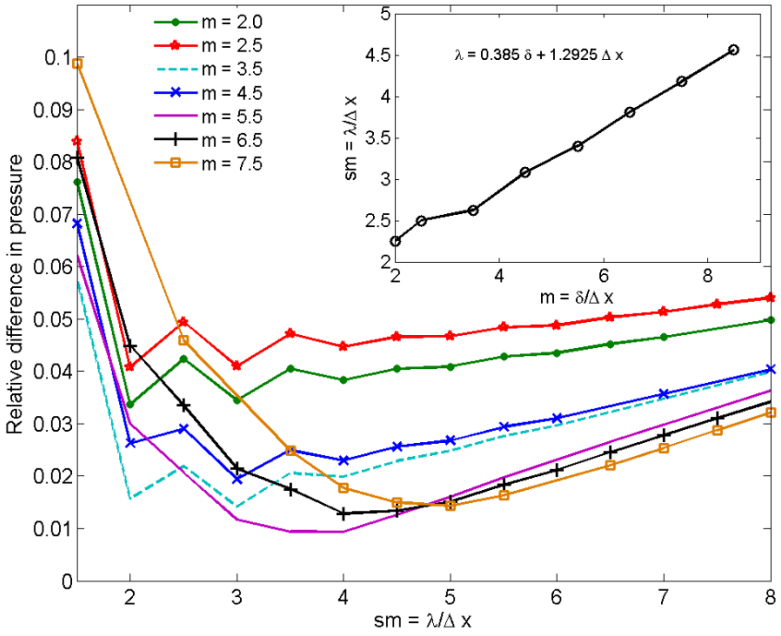

Fig. 3.4 Variation in relative difference in pressure with normalized smoothing length (sm) for different m. The inset shows the interpolated sm values for each m such that the pressure at the source node matches exactly with the exact local solution [77].

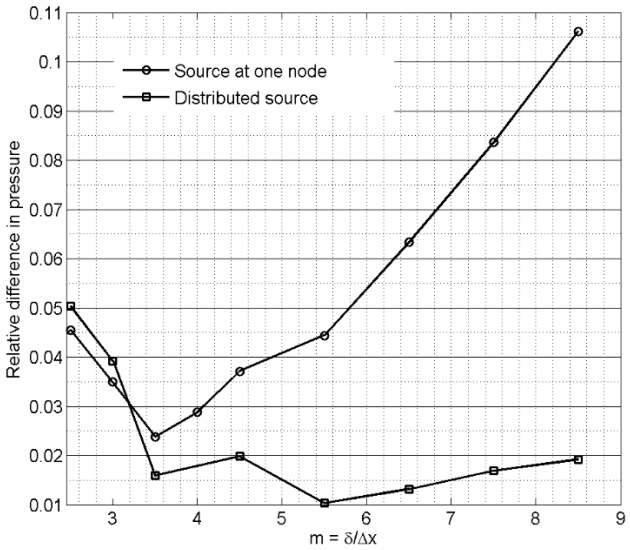

(a)

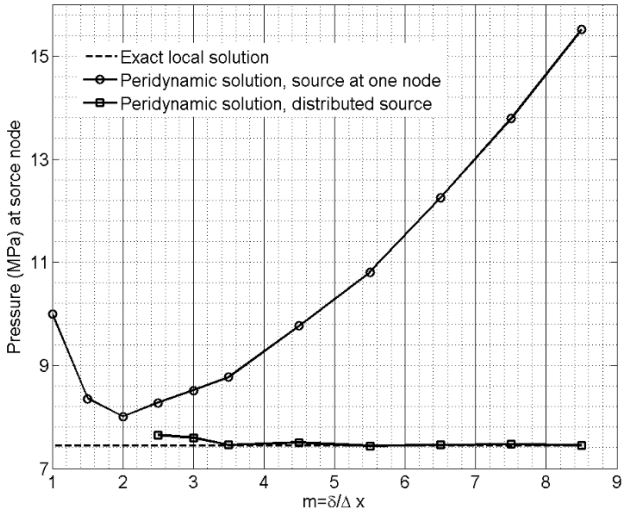

(b)

Fig. 3.5 (a) Variation in the relative difference in pressure with m for source specified at only one node and a distributed source in the optimum smoothing length inside the horizon of source node, (b) variation is source node pressure with m from exact local solution and peridynamic solution for source specified at only one node and distributed source in the optimum smoothing length inside the horizon of source node [77].

3.3.1.4 Convergence study

Since peridynamic formulations are non-local, the exact non-local solution exists for each given horizon size, δ. A larger $m = \frac{\delta}{\Delta x}$ gives a more exact non-local solution for a fixed horizon size (m convergence). In addition, the non-local solution converges to the classical solution when $\delta \to 0$, (δ convergence). In practical simulations, m must be large enough to obtain accurate results but small enough to achieve a reasonable computation time. To optimize m for the following simulations, we performed an m-convergence test for the fixed δ values (L/10, L/20, and L/40) by increasing m from 2.5 to 9 and investigated the relative pressure difference between the peridynamic solution and the exact analytical local solution. Fig. 3.6 shows the results of the m-convergence test. As shown in Fig. 3.6, the relative difference substantially decreases as m increases for $m < 5$. However, for $m \geq 5$, the relative difference becomes almost constant in each δ case, which may suggest that the numerical peridynamic solution reaches the exact non-local solution when $m \geq 5$. Hence we select $m = 5.5$ for all the subsequent simulations. In addition, to obtain a close match to an analytical solution (less than 1% error) and to minimize the computation time we chose $\delta = L / 20$.

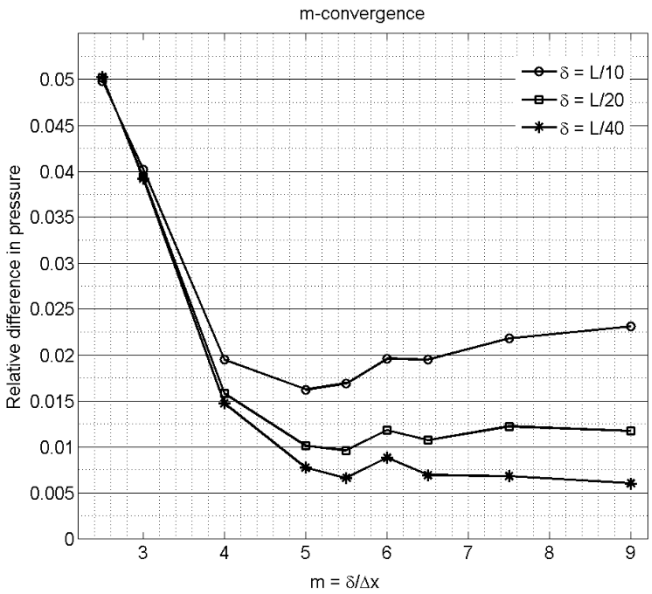

Fig. 3.6 m-convergence curves of the relative difference in fluid pressure with horizon sizes and the number of nodes inside the horizon, m [77].

3.3.1.5 Peridynamics solution

Fig 3.7 shows the steady-state peridynamic solution of the five-spot pattern problem discussed above. As shown in Fig. 3.7 (a), the pressure contours are exactly normal to the four boundaries since we set a no-flow boundary condition through the ghost nodes. As shown in Fig 3.7 (b), the pressure distribution along the diagonal line from the injector to the producer in the peridynamic solution is exactly the same as the solution of the local model. In addition, as shown in Fig 3.7 (c), the pressure distribution along the y-boundary nodes ($y = \Delta y / 2$ and $y = L - \Delta y / 2$) in the peridynamic solution also shows good agreement with the exact local solution. Finally, as shown in Fig 3.7 (d), the volumetric flux at the y-boundary nodes in the peridynamic solution almost shows the same variation of the exact local solution except for the nodes inside the horizon of the source

nodes. The reason of the discrepancy near the source node is the following. In peridynamics, the approximate peridynamic pressure gradient which directly affects volumetric flux is obtained as the average of the contributions from all the nodes inside the horizon. Hence, even if the pressure gradient along the y boundary is the same as local exact solution, the volumetric flux is heavily smeared out the local exact solution by the effect of other pressure points inside the horizon. This outcome is in the line with non-local peridynamic theory where information at any node is a characteristic of its horizon or non-local neighborhood.

3.3.2 CASE2

Heterogeneities such as fractures in a porous medium result in discontinuities in the pressure field and other derived quantities. The classical local model faces difficulties simulating such problems since spatial derivatives are undefined at the discontinuities. Bobaru and Duangpanya [71] captured such boundaries for the problem of heat flow modeling by searching for such boundaries and modifying the conductance of the bonds crossing them. Here, we show that our state based peridynamic formulation can simulate and predict such discontinuities without any modification to the formulation or any additional computational expense. The advantage to the bond based model is that no additional search for such boundaries is needed and the conductance of the bond crossing such boundaries emerges from the formulation itself. To demonstrate this feature, we consider a simple test case (Fig. 3.8) where we introduce an impermeable block (dimension: $3L/4 \times L/4$) of zero permeability in the problem discussed in Case 1.

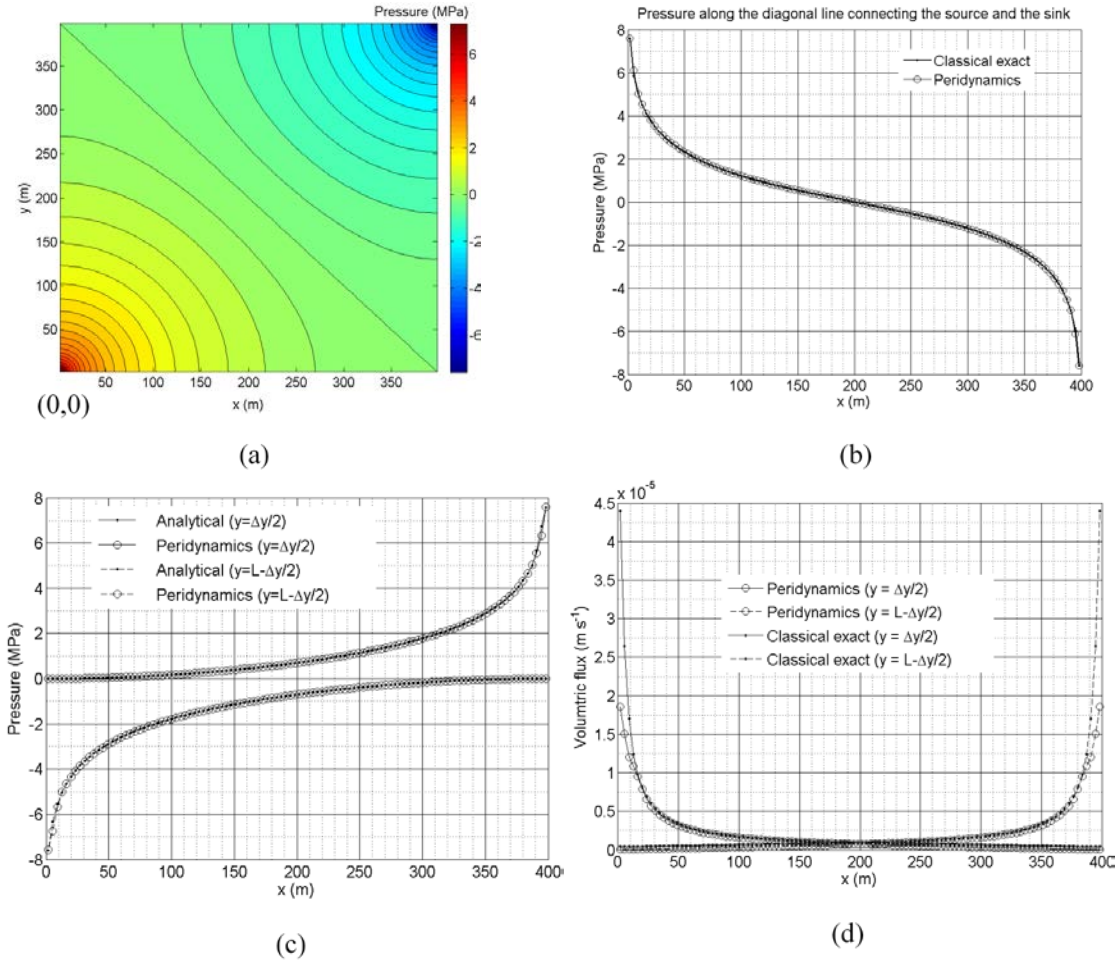

Fig. 3.7 (a) Pressure contours, (b) pressure along the diagonal line connecting the source and the sink points from the classical exact solution and the peridynamic solution , (c) pressure along the y-boundaries $(y = \Delta y/2 \text{ and } L - \Delta y/2)$ from the classical exact solution and the peridynamic solution, and (d) volumetric flux pressure along the y-boundaries $(y = \Delta y/2 \text{ and } L - \Delta y/2)$ from the classical exact solution and the peridynamic solution [77].

3.3.2.1 Numerical discretization

The domain discretization is the same as the previous case. The simulation domain $(L \times L)$ is discretized into 110×110 and $m = 5.5$. A mid-point numerical integration is used

to convert Equation (3.78) for the node $\mathbf{x}_i$ into coupled algebraic equations involving neighbor nodes $\mathbf{x}_n$ inside its horizon.

$$\frac{8}{\pi\mu\delta^2}\sum_n \frac{\xi\left(\mathbf{k}_m^a\left[\mathbf{x}_i,\mathbf{x}_n\right]-\frac{1}{4}tr\left(\mathbf{k}_m^a\left[\mathbf{x}_i,\mathbf{x}_n\right]\mathbf{I}\right)\right)\xi}{\|\xi\|^2}\left(\frac{p(\mathbf{x}_n)-p(\mathbf{x}_i)}{\|\xi\|^2}\right)A_{xn}+I_v\left[\mathbf{x}_i\right]=0 \quad (3.118)$$

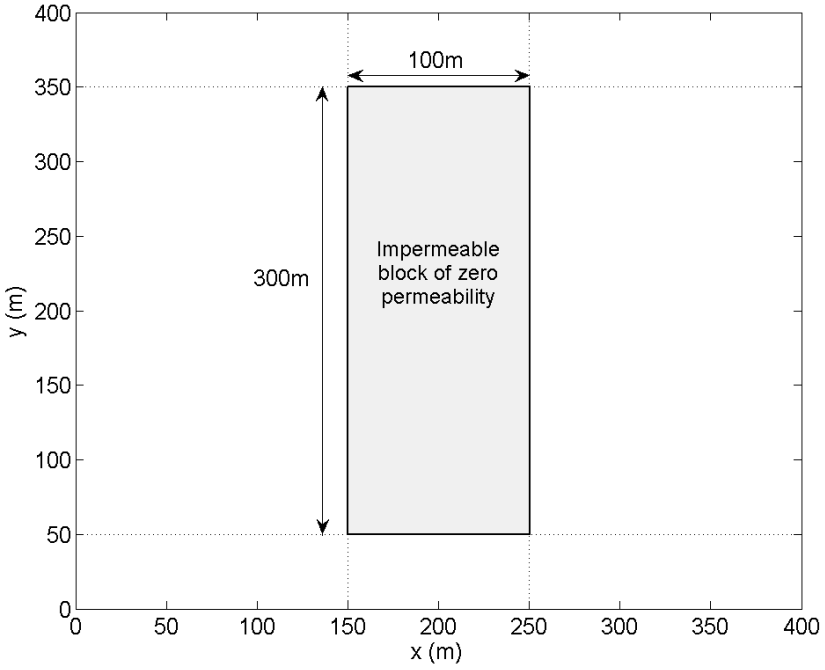

Fig. 3.8 Dimensions of the impermeable block of zero permeability [77].

3.3.2.2 Peridynamic solution

Fig. 3.9 (a) shows the pressure contours in the domain. Due to the non-local nature of the peridynamic formulation, we find a continuous variation in the fluid pressure across the boundary of the impermeable block. Fig. 3.9 (b) show that the peridynamic formulation

does capture the introduced discontinuity. Flow originates at the point source, goes around the impermeable block and reaches the point-sink. Because of the non-locality, we also see the fluid penetrating inside the discontinuous region up to a thickness δ. Note that the peridynamic formulation approaches the classical local model in the limit of $\delta \to 0$. Therefore, for a horizon much smaller than the one chosen here, the stream lines as expected from the local model would approach the boundary of the discontinuous region. In Fig. 3.9 (c), we plot the fluid pressure at y = L/2 to demonstrate the discontinuity in fluid pressure being captured by the peridynamic formulation. Here, we also see the pressure inclusion into the impermeable region due to the non-locality. Finally, in Fig. 3.9 (d), we report the x and y components of the volumetric flux at y = L/2. The x component of the volumetric flux near the domain boundaries is close to being zero satisfying the imposed no-flow boundary condition. The y component of the volumetric flux shows the expected jump inside the impermeable boundary in a layer of thick δ around it due to non-locality. Case 2 shows the peridynamic formulation simulates the problem with discontinuities with no additional computational cost. However, the non-locality smear out the sharp change at the discontinuous boundary.

To capture the discontinuities without smearing them out, the horizon size has to be much smaller in the original formulation. Here we propose the following modification to capture the sharp discontinuities without forcing the horizon size to approach zero. In Equation (3.50), we predict the flow with effective permeability $\mathbf{k}_m^a\left[\mathbf{x},\mathbf{x}'\right]$ obtained from the arithmetic mean of the permeability at the two end nodes. This represents the bond between any two nodes as two flow channels of different permeability ($\mathbf{k}\left[\mathbf{x}\right]$ and $\mathbf{k}\left[\mathbf{x}'\right]$) in parallel. However, if we represent the bond as two flow channels of different permeability in series, the mean bond permeability would be obtained from the harmonic mean of the permeability at the two end points of the bond as

$$\mathbf{k}_m^h\left[\mathbf{x},\mathbf{x}'\right]=\frac{2\mathbf{k}\left[\mathbf{x}\right]\mathbf{k}\left[\mathbf{x}'\right]}{\left(\mathbf{k}\left[\mathbf{x}\right]+\mathbf{k}\left[\mathbf{x}'\right]\right)} \tag{3.119}$$

In Fig. 3.10, we regenerate the results reported in Fig 3.9, from our peridynamic formulation of Case 2, after replacing $\mathbf{k}_m^a\left[\mathbf{x},\mathbf{x}'\right]$ with $\mathbf{k}_m^h\left[\mathbf{x},\mathbf{x}'\right]$, keeping all other model parameters the same. As shown in Fig. 3.10, redefining the mean bond permeability using the harmonic mean captures the expected discontinuities very closely. Please note that, in the steady state solution, we did not solve for the points inside the impermeable block since all the bonds connected to the points inside the block would have zero mean permeability ($\mathbf{k}_m^h\left[\mathbf{x},\mathbf{x}'\right]=0$). We imposed the reference pressure ($p=0$) as a Dirichlet-like condition. This steady state solution has also been verified with the solution from the corresponding transient problem with initial pressure being the same as the reference pressure.

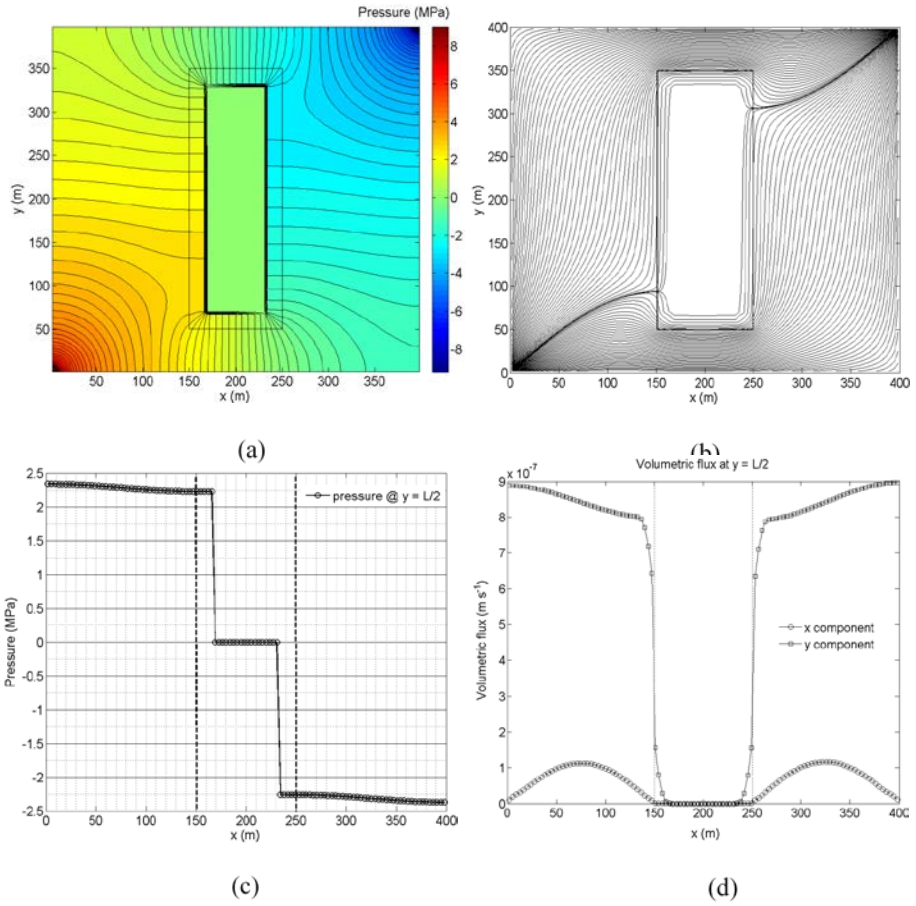

Fig. 3.9 Peridynamic results for the mean bond permeability resulting as the arithmetic mean of nodal permeability, (a) pressure contours inside the domain, (b) stream lines inside the domain from the peridynamic solution (c) pressure along $y = L/2$ from the peridynamic solution, and (d) volumetric flux along $y = L/2$ from the peridynamic Solution [77].

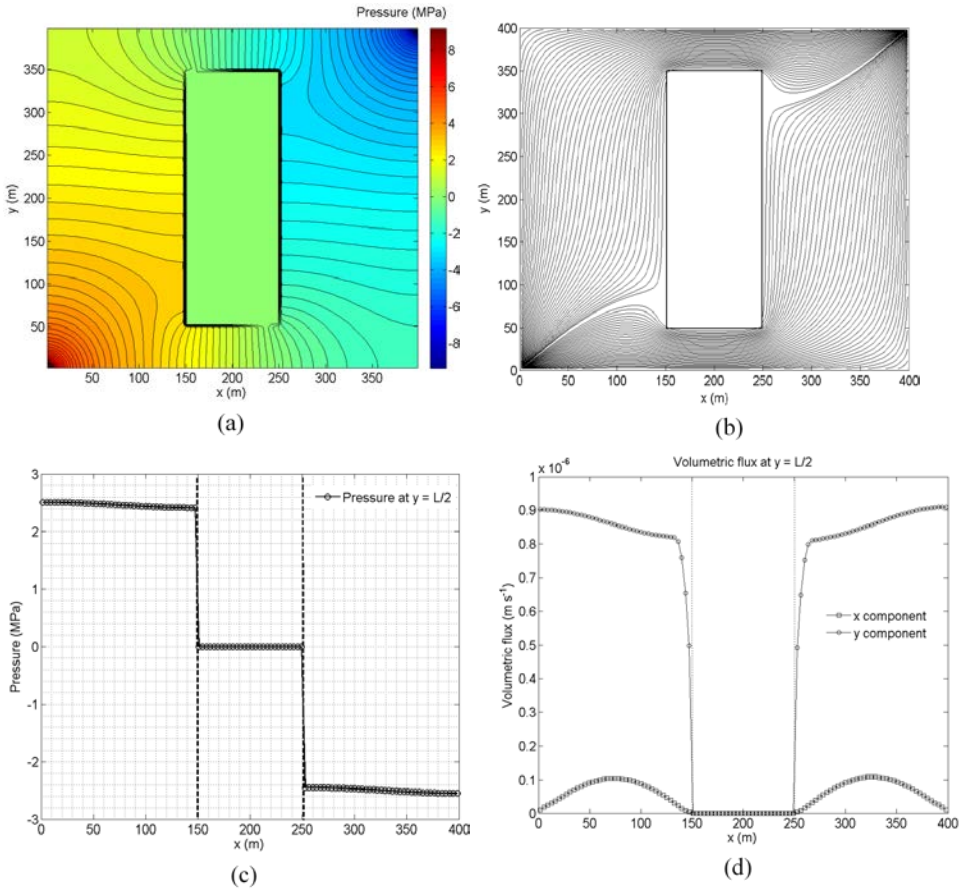

Fig. 3.10 Peridynamic results for the mean bond permeability given by the harmonic mean of nodal permeability, (a) pressure contours inside the domain, (b) stream lines inside the domain from the peridynamic solution (c) pressure along y= L/2 from the peridynamic solution, and (d) volumetric flux along y= L/2 from the peridynamic solution [77].

3.3 Conclusions

Using variational principles and correspondence with the classical local theory incorporating the continuity equation and Darcy's law, we derived a generalized non-local, state-based peridynamic formulation of the governing mass conservation equation for single-phase flow of a liquid of small and constant compressibility thorough a porous medium. The governing integral equations of the peridynamic theory are obtained for a non-local region of finite length scale that allows local as well as non-local potential differences to drive the volumetric flux. The formulation is general as the fluid mass over any arbitrary bounded body remains conserved for any constitutive mode chosen to relate mass flow state with the flow potential state. Currently, we have chosen a constitutive model where flow in a bond only depends on the potential difference in that bond unlike the generalized state-based peridynamic theory where the collective potential difference in all the bonds connected to a given material point would contribute. The non-local constitutive parameters in the model are represented in terms of the material properties by imposing a match with the classical local theory in the limit of the horizon approaching zero.

We have also developed a bond-based peridynamic formulation for a fluid flowing through a homogenous isotropic porous medium that is recovered from the state-based formulation as a special case. We validated the model for a fluid of constant properties flowing through a homogeneous isotropic porous medium.

As an example application, we demonstrate the method by simulating the flow of fluids in a two dimensional domain with multiple pressures source and sinks. We find that introducing the mass source at one point result in significantly limited diffusion from the source in non-local model. On the other hand, as required in peridynamic theory, if the

mass source is distributed in whole horizon volume of the source point, it results in an under-prediction of the source point pressure. For a better match with the exact local solution, we find an optimum radial distance from the source point as a function of horizon size and discretization size to specify the mass source as a volume constraint. For the 5-spot pattern problem, through an m-convergence test, we have shown that the non-local peridynamic model of porous flow in 2D converges to the exact local solution in the limit of the peridynamic horizon approaching zero while keepings the nodes inside the horizon fixed. For the optimum size of horizon and volume constraint for the mass source, the developed peridynamics model provides a very close match with the exact local solution of the test case. We also investigate the same in a domain with existing discontinuities. The model captures the sudden change in the constitutive properties though non-locality forces the horizon size to be as small as possible for heterogeneities to be captured sharply. Reducing the horizon size imposes the constraint of longer computational time. However, with the techniques of adaptive refinement, scaling [82] and parallelization this computation time can be reduced.

CHAPTER4: DEVELOPMENT OF A PERIDYNAMICS BASED HYDRAULIC FRACTURING MODEL

4.1 Introduction

In this chapter[2], a comprehensive 3-D hydraulic fracturing model is developed and presented based on a recently developed non-local theory of continuum mechanics known as peridynamics [61, 83]. This new approach to modeling hydraulic fractures overcomes some of the intrinsic limitations of the corresponding local theory in dealing with discontinuous displacement fields. The essence of the peridynamic model is that integration, rather than differentiation, is used to compute the force at a material point. Since the spatial derivatives are not used, the equations remain equally valid at points or surfaces of discontinuity [61]. The peridynamics theory has been successfully applied to diverse engineering problems [61, 83] involving autonomous initiation, propagation, branching and coalescence of fractures in heterogeneous elastic media. However, peridynamics has not been applied to simulate fluid pressure driven deformation and damage of porous media. Turner [84] utilized the theory of interacting continua [85-87] and presented a formulation for incorporating the effects of pore pressure in the state-based peridynamic formulation of solid mechanics. However, to avoid the complexities of a fully coupled geomechanics and fluid flow model, he assumed the fluid pressure to be either known or opted to solve for it numerically or analytically through classical means. In our

[2] This Chapter forms the basis of the following publication: Journal of Computational Mechanics: Ouchi, H., A. Katiyar, J. York., J. T. Foster, and M. M. Sharma, A fully coupled porous flow and geomechanics model for fluid driven cracks: a peridynamics approach. 2015. 55(3): p. 561-576.

fully implicitly coupled, 3-D peridynamic formulation of fluid driven deformation and damage, we follow his approach [84] to include the effects of pore pressure into the peridynamic equation of motion. However, we also solve for the fluid pressure in the medium as well as in the fracture space using our recently developed peridynamic porous flow formulation [77]. The additional steps of coupling for the appropriate fluid-solid interaction in an arbitrary heterogeneous medium are presented in the mathematical modeling section. In the next section, we present the mathematics of our peridynamics based hydraulic fracturing model. We also report a novel way to implement the non-local traction boundary condition obtained using the peridynamic theory and the classical theory. An overview of our simulator's numerical algorithm is presented followed by our approach to our parallelization scheme. In the following section, we verify our proposed traction boundary condition by comparing our results with the results of a 2-D elastic body in plane-strain. In the next section, we verify the peridynamic poroelastic model through comparison with the classical 1-D consolidation problem. We demonstrate that the non-local model can recover the well-known classical solution of poroelasticity. Then, we simulate the propagation of a single fracture in a 2-D poroelastic medium. The peridynamic solution of fracture geometry and injection pressure in 2-D plane strain is verified by comparing the numerical results with the analytical 2-D KGD model [11, 12]. The stress field around a fracture of known length and fluid pressure from peridynamic formulation is also verified with the well-known analytical solution by Sneddon [88]. Finally, we simulate the propagation of a single fracture in a 3-D poroelastic medium. The peridynamic solution of fracture geometry and injection pressure is compared by the solution of PKN model [13, 14] . The efficiency of parallelization is also discussed.

4.2 Mathematical model

4.2.1 PERIDYNAMICS BASED POROELASTIC MODEL

In order to model the interaction between reservoir deformations and pore pressure changes, i.e. model the poroelastic effect, we need to couple the peridynamics porous flow formulation with the peridynamics solid mechanics formulation. For this purpose, both the peridynamics constitutive relations for the equation of motion (Equation (2.9)) and the peridynamics mass conservation for fluid flow are modified by considering the effect of fluid pressure and the effect of deformation respectively.

For the peridynamics equation of motion (Equation (2.9)), the following effective force scalar state, which was first proposed by Dan Turner, is introduced [84]. The relationship between force scalar state (Equation (2.9)) and the effective force scalar state (Equation (4.1)) is similar to the relationship between total stress tensor and effective stress tensor given by Equation (4.3).

$$\underline{t}\left[\mathbf{x},t\right]\langle\boldsymbol{\xi}\rangle = \frac{3\left(K\theta-\alpha P\right)}{m}\underline{\omega}\underline{x}\langle\boldsymbol{\xi}\rangle + \frac{15G}{m}\underline{\omega}\underline{e}^{d}\langle\boldsymbol{\xi}\rangle \tag{4.1}$$

$$\alpha = 1-\frac{K}{K_m} \tag{4.2}$$

$$\boldsymbol{\sigma}_{eff} = \boldsymbol{\sigma}_{total} - \alpha P\mathbf{I} \tag{4.3}$$

Where,

$\mathbf{I}$: identity tensor

K_m : bulk modulus of rock grain [Pa]

P : pore pressure [Pa]

α : Biot's coefficient

$\boldsymbol{\sigma}_{eff}$: effective stress tensor [Pa]

$\boldsymbol{\sigma}_{total}$: total stress tensor [Pa]

In the same way, under a 2-D plane strain condition, Equation (4.1) is expressed by the following formulation based on the 2-D effective force-state [89].

$$\underline{t}\left[\mathbf{x},t\right]\langle\boldsymbol{\xi}\rangle = \frac{2\left(\left(K-\frac{G}{3}\right)\theta-\alpha P\right)}{m}\underline{\omega}\underline{x}\langle\boldsymbol{\xi}\rangle + \frac{8G}{m}\underline{\omega}\underline{e}^{d}\langle\boldsymbol{\xi}\rangle \tag{4.4}$$

In the mass conservation equation , a novel porosity formulation derived by Tran et.al [90] is introduced to simulate changes in porosity due to deformation of the porous body. This formulation allows simulating porosity as a function of volumetric strain that in turn is a function of pore pressure, mean total stress, and temperature.

$$\phi^{(n+1)}\left[\mathbf{x}\right] = \phi^{(n)}\left[\mathbf{x}\right]\left(1-C_r\Delta P\right) + \left(1-\varepsilon_v^{(n)}\right)\left\{\alpha C_b\left(\Delta P+\Delta\sigma_m\right)+\beta\Delta T\right\} \tag{4.5}$$

Where,

C_b : compressibility of rock ($=\frac{1}{K}$) [1/Pa]

C_r : compressibility of rock grain ($=\frac{1}{K_m}$) [1/Pa]

T : temperature [K]

ε_v : volumetric strain

By neglecting temperature variation, replacing volumetric strain with local dilatation θ_{local} , replacing total mean stress change ($\Delta\sigma_m$) by $K\Delta\varepsilon_v - \alpha\Delta P$, and rearranging the original formulation, we obtain the following discretized formulation for the porosity,

$$\phi^{(n+1)}[\mathbf{x}] = \phi^{(n)}[\mathbf{x}](1 - C_r\Delta P) + \alpha\left(1 - \varepsilon_v^{(n)}\right)\{C_r\Delta P + \Delta\theta_{local}\} \tag{4.6}$$

Where,

θ_{local} : local dilatation

Local dilatation θ_{local} is evaluated based on immediate neighborhood $H_{\mathbf{x}local}$ defined by the following formulation.

$$\theta_{local} = \begin{cases} \dfrac{2}{m}\displaystyle\int_{H_{\mathbf{x}local}} \underline{\omega}\underline{\mathbf{X}}\langle\boldsymbol{\xi}\rangle e\langle\boldsymbol{\xi}\rangle dA_{\mathbf{x}'} & for\ 2D \\ \dfrac{3}{m}\displaystyle\int_{H_{\mathbf{x}local}} \underline{\omega}\underline{\mathbf{X}}\langle\boldsymbol{\xi}\rangle e\langle\boldsymbol{\xi}\rangle dV_{\mathbf{x}'} & for\ 3D \end{cases} \tag{4.7}$$

By solving Equation (2.7) and Equation (3.30) simultaneously with Equation (4.2) and Equation (4.6) as governing equations, poroelastic behavior in a reservoir is simulated using the peridynamics theory.

4.2.2 HYDRAULIC FRACTURING MODEL

In order to simulate hydraulic fractures using peridynamics theory, the volume of hydraulic fractures and stress interaction between fracturing fluid and the reservoir have to be properly evaluated in accordance with the theory. Here, a new mathematical framework of hydraulic fracturing is developed.

4.2.2.1 Governing equations

For developing a peridynamics-based hydraulic fracturing model, the mass conservation equation for the fracturing fluid is newly defined for solving fracturing fluid pressure. This governing equation is coupled with the pre-existing two governing equations for the peridynamics based poroelastic model (Equation (2.7) and (3.30)). In the peridynamic based hydraulic fracturing model, each element can have five primary unknowns (displacement of x, y, z direction, pore pressure P , and fracturing fluid pressure P_f) by solving the three governing equations (the momentum valance equation (vector formulation), the mass conservation equation for porous pressure (scalar formulation), and the mass conservation equation for fracturing fluid respectively (scalar formulation)). However, the mass conservation equation for the fracturing fluid is not solved in every elements. As shown in Fig. 4.1, it is only solved in the elements where fracture volume exists. Initially, the governing equation for fracturing fluid is only solved in perforated elements since no fracture has propagated in the other elements. However, as shown in Fig. 4.1, as the fracture propagates, the elements where the mass conservation equation for fracturing fluid are increasing. The number of primary unknowns solved in elements are adaptively changing with fracture propagation in our peridynamics based hydraulic fracturing model. Here, we review the three governing equations (the momentum balance

equation (2.8), the mass conservation equation for porous fluid (4.8), and the mass conservation equation for fracturing fluid (4.12)) in this model.

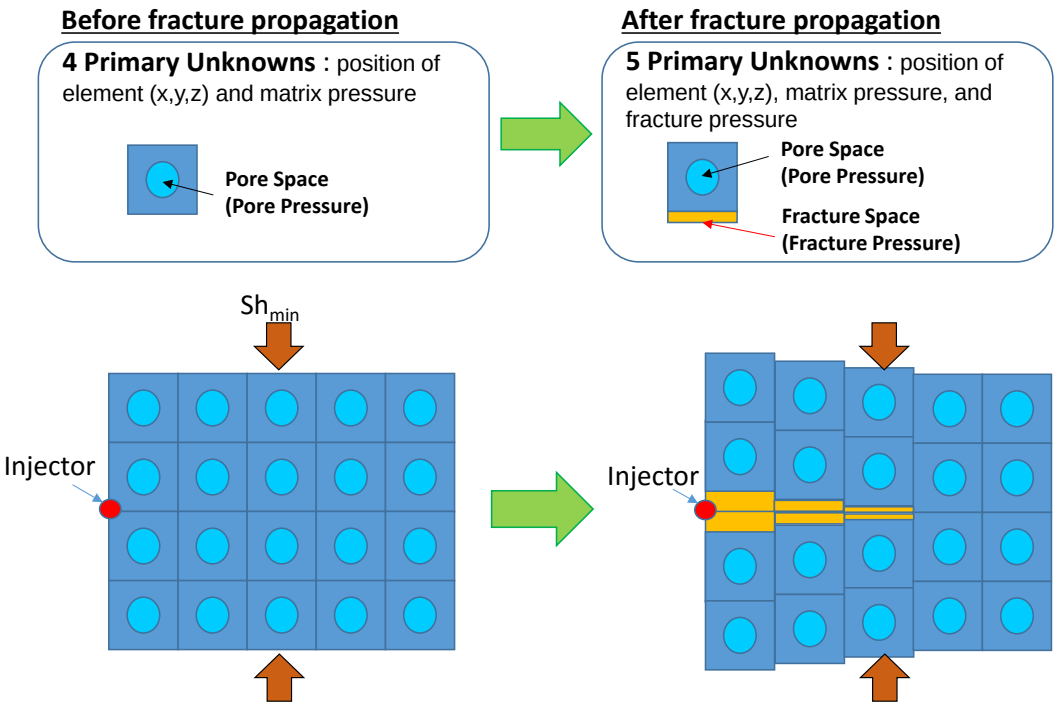

Fig. 4.1 Concept of the peridynamics-based hydraulic fracturing model[91].

Momentum balance equation

The force scalar state $\underline{t}\left[\mathbf{x},t\right]\left\langle \boldsymbol{\xi}\right\rangle$ in Equation (2.8) changes depending on the bond failure and whether the bond passes through the fracture space or not. A detailed discussion of the force scalar state is presented in the next section (4.2.2.2).

$$\rho\ddot{u}=\int_{H_x}\left(\underline{T}\left[\mathbf{x},t\right]\left\langle \boldsymbol{\xi}\right\rangle-\underline{T}\left[\mathbf{x}',t\right]\left\langle -\boldsymbol{\xi}\right\rangle\right)dV_{\mathbf{x}'}+\mathbf{b}\left[\mathbf{x}\right] \tag{2.7}$$

$$\underline{T}[\mathbf{x},t]\langle\xi\rangle = \underline{t}[\mathbf{x},t]\langle\xi\rangle \frac{\underline{\mathbf{Y}}\langle\xi\rangle}{\left\|\underline{\mathbf{Y}}\langle\xi\rangle\right\|} = \underline{t}[\mathbf{x},t]\langle\xi\rangle \frac{\xi+\eta}{\|\xi+\eta\|} \tag{2.8}$$

Mass conservation equation for pore fluid

In order to consider the convective transport from the fracture space to the matrix pore space, or in other words to consider "leak-off", a source term $I[\mathbf{x}]$ is added to Equation (3.30) in the hydraulic fracturing model.

$$\frac{\partial}{\partial t}\left(\rho_w[\mathbf{x}]\phi[\mathbf{x}]\right) = \int_{H_x}\left(\underline{Q}[\mathbf{x},t]\langle\xi\rangle - \underline{Q}[\mathbf{x}',t]\langle-\xi\rangle\right)dV_{\mathbf{x}'} + R[\mathbf{x}] + I[\mathbf{x}] \tag{4.8}$$

$$\underline{Q}[\mathbf{x},t]\langle\xi\rangle = \frac{\gamma}{2\mu}\underline{\omega}\langle\xi\rangle\rho_0 \frac{\xi\mathbb{k}[\mathbf{x},\mathbf{x}']\xi}{\|\xi\|^4}\left(\Phi[\mathbf{x}'] - \Phi[\mathbf{x}]\right) \tag{3.30}$$

$$\mathbb{k}[\mathbf{x},\mathbf{x}'] = \mathbf{k}[\mathbf{x}] - \frac{1}{2+d_{num}} tr\left(\mathbf{k}[\mathbf{x}]\right)\mathbf{I} \tag{4.9}$$

$$I[\mathbf{x}] = -\frac{\rho_f[\mathbf{x}]k_{leak}A}{V\mu_f}\frac{d\Phi}{dl} = \frac{\rho_f[\mathbf{x}]k_{leak}\Delta A_p[\mathbf{x}]\left(\Phi_f[\mathbf{x}] - \Phi[\mathbf{x}]\right)}{\Delta V[\mathbf{x}]\mu_f\left(l_p/2\right)} \tag{4.10}$$

$$k_{leak} = \mathbf{n}_{surf}\cdot\left(\mathbf{K}[\mathbf{x}]\mathbf{n}_{surf}\right) \tag{4.11}$$

Where,

ΔA_p : the surface area of one of the faces of a material point [m2]

d_{num} : dimension number (2-D = 2, 3-D = 3)

k_{leak} : matrix permeability at a material point [m^2]

l_p	:	characteristic length of a material point	[m]
L	:	leak-off term	[kg/m^3]
$\mathbf{n}_{surf}$	:	unit normal vector perpendicular to a fracture surface	
R	:	mass source term	[kg/m^3]
ΔV_p	:	the volume of the material point	[m^3]
Φ_f	:	fracturing fluid potential	[Pa]
μ_f	:	fracturing fluid viscosity	[m s]
ρ_f	:	fracturing fluid density	[kg/m^3]

As shown in Fig. 4.2, the leak-off term Equation (4.10) is derived simply by assuming Darcy's law.

Mass conservation and flow equations for fracturing fluid

Based on lubrication theory, we have modeled fracturing fluid flow inside a fracture opening as a non-local porous flow with fracture permeability being related to the fracture width.

$$\frac{\partial}{\partial t}\left(\rho_f\left[\mathbf{x}\right]\phi_f\left[\mathbf{x}\right]\right) = \int_{H_{xlocal}} \left(\underline{Q}_f\left[\mathbf{x},t\right]\langle\boldsymbol{\xi}\rangle - \underline{Q}_f\left[\mathbf{x}',t\right]\langle-\boldsymbol{\xi}\rangle\right) dV_{\mathbf{x}'} + R_f\left[\mathbf{x}\right] - I\left[\mathbf{x}\right] \tag{4.12}$$

$$\underline{Q}_f\left[\mathbf{x},t\right]\langle\boldsymbol{\xi}\rangle = \frac{\gamma}{2}\frac{\rho_f\left[\mathbf{x}\right]}{\mu_f}\frac{k_f\left[\mathbf{x}\right]}{2\|\boldsymbol{\xi}\|^2}\left(\Phi_f\left[\mathbf{x}'\right] - \Phi_f\left[\mathbf{x}\right]\right) \tag{4.13}$$

Where,

H_{xlocal} : local neighborhood of $\mathbf{x}$ (horizon size = $1.5\Delta l$)

k_f : fracture permeability [m^2]

$\underline{Q}_f\langle\boldsymbol{\xi}\rangle$: peridynamics flow scalar state for fracturing fluid [kg/m^6]

R_f : source term for fracture space [kg/m^3]

ϕ_f : fracture porosity

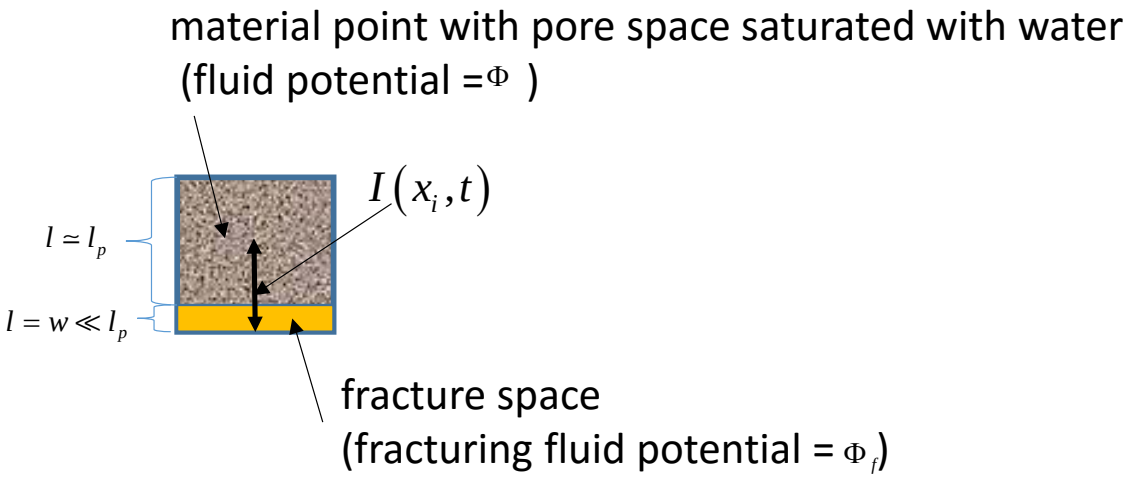

Fig. 4.2 Illustration of fluid leak-off model.

Fracture porosity in the above formulation is the fraction of fracture volume in the control volume of a discretized material point, and is given by the following formulation.

$$\phi_f[\mathbf{x}] = \begin{cases} 0 & for\ d \le d_{cr} \\ \theta_{local} - \theta_{local}(s_{cr}) & for\ d > d_{cr} \end{cases} \tag{4.14}$$

Where, $\theta_{local}(s_{cr})$ is the local dilatation evaluated at the critical strain. $\theta_{local}(s_{cr})$ in our discretized domain is given by the following formulation,

$$\theta_{local\_i}\left(s_{cr}\right)=\sum_{j=1}^{N_{local}}\left\{\frac{\underline{\omega}_i\left\|\mathbf{x}_j-\mathbf{x}_i\right\|e_i^{*(n+1)}dV_{\mathbf{x}_j}}{m_{local}}\right\}$$
$$=\sum_{j=1}^{N_{local}}\left\{\frac{\underline{\omega}_i\left\|\mathbf{x}_j-\mathbf{x}_i\right\|\left(\min\left(\left\|\mathbf{y}_j^{(n+1)}-\mathbf{y}_i^{(n+1)}\right\|,\mathrm{s}_{cr}\left\|\mathbf{x}_j-\mathbf{x}_i\right\|\right)-\left\|\mathbf{x}_j-\mathbf{x}_i\right\|\right)dV_{\mathbf{x}_j}}{m_{local\_i}}\right\}$$

(4.15)

$$m_{local\_i}=\sum_{j=1}^{N_{local}}\underline{\omega}\left\{\omega_i\left\|\mathbf{x}_j-\mathbf{x}_i\right\|^2dV_{\mathbf{x}_j}\right\} \tag{4.16}$$

$$s_{cr}=\left.\frac{\left\|\boldsymbol{\xi}+\boldsymbol{\eta}\right\|-\left\|\boldsymbol{\xi}\right\|}{\left\|\boldsymbol{\xi}\right\|}\right|_{\omega_\xi=\omega_c}=\left.\frac{\left\|\mathbf{y}_j^{(n+1)}-\mathbf{y}_i^{(n+1)}\right\|-\left\|\mathbf{x}_j-\mathbf{x}_i\right\|}{\left\|\mathbf{x}_j-\mathbf{x}_i\right\|}\right|_{\omega_\xi=\omega_c} \tag{4.17}$$

Where,

ω_c : critical energy density [J/m^6]

ω_ξ : energy density in a bond [J/m^6]

The fracture permeability k_f is determined using the fracture width w which is estimated based on fracture porosity.

$$k_f=\frac{w^2}{12} \tag{4.18}$$

$$w=\frac{\Delta V\phi_f}{\Delta A_p} \tag{4.19}$$

4.2.2.2 Force scalar state under fracture space

The force scalar state in Equation (2.8) changes depending on the following three conditions (unbroken bond, broken bond without fracture surface, and broken bond with fracture surface).

Force scalar state for unbroken bond

If a bond is not broken, the force scalar state in 3D and 2D is expressed as shown below in Equation (4.1) and (4.4) respectively.

$$\underline{t}\left[\mathbf{x},t\right]\langle\boldsymbol{\xi}\rangle = \frac{3\left(K\theta-\alpha P\right)}{m}\underline{\omega}\underline{x}\langle\boldsymbol{\xi}\rangle + \frac{15G}{m}\underline{\omega}\underline{e}^{d}\langle\boldsymbol{\xi}\rangle \tag{4.1}$$

$$\underline{t}\left[\mathbf{x},t\right]\langle\boldsymbol{\xi}\rangle = \frac{2\left(\left(K-\frac{G}{3}\right)\theta-\alpha P\right)}{m}\underline{\omega}\underline{x}\langle\boldsymbol{\xi}\rangle + \frac{8G}{m}\underline{\omega}\underline{e}^{d}\langle\boldsymbol{\xi}\rangle \tag{4.4}$$

Force scalar state for broken bond without fracture space

If the stored energy in a bond exceeds the critical energy, the mechanical term in Equation (4.1) and (4.4) disappears. However, the pore pressure term still remains since pore space is continuous even if the grain contact is broken.

$$\underline{t}\left[\mathbf{x},t\right]\langle\boldsymbol{\xi}\rangle = \begin{cases} -\dfrac{3\alpha P}{m}\underline{\omega}\underline{x}\langle\boldsymbol{\xi}\rangle & for\,3D \\ -\dfrac{2\alpha P}{m}\underline{\omega}\underline{x}\langle\boldsymbol{\xi}\rangle & for\,2D \end{cases} \tag{4.20}$$

Force scalar state for broken bond with fracture space

In our model, as shown in Fig. 4.3, fracture space is created when the following two conditions are satisfied simultaneously.

- Damage exceeds the critical damage at both the two nearest material points
- The energy density in the bond between the two nearest material points exceeds the critical energy density (in other words, the bond between the two nearest material points breaks). This condition is referred to as “dual points”.

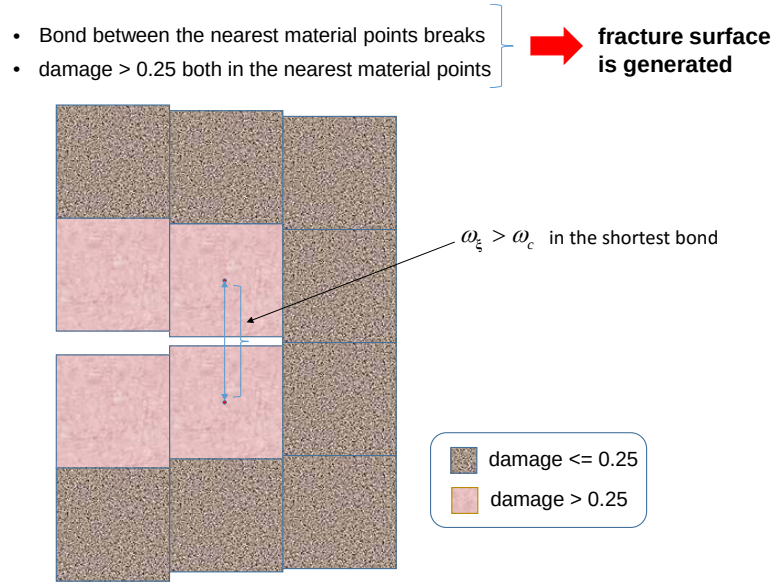

Fig. 4.3 Definition of fracture space.

If a fracture space is created and the fracture surface intersects a broken bond, the force scalar state of the broken bond (Equation (4.20) is replaced by the following formulation since the fracture surface must act as a traction boundary which is pushed by a normal stress equivalent to the fracturing fluid pressure P_f .

$$\underline{t}\left[\mathbf{x},t\right]\langle\boldsymbol{\xi}\rangle=\begin{cases}-\dfrac{3P_f}{m}\underline{\omega}\underline{x}\langle\boldsymbol{\xi}\rangle & for\,3D\\ -\dfrac{2P_f}{m}\underline{\omega}\underline{x}\langle\boldsymbol{\xi}\rangle & for\,2D\end{cases} \tag{4.21}$$

By replacing the force scalar state of every bond passing through the fracture surface with Equation (4.21), the fracture surface can act as a traction boundary with the fracturing fluid pressure P_f. The validity of replacing Equation (4.20) with Equation (4.21) can be shown by inserting Equation (4.21) into the force areal density formulation defined in Equation (2.27). As shown in Equation (4.23) and (4.25), the calculated areal force densities are exactly same as the fracturing fluid pressure P_f both in 2D and 3D as shown below. Note that in this derivation, the fracture surface is assumed to be parallel to the x direction and $\underline{\omega}=1/r$ (default influence function in this research).

In 3-D, if we assume the influence function, $\underline{\omega}=1/r$, the weighted volume in 3D configuration is calculated as following.

$$\begin{aligned} m &= \underline{\omega}\underline{x}\langle\boldsymbol{\xi}\rangle\bullet\underline{x}\langle\boldsymbol{\xi}\rangle=\int_{H_x}\underline{\omega}\underline{x}\langle\boldsymbol{\xi}\rangle\underline{x}\langle\boldsymbol{\xi}\rangle\,dV_{\mathbf{x}'}\\ &=\int_0^{\delta}\int_0^{2\pi}\int_0^{\pi}\left[\frac{1}{r}\left\{\begin{pmatrix} r\cos\varphi\\ r\sin\varphi\cos\theta\\ r\sin\varphi\sin\theta\end{pmatrix}\cdot\begin{pmatrix} r\cos\varphi\\ r\sin\varphi\cos\theta\\ r\sin\varphi\sin\theta\end{pmatrix}\right\}\right]r^2\sin\varphi\,d\varphi\,d\theta\,dr\\ &=\delta^4\pi \end{aligned} \tag{4.22}$$

From Equation (2.27), (4.21), and (4.22), we obtain exactly the same traction as the fluid pressure, P_f.

$$\begin{aligned}
\boldsymbol{\sigma}\mathbf{n} &= \int_L \int_{R^+} \left\{ \frac{3P_f}{m} \underline{\omega}\underline{x}\langle \boldsymbol{\xi} \rangle - \frac{3P_f}{m} \underline{\omega}\underline{x}\langle -\boldsymbol{\xi} \rangle \right\} dV_{\mathbf{x}'} d\hat{l} \\
&= \int_0^{\delta} \int_0^{2\pi} \int_x^{\delta} \int_0^{\cos^{-1}(x/r)} \left\{ \frac{1}{r} \frac{6P_f}{\delta^4 \pi} \begin{pmatrix} r\cos\varphi \\ r\sin\varphi\cos\theta \\ r\sin\varphi\sin\theta \end{pmatrix} \right\} r^2 \sin\varphi d\varphi dr d\theta dx \qquad (4.23) \\
&= \begin{pmatrix} P_f \\ 0 \\ 0 \end{pmatrix}
\end{aligned}$$

In 2-D if we assume the influence function ($\underline{\omega} = 1/r$), the weighted volume in 2D configuration is given by,

$$\begin{aligned}
m &= \underline{\omega}\underline{x}\langle \boldsymbol{\xi} \rangle \bullet \underline{x}\langle \boldsymbol{\xi} \rangle = \int_{H_x} \underline{\omega}\underline{x}\langle \boldsymbol{\xi} \rangle \underline{x}\langle \boldsymbol{\xi} \rangle dA_{\mathbf{x}'} \\
&= \int_0^{\delta} \int_0^{2\pi} \frac{1}{r} \begin{pmatrix} r\cos\theta \\ r\sin\theta \end{pmatrix} \cdot \begin{pmatrix} r\cos\theta \\ r\sin\theta \end{pmatrix} r d\theta dr \qquad (4.24) \\
&= \frac{2\delta^3 \pi}{3}
\end{aligned}$$

From Equation (2.27), (4.21), and (4.24), we obtain

$$\begin{aligned}
\boldsymbol{\sigma}\mathbf{n} &= \int_L \int_{R^+} \left\{ \frac{3P_f}{m} \underline{\omega}\underline{x}\langle \boldsymbol{\xi} \rangle - \frac{3P_f}{m} \underline{\omega}\underline{x}\langle -\boldsymbol{\xi} \rangle \right\} dA_{\mathbf{x}'} d\hat{l} \\
&= \int_0^{\delta} \int_0^{2\pi} \int_{\sin^{-1}\left(\frac{z}{r}\right)}^{\pi - \sin^{-1}\left(\frac{z}{r}\right)} \frac{1}{r} \frac{4P_f}{\left(\frac{2d^3\pi}{3}\right)} \begin{pmatrix} r\cos\theta \\ r\sin\theta \end{pmatrix} r d\theta dr dz \qquad (4.25) \\
&= \begin{pmatrix} P_f \\ 0 \end{pmatrix}
\end{aligned}$$

4.2.2.3 Non-local traction boundary condition

The traction boundary in peridynamics is imposed through the force density term in the governing equation of motion. Such a condition is referred to as a force loading condition [61]. The force density representing the traction boundary force can be numerically imposed either on just the boundary nodes or in several layers of nodes inside a non-zero volume of thickness δ along the boundary. Ha and Bobaru [92] have investigated the numerical implementation of the traction boundary condition in peridynamics and demonstrated the applicability of force density to just a single layer of boundary nodes. They also discuss the application of an areal force density, the peridynamics analogue of the classical traction vector to determine the required force density at the boundary nodes. However, for simplicity, they convert the constant traction boundary vector into the force density by just using nodal area and volume and found that the peridynamic solution converges to the corresponding classical one in the limit of the horizon size going to zero.

In this research, we present a different method to impose the traction boundary condition based on Silling's definition [61] of peridynamic areal force density. As shown in (2.27) and Fig. 2.6, since peridynamics is non-local theory, traction, in other words areal force density, at a given point $\mathbf{x}$ on the plane defined by a normal vector $\mathbf{n}$ is given by the integration of force density of all the bonds passing through the plane. To impose the traction boundary condition $\tau_{boundary}$, as shown in Fig. 4.4, we assume mechanical equilibrium in the medium. This results in the force density in the bonds connecting the material point $\hat{\mathbf{x}}$ in region L with point $\mathbf{x}'$ in region $B_{outside}$ being characterized by the magnitude of traction as follows,

$$t\left[\hat{\mathbf{x}}\right]\left\langle \mathbf{x}'-\hat{\mathbf{x}}\right\rangle = t\left[\mathbf{x}'\right]\left\langle \mathbf{x}'-\hat{\mathbf{x}}\right\rangle$$
$$= \begin{cases} \dfrac{2\tau_{boundary}}{m}\underline{\omega}\left\|\mathbf{x}'-\hat{\mathbf{x}}\right\| & for\ 2D \\ \dfrac{3\tau_{boundary}}{m}\underline{\omega}\left\|\mathbf{x}'-\hat{\mathbf{x}}\right\| & for\ 3D \end{cases} \tag{4.26}$$

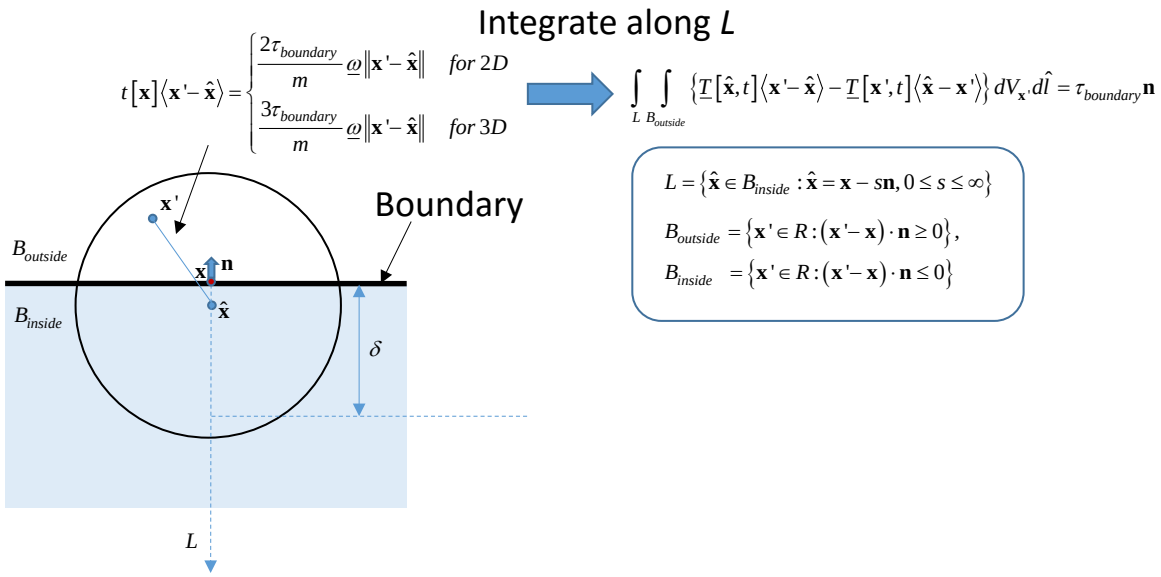

Fig. 4.4 Illustration of the traction boundary condition.

For an ordinary peridynamic material, it can be shown that for the force scalar state in Equation (4.26), the peridynamic force areal density at the domain boundary comes out be the same as the required traction force $\tau_{boundary}$.

$$\int_{L}\int_{B_{outside}} \left\{\underline{T}\left[\hat{\mathbf{x}},t\right]\left\langle \mathbf{x}'-\hat{\mathbf{x}}\right\rangle - \underline{T}\left[\mathbf{x}',t\right]\left\langle \hat{\mathbf{x}}-\mathbf{x}'\right\rangle\right\} dV_{\mathbf{x}'}d\hat{l} = \tau_{boundary}\mathbf{n} \tag{4.27}$$

Where, let L and $B_{outside}$ are given by

$$L = \left\{\hat{\mathbf{x}} \in B_{inside} : \hat{\mathbf{x}} = \mathbf{x} - s\mathbf{n}, 0 \le s \le \infty\right\} \tag{4.28}$$

$$B_{outside} = \left\{ \mathbf{x}' \in R : \left(\mathbf{x}' - \mathbf{x} \right) \cdot \mathbf{n} \geq 0 \right\} \tag{4.29}$$

Hence, the required traction boundary condition $\tau_{boundary}$ is satisfied by imposing the following force density $\mathbf{b}\left[\mathbf{x}\right]$ on the simulation domain.

$$\mathbf{b}\left[\mathbf{x}\right] = \begin{cases} \int\limits_{B_{outside}} \left\{ \dfrac{4\tau_{boundary}\,\underline{\omega}}{m} \right\} \left(\mathbf{x}' - \hat{\mathbf{x}} \right) dV_{\mathbf{x}'} & for\ 2D \\ \int\limits_{B_{outside}} \left\{ \dfrac{6\tau_{boundary}\,\underline{\omega}}{m} \right\} \left(\mathbf{x}' - \hat{\mathbf{x}} \right) dV_{\mathbf{x}'} & for\ 3D \end{cases} \tag{4.30}$$

Since force equilibrium is satisfied by the application of the initial condition, Equation (4.30) can be replaced by,

$$\mathbf{b}\left[\mathbf{x}\right] = \begin{cases} -\int\limits_{B_{inside}} \left\{ \dfrac{4\tau_{boundary}\,\underline{\omega}}{m} \right\} \left(\mathbf{x}' - \hat{\mathbf{x}} \right) dV_{\mathbf{x}'} & for\ 2D \\ -\int\limits_{B_{inside}} \left\{ \dfrac{6\tau_{boundary}\,\underline{\omega}}{m} \right\} \left(\mathbf{x}' - \hat{\mathbf{x}} \right) dV_{\mathbf{x}'} & for\ 3D \end{cases} \tag{4.31}$$

Where, $B_{outside}$ is given by,

$$B_{inside} = \left\{ \mathbf{x}' \in R : \left(\mathbf{x}' - \mathbf{x} \right) \cdot \mathbf{n} < 0 \right\} \tag{4.32}$$

4.2.2.4 Initial condition (background force vector state)

If the simulation domain is composed of multiple materials, such as layers which have different Young's modulus and Poisson's ratio, it is difficult to represent the in-situ stress state by just applying a traction boundary condition due to stress concentration along the different material boundaries. In order to avoid the stress concentration between the two different materials and to impose arbitrary initial stress condition directly on material

points, we introduce Silling's definition [2] of the peridynamic background force vector state $T_0\left[\mathbf{x}\right]\langle\boldsymbol{\xi}\rangle$ which allows us to allocate effective Piola-Kirchhoff stress tensor $\boldsymbol{\sigma}_{eff}$ in the classical theory. The peridynamic background force vector state for the material point $\mathbf{x}$ with initial stress condition $\boldsymbol{\sigma}_{eff}$ is given by the following formulation.

$$\underline{T}_0\left[\mathbf{x}\right]\langle\boldsymbol{\xi}\rangle = \underline{\omega}\boldsymbol{\sigma}_{eff}\mathbf{K}^{-1}\boldsymbol{\xi} \tag{4.33}$$

$$\mathbf{K} = \int_{H_{\mathbf{x}}} \underline{\omega}\boldsymbol{\xi}\otimes\boldsymbol{\xi}dV_{\mathbf{x}'} \tag{4.34}$$

Where,

$\mathbf{K}$	:	non-local shape tensor	[m^2]
$\underline{T}_0$	:	background force vector state	[N/m^6]
$\otimes$	:	dyadic product	

By adding Equation (4.33) to the ordinary peridynamic force vector state (2.8) as a background force vector state, an arbitrary initial stress condition can be allocated in the simulation domain.

$$\underline{T}\left[\mathbf{x},t\right]\langle\boldsymbol{\xi}\rangle = \underline{t}\left[\mathbf{x},t\right]\langle\boldsymbol{\xi}\rangle\frac{\boldsymbol{\xi}+\boldsymbol{\eta}}{\left\|\boldsymbol{\xi}+\boldsymbol{\eta}\right\|} + T_0\left[\mathbf{x}\right]\langle\boldsymbol{\xi}\rangle \tag{4.35}$$

Since we assume force equilibrium as the initial condition, the following force density is applied as a traction boundary condition in the case where the background force vector state is given.

$$b[\mathbf{x}] = \int_{B_{outside}} \left\{ T_0[\mathbf{x}]\langle \xi \rangle - T_0[\mathbf{x}']\langle -\xi \rangle \right\} dV_{\mathbf{x}'} = -\int_{B_{inside}} \left\{ T_0[\mathbf{x}]\langle \xi \rangle - T_0[\mathbf{x}']\langle -\xi \rangle \right\} dV_{\mathbf{x}'} \quad (4.36)$$

In addition, the total energy density stored in a bond is evaluated by Equation (4.37) if the background force vector state is used since the total energy density stored in a bond for bond failure must be evaluated under tensile conditions as shown in equation (4.38).

$$\omega_\xi = \int_0^{\eta(t_{final})} \left\{ \underline{T}^*_{back}[\mathbf{x},t]\langle \xi \rangle - \underline{T}^*_{back}[\mathbf{x}',t]\langle -\xi \rangle \right\} \bullet d\eta \quad (4.37)$$

$$\underline{T}^*_{back}[\mathbf{x},t]\langle \xi \rangle - \underline{T}^*_{back}[\mathbf{x}',t]\langle -\xi \rangle$$
$$= \max\left\{ \left(\left(\underline{t}[\mathbf{x},t]\langle \xi \rangle - \underline{t}[\mathbf{x}',t]\langle -\xi \rangle \right) + \left(T_0[\mathbf{x}]\langle \xi \rangle - T_0[\mathbf{x}']\langle -\xi \rangle \right) \cdot \frac{\xi + \eta}{\|\xi + \eta\|} \right), 0.0 \right\} \frac{\xi + \eta}{\|\xi + \eta\|} \quad (4.38)$$

4.3 Numerical solution method

The numerical solution method for our hydraulic fracturing model is described in detail in this section. Fig. 4.5 shows the flowchart of the hydraulic fracturing model developed in this research. As shown in the figure, by discretizing the governing equations and solving them implicitly by a Newton-Raphson method, we can obtain deformation, pore pressure change, and fracturing fluid pressure at the current time step. The details of each numerical procedure are discussed below.

4.3.1 DISCRETIZATION

As shown in Fig. 4.5, the simulation domain is discretized into finite material points in a cubic lattice with lattice length Δl_p and lattice volume $\Delta V\left(=\Delta {l_p}^3\right)$. Each material point has its associated pore space and is also allowed to have a fracture volume on the surface of the cube based on the element's damage and bond length with its adjacent neighbors as explained in Section 4.2.2.2. Based on the spatial discretization above, the discretized formulations of the three governing equations (Equation (2.7), (3.30), and (4.11)) are given as follows,

Momentum balance

$$\begin{aligned}&\rho\frac{1}{\left(t^{(n+1)}-t^{(n)}\right)}\left\{\frac{\left(\mathbf{y}_i{}^{(n+1)}-\mathbf{y}_i{}^{(n)}\right)}{\left(t^{(n+1)}-t^{(n)}\right)}-\frac{\left(\mathbf{y}_i{}^{(n)}-\mathbf{y}_i{}^{(n-1)}\right)}{\left(t^{(n)}-t^{(n-1)}\right)}\right\}\\&=\sum_{j=1}^{N}\left[\frac{\omega}{m}\left\{\begin{bmatrix}(1-\psi)\begin{bmatrix}\beta_1\left((3K_i-5G_i)\theta_i^{(n+1)}+(3K_j-5G_j)\theta_j^{(n+1)}\right)\\-3(1-\chi)\alpha\left(P_i^{(n+1)}+P_j^{(n+1)}\right)\end{bmatrix}-6\psi\chi P_{fi}\end{bmatrix}\left\|\mathbf{x}_j-\mathbf{x}_i\right\|\\+15\beta_2\left(G_i+G_j\right)e_i\end{bmatrix}\right\}\frac{\left(\mathbf{y}_j{}^{(n+1)}-\mathbf{y}_i{}^{(n+1)}\right)}{\left\|\mathbf{y}_j{}^{(n+1)}-\mathbf{y}_i{}^{(n+1)}\right\|}\Delta V_j\right]\\&+\mathbf{b}\left(\mathbf{x}_i\right)\end{aligned} \tag{4.39}$$

$$\psi=\begin{cases}0 & if\ \omega_\xi\le\omega_c\\1 & if\ \omega_\xi>\omega_c\end{cases} \tag{4.40}$$

$$\chi=\begin{cases}0 & if\ the\ bond\ does\ not\ pass\ through\ fracture\ surface\\1 & if\ the\ bond\ passes\ through\ fracture\ surface\end{cases} \tag{4.41}$$

$$\beta_1=\begin{cases}1 & for\ 3D\\2/3 & for\ 2D\end{cases} \tag{4.42}$$

$$\beta_2=\begin{cases}1 & for\ 3D\\8/15 & for\ 2D\end{cases} \tag{4.43}$$

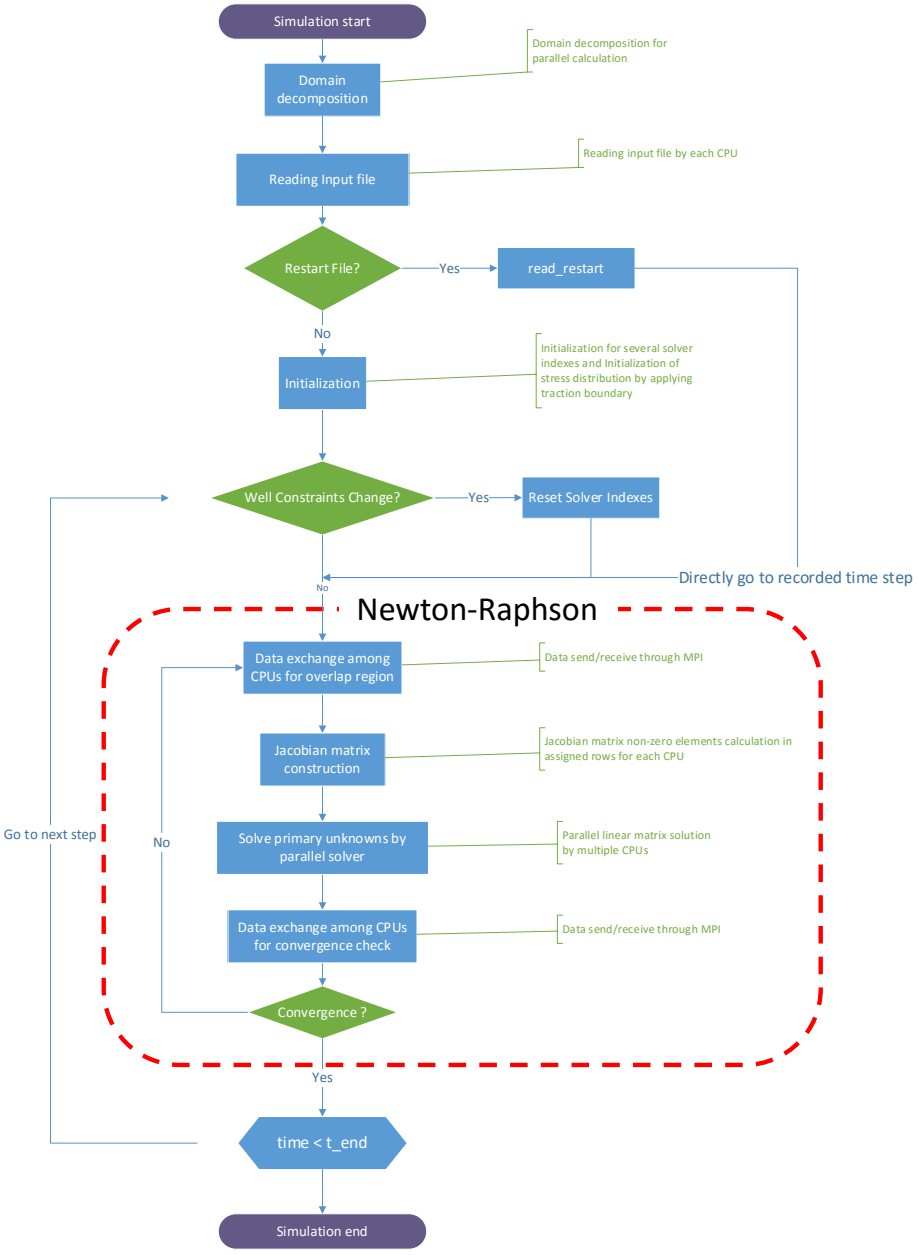

Fig. 4.5 Flow chart of the hydraulic fracturing model.

Mass conservation equation for porous flow

$$\frac{\left(\rho_{wi}^{(n+1)}\phi_{mi}^{(n+1)}-\rho_{wi}^{(n+1)}\phi_{mi}^{(n+1)}\right)}{t_i^{(n+1)}-t_i^{(n)}}$$
$$=\sum_{j=1}^{N}\left\{\frac{\gamma\rho_{wij}}{\mu_w}\frac{\xi\left(\overline{\mathbf{K}}_{mij}-0.25trace\left(\overline{\mathbf{K}}_{ij}\right)\mathbf{I}\right)\xi}{\left\|\mathbf{x}_j-\mathbf{x}_i\right\|^4}\left(\Phi_j-\Phi_i\right)\right\}\beta_3\Delta V_j \qquad (4.44)$$
$$+R_m\left(x_i,t\right)+\frac{\rho_{fi}k_{leaki}\left(P_{fi}-P_{mi}\right)}{2\mu_f\Delta l_p{}^2}$$

$$\beta_3=\begin{cases}1 & for\ 3D\\ 1/\Delta l_p & for\ 2D\end{cases} \qquad (4.45)$$

Mass conservation equation for fracturing fluid

$$\frac{\left(\rho_{fi}^{(n+1)}\phi_{fi}^{(n+1)}-\rho_{fi}^{(n+1)}\phi_{fi}^{(n+1)}\right)}{t_i^{(n+1)}-t_i^{(n)}}$$
$$=\sum_{j=1}^{N_f}\left\{\frac{\gamma\rho_{fij}}{4\mu_f}\frac{\overline{k}_{fij}}{\left\|\mathbf{x}_j-\mathbf{x}_i\right\|^2}\left(\Phi_{fj}-\Phi_{fi}\right)\right\}\beta_3\Delta V_j+R_f\left(\mathbf{x}_i\right)-\frac{k_{leaki}\left(\Phi_{fi}-\Phi_{mi}\right)}{\mu_f\Delta l_i{}^2} \qquad (4.46)$$

Where,

N : number of neighbors

N_f : number of local neighbors

ρ_{mij} : porous fluid density in the bond between material point i and material point j evaluated by up-winding method [kg/m^3]

ρ_{fij} : fracturing fluid density in the bond between material point i and material point j evaluated by up-winding method [kg/m^3]

up-script

(n) : time step (n)

$(n+1)$: time step (n+1)

sub-script

i : material point i

j : material point j

ij : bond between material point i and material point j

In the above formulations, the density of the porous fluid and fracturing fluid in the bond are evaluated based on the following formulation (up-winding method).

$$\rho_{wij} = \begin{cases} \rho_{wi} & if\ \Phi_i \geq \Phi_j \\ \rho_{wj} & if\ \Phi_i < \Phi_j \end{cases} \tag{4.47}$$

$$\rho_{fj} = \begin{cases} \rho_{fi} & if\ \Phi_{fi} \geq \Phi_{fj} \\ \rho_{fj} & if\ \Phi_{fi} < \Phi_{f_j} \end{cases} \tag{4.48}$$

The average matrix permeability, and fracture permeability between material point i and material point j in the above Equation (4.44), and (4.46) are evaluated by the harmonic averaging method in this model.

$$\bar{\mathbf{K}}_{mij} = 2 \begin{pmatrix} \frac{k_{11i}k_{11j}}{k_{11i}+k_{11j}} & \frac{k_{12i}k_{12j}}{k_{12i}+k_{12j}} & \frac{k_{13i}k_{13j}}{k_{13i}+k_{13j}} \\ \frac{k_{21i}k_{21j}}{k_{21i}+k_{21j}} & \frac{k_{22i}k_{22j}}{k_{22i}+k_{22j}} & \frac{k_{23i}k_{23j}}{k_{23i}+k_{23j}} \\ \frac{k_{31i}k_{31j}}{k_{31i}+k_{31j}} & \frac{k_{32i}k_{32j}}{k_{32i}+k_{32j}} & \frac{k_{33i}k_{33j}}{k_{33i}+k_{33j}} \end{pmatrix} \tag{4.49}$$

$$\bar{k}_{fij} = \frac{2k_{fi}k_{fj}}{k_{fi} + k_{fj}} \tag{4.50}$$

By subtracting the right side from the left side of the formulation (4.39), (4.44), and (4.46), we obtain the following residual equations.

$$\begin{aligned}
\mathbf{R}_{si} &= \begin{pmatrix} R_{sxi} \\ R_{syi} \\ R_{szi} \end{pmatrix} \equiv \rho \frac{1}{\left(t^{(n+1)} - t^{(n)}\right)} \left\{ \frac{\left(\mathbf{y}_i^{(n+1)} - \mathbf{y}_i^{(n)}\right)}{\left(t^{(n+1)} - t^{(n)}\right)} - \frac{\left(\mathbf{y}_i^{(n)} - \mathbf{y}_i^{(n-1)}\right)}{\left(t^{(n)} - t^{(n-1)}\right)} \right\} \\
&- \sum_{j=1}^{N} \left[\frac{\omega}{m} \begin{Bmatrix} (1-\psi) \begin{bmatrix} \beta_1 \left(3\bar{K}_{ij} - 5\bar{G}_{ij}\right)\left(\theta_i^{(n+1)} + \theta_j^{(n+1)}\right) \\ +30\beta_2 \bar{G}_{ij} e_i \end{bmatrix} \\ -3(1-\chi)\alpha\left(P_i^{(n+1)} + P_j^{(n+1)}\right) - 6\psi\chi P_{fi} \end{Bmatrix} \left\| \mathbf{x}_j - \mathbf{x}_i \right\| \right] \frac{\left(\mathbf{y}_j^{(n+1)} - \mathbf{y}_i^{(n+1)}\right)}{\left\| \mathbf{y}_j^{(n+1)} - \mathbf{y}_i^{(n+1)} \right\|} \Delta V_j \\
&- \mathbf{b}\left(\mathbf{x}_i\right)
\end{aligned} \tag{4.51}$$

$$\begin{aligned}
R_{mi} &\equiv \frac{\left(\rho_{mi}^{(n+1)} \phi_{mi}^{(n+1)} - \rho_{mi}^{(n)} \phi_{mi}^{(n)}\right)}{t_i^{(n+1)} - t_i^{(n)}} \\
&- \sum_{j=1}^{N} \left\{ \frac{\gamma \rho_{wij}}{\mu_w} \frac{\boldsymbol{\xi}\left(\bar{\mathbf{K}}_{mij} - 0.25 trace\left(\bar{\mathbf{K}}_{mij}\right)\mathbf{I}\right)\boldsymbol{\xi}}{\left\| \mathbf{x}_j - \mathbf{x}_i \right\|^4} \left(P_j - P_i\right) \right\} \beta_3 \Delta V_j \\
&- R_m\left(x_i, t\right) - \frac{\rho_{fi} k_{leaki} \left(P_{fi} - P_{mi}\right)}{2\mu_f \Delta l_p{}^2}
\end{aligned} \tag{4.52}$$

$$\begin{aligned}
R_{fi} &\equiv \frac{\left(\rho_{fi}^{(n+1)} \phi_{fi}^{(n+1)} - \rho_{fi}^{(n)} \phi_{fi}^{(n)}\right)}{t_i^{(n+1)} - t_i^{(n)}} \\
&- \sum_{j=1}^{N_f} \left\{ \frac{\gamma \rho_{fii}}{4\mu_f} \frac{\bar{k}_{fij}}{\left\| \mathbf{x}_j - \mathbf{x}_i \right\|^2} \left(P_{fj} - P_{fi}\right) \right\} \beta_3 \Delta V_j - R_f\left(\mathbf{x}_i\right) + \frac{k_{leaki} \left(P_{fi} - P_{mi}\right)}{\mu_f \Delta l_p{}^2}
\end{aligned} \tag{4.53}$$

These residual equations are considered to be nonlinear functions of the following variables.

- $\mathbf{y}_i^{(n+1)}$ and $\mathbf{y}_j^{(n+1)}$ (the position vector of the material point i and its neighbor j in (n+1) step)
- $P_i^{(n+1)}$ and $P_j^{(n+1)}$ (the porous fluid pressure of the material point i and its neighbor j in (n+1) step)
- $P_{fi}^{(n+1)}$ and $P_{fj}^{(n+1)}$ (the fracturing fluid pressure of the material point i and its local neighbor j in (n+1) step)

Hence, we can obtain the position vector, pore pressure and fracturing fluid pressure of each material point by solving Equations (4.51), (4.52), and (4.53) by setting $\mathbf{R}_{si} = 0$, $R_{mi} = 0$, $R_{fi} = 0$ for all the material points.

However, as shown in Fig. 4.6, not every material point has fracture volume even after injection begins. In other words, fracture porosity is zero in most of the material points during the simulation. Hence, fracturing fluid pressure from Equation (4.53) cannot be solved for in those material points. In order to keep the number of primary unknowns the same in every material point during the simulation, Equation (4.53) is replaced by the following dummy formulation in the material points which have no fracture volume. This formulation allows us to assign a dummy fracturing fluid pressure to non-fractured material points.

$$R_{fi} \equiv \frac{\phi_{f\_dummy}\left(\rho_{fi}^{(n+1)} - \rho_{fi}^{(n+1)}\right)}{t_i^{(n+1)} - t_i^{(n)}} = 0 \qquad (4.54)$$

Where, ϕ_{f_dummy} is dummy fracture porosity (= 1e-12).

4.3.2 NONLINEAR SOLUTION METHOD (NEWTON-RAPHSON METHOD)

The non-linear simultaneous equations given by setting $\mathbf{R}_{si} = 0$, $R_{mi} = 0$, and, $R_f = 0$ at all material points, i (i = 1 to N_{elm}) can be solved for the primary unknowns $\mathbf{y}_i^{(n+1)}$, $P_i^{(n+1)}$, $P_{fi}^{(n+1)}$ by using a Newton-Raphson method. The solution procedure of Newton-Raphson method is given below.

The relationship between modification vector $\Delta\boldsymbol{\varsigma}^{(k+1)}$ and residual vector $\mathbf{f}^{(k+1)}$ for the i[th] material point at the (k+1)[th] Newton-Raphson iteration are given by the following formulation.

$$\mathbf{D}_i^{(k+1)}\Delta\boldsymbol{\varsigma}_i^{(k+1)} + \sum_j^{N_i}\mathbf{O}_{ij}^{(k+1)}\Delta\boldsymbol{\varsigma}_j^{(k+1)} = \mathbf{f}_i^{(k+1)} \quad (i = 1 \sim N_{elm}) \tag{4.55}$$

$$\mathbf{D}_i^{(k+1)} = \begin{pmatrix} \frac{\partial R_{sxi}}{\partial y_{xi}^{(k)}} & \frac{\partial R_{sxi}}{\partial y_{yi}^{(k)}} & \frac{\partial R_{sxi}}{\partial y_{zi}^{(k)}} & \frac{\partial R_{sxi}}{\partial P_i^{(k)}} & \frac{\partial R_{sxi}}{\partial P_{fi}^{(k)}} \\ \frac{\partial R_{syi}}{\partial y_{xi}^{(k)}} & \frac{\partial R_{syi}}{\partial y_{yi}^{(k)}} & \frac{\partial R_{syi}}{\partial y_{zi}^{(k)}} & \frac{\partial R_{syi}}{\partial P_i^{(k)}} & \frac{\partial R_{syi}}{\partial P_{fi}^{(k)}} \\ \frac{\partial R_{szi}}{\partial y_{xi}^{(k)}} & \frac{\partial R_{szi}}{\partial y_{yi}^{(k)}} & \frac{\partial R_{szi}}{\partial y_{zi}^{(k)}} & \frac{\partial R_{szi}}{\partial P_i^{(k)}} & \frac{\partial R_{szi}}{\partial P_{fi}^{(k)}} \\ \frac{\partial R_{mi}}{\partial y_{xi}^{(k)}} & \frac{\partial R_{mi}}{\partial y_{yi}^{(k)}} & \frac{\partial R_{mi}}{\partial y_{zi}^{(k)}} & \frac{\partial R_{mi}}{\partial P_i^{(k)}} & \frac{\partial R_{mi}}{\partial P_{fi}^{(k)}} \\ \frac{\partial R_{fi}}{\partial y_{xi}^{(k)}} & \frac{\partial R_{fi}}{\partial y_{yi}^{(k)}} & \frac{\partial R_{fi}}{\partial y_{zi}^{(k)}} & \frac{\partial R_{fi}}{\partial P_i^{(k)}} & \frac{\partial R_{fi}}{\partial P_{fi}^{(k)}} \end{pmatrix} \tag{4.56}$$

$$\mathbf{O}_j^{(k+1)} = \begin{pmatrix} \frac{\partial R_{sxi}}{\partial y_{xj}^{(k)}} & \frac{\partial R_{sxi}}{\partial y_{yj}^{(k)}} & \frac{\partial R_{sxi}}{\partial y_{zj}^{(k)}} & \frac{\partial R_{sxi}}{\partial P_j^{(k)}} & \frac{\partial R_{sxi}}{\partial P_{fj}^{(k)}} \\ \frac{\partial R_{syi}}{\partial y_{xj}^{(k)}} & \frac{\partial R_{syi}}{\partial y_{yj}^{(k)}} & \frac{\partial R_{syi}}{\partial y_{zj}^{(k)}} & \frac{\partial R_{syi}}{\partial P_j^{(k)}} & \frac{\partial R_{syi}}{\partial P_{fj}^{(k)}} \\ \frac{\partial R_{szi}}{\partial y_{xj}^{(k)}} & \frac{\partial R_{szi}}{\partial y_{yj}^{(k)}} & \frac{\partial R_{szi}}{\partial y_{zj}^{(k)}} & \frac{\partial R_{szi}}{\partial P_j^{(k)}} & \frac{\partial R_{szi}}{\partial P_{fj}^{(k)}} \\ \frac{\partial R_{mi}}{\partial y_{xj}^{(k)}} & \frac{\partial R_{mi}}{\partial y_{yj}^{(k)}} & \frac{\partial R_{mi}}{\partial y_{zj}^{(k)}} & \frac{\partial R_{mi}}{\partial P_j^{(k)}} & \frac{\partial R_{mi}}{\partial P_{fj}^{(k)}} \\ \frac{\partial R_{fi}}{\partial y_{xj}^{(k)}} & \frac{\partial R_{fi}}{\partial y_{yj}^{(k)}} & \frac{\partial R_{fi}}{\partial y_{zj}^{(k)}} & \frac{\partial R_{fi}}{\partial P_j^{(k)}} & \frac{\partial R_{fi}}{\partial P_{fj}^{(k)}} \end{pmatrix} \tag{4.57}$$

$$\Delta\boldsymbol{\varsigma}_i^{(k+1)} = \begin{pmatrix} y_{xi}^{(k+1)} - y_{xi}^{(k)} \\ y_{yi}^{(k+1)} - y_{yi}^{(k)} \\ y_{zi}^{(k+1)} - y_{zi}^{(k)} \\ P_i^{(k+1)} - P_i^{(k)} \\ P_{fi}^{(k+1)} - P_{fi}^{(k)} \end{pmatrix} \tag{4.58}$$

$$\Delta\boldsymbol{\varsigma}_j^{(k+1)} = \begin{pmatrix} y_{xj}^{(k+1)} - y_{xj}^{(k)} \\ y_{yj}^{(k+1)} - y_{yj}^{(k)} \\ y_{zj}^{(k+1)} - y_{zj}^{(k)} \\ P_j^{(k+1)} - P_j^{(k)} \\ P_{fj}^{(k+1)} - P_{fj}^{(k)} \end{pmatrix} \tag{4.59}$$

$$\mathbf{f}_i^{(k+1)} = \begin{pmatrix} -R_{sxi}^{(k+1)} \\ -R_{syi}^{(k+1)} \\ -R_{szi}^{(k+1)} \\ -R_{mi}^{(k+1)} \\ -R_{fi}^{(k+1)} \end{pmatrix} \tag{4.60}$$

From Equation (4.55), the linear simultaneous equations for all the material points are given by,

$$\mathbf{J}\Delta\boldsymbol{\varsigma}^{(k+1)} = \begin{pmatrix} \mathbf{D}_1^{(k+1)} & \cdots & \mathbf{O}_{1\,j}^{(k+1)} & \cdots \\ \vdots & \ddots & & \vdots \\ \vdots & & \ddots & \vdots \\ \cdots & \mathbf{O}_{N_{elm}\,j}^{(k+1)} & \cdots & \mathbf{D}_{N_{elm}}^{(k+1)} \end{pmatrix} \begin{pmatrix} \Delta\boldsymbol{\varsigma}_1^{(k+1)} \\ \vdots \\ \vdots \\ \Delta\boldsymbol{\varsigma}_{N_{elm}}^{(k+1)} \end{pmatrix} = \begin{pmatrix} \mathbf{f}_1^{(k+1)} \\ \vdots \\ \vdots \\ \mathbf{f}_{N_{elm}}^{(k+1)} \end{pmatrix} \tag{4.61}$$

Where, $\mathbf{J}$ is Jacobian matrix. By solving the linear simultaneous equations (4.61) for $\Delta\boldsymbol{\varsigma}^{(k+1)}$, we update the values of primary unknowns for the next Newton-Raphson iteration.

$$\begin{pmatrix} y_{xi}^{(k+1)} \\ y_{yi}^{(k+1)} \\ y_{zi}^{(k+1)} \\ P_i^{(k+1)} \\ P_{fi}^{(k+1)} \end{pmatrix} = \Delta\boldsymbol{\varsigma}_i^{(k+1)} + \begin{pmatrix} y_{xi}^{(k)} \\ y_{yi}^{(k)} \\ y_{zi}^{(k)} \\ P_i^{(k)} \\ P_{fi}^{(k)} \end{pmatrix} \tag{4.62}$$

The equations (4.52) to (4.62) are solved iteratively until the primary variables corresponding to all material points converge within a tolerance limit. Once this convergence is achieved, the Newton-Raphson iteration is stopped, and the equations are solved for the next time step.

4.3.3 WELL BOUNDARY CONDITIONS

Mass flow rate from wellbore

The total mass injection rate from well I to the fracture volume is calculated by the following formulation.

$$q_I = \sum_{J=1}^{N_{perf}} q_{I\_J} \tag{4.63}$$

Where,

N_{perf} : total number of perforation in well I

q_I : total mass injection rate for well I from all perforations [kg/m^3/s]

q_{I_J} : mass injection rate from perforation J in well I [kg/m^3/s]

As shown in Fig. 4.7, since the fracture volume is assumed to be on the surface of discretized material points, the mass flow rate from the wellbore to the fracture volume from the perforated material point I is given by the following Darcy's law based formulation,

$$\begin{aligned} q_{I\_J} &= -\frac{\rho_{fJ} k_{f@wellbore}\, ff\, A}{\mu_f} \frac{\Delta P}{(\Delta l / 2)} \\ &= -\frac{\rho_{fJ} k_{f@wellbore}\, ff\, (w \Delta l_p)}{\mu_f} \frac{(P_{fJ} - P_{BHI})}{(\Delta l_p / 2)} \end{aligned} \tag{4.64}$$

Where,

ff : the ratio of the surface area (= 0.5)

P_{BPI} : bottom-hole flowing pressure of well I [Pa]

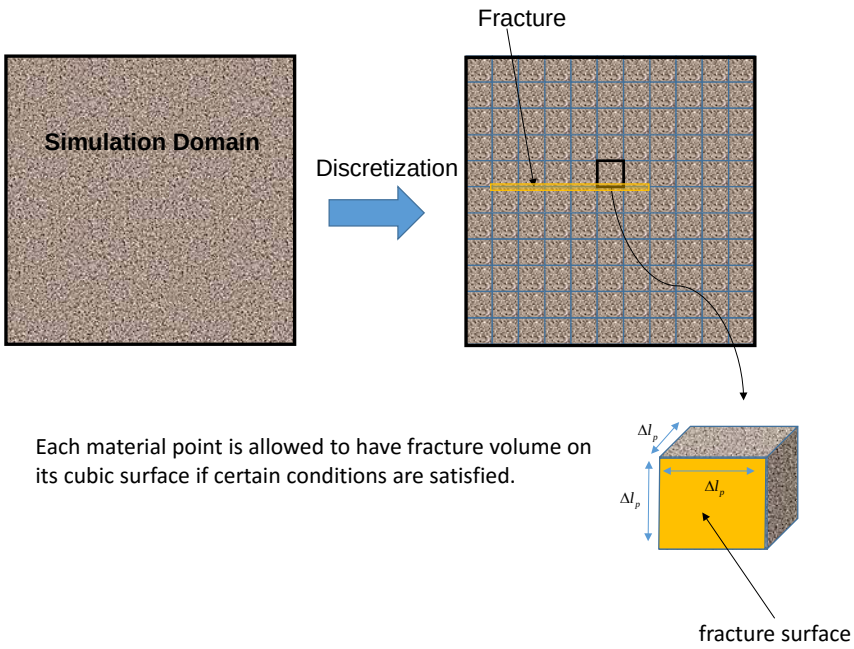

Fig. 4.6 Dual permeability concept.

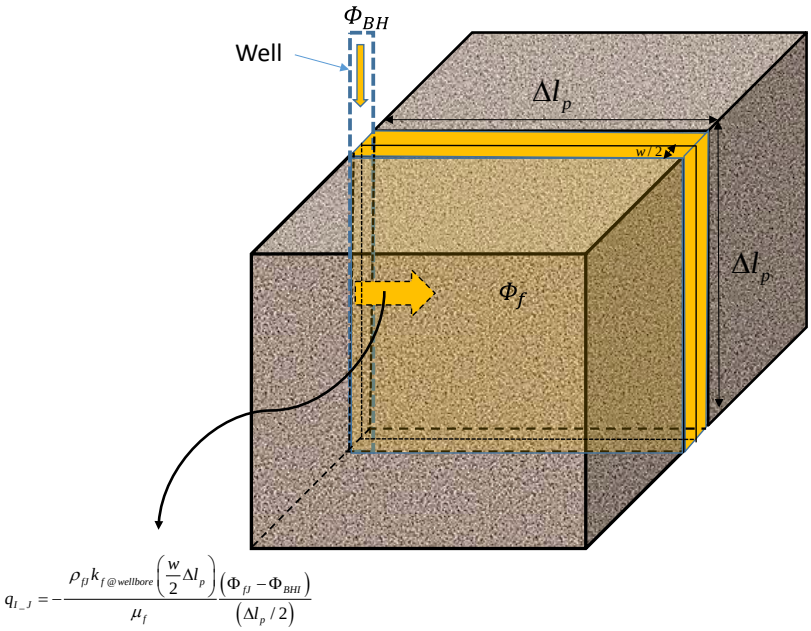

Fig. 4.7 Fluid flow model for a well.

Equation (4.64) is applied as a source term for fracture space $\mathbf{R}_f$ in Equation (4.53).

Wellbore boundary conditions

In this model, either of the following two wellbore boundary conditions can be applied.

- constant bottom-hole flowing pressure boundary condition
- constant injection rate boundary condition

Although the shape of Jacobian matrix $\mathbf{J}$ does not change in the constant bottom-hole pressure boundary condition, it changes in the constant injection rate boundary condition since the following additional governing equation needs to be solved for obtaining the bottom-hole flowing pressure P_{BH}.

$$R_{wellI} = q_{totalI} - q_I = q_{totalI} - \sum_{J=1}^{N_{perf}} q_{I\_J} = 0 \tag{4.65}$$

Where, q_{toal} is total target injection rate (dimension: [kg/m^3/s]). In the (k+1)th Newton-Raphson iteration, in the last row of Jacobian matrix $\mathbf{J}$, the following partial differential term $\mathbf{O}_{WL}$ and $\mathbf{D}_W$ appears due to the additional governing Equation (4.65).

$$\sum_{J=1}^{N_{perf}} \mathbf{O}_{WLI\_J} \Delta\varsigma_J^{(k+1)} + D_{WI} \Delta\varsigma_{BHI} = f_{wellI} \tag{4.66}$$

$$\mathbf{O}_{WLI\_J} = \left(\frac{\partial R_{wellI}}{\partial y_{xJ}} \quad \frac{\partial R_{wellI}}{\partial y_{yJ}} \quad \frac{\partial R_{wellI}}{\partial y_{zJ}} \quad \frac{\partial R_{wellI}}{\partial P_J} \quad \frac{\partial R_{wellI}}{\partial P_{fJ}} \right) \tag{4.67}$$

$$D_{WI} = \left(\frac{\partial R_{wellI}}{\partial P_{BHI}} \right) \tag{4.68}$$

$$f_{wellI} = \left(P_{BHI}{}^{(k+1)} - P_{BHI}{}^{(k)} \right) \tag{4.69}$$

In addition, under the constant injection rate boundary condition, the form of Jacobian matrix in (k+1)th Newton-Raphson iteration also changes from Equation (4.55) to Equation (4.70) (at the material point J where well is perforated), due to the partial derivative term by P_{BHI} .

$$\mathbf{D}_J{}^{(k+1)} \Delta \boldsymbol{\varsigma}_J{}^{(k+1)} + \sum_j^{N_J} \mathbf{O}_{Jj}{}^{(k+1)} \Delta \boldsymbol{\varsigma}_j{}^{(k+1)} + \mathbf{W}_{RI\_J} \Delta \boldsymbol{\varsigma}_{BHI}{}^{(k+1)} = \mathbf{f}_J{}^{(k+1)} \tag{4.70}$$

$$\mathbf{O}_{WRI\_J} = \begin{pmatrix} \frac{\partial R_{sxJ}}{\partial P_{BHI}} \\ \frac{\partial R_{syJ}}{\partial P_{BHI}} \\ \frac{\partial R_{szJ}}{\partial P_{BHI}} \\ \frac{\partial R_{mJ}}{\partial P_{BHI}} \\ \frac{\partial R_{fJ}}{\partial P_{BHI}} \end{pmatrix} \tag{4.71}$$

$$\Delta \boldsymbol{\varsigma}_{BHI}{}^{(k+1)} = P_{BHI}{}^{(k+1)} - P_{BHI}{}^{(k)} \tag{4.72}$$

If there are multiple constant rate injection wells, equations (4.55), (4.66), and (4.70), are given as following.

$$\mathbf{J}\Delta\boldsymbol{\varsigma}^{(k+1)} = \begin{pmatrix} \mathbf{D}_1^{(k+1)} & \cdots & \mathbf{O}_{1j}^{(k+1)} & \cdots & \vdots & \vdots & \vdots \\ \vdots & \ddots & & \vdots & \mathbf{O}_{WR1\_i} & & \\ \vdots & & \ddots & \vdots & \vdots & \vdots & \mathbf{O}_{WRN_{well}\_J} \\ \cdots & \mathbf{O}_{N_{elm}j}^{(k+1)} & \cdots & \mathbf{D}_{N_{elm}}^{(k+1)} & \vdots & \vdots & \\ \cdots & \mathbf{O}_{WL1\_i} & \cdots & \cdots & D_{W1} & & \vdots \\ \cdots & & \cdots & \cdots & & \ddots & \\ \cdots & & \mathbf{O}_{WLN_{well}\_J} & & \cdots & & D_{WN_{well}} \end{pmatrix} \begin{pmatrix} \Delta\boldsymbol{\varsigma}_1^{(k+1)} \\ \vdots \\ \vdots \\ \Delta\boldsymbol{\varsigma}_{N_{elm}}^{(k+1)} \\ \Delta\boldsymbol{\varsigma}_{BH1}^{(k+1)} \\ \vdots \\ \Delta\boldsymbol{\varsigma}_{BHN_{well}}^{(k+1)} \end{pmatrix} = \begin{pmatrix} \mathbf{f}_1^{(k+1)} \\ \vdots \\ \vdots \\ \mathbf{f}_{N_{elm}}^{(k+1)} \\ f_{well1} \\ \vdots \\ f_{wellN_{well}} \end{pmatrix} \tag{4.73}$$

4.3.4 PARALLELIZATION

Peridynamics simulation is more numerically expensive compared to other local methods such as the finite element method or finite difference method due to the enormous number of connections with neighbors. In order to deal with the numerical expense, our peridynamics based hydraulic fracturing simulator is parallelized based on a domain decomposition method using Sandia National Laboratory's Trilinos library [93]. Fig. 4.5 shows the flowchart of the parallelized version of the hydraulic fracturing model. As shown in Fig. 4.5, at the beginning of the simulation, the simulation domain is divided into multiple domains based on hyper graph theory to achieve equal load balancing among central processing units (CPU) by using Trilinos partitioning library "Isorropia" [93]. Fig. 4.8 shows an example of domain decomposition where 50*50*30 material points are divided into 128 domains for parallel calculation. After the domain is decomposed, different CPUs is assigned to each sub-domain. Each CPU calculates the non-zero elements of the Jacobian matrix in the rows corresponding to its own sub-domain.

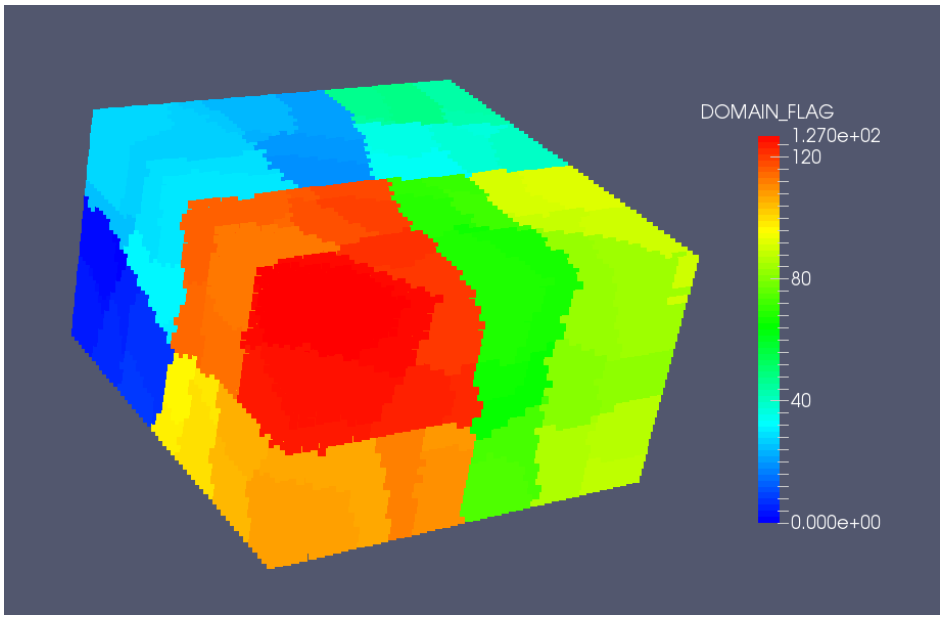

Fig. 4.8 Domain decomposition example.

Fig. 4.9 shows an example to demonstrate parallel Jacobian matrix construction. In this demonstration, the simulation domain composed of 4*4*1 material points is divided into two CPU domains. The horizon size in this case is assumed to be 1.0 and Poisson's ratio = 0.25 for simplicity. As shown in Fig. 4.9, some of the diagonal terms and off-diagonal terms in the Jacobian matrix require the primary unknowns of the other CPU domain for calculating the partial derivative values due to the non-local connection between local domains. For example, in order to calculate the non-zero elements in the second row in the Jacobian matrix, CPU1 needs to obtain primary unknowns from solver number 9 from CPU2. The exchange of such primary unknowns is accomplished by a message passing interface (MPI) utility in the Trilinos library "Epetra" [93]. After assembling non-zero elements of the Jacobian matrix, it is solved by the GMRES method with incomplete LU decomposition by using a parallel linear solver library called "Aztecoo" in Trilinos [93]. The efficiency of the parallelization of our hydraulic fracturing model is discussed in Section 4.2.4.4.

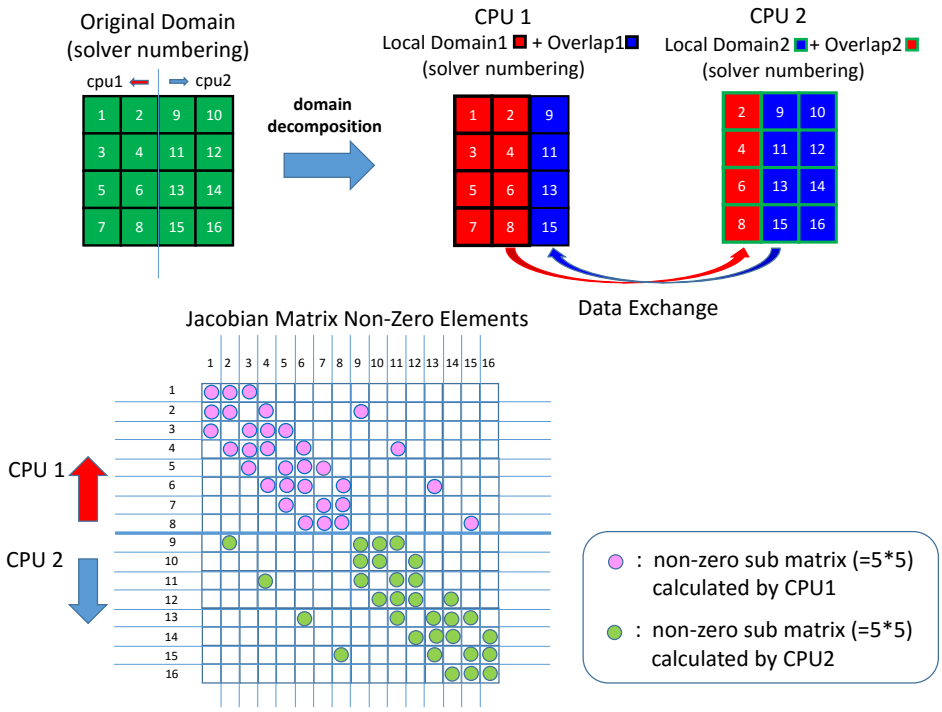

Fig. 4.9 Parallelization matrix, an example (2CPU case).

4.4 Model verification

4.4.1 TRACTION BOUNDARY CONDITION

In the previous section we proposed a novel way to impose traction boundary conditions. Here, we verify this approach by comparing the deformation of a 2-D elastic body under plane-strain conditions. A2-D square domain of length $L = 100m$ in a Cartesian coordinate system, with Young's modulus $E = 30\ GPa$ and Poisson's ratio $\nu = 0.25$ under confining boundary stress $Tx = 12\ MPa$ and $Ty = 18\ MPa$ in the x and y directions respectively equilibrates to the following plane strain solution:

$$\varepsilon_x = \frac{T_x(1-\nu) - T_y\nu}{E/(1+\nu)} = 1.875\times10^{-4} \tag{4.74}$$

$$\varepsilon_y = \frac{T_y(1-\nu) - T_x\nu}{E/(1+\nu)} = 4.375\times10^{-4} \tag{4.75}$$

Where,

ε_x : strain in the x direction

ε_y : strain in the y direction

The peridynamic strain for a uniform discretization of $\Delta x = \Delta y = 1m$ and a horizon size $\delta = 3m$, results in $\varepsilon_x = 1.879\times10^{-4}$ and $\varepsilon_y = 4.371\times10^{-4}$ which deviates less than 0.3 % from the classical solution. This supports the validity of the proposed method of imposing the non-local traction boundary condition.

4.4.2 VALIDATION OF POROELASTIC MODEL

Next, we validate the coupling of the peridynamic formulations of porous fluid flow and solid mechanics by solving the classical 1-D consolidation problem and comparing the peridynamic solution with the corresponding analytical solution [94]. Consider a fluid-filled poroelastic layer extending from the surface $z = 0$ down to a depth $z = h$ and resting on a surface, z = h (Fig. 4.10). At time t < 0, all the boundaries are no-flow boundaries, and those in the x and y directions are constrained so that they cannot deform in the lateral direction. The pore fluid pressure is assumed to be p = 0.1 MPa. A normal traction of magnitude Tz is then applied at the upper surface, resulting in deformation of the poroelastic layer and an increased pore pressure being induced in the layer. At t = 0, the

top surface at z = 0 is opened to the atmosphere (p boundary = 0.1MPa). Gradually, the pore fluid drains out of the upper surface, and the pore pressure relaxes until it drops down to atmospheric pressure. As this happens, the layer continues to deform vertically downward. Due to the medium being constrained in the lateral direction, the only non-zero displacement is the vertical displacement w (z, t). The analytical solution for the normalized pore fluid pressure is,

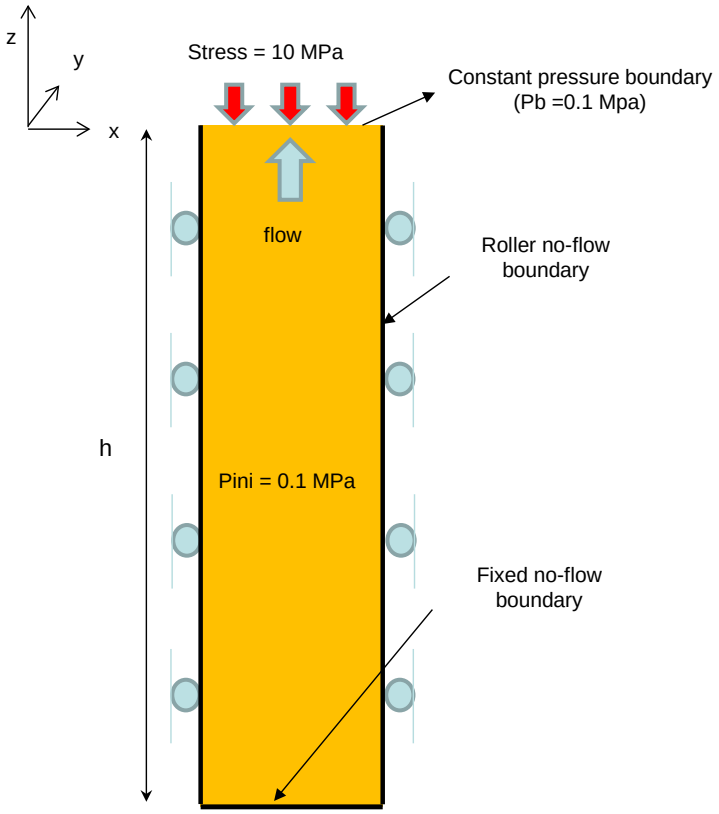

Fig. 4.10 1-D consolidation problem [95].

$$\frac{\left(P_{ref}-P(z,t)\right)}{\left(P_{ref}-P_{boundary}\right)}=1-\sum_{n=0}^{\infty}(-1)^{n}\left\{erfc\left[\frac{2n+z/h}{\left(8t/t_{eq}\right)^{0.5}}\right]+erfc\left[\frac{2(n+1)-h/z}{\left(8t/t_{eq}\right)^{0.5}}\right]\right\} \qquad (4.76)$$

$$t_{eq} = {4\mu Sh^2}\Big/{k_m} \tag{4.77}$$

$$S = \left[C_f - 1/K_m\right]\phi + \left[1 - \frac{2(1-2\nu)}{3(1-\nu)}\alpha\right]\frac{\alpha}{K} \tag{4.78}$$

Where,

C_f	:	fluid compressibility	[1/Pa]
$erfc(x)$	:	complementary error function	
k_m	:	matrix permeability	[m^2]
S	:	storage coefficient	[1/Pa]
t_{eq}	:	equivalent time	[s]

The analytical solution for the normalized displacement at position *z* and time t is

$$w(z,t) = \frac{1}{\left(K + {4G}/{3}\right)}\left[T_z\left(z-h\right) + h\alpha P_{ref}\sum_{n=1,3,5,\ldots}^{\infty}\frac{8}{n^2\pi^2}\cos\left(\frac{n\pi z}{2h}\right)e^{\left(\frac{-n^2\pi^2 t}{2t_{eq}}\right)}\right] \tag{4.79}$$

To solve this problem using our peridynamic poroelastic formulation, we consider a 2D domain of height h = 162 m and breadth b = 108 m. The simulation parameters are fluid viscosity $\mu = 10^{-3}\,kg/m/s$, fluid compressibility $C_f = 5\times10^{-10}\,Pa$, medium permeability $k_m = 6.0\times10^{-15}\,m^2 \simeq 6\,mD$, medium porosity $\phi = 0.02$, bulk modulus of rock $K = 20\,GPa$ shear modulus of rock $G = 12\,GPa$, bulk modulus of the rock matrix material $K_m = 400\,GPa$, rock density $\rho = 3000\,kg/m^3$, and magnitude of normal traction $T_z = 10\,MPa$. We use uniform discretization of grid spacing $\Delta x = \Delta z = L/n$ for the two-dimensional domain where computational nodes are placed at the center of the square cells of length _*x*.

Each node is assigned an area equal to the square cell area $\left(\Delta x^2\right)$. A mid-point numerical integration is used to convert the governing integral equation (2.7) and (3.30) for a node $\boldsymbol{x}_i$ into coupled algebraic equations involving neighbor nodes $\boldsymbol{x}_j$ inside the horizon of the node $\boldsymbol{x}_i$. In 2-D, the resulting algebraic equation is shown in Equation (4.39) and (4.44). Similarly the porous flow equation is obtained in its algebraic form. The coupled peridynamic formulation is solved implicitly and the pressure and vertical displacement are obtained along the *z* direction in the middle of the domain where boundary effects can be neglected. We define the relative difference in fluid pressure along the *z* direction as the following to compare the peridynamic solution with the analytical solution:

$$\text{Rel difference}_P = \frac{\left\| P_{analytical}\left(z\right) - P_{peridynamics}\left(z\right) \right\|^2}{\left\| P_{peridynamics}\left(z\right) \right\|^2} \tag{4.80}$$

The peridynamic formulations are non-local and include a length-scale determined by the horizon size δ. For a fixed horizon size, as the domain discretization is refined, $m = \delta / x$ increases to approach infinity and the exact non-local solution is obtained. For a peridynamic solution with a fixed horizon, *m* should be large enough to minimize the error in numerical approximation but also small enough for computational ease. This requires a *m*−convergence test to obtain a suitable *m* value. Further the exact non-local peridynamic solution is different from that obtained from the classical local model. The peridynamic solution of problems without singularities approaches the one from the classical local model as the horizon $\delta \to 0$, while keeping *m* fixed or increasing with rate slower than the rate at which δ decreases [71, 82]. As shown in Fig. 4.11, we perform an *m*-convergence test for fixed δ values of *L*/18, *L*/27 and *L*/36 and investigate the variation in relative difference between a numerical peridynamic solution and the exact

analytical solution with increasing m in Fig. 4.11. For each δ value, m is increased from 2 to 5 and the relative difference substantially decreases as m increases, highlighting the error in numerical approximation due to the smaller number of nodes in the horizon for smaller m. For $m \geq 4$, the relative difference increases only slightly for all δ values. This suggests that an exact non-local solution is reached and may not be substantially different than the exact local solution as for $m = 5$, reducing δ did not reduce the relative difference in fluid pressure. Therefore, based on the data in Fig. 4.11, we choose $m = 5$ for the presented peridynamic solution. In Fig. 4.12, the variation in the normalized pore pressure with a normalized position in the z-direction is compared with the exact analytical solution at the following different non-dimensional times.

$$t^* = \frac{t}{t_{eq}} = \frac{tk_m}{4\mu Sh^2} \tag{4.81}$$

The peridynamic solution is in good agreement with the exact analytical solution, however, the comparatively larger deviation at the larger time. In Fig. 4.13, we compare normalized displacement in the column with non-dimensional time. The peridynamic solution is again in good agreement with the corresponding analytical solution.

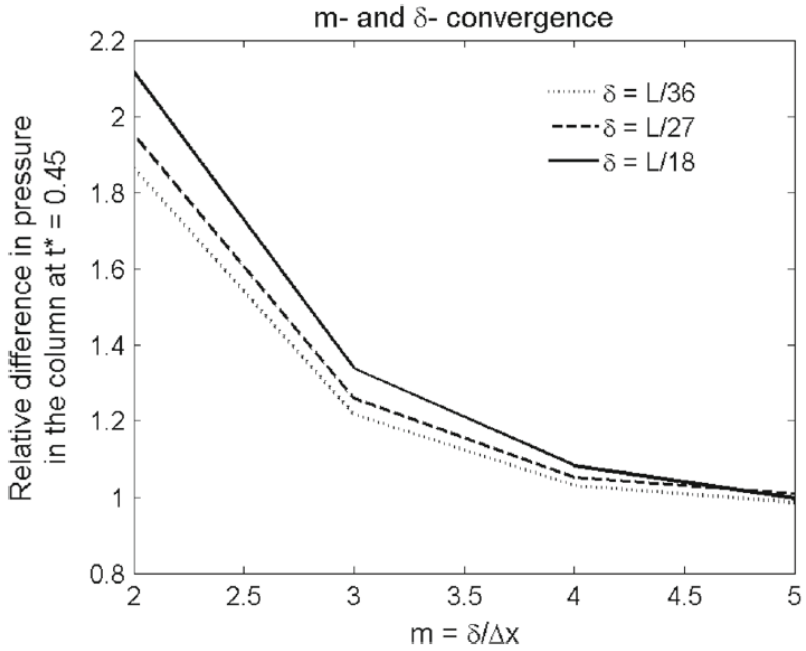

Fig. 4.11 M and delta convergence [95].

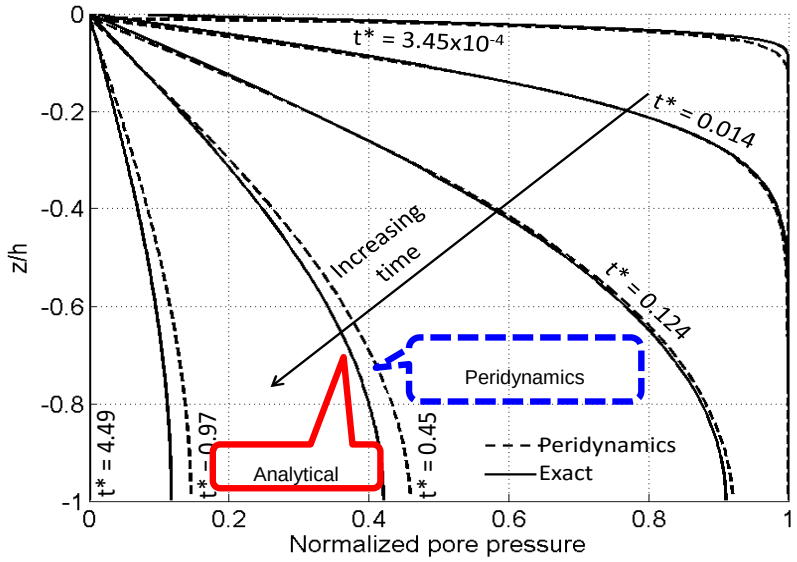

Fig. 4.12 Normalized pressure change with time [95].

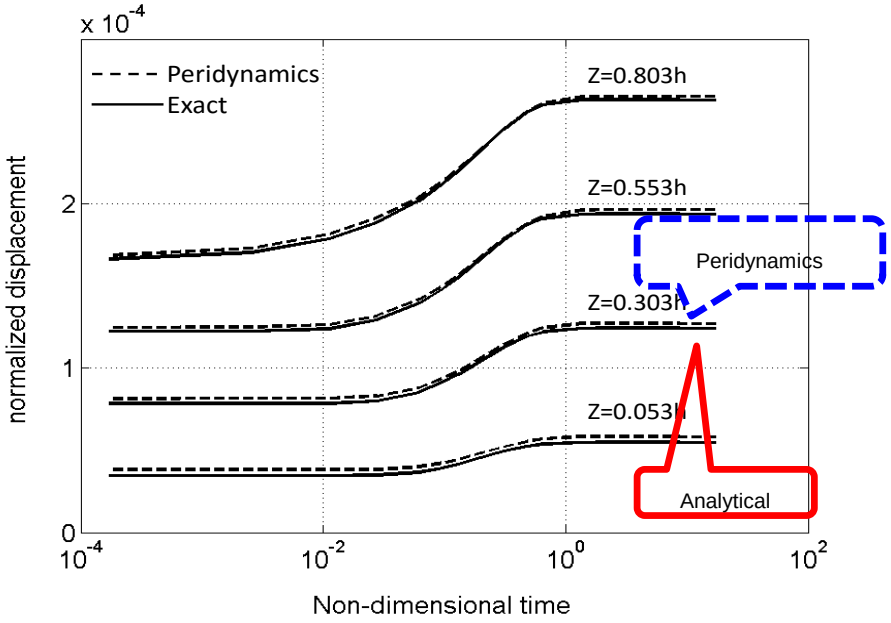

Fig. 4.13 Normalized displacement changing with time [95].

4.4.3 TWO DIMENSIONAL SINGLE FRACTURE PROPAGATION (KGD MODEL)

For the 2D fracture propagation model validation, we simulate single fracture propagation in a homogeneous 2D poroelastic domain in a plane strain setting due to injection of a Newtonian and compressible fluid through a point source (Fig. 4.14). The initial pore fluid pressure is assumed to be p_0.With respect to fluid flow, all the boundaries are no-flow boundaries. At time $t < 0$, the corners of the 2-D domain are fixed to limit the rotational degrees of freedom and normal compressive stresses of magnitude T_x and T_y are applied at the x and y boundaries respectively. An equilibrium condition is achieved resulting in negative values of the dilatation due to the domain being compressed from its reference configuration. In the present problem, the local material points surrounding the mass injection location are modeled as the dual points and are now onwards referred as "injection dual points". Note that the dual points also represent the fracture space which

suggests that an initial fracture length equal to the grid spacing exists from the beginning. Based on the boundary stresses, fracture propagation is expected along the x-axis since the minimum horizontal stress is assumed to be in the y-direction in this problem. At time $t = 0$, fluid is injected in the injection dual points through the source term $R[\boldsymbol{x}]$ in the fracture flow governing equation. The fracture pressure at the injection dual points increases causing the injection dual points to displace away from each other. Since the stress in the y-direction is lower, the points displace more in the y-direction and a fracture surface along x-axis begins to open. The dual points displaced along the y-direction pull the neighboring points along x-axis away from each other resulting in bonds across x-axis to fail, which leads to an increase in damage. Once any two adjacent material points separate beyond the critical stretch s_{cr} and $d > d_{cr}$ for both the points, these material points are transformed into dual points (become part of the fracture). An additional fracture flow equation is solved for these points and the fracture pressure is computed. The newly formed dual points across the x-axis with higher fracture pressure displace in the y-direction away from the x-axis resulting in damage evolution and fracture propagation.

The peridynamic solution is compared with the approximate analytical solution obtained from the KGD model [11, 12]. The KGD model assumes the medium to be homogeneous, isotropic and linearly elastic, injection fluid to be Newtonian and fluid flow in the fracture to be laminar with no gravity. The approximate solutions for fracture length l_f, maximum fracture opening $w_{\max}$ and net pressure $P_{injection}$ at the injection point were derived as,

$$l_f = 2\left[0.539\left(\frac{E'q^3}{\mu}\right)^{\frac{1}{6}} t^{\frac{2}{3}}\right] \tag{4.82}$$

$$w_{\max} = 2.36\left(\frac{q^3\mu}{E'}\right)^{\frac{1}{6}} t^{\frac{1}{3}} \tag{4.83}$$

$$P_{injection} = S_{h\min} + 1.09\left(E'^2\,\mu\right)^{\frac{1}{3}} t^{-\frac{1}{3}} \tag{4.84}$$

$$E' = \frac{E}{1-\nu^2} \tag{4.85}$$

Where,

q	:	the mass injection rate per unit fracture height	[kg/m2/s]
t	:	time	[s]

Since the KGD model does not incorporate fluid leak-off from the fracture, we considered a medium with very low permeability (of the order of nano-Darcy) to simulate the same. Since the pressure gradient for fluid to flow in the fracture (through lubrication theory) decreases by the third power of the distance from fracture tip, the KGD model assumes a constant average pressure throughout the fracture length except near the tip where fluid pressure drops to zero. To capture such an assumption with our coupled formulation where fracture permeability is obtained through fracture width, the fracture length to be simulated must be large. However that adds to the computational cost. Therefore, we modeled this assumption by considering infinite conductivity for fluid flow inside the fracture with permeability k_f being a function of the local damage.

$$k_f = k_{f\max}\left(\frac{d-d_{cr}}{1-d_{cr}}\right)^{ndamage} \tag{4.86}$$

Where,

$k_{f\max}$: the maximum allowable permeability inside the fracture [m^2]

n_{damage}: the power law coefficient.

Note that the absolute value of $k_{f\max}$ does not matter when simulating an infinite fracture conductivity as long as it is a relatively large value. Table 4.1 reports the simulation parameters. We choose $m = \frac{\delta}{\Delta x} = 3$ and perform a δ convergence test with respect to the predicted fracture length to find an appropriate horizon size to simulate the problem. As expected, we find that the relative difference in the fracture length predicted from the peridynamic formulation and the KGD model (4.82) decreases with decreasing horizon size (Fig. 4.15).We choose the smallest horizon size $\delta = 3L_x / 400$ and $m = \frac{\delta}{\Delta x}$ for performing the peridynamic simulations. We note that the damage field does not evolve during every time step as other field variables; however, using this variable in closure relations to identify the proper flow regime has not shown any adverse effects or oscillations in the numerical solution. In Fig. 4.16(a–c), we compare the variation in injection pressure, fracture half-length and maximum fracture opening with time and in Fig. 4.16(d) the variation in fracture width with distance from fracture tip at t = 22.05 s. The peridynamic predictions are in good agreement with the corresponding results from the KGD model. The KGD model does not have any compressive boundary stress and the model assumes that the stress intensity factor at any time is the critical stress intensity factor so that the fracture initiates and propagates for any deformation in the medium. However, in the peridynamic formulation, the domain is initially compressed by far field stresses, therefore, the fracture initiates only after enough fracture pressure is built to break the required bonds for crack initiation. This is why injection pressure in peridynamics is initially higher than the KGD model. For late time, the peridynamic prediction of fracture

pressure is slightly lower due to the formulation being non-local and reflection of stress waves from boundaries of the finite domain. Note that we propose an additional equation to solve for fracture flow and the resulting fracture pressure was used in the force density calculation for the interaction of the material points across the fracture surface. The validity of the proposed modification in the force density of the bonds crossing the fracture surface can be seen through prediction of the effective normal stress distribution in the y-direction, δ_{yy} that is obtained from equation (4.26).We plot in Fig. 4.17 (a) the contours of δ_{yy} from the peridynamic formulation and compare the same in Fig. 4.17 (b) with the Sneddon solution [88] that analytically predicts the stress field around a 2-D fracture of finite length with constant internal pressure p_f in an infinite medium. In Fig. 4.17 (c–d), we plot the variation in δ_{yy} along $(y = 0)$ and normal $(x = 0)$ to fracture opening respectively from peridynamics and the Sneddon solution given below.

$$\sigma_{yy} = P_f \left[1 - \frac{\bar{S}}{\left(\bar{S}_1 \bar{S}_2\right)^{\frac{1}{2}}} \cos\left(\theta - \frac{\theta_1 + \theta_2}{2} \right) - \frac{\bar{S}}{\left(\bar{S}_1 \bar{S}_2\right)^{\frac{3}{2}}} \sin\theta \sin\left(\frac{3}{2}\left(\theta_1 + \theta_2\right) \right) \right] \quad (4.87)$$

$$\theta = \tan^{-1}\left(-\frac{\bar{x}}{\bar{y}} \right) \quad (4.88)$$

$$\theta_1 = \tan^{-1}\left(-\frac{\bar{x}}{1 + \bar{y}} \right) \quad (4.89)$$

$$\theta_2 = \tan^{-1}\left(-\frac{\bar{x}}{1 - \bar{y}} \right) \quad (4.90)$$

Where x, y, S_1, S_2, and S are the coordinates and distances shown in Fig. 4.18 normalized with the fracture half length $l_f / 2$. For comparison, time $t = 6.2$ s is chosen

so that the fracture length ($l_f = 2.5m$) is shorter in comparison to domain length to minimize the effects of reflection of stress waves from the boundary and simulate an infinitely long domain as required for the Sneddon solution. The fracture pressure p_f at $t = 6.2\ s$ is 9.09 MPa. The contours of σ_{yy} from peridynamics show good agreement with the one from the Sneddon solution. The peridynamic prediction of σ_{yy} is more diffuse because the formulation is non-local; only in the limit of non-locality going to zero does the peridynamic formulation converge to the corresponding local solution. The agreement between the peridynamic solution of σ_{yy} with the Sneddon solution is more quantitative in Fig. 4.17 (c–d) where we plot σ_{yy} along $y = 0$ and $x = 0$. It is important to note that the average value of $\sigma_{yy} + T_y$ along the fracture length in Fig. 4.17 (c) is 9.04Mpa. This 0.55 % deviation in total stress $(\sigma_{yy} + T_y)$ at the fracture surface from fracture $p_f = 9.09$ supports the validity of the proposed force density in equation (4.21) for bonds crossing the fracture surface. In Fig. 4.17 (c), the prediction of σ_{yy} at the boundary changes abruptly for the horizon not being a full disk. The peridynamic solutions are generally known to be affected by the boundary, however, away from the boundary the peridynamic predictions are consistent with the continuum formulation [71].

Table 4.1 Simulation parameters for fracture propagation in 2-D

Domain section	Value
Dimension of the 2D domain in X direction (m)	40.0
Dimension of the 2D domain in Y direction (m)	32.0
Boundary stress in x direction (MPa)	12.0
Boundary stress in y direction (MPa)	8.0
Bulk modulus of the domain (GPa)	60.0
Shear modulus of the domain (GPa)	24.0
Initial pore pressure (MPa)	3.2
Medium permeability (nD)	10.0
Well section	
Mass injection rate (kg/m/sec)	0.025
Fracturing fluid viscosity	0.001
Numerical section	
Critical damage	0.25
Number of elements	200*160
Element size (m)	0.2
Horizon size (m)	0.6

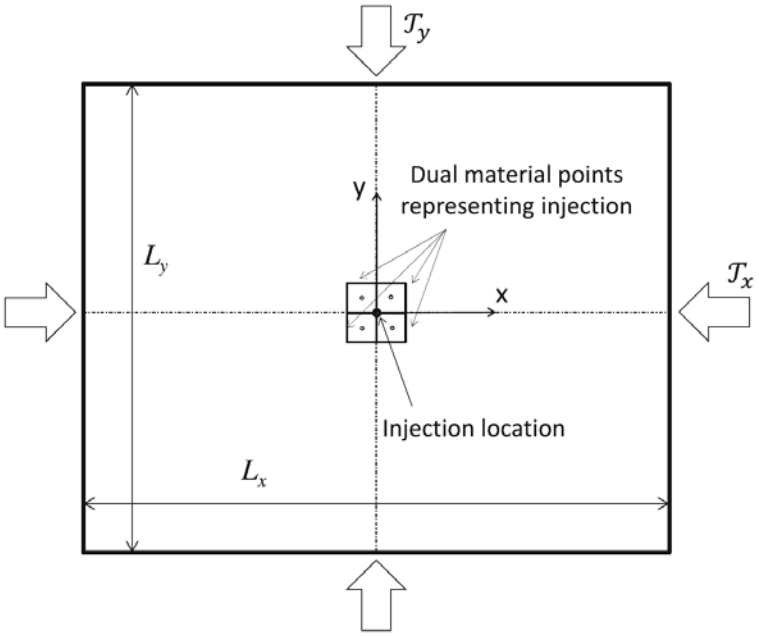

Fig. 4.14 Simulation domain for 2-D model verificaiton [95].

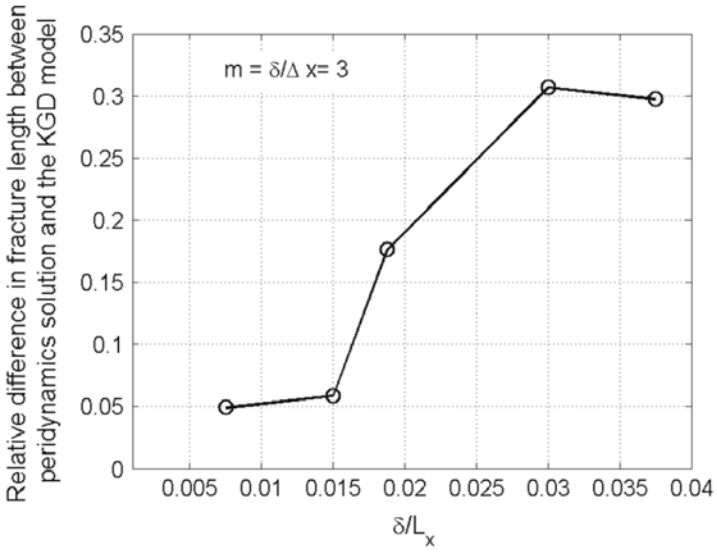

Fig. 4.15 Element size sensitivity [95].

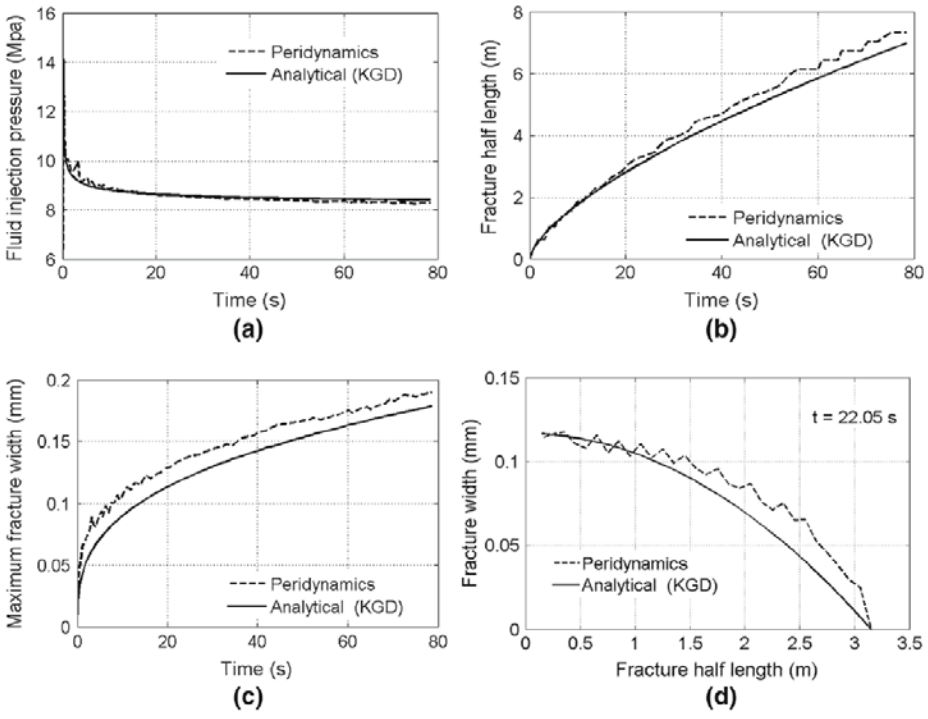

Fig. 4.16 Comparison with KGD solution (fracture half length, width, and wellbore pressure)[95].

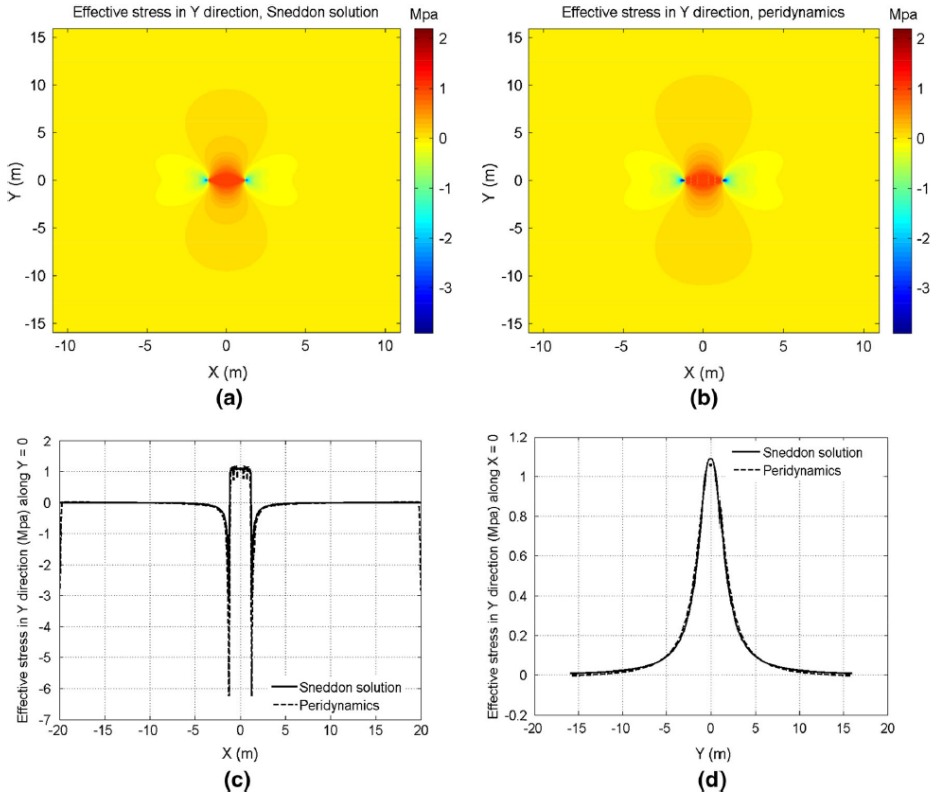

Fig. 4.17 Comparison with Sneddon solution[95].

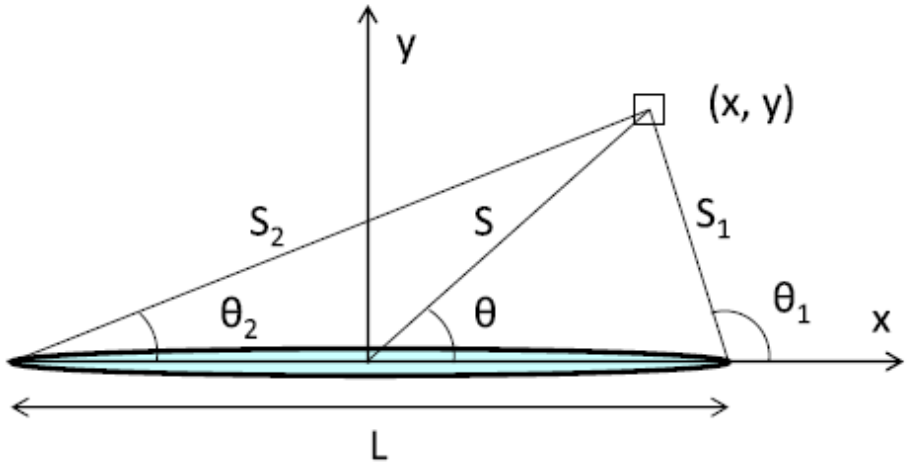

Fig. 4.18 Schematic view for the Sneddon solution[95].

4.4.4 THREE DIMENSIONAL SINGLE FRACTURE PROPAGATION (COMPARISON WITH PKN MODEL)

For the 3D model validation, we simulate single fracture propagation due to injection of a Newtonian and compressible fluid through a point source in a 3D poroelastic domain (Fig. 4.19) and compare the result with the following approximated analytical solution known as the PKN model [13, 14].

Fracture half length

$$l_f = 0.524\left(\frac{E'q^3}{\mu h^4}\right)^{1/5} t^{4/5} \tag{4.91}$$

Fracture width at well bore

$$w_{\max} = 3.04\left(\frac{q^2\mu}{Eh}\right)^{1/5} t^{1/5} \tag{4.92}$$

Wellbore pressure

$$P_{injection} = S_{h\min} + 1.52\left(\frac{q^2\mu E'^4}{h^6}\right)^{1/5} t^{1/5} \tag{4.93}$$

Where,

h : fracture height [m]

In this verification, At time t < 0, the simulation domain is initialized by applying compressive normal stresses of T_x, T_y, and T_z at the x, y, and z boundary respectively. An equilibrium condition is achieved resulting in negative values of the dilatation due to the domain being compressed from its reference configuration. During initialization, pore pressure is assumed to be a constant value P_0. At time $t > 0$, the injection points are set as

the “injection dual points” as shown in Fig. 4.19. Fracture propagation is simulated by injecting water at a constant rate from the injection dual points. During the fracture propagation simulation, the same compressive stresses as the initialization (T_x and T_y) are applied at x and y boundary of the simulation domain. However, the z boundary (top boundary and the bottom boundary) is fixed to achieve the same boundary condition as the PKN model. With regard to fluid flow, a no-flow boundary condition is applied to all the boundaries. The details of the simulation conditions are summarized in Table 4.2. Fig. 4.20 shows results for the fracture half length, fracture width, and wellbore pressure and their change with time.

At time t > 0, the hydraulic fracture begins to propagate radially from the injection point perpendicular to the minimum principal stress direction (y-direction). Once the fracture reaches the boundary in the z direction, it propagates only in the x direction. Since the fracture propagates radially without completely filling the z direction at the beginning of the simulation, the predicted fracture propagation speed is a little bit faster than the PKN solution and the predicted wellbore pressure is higher than the PKN solution. However, as shown in Fig. 4.20, once the fracture reaches the z-boundary, the predicted fracture half length, width, and wellbore pressure shows good agreement with the PKN solution. This results shows that for this idealized case our 3D fracture propagation model is consistent with the fracture propagation predicted by the PKN model.

Table 4.2 Simulation parameters for fracture propagation in 3-D.

Domain section	Value
Dimension of the 3D domain in X direction (m)	20
Dimension of the 3D domain in Y direction (m)	20
Dimension of the 3D domain in Y direction (m)	10
Boundary stress in x direction (MPa)	41
Boundary stress in y direction (MPa)	40
Boundary stress in z direction (MPa)	60
Bulk modulus of the domain (GPa)	20
Shear modulus of the domain (GPa)	12
Initial pore pressure (MPa)	38
Medium permeability (nD)	10
Well section	
Mass injection rate (kg/m/sec)	0.163
Fracturing fluid viscosity	0.0005
Numerical section	
Critical damage	0.25
Number of elements	100*100*20
Element size (m)	0.2
Horizon size (m)	0.4

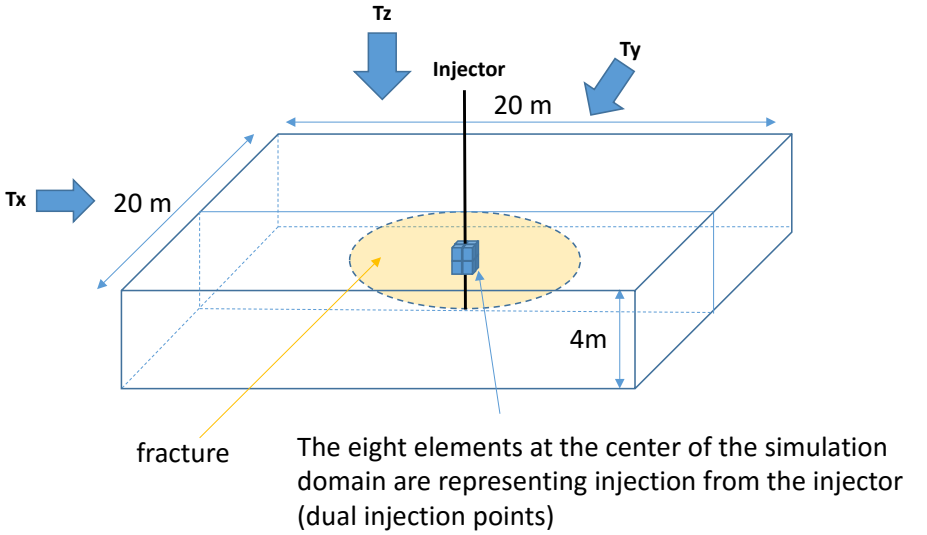

Fig. 4.19 Simulation domain with boundary conditions (3-D case).

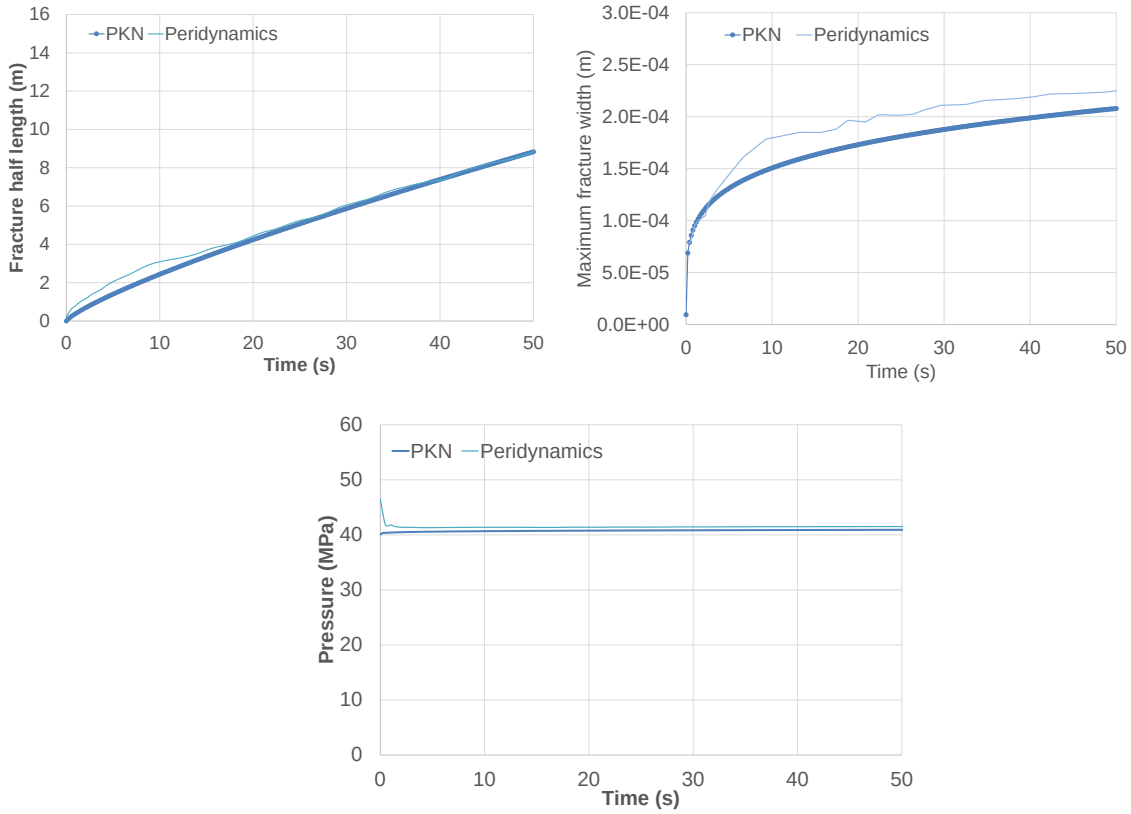

Fig. 4.20 Comparison with PKN solution (fracture half-length, maximum fracture width, and wellbore pressure change with time).

4.4.5 PERFORMANCE TEST FOR THE PARALLELIZED CODE

For evaluating the performance of our parallel code, we simulated the same single hydraulic fracture propagation problem as the PKN verification case by changing the number of CPUs in a supercomputer named “Stampede” that is operated by the Texas Advanced Computing Center (TACC). We changed the number of CPUs used in the simulation from 1 to 128 and evaluated the simulation results and the simulation time in each case. Table 4.3 shows the number of CPUs vs. the simulation time. Fig. 4.21 shows

the fracture half-length and fracture maximum width change with time in each case. Fig. 4.22 shows the number of CPUs vs. speed-up.

As shown in Fig. 4.21, predicted fracture length and width are exactly the same regardless of the number of CPUs. This result shows our parallel code works properly. As shown in Table 4.3 and Fig. 4.22, the calculation time decreases as the number of CPUs used in the simulation increases though the speed-up (the calculation time in multiple CPU / the calculation time in one CPU) is not linear. The calculation time in the one CPU case is about 17.2 hours, while the calculation time in the 128 CPU case is about 0.6 hours. A 30 times speed up is achieved by the parallelization. These results show that we can simulate problems that are one order to two orders of magnitude larger by using the parallelization code and get reasonable simulation times (a few hours).

Table 4.3 Number of CPU vs. caluculation time.

Number of CPU	Calculation time (hour)
1	17.2
2	8.8
4	5.4
8	4.2
16	2.3
32	1.3
64	0.9
128	0.6

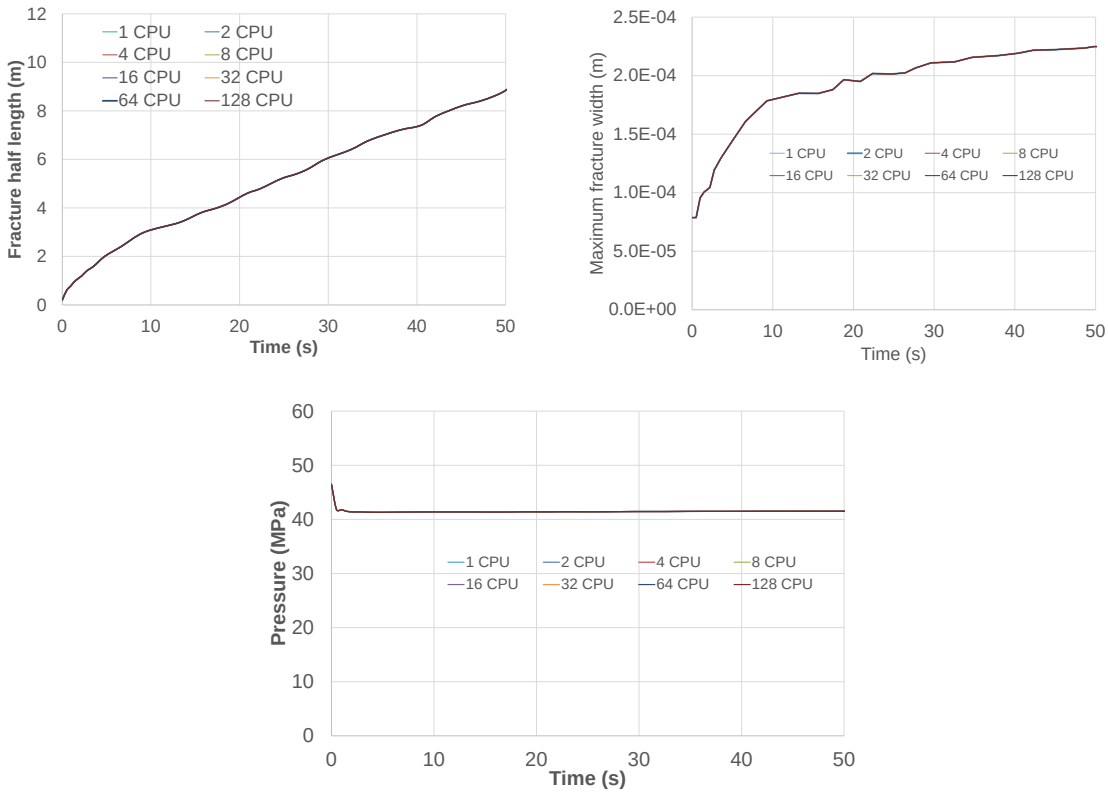

Fig. 4.21 Comparison among multiple CPU cases.

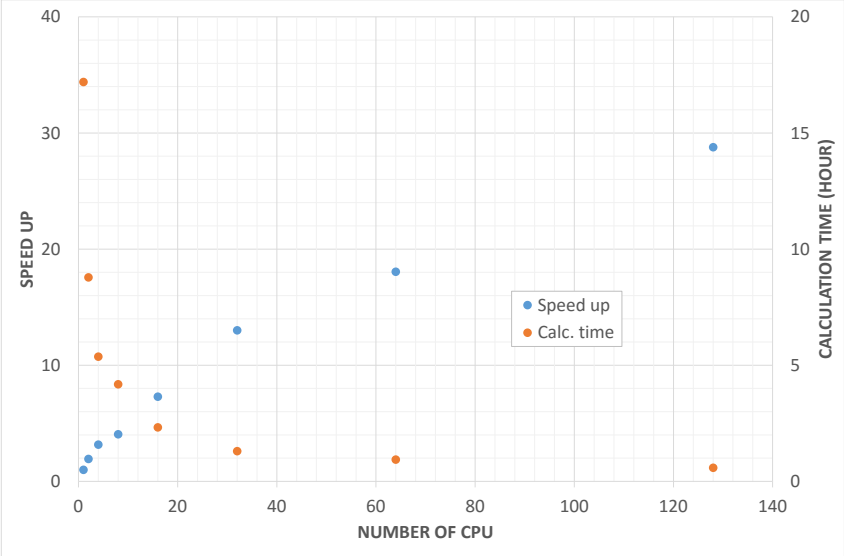

Fig. 4.22 Parallelization efficiency.

4.5 Conclusion

We have developed a new peridynamics based model to simulate the growth of fluid driven cracks. Multiple, non-planar, competing fractures can now be simulated in unconventional reservoirs more realistically and this will allow us to better design wells and hydraulic fractures to better drain the reservoir volume. Computational modeling of the hydraulic fracturing process is a challenging problem. Virtually all current approaches to hydraulic fracture modeling rely on finite difference, finite element (FEM) or boundary element methods (BEM) to solve PDEs of the LEFM based fracture formulation. However, computing derivatives on domains containing fractures causes problems with such methods. In addition, PDEs of the classical local formulation do not have any characteristic length scale to capture non-local physics around the crack tip. With our interest in investigating the complex geometry and network of fluid-driven fractures in unconventional reservoirs, a generalized 3-D state-based peridynamic model is developed by modifying the existing peridynamic formulation of solid mechanics for porous and fractured media and coupling it with a previously developed peridynamic formulation of porous flow. The coupled poroelastic formulation produces a close match with the analytical solution for the classical 1D consolidation problem. The coupling includes an additional equation for flow inside the created fracture space. For simplicity, we currently consider only Newtonian and slightly compressible fracturing fluid. A novel approach is presented to impose the non-local traction boundary condition and the resulting deformations for 2-D plane-strain problem are in close agreement with the corresponding analytical solution. A previously developed energy-based criterion is used to simulate autonomous material failure and fracture propagation. Fluid-driven fracture propagation is verified in a 2-D plane-strain setting and 3-D setting against the corresponding classical

analytical solution from the KGD model and PKN model respectively. In spite of the limitations to represent the KGD and PKN crack numerically, a close prediction of the fracture geometry and injection pressure from the peridynamic model in both verification cases supports its ability to simulate complex fracture propagation patterns. Since the formulation solves the flow physics outside as well as inside the fracture, unlike several previous models, it provides an excellent means to simulate the effects of heterogeneity (in the form of mechanical properties, permeability heterogeneity and anisotropy and natural fractures). In addition, the peridynamic model presented here, being based on particle based discretization, overcomes the limitation of re-meshing during fracture propagation in previous continuum mechanics models. In this chapter, we have confirmed the validity of the newly developed model to simulate a simple planar, fluid driven fracture propagating in a poroelastic homogeneous medium. In the next chapter we investigate the role of formation heterogeneity in the creation of complex fracture geometry and fracture networks.

CHAPTER5: INTERACTION BETWEEN HYDRAULIC FRACTURES AND NATURAL FRACTURES

5.1 Introduction

In many shale gas/oil fields, microseismic mapping techniques have shown the growth of complex fracture networks and asymmetric fracture propagation. Studies suggest that the creation of such complicated fracture networks is generated by the interaction of hydraulic fractures with natural fractures or other planes of weakness. To fully understand how such complex fracture networks are formed, we need to understand how a hydraulic fracture (HF) interacts with a single natural fracture (NF) or a network of natural fractures or planes of weakness such as faults. Many researchers have tried to investigate the mechanism of this interaction through experiments [27, 49, 52, 96], analytical formulations [51, 97], and numerical simulations [26, 39, 98]. However, despite these efforts, our understanding of this subject still remains fairly limited.

In the previous chapter, we fully coupled the pre-existing peridynamic theory for solid mechanics with the new peridynamic fluid flow model, and developed a new hydraulic fracturing model. Since this model simulates the pore pressure inside the fracture, in addition to the stresses outside of the fracture the stresses and the pore pressure both inside and outside a fracture, it allows us to take into account the effect of poroelasticity. Here[3], we investigate the interaction between HF and NF by using our newly developed

[3] This Chapter forms the basis of the following publication: Ouchi, H., A. Katiyar, J. T. Foster, and M. M. Sharma, A Peridynamics Model for the Propagation of Hydraulic Fractures in Heterogeneous, Naturally Fractured Reservoirs. in SPE Hydraulic Fracturing Technology Conference. 2015. Society of Petroleum Engineers.

hydraulic fracturing simulator which includes both mechanical the poroelastic stress shadow effects.

In this chapter, we introduce a new formulation for defining shear failure of the NF surface in peridynamics and define NF as a special surface which has both tensile and shear failure criteria. Then, we demonstrate the validity of our NF model by comparing its 2D predictions with published experimental results for interaction between HF and NF. The key parameters for the 2D interaction are also investigated through a sensitivity analysis using a 2D plain strain model. Then, we highlight the applicability of our model to predict the generation of complex fracture networks by simulating multiple competing hydraulic fractures through a network of natural fractures in a 2D field-scale domain. Finally, the effect of 3D interactions between HF and NH is investigated by using a parallelized 3D fracture propagation model.

5.2 Definition of Pre-existing Fractures (Natural Fractures) in Peridynamics Theory

Here, we introduce a new definition of pre-existing fractures in our model for simulating the interaction between hydraulic fractures (HF) and natural fractures (NF). In peridynamics theory, as shown in Chapter 2 and Chapter 4, fracture elements are typically defined as elements for which damage exceeds the critical damage. This treatment is also valid for pre-existing fractures if the simulation domain is not under compression. However, if we define pre-existing fractures under in-situ conditions (or compression) as merely damaged elements, it leads to non-physical results. For example, as an extreme case, if a natural fracture (NF) is defined just by breaking all the bonds crossing the NF surface, as shown in Fig. 5.1, huge stress concentration occurs along the NF due to zero repelling force from the other side of the NF. As shown in Equation (2.26), once a bond is

broken, the force vector state $\underline{T}[\mathbf{x},t]\langle\boldsymbol{\xi}\rangle$ becomes zero and no force is exerted through the bond. Hence, as shown in Fig. 5.2, defining a NF just by breaking all the bonds along the NF is like creating vacant space next to one side of the NF, which causes unrealistic stress concentration along the NF.

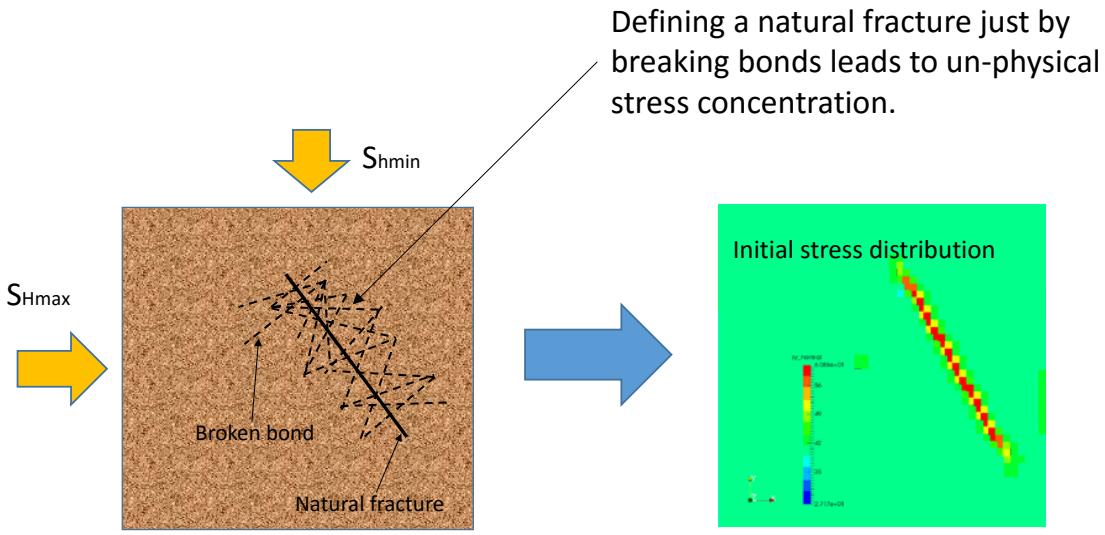

Fig. 5.1 Unphysical stress concentration.

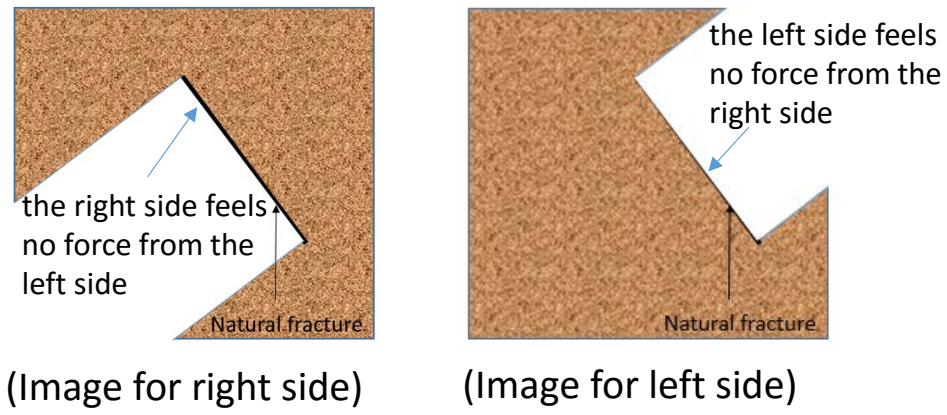

Fig. 5.2 Physical meaning of breaking all the bonds along NF.

In order to avoid such non-physical results shown above, instead of just breaking bonds along a pre-existing fracture surface, we defined a pre-existing fracture as a special surface where all the bonds passing through the surface have different failure criteria than all the other ordinary bonds. All the bonds crossing a pre-existing fracture follow the same constitutive law as the ordinary bonds (as proposed in Equation (2.26)) before they break (in other words, they behave as if no NF existed before they broke). However, since these bonds have both tensile and shear failure criteria, unlike the ordinary bonds, the time when these bonds break is different from the ordinary bonds. These failure criteria are proposed in the following manner.

Tensile failure criteria for NF

The tensile failure criterion for the bonds crossing NF is given by Equation (5.2) where the modification factor α_{NF} is multiplied by the failure criterion for the rock. Since we can select either of the two bond failure criteria (critical strain criterion or critical energy criterion) in our model, different tensile failure models are shown below.

The critical strain criteria

$$s_{c\_NF} = \alpha_{NF} s_{c\_rock} \quad \left(0 \le \alpha_{NF} \le 1\right) \tag{5.1}$$

The critical energy criteria

$$\omega_{c\_NF} = \alpha_{NF} \omega_{c\_rock} \quad \left(0 \le \alpha_{NF} \le 1\right) \tag{5.2}$$

Where,

ω_{c_NF}: critical energy density for the NF [J/m^6]

ω_{c_rock} : critical energy density for the rock [J/m^6]

Shear failure criterion for NF

Since the original peridynamics formulation does not have a shear failure criterion, we introduce one based on a Mohr-Coulomb type shear failure criterion.

$$\tau_{NF} > K_{NF}\sigma_{NF} + \tau_{NF0} \tag{5.3}$$

Where,

σ_{NF} : effective normal stress acting on NF [Pa]

τ_{NF} : shear stress acting on NF surface [Pa]

τ_{NF0} : cohesion of NF surface [Pa]

If one of the two elements comprising a bond satisfies Equation (5.3), the bond is considered to fail in shear. The detailed procedure for deciding shear failure of the bonds passing through a NF is given as following.

(1) **Stress tensor calculation**: Since peridynamics does not need stress state for solving the peridynamic momentum balance equation, stress tensor $\boldsymbol{\sigma}_i$ for each element *i* is additionally calculated from the tractions in x, y, and z direction which are given by Equation (2.28).

(2) **Shear failure evaluation**: As shown in Fig. 5.3, normal and tangential stress components acting on the NF surface are evaluated in the element inside a non-

local area of the NF by the following formulations (Equation (5.4) and (5.5)). Finally, the shear failure criterion is checked in every element inside the nonlocal area of the NF by inserting Equation (5.4) and (5.5) into (5.3).

$$\sigma_{NF\_i} = \left(\boldsymbol{\sigma}_i \mathbf{n}_{NF}\right) \cdot \mathbf{n}_{NF} \tag{5.4}$$

$$\tau_{NF\_i} = \sqrt{\left\|\boldsymbol{\sigma}_i \mathbf{n}_{NF}\right\|^2 - \sigma_{NF\_i}^2} \tag{5.5}$$

Where,

$\mathbf{n}_{NF}$: unit normal vector to NF surface

$\boldsymbol{\sigma}_i$: effective stress tensor for element *i* [Pa]

σ_{NF_i} : Normal effective stress to NF at element *i* [Pa]

τ_{NF_i} : Shear stress to NF at element *i* [Pa]

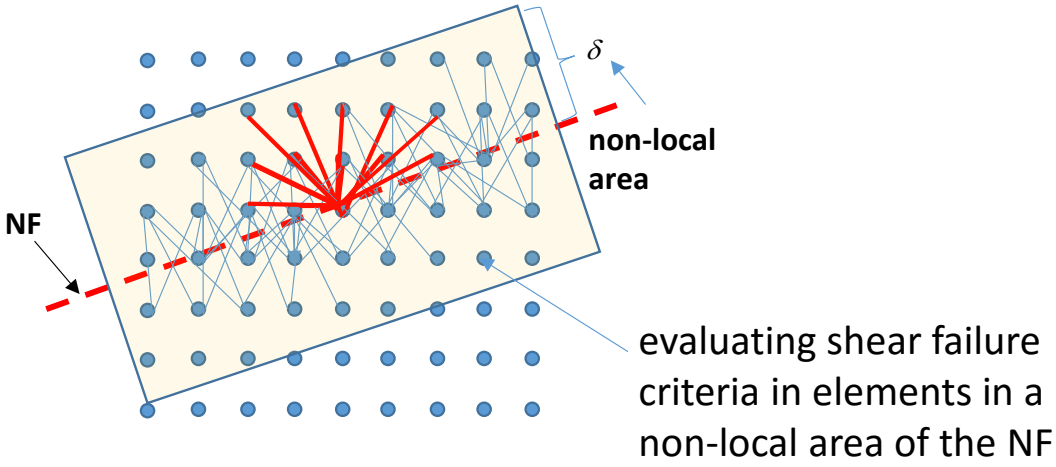

Fig. 5.3 Shear failure evaluation elements.

Once the shear failure criterion is satisfied in a bond crossing a NF, as shown in Fig. 5.4, the tangential component of the force vector state of the bond is reduced by multiplying the factor β_{NF} $\left(0 \le \beta_{NF} \le 1\right)$ in order to account for the change from static to dynamic friction. In addition, the critical energy density (or critical strain) for the shear failed bond is set to zero. These ideas are implemented by the following formulation.

$$\begin{aligned} \underline{T}\left[\mathbf{x},t\right]\langle\xi\rangle &= \left(\underline{t}\left[\mathbf{x},t\right]\langle\xi\rangle \frac{\underline{\mathbf{Y}}\langle\xi\rangle}{\left\|\underline{\mathbf{Y}}\langle\xi\rangle\right\|} \cdot \mathbf{n}_{NF} \right) \mathbf{n}_{NF} \\ &\quad + \beta_{NF} \left(\underline{t}\left[\mathbf{x},t\right]\langle\xi\rangle \frac{\underline{\mathbf{Y}}\langle\xi\rangle}{\left\|\underline{\mathbf{Y}}\langle\xi\rangle\right\|} - \left(\underline{t}\left[\mathbf{x},t\right]\langle\xi\rangle \frac{\underline{\mathbf{Y}}\langle\xi\rangle}{\left\|\underline{\mathbf{Y}}\langle\xi\rangle\right\|} \cdot \mathbf{n}_{NF} \right) \mathbf{n}_{NF} \right) \\ &= \beta_{NF}\, \underline{t}\left[\mathbf{x},t\right]\langle\xi\rangle \frac{\underline{\mathbf{Y}}\langle\xi\rangle}{\left\|\underline{\mathbf{Y}}\langle\xi\rangle\right\|} + \left(1-\beta_{NF}\right) \left(\underline{t}\left[\mathbf{x},t\right]\langle\xi\rangle \frac{\underline{\mathbf{Y}}\langle\xi\rangle}{\left\|\underline{\mathbf{Y}}\langle\xi\rangle\right\|} \cdot \mathbf{n}_{NF} \right) \mathbf{n}_{NF} \end{aligned} \tag{5.6}$$

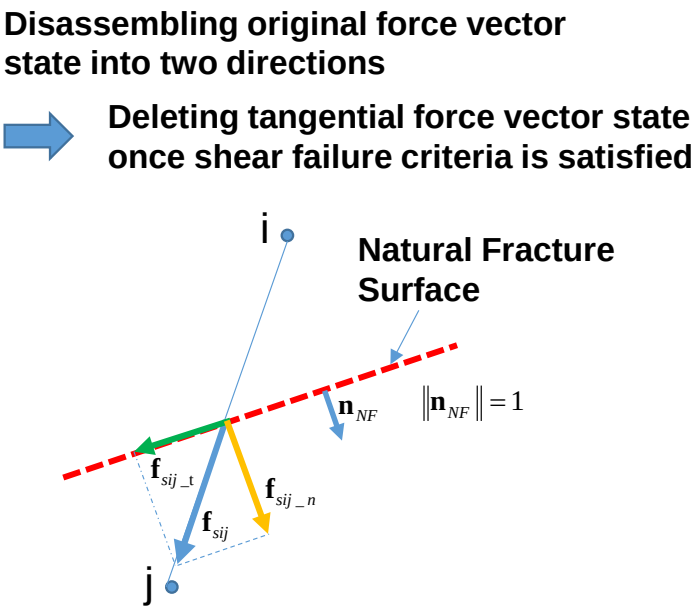

Fig. 5.4 Tangential component reduction from force vector state.

5.3 Verification of the Shear Failure Model

We introduced the new shear failure criterion for defining a NF surface in the previous section. Here, we verify this model by comparing with the following analytical solution proposed by Donath (1966) and Jaeger and Cook (1979)[99, 100]. As shown in Fig. 5.5, if we conduct a stress test on a rock sample which has a weaker bedding plane at an angle β from the vertical, the strength of the rock is analytically estimated by the following solution.

$$\sigma_1 = \sigma_3 + \frac{2\left(\tau_{NF0} + K_{NF}\sigma_3\right)}{\left(1 - K_{NF}\cot\left(\beta\right)\right)\sin\left(2\beta\right)} \tag{5.7}$$

We consider a 2-D plain strain elastic domain of height y = 50 cm and breadth x = 25 cm and discretize it into 100 grids in the y direction and 50 grids in the x direction. The following boundary conditions are applied to the four boundaries (x-plus, x-minus, y-plus, and y-minus) of the domain during simulation time.

- **x-minus boundary:** free traction ($T_x = 0.0$ MPa) boundary condition is applied.
- **x-plus boundary:** free traction ($T_x = 0.0$ MPa) boundary condition is applied.
- **y-minus boundary:** fixed boundary (all displacements are zero).
- **y-plus boundary:** the constant velocity boundary ($v = 1.667 \times 10^{-2}$ m/s) is applied.

We define a weaker plane in this domain by using the shear failure model defined in the previous section with the following mechanical properties (shear trend $K_{NF} = 0.89$, and cohesion $\tau_{NF0} = 5MPa$) and solve for the stress at which shear failure occurs by changing the angle of the weaker plane from 10 degrees to 80 degrees and compare the results with Equation (5.7). The simulation parameters used for these cases are summarized in Table 5.1.

Fig. 5.6 shows the stress-strain relationship in each case. As shown in Fig 5.6, in every case, stress increases linearly with strain before failure occurs. However, once a failure occurs, stress drops sharply due to less resistance to slippage along the weaker plane. Fig. 5.7 shows a comparison between the simulation results and analytical solutions for the critical stress (the stress at which failure occurs). As shown in Fig. 5.7, the simulation results show good agreement with Equation (5.7). This result supports the validity of our newly introduced shear failure model.

Table 5.1 Simulation parameters (1-D unconfined compressional tests with the weaker surface).

Parameters	**Values**
Young's modulus of rock (GPa)	8.40
Shear modulus of rock (GPa)	3.36
Weaker surface shear trend K_{NF}	0.89
Weaker surface angle β (degree)	10, 20,30,40,50,60,70,80
Weaker surface cohesion τ_{NF0} (MPa)	5

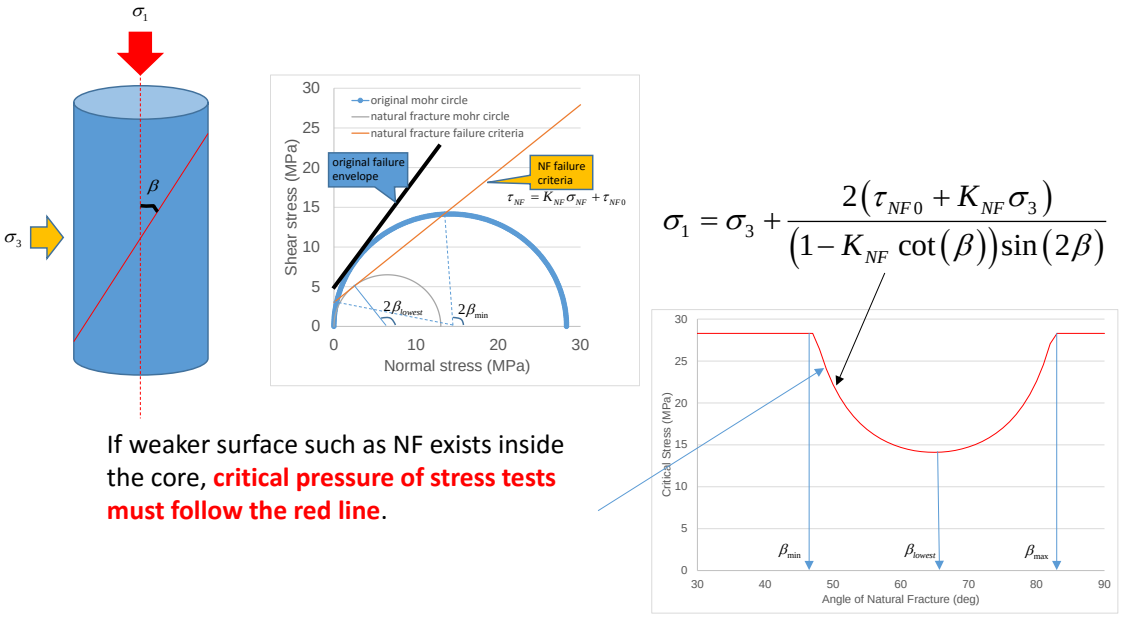

If weaker surface such as NF exists inside the core, **critical pressure of stress tests must follow the red line**.

Fig. 5.5 Critical strength vs. weaker surface angle.

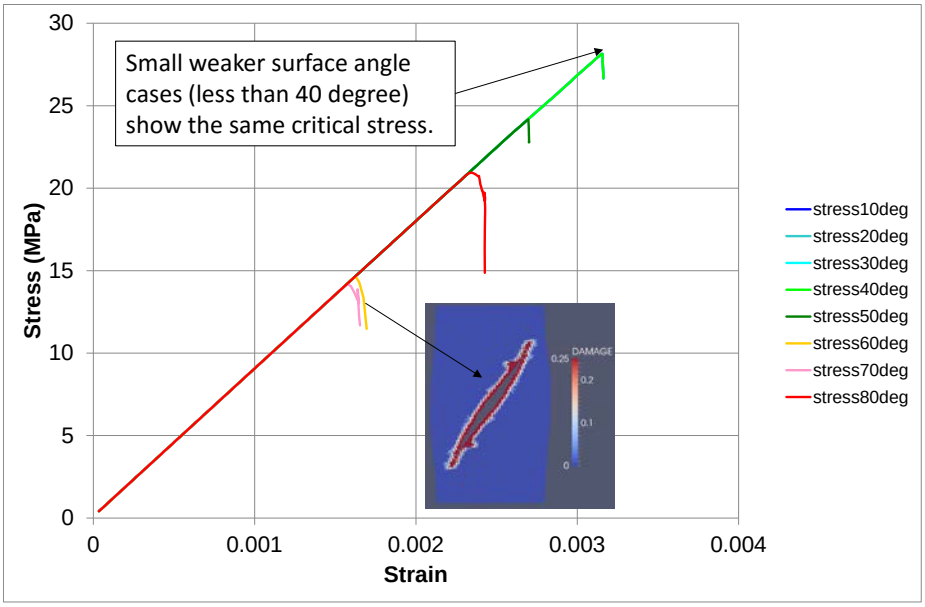

Fig. 5.6 Stress-strain relation in cases with weaker surfaces present at different angles to the horizontal[91].

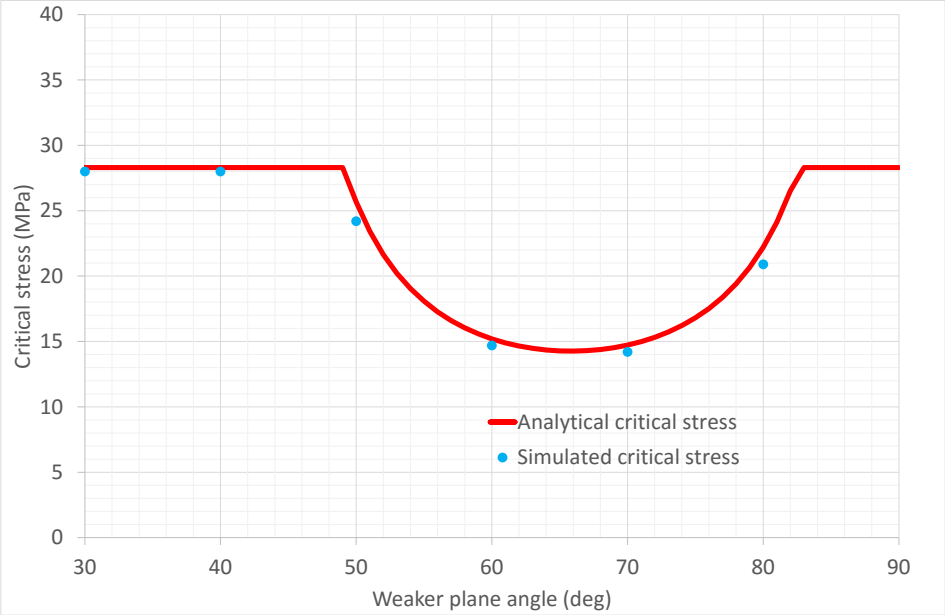

Fig. 5.7 Comparison between simulation results and analytical solution (1D unconfined stress test).

5.4 Comparison with Experimental Results

For validating our simulator's predictions regarding the interaction between HF and NF, we compare our simulation results with the experimental results done by Zhou el al [49]. Zhou et al. performed a series of hydraulic fracturing experiments where ordinary printer papers were used to mimic a natural fracture. Fig. 5.8 shows a schematic of these experiments. By changing three parameters ─ shear strength of the natural fracture (types of paper used), the angle between the hydraulic fracture and the natural fracture, and the stress contrast ─ Zhou et al. investigated how a hydraulic fracture interacted with a natural fracture. We simulated their reported hydraulic fracturing experiments with 0.11 mm thickness paper. Table 5.2 reports the parameters for the experiments and the parameters used in the corresponding numerical simulations. To calibrate the model, we simulate the

unconfined stress test with a critical strain bond failure model to reproduce the unconfined compressive stress (UCS) measured in the experiments reported by Zhou et al. Fig. 5.9 shows the results of numerical simulations and the resulting critical strain value. The critical strain value of $1.183*10^{-3}$ shows good agreement with experimental results and was used for the rest of the numerical simulations unless mentioned otherwise. Table 5.3 reports a summary of each experiment, where "arrested" means fracturing fluid flows along a natural fracture without dilating the natural fracture due to shear slippage, and "dilated" means the natural fracture dilates by the fracturing fluid. As shown in Table 3, the hydraulic fracture tends to cross the natural fracture if the approach angle is more than 60˚ and the hydraulic fracture tends to dilate the natural fracture at low values of the stress contrast.

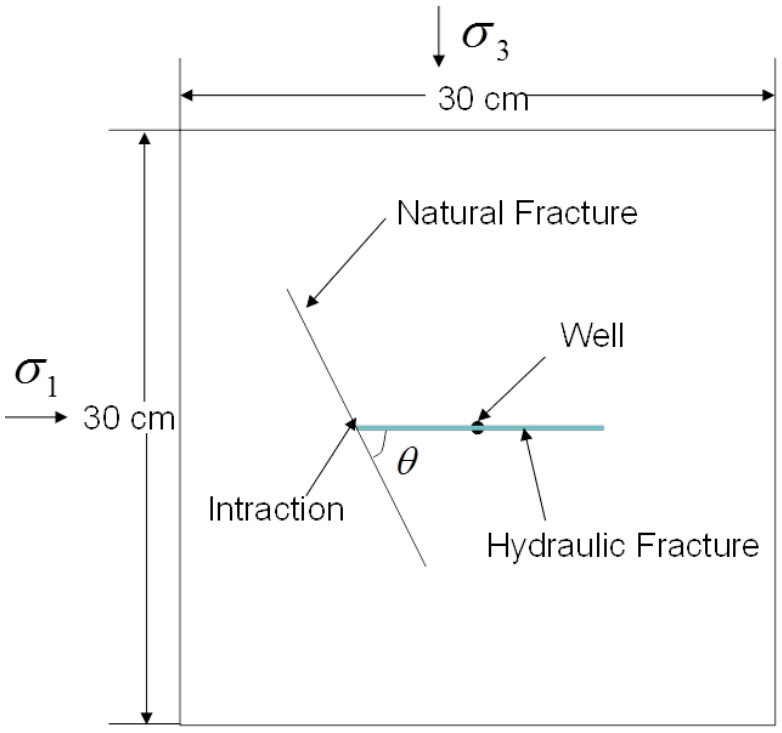

Fig. 5.8 Experimental setting[91].

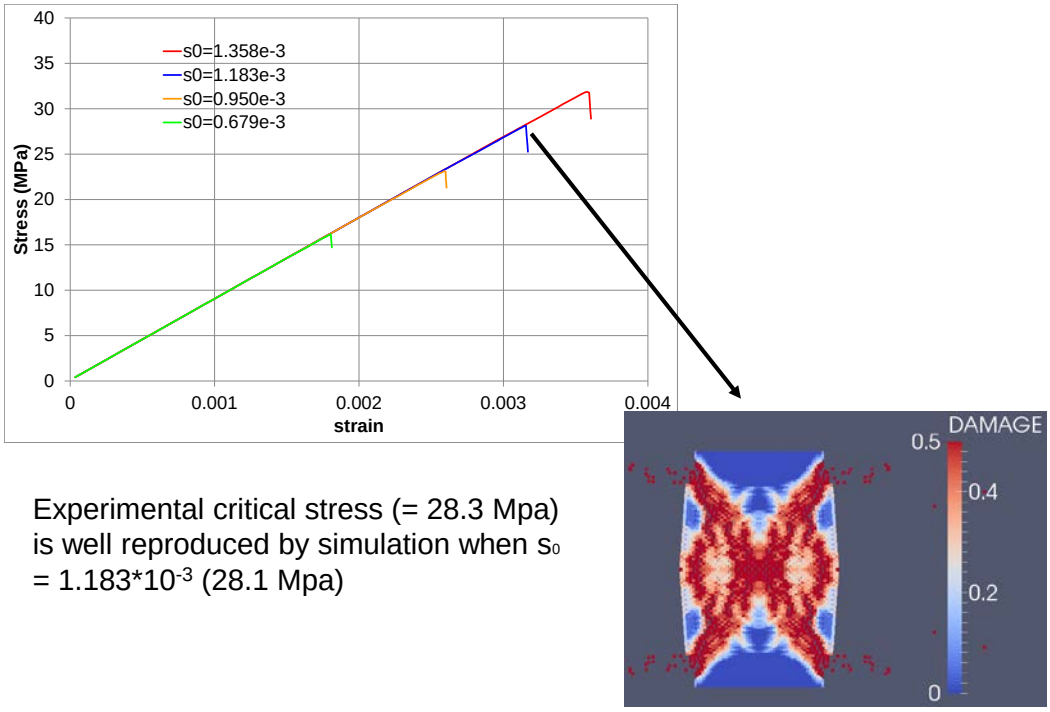

Fig. 5.9 Comparing the critical strain value[91].

To simulate these experiments, a 30 cm square 2D domain is divided into 40,000 (= 200 x 200) 2D square elements. As shown in Fig. 5.8, a natural fracture surface is explicitly defined in the simulation domain. Bonds which cross the natural fracture surface are assigned a critical strain $S_0 = 0.592*10^{-3}$ ($=\alpha_{NF} = 0.5$) —half of the critical strain for the rock as no experimental data exists— for the tensile failure criteria. The shear failure criteria is the same as the experiment (shear coefficient = 0.89 and cohesion = 3.2 MPa). The fluid injection rate was equally allocated into the four center-most elements which act as injection points.

Fig. 5.10 shows how the HF interacts with the NF depending on its approach angle with respect to the NF and the horizontal stress contrast both in experiments and simulations. In Fig. 5.10, experimental results and simulation results are distinguished by color of the markers: black color shows experimental results and red color shows

simulation results. Also, the interaction behaviors are distinguished by the shape of markers: a square maker shows HF crosses NF, a triangle marker shows NF is dilated by HF, and a circle marker shows HF is arrested by NF (without opening further but fluid intrudes into NF). As shown in Fig. 5.10, the experimental results of Zhou et al. reveal the two main characteristics of the interaction between HF and NF: (1) a HF is more likely to turn in when the approach angle is low, (2) a HF is more likely to cross a NF at a high principal horizontal stress difference. Our simulation results, as shown in Fig. 5.10, show very good agreement with the experimental results regardless of the combination of approaching angle and horizontal principal stress. The reason for this observed and simulated interaction behavior between HF and NF is explained as follows: For the 30˚approach angle cases, as shown in Fig. 5.12, on approaching a NF, a HF did not cross it since shear failure occurred on the NF surface more easily (true for all the low approach angle cases). Once shear failure occurs on the two natural fracture surfaces, the surface closer to the hydraulic fracture slips but due to the discontinuity (broken bonds across the natural fracture), less force acts on the other surface. This makes it difficult for the natural fracture to open in Mode I along the original hydraulic fracture propagation direction and, therefore, the hydraulic fracture does not pass through the natural fracture. As shown in Fig. 5.11, the distance from initial stress condition to the shear failure criteria is much closer in the lower approaching angle cases (case7, case8, and case9) than the higher approaching angle cases (from case1 to case 6), which allows the lower approaching angle cases to more easily fail in shear. In addition, the effective stress reduction due to high leak-off caused by high material permeability (= 0.1 mD) accelerates the failure tendency in the experiments. In addition, as shown in Fig. 5.11 for an approach angle of 30˚, the normal stress acting on the natural fracture surface is closer to the minimum principal

stress. This makes it easier for the fracture fluid to dilate the natural fracture which has a smaller fracture toughness.

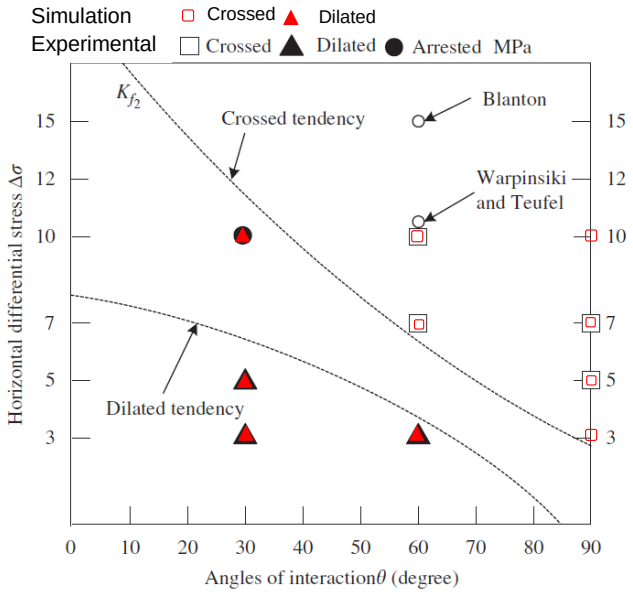

Fig. 5.10 Simulation results vs. experimental results (simulation results are added in the original figure[49])[91].

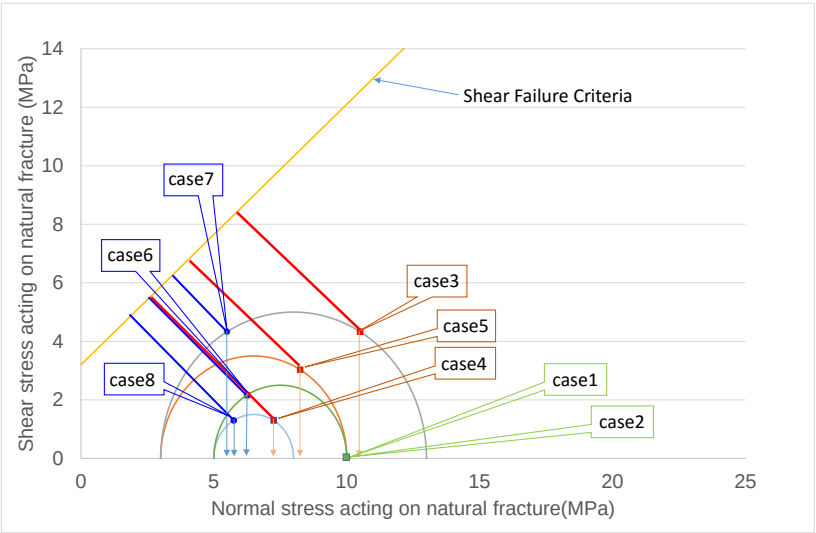

Fig. 5.11 Distance from shear failure criteria[91].

Table 5.2: Experimental and corresponding simulation parameters[91].

Parameters	**Value (experiment)**	**Value (simulation)**
Domain size (cm*cm)	30*30*30	30*30
Bulk modulus (GPa)	5.18	5.18
Poisson's ratio	0.23	0.23
Unconfined compressive stress (MPa)	28.34	28.1
Permeability (mD)	0.1	0.10
Porosity (%)	1.85	1.85
Injected fluid viscosity (cp)	135.0	135.0
Injection rate	$4.2*10^{-9}$ (m^3/s)	$2.1*10^{-8}$ ($m^3/s/m$)
Distance between well and natural fracture (cm)		4.0
Natural fracture length (cm)	around 8.0	8.0
Approach angle (degree)	30, 60, 90	30, 60, 90
Horizontal stress difference (MPa)	3, 5, 7, 10	3, 5, 7, 10
Vertical stress (MPa)	20.0	-
Tensile strength multiplier	-	0.5
Shear failure coefficient	0.89	0.89
Cohesion (MPa)	3.2	3.2
Numerical section		
Number of elements	-	200*200
Horizon size ($= \frac{\delta}{\Delta x}$ = 0.45 cm / 0.15 cm)	-	3.0
Critical strain	-	$1.183*10^{-3}$
Critical damage	-	0.25

Table 5.3: Summary of the experimental and simulation predictions(Case numbers are added for simulations)[91].

Case	Approaching Angle (deg)	Sigma1 (MPa)	Sigma3 (MPa)	Result (experiment)	Result (simulation)
case1	90	10	5	Crossed	Crossed
case2	90	10	3	Crossed	Crossed
case3	60	10	3	Crossed	Crossed
case4	60	13	3	Crossed	Crossed
case5	60	8	5	Dilated	Dilated
case6	30	10	5	Dilated	Dilated
case7	30	8	5	Dilated	Dilated
case8	30	13	3	Arrested	Dilated

For the 60˚approach angle cases, as shown in Fig. 5.13, the hydraulic fracture dilates the natural fracture in the lower stress contrast case (Case5), while the hydraulic fracture continues to propagate immediately after dilating the natural fracture in the higher stress contrast cases (Case3 and Case 4). As shown in Fig. 5.14, since the pore pressure around the fracture increases due to the high matrix permeability (= 0.1 mD), the effective stress near the fracture tip decreases from the initial condition and on approaching the natural fracture causes it to fail under shear. However, in the higher stress contrast cases, although the hydraulic fracture initially dilates the natural fracture, it finally crosses because the normal stress acting on the natural fracture is close to the maximum principal stress.

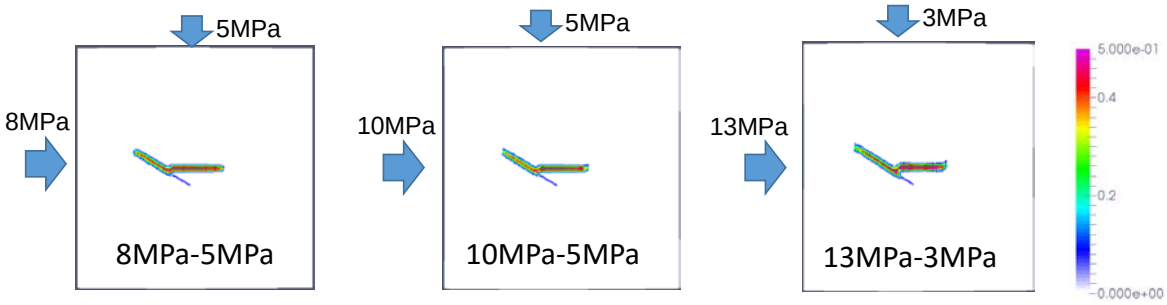

Fig. 5.12 Damage distribution after 300 sec (approach angle = 30 degree) [91]. Note that the simulation domain is enlarged 50 times.

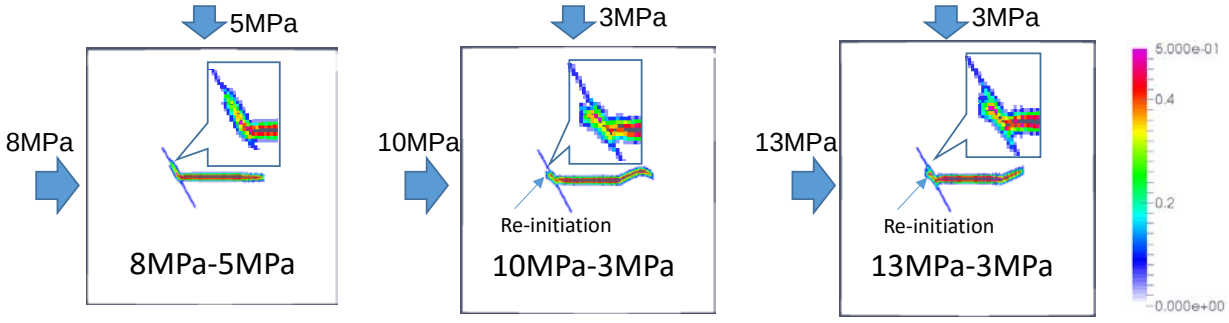

Fig. 5.13 Damage distribution after 300 sec (approach angle = 60 degree)[91].

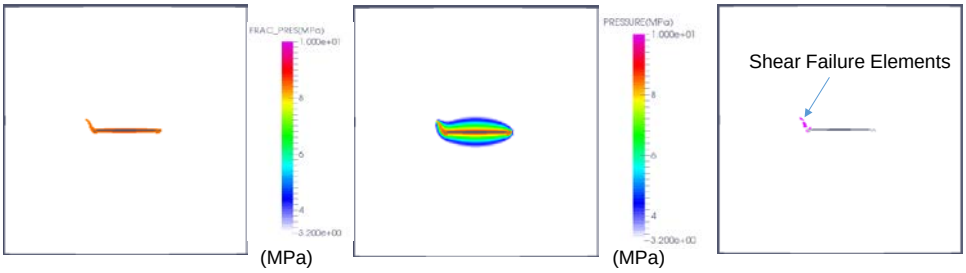

Fig. 5.14 Effect of poroelasticity[91].

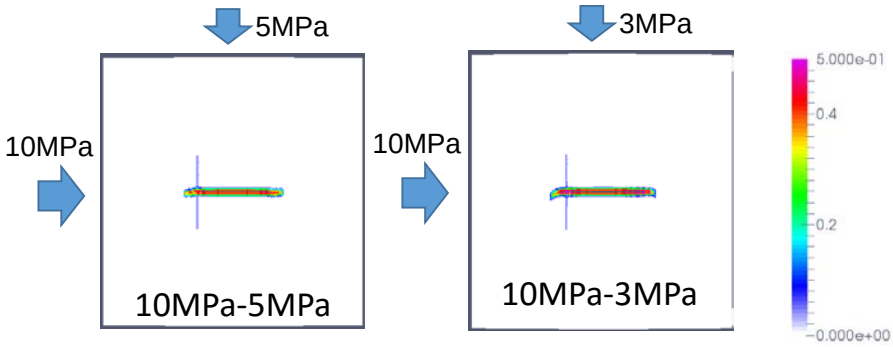

Fig. 5.15 Damage distribution after 300 sec (approach angle = 90 degree)[91].

The simulated 90˚ approach angle cases shown in Fig. 5.15 are also in good agreement with experiments. As shown in Fig. 5.11, the initial stress condition in the 90˚cases is far from the shear failure criteria. In addition, the initial normal stress acting on

the natural fracture surface is the maximum principal stress. Therefore, the hydraulic fracture passes through the natural fracture without any offset.

5.4 Sensitivity Analysis

To analyze the effect of rock properties and poroelasticity on the interaction between a hydraulic fracture and a natural fracture, we conducted a sensitivity analysis for these parameters based on Case 5 (Base Case) in the previous section (approach angle = 60º and stress contrast = 3 MPa). Note that the reason we select Case 5 as the Base Case is because judging from the results of the previous section, Case 5 is located near the boundary between "fracture crossing" and "fracture dilation" due to the intermediate approaching angle and low horizontal principal stress difference. Hence, the effect of other parameters on fracture interaction may be easily understood. The following parameters are changed in these simulations: critical strain and the Young's modulus of the rock, critical strain of the natural fracture, matrix permeability, injection rate, initial natural fracture permeability, and shear failure criteria. In the critical strain and Young's modulus sensitivity case, the critical strain is modified as a function of the square root of Young's modulus to keep the energy release rate of bonds constant ($G_c = \frac{K_{Ic}^{\ 2}}{E/(1-\nu^2)} \Leftrightarrow K_{IC} = \sqrt{\frac{G_c E}{(1-\nu^2)}}$). Also, in the initial natural fracture permeability cases, since our simulator does not allow us to keep constant initial fracture space and initial fracture permeability regardless of deformation, the initial natural fracture permeability is assumed to be equal to the matrix permeability. Modified parameters in each case are summarized in Table 5.4. Fracture propagation and damage distribution after 350 sec in each case is shown in Fig. 5.16 - Fig. 5.21. This sensitivity analysis reveals that

poroelasticity has a significant effect on the interaction between a hydraulic fracture and a natural fracture if the leak-off rate is high. In addition, the relative magnitude of the following mechanical properties (fracture toughness of the rock, fracture toughness of the natural fracture, and shear strength of the natural fracture) also affect the interaction between a hydraulic fracture and a natural fracture.

Table 5.4 Case settings of the sensitivity analysis.

Parameter	Case	Value
Young's modulus & Critical strain	1	E = 4.0 GPa, Scrit = 0.81*10-3
	2	Base (E = 8.4 GPa, Scrit = 1.18*10-3)
	3	E = 20.0 GPa, Scrit = 1.82*10-3
NF critical strain	1	Scrit = 1.18*10-3
	2	Base (Scrit = 0.59*10-3)
	3	Scrit = 0.0
Injection rate	1	1.1*10-8 m3/s/m
	2	Base (2.1*10-8 m3/s/m)
	3	1.1*10-8 m3/s/m
Rock permeability	1	0.001 mD
	2	0.01 mD
	3	Base (0.1 mD)
Shear strength	1	Coeffient = 0.89, Cohesion = 0.0 MPa
	2	Base(Coeffient = 0.89, Cohesion = 3.2 MPa)
	3	Coeffient = 0.89, Cohesion = 7.0 MPa
Initial natural fracture permeability	1	Base (0.0 mD)
	2	1.0 mD

In Fig. 5.16, we investigated the role of the Young's modulus and accordingly modified the critical strain of the rock. As shown in Fig. 5.16, the hydraulic fracture crossed the natural fracture for the lowest critical strain and Young's modulus case ($S_{crit} = 0.81*10^{-3}$ and E = 4 GPa), while for higher critical strain and Young's modulus cases (($S_{crit} = 1.18*10^{-3}$ and E = 8.4 GPa) and ($S_{crit} = 1.82*10^{-3}$ and E = 20 GPa)), the hydraulic fracture turned along the natural fracture. Since in peridynamics the critical strain of a natural

fracture is directly related to its fracture toughness, these results suggest that if the fracture toughness of the rock is enough low, the hydraulic fracture will cross the natural fracture even under high leak-off conditions since the energy required to open up the natural fracture is less than that for the rock matrix.

In Fig. 5.17, we vary the critical strain of the bonds crossing the natural fracture. The hydraulic fracture crossed the natural fracture for the highest critical strain case ($S_{crit} = 1.18*10^{-3}$) while it turned along the natural fracture for the zero critical strain case and the Base Case ($S_{crit} = 0.59*10^{-3}$). These results suggest that the high fracture toughness of a natural fracture would restrict the turning of a hydraulic fracture along the natural fracture. These results also suggest that the values of the toughness of the natural fracture chosen for Cases 3 and 4 in the previous section may be smaller than those used in the experiments allowing the fracture to turn towards the natural fracture.

In Fig. 5.18, we investigate the impact of injection rate on the interaction of the hydraulic fracture with the natural fracture. For a comparison between the different injection rate cases, we keep the injected volume the same, therefore, we select the injection time accordingly. The chosen injection rates do not affect the interaction between the hydraulic fracture and the natural fracture; in all three cases, the hydraulic fracture turns along the natural fracture. However, it is curious to note that the higher and the lower injection rate cases yield longer fracture lengths in comparison to the Base Case. In the lower injection rate case with the longer injection time, due to relatively large leak-off and the resulting lower effective stress on the natural fracture, the larger region of shear failure results in a longer fracture along the natural fracture. On the other hand, in the higher injection rate case with the smaller injection time, fracture length along the natural fracture is longer than the Base Case due to the relatively small leak-off.

The matrix permeability shows a significant influence on the interaction between a natural fracture and a hydraulic fracture (Fig. 5.19). In the lower matrix permeability cases (k = 0.001 mD and k = 0.01 mD), the fractures passed through the natural fractures. In contrast, the fracture turned along the natural fracture for the base case (k = 0.1 mD). Higher matrix permeability causes high leak-off and a significant increase in pore pressure. This leads to a large reduction in the normal effective stress acting on a natural fracture surface, which makes it easier for a natural fracture to fail both in tensile and in shear modes. The fracture propagation pattern in the presence of natural fractures can completely change under high leak-off conditions. These results highlight the fact that poroelasticity plays an important role in the interaction between a natural fracture and a hydraulic fracture if leak-off is significant. This is consistent with the findings of Agarwal and Sharma [101]. Note that if we set the matrix permeability to more than 1 mD, the hydraulic fracture does not propagate due to excessive leak-off for the given injection rate. A matrix permeability of 0.1 mD is almost the maximum value that allows fracture initiation under the given injection rate.

In Fig. 5.20, we simulate different cohesion values to modify the shear failure criterion of the natural fracture. With the larger cohesion value (shear coefficient = 0.89, cohesion = 7.0 MPa), as expected, the hydraulic fracture does not turn along the natural fracture even under high leak-off conditions. This suggests that the criterion for shear failure controls whether a fracture turns along a natural fracture or not. We also find that the fracture propagation speed along a natural fracture changes depending on the failure criterion. The fracture propagation speed in the lowest cohesion case (shear coefficient = 0.89, cohesion = 0.0 MPa) was faster than the second lowest cohesion case (shear coefficient = 0.89, cohesion = 3.2 MPa) due to the larger shear failure region.

We also find in Fig. 5.21 that the higher initial permeability of the natural fracture (than the surrounding rock) causes the hydraulic fracture to accelerate as the fracturing fluid preferentially flows into the natural fracture.

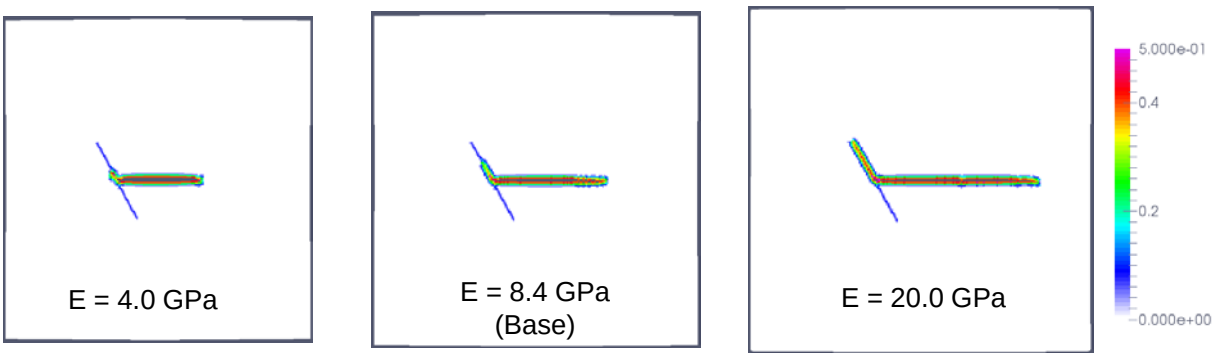

Fig. 5.16 Effect of Young's modulus and critical strain of the rock (damage distribution after 350 sec)[91].

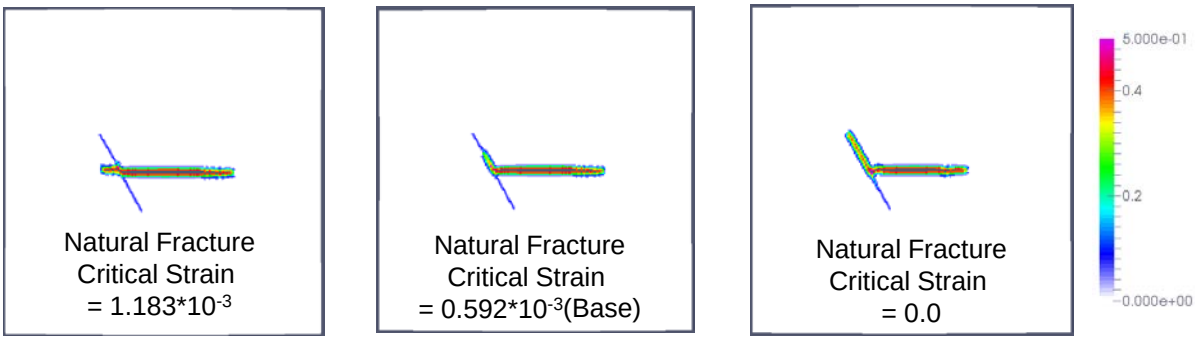

Fig. 5.17 Effect of critical strain of the natural fracture (damage distribution after 350 sec)[91].

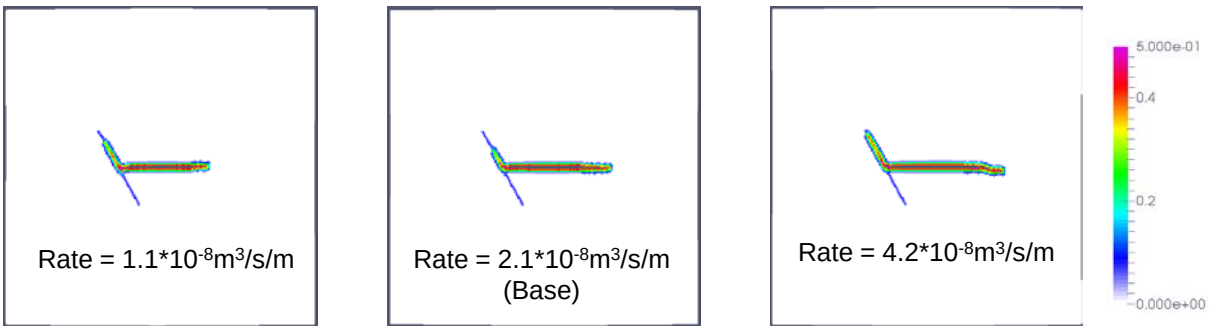

Fig. 5.18 Effect of injection rate (damage distribution after 700 sec, 350 sec, 175 sec respectively)[91].

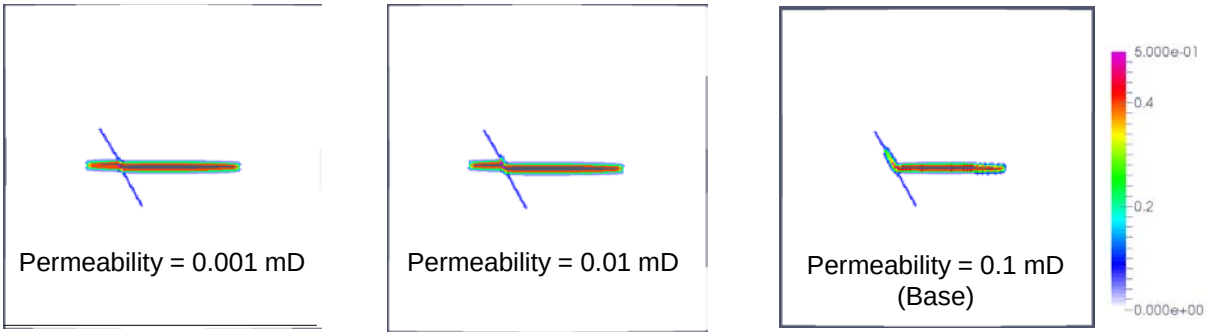

Fig. 5.19 Effect of rock permeability (damage distribution after 250 sec)[91].

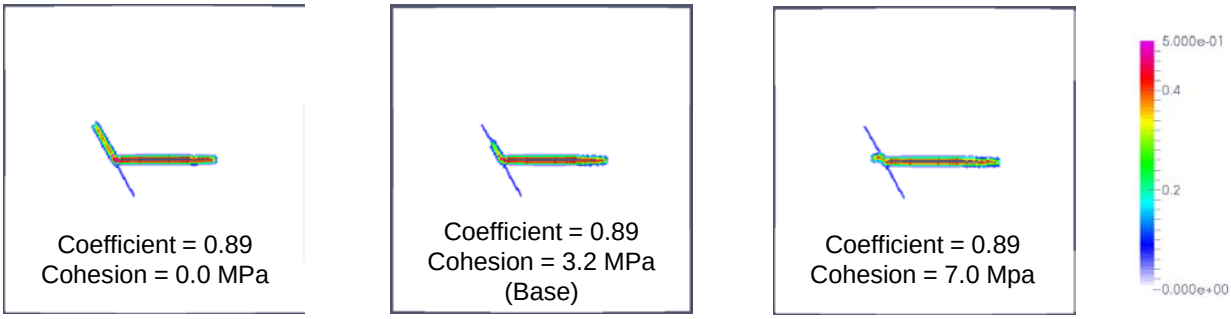

Fig. 5.20 Effect of shear strength (damage distribution after 250 sec)[91].

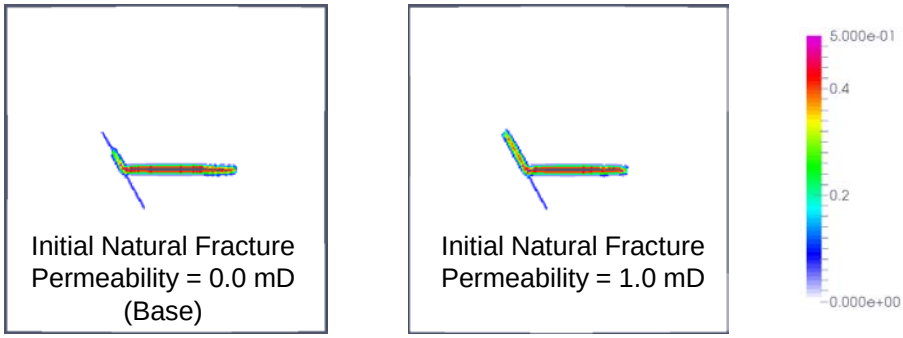

Fig. 5.21 Effect of initial natural fracture permeability (damage distribution after after 250 sec)[91].

5.5 Growth of Multiple Hydraulic Fractures in Naturally Fractured Reservoirs

To demonstrate the applicability of our peridynamic hydraulic fracturing model to a field scale simulation, two cases of domain size 5,200 ft x 5,200 ft are considered. The only difference between the two cases is the presence or absence of natural fractures. As shown in Fig. 5.22, one model has 100 arbitrarily oriented natural fractures (NF case) and another has no natural fractures (no-NF case). Five equi-spaced vertical wells 200 ft apart are placed as shown in Fig. 5.22. Water is injected from the five wells at a flow rate of 0.12 bbl/min/ft to propagate fractures. Competing fracture growths from the five wells is simulated in both the cases. Table 5.5 shows the simulation parameters for these cases. Fig. 5.23 and Fig. 5.24 show the property distribution (damage, fracturing fluid pressure, matrix pressure, matrix porosity, normal stress in the x direction (S_{xx}), normal stress in the y direction (S_{yy})) after 2000 sec and 4000 sec for No-NF case respectively. Fig. 5.25 and Fig. 5.26 show the property distribution after 3000 sec and 6000 sec for NF cases respectively. In the no-NF case, as shown in Fig. 5.23, at the early stage of the injection, although water was injected at the same rate from each well, fracture geometry and fracture

pressures were slightly different for each well due to stress interference among wells. The center fracture showed a shorter and wider geometry and a higher fracture pressure, while the outer fracture showed a longer and narrower geometry and a lower fracture pressure. However, at the late stage of the injection, as shown in Fig. 5.24, the center fracture (the third fracture from the left) grows longer than the intermediate fractures (second fracture and fourth fracture from the left). As the five fractures simultaneously propagate, the area under tensile stress conditions (blue Sxx area in Fig. 5.24 (e)) gradually grows in front of each fracture. Due to the superposition effect of every fracture, the tensile domain becomes largest in front of the center fracture (the third fracture from the left). This may induce the center fracture to propagate into the tensile domain more than the intermediate ones. Once the center fracture becomes longer than the intermediate fractures, the propagation of intermediate fractures is severely impeded by the stress interference from the center fracture and the outside fractures. However, the width of the center fracture near the injection point becomes narrowest since this point still has the maximum stress interference from the other wells.

On the other hand, the NF case shows a completely different fracture propagation pattern. Each fracture tends to grow more in a region that has a higher density of natural fracture, as those regions are already damaged and easier to open. This leads to asymmetrical fracture propagation from the well, relatively longer fracture length and smaller fracture pressure than the no-NF case. Also, in agreement with the observations made in the previous section, fractures dilate low approach angle natural fractures and cross high approach angle natural fractures (Fig. 5.25 and Fig. 5.26). These results show the ability of a peridynamics-based fracture propagation theory to easily model heterogeneity and complex networks of natural fractures. The existence of natural fractures drastically changes fracture propagation patterns and generates a complicated fracture geometry.

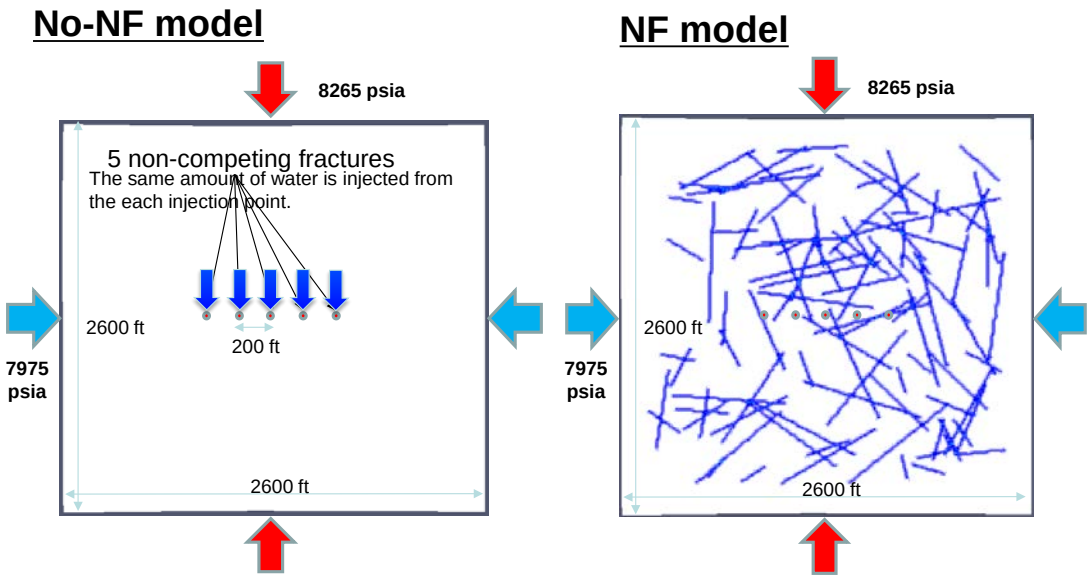

Fig. 5.22 Plane view of the two field cases (no-NF case and NF case) (modified from [91]).

Table 5.5 Simulation parameters for fracture propagation in field case (modified from [91]).

Parameter	Value
Dimension of the 2D domain in X direction L_x (ft)	2600
Dimension of the 2D domain in Y direction L_y (ft)	2600
Boundary stress in x direction $\mathcal{T}_x$ (psia)	7975
Boundary stress in y direction $\mathcal{T}_y$ (psia)	8265
Young's modulus of the domain (psia)	$1.60*10^6$
Shear modulus of the domain (psia)	$0.96*10^6$
Reference pore pressure p_0 (psia)	464
Injection rate (bbl/min/ft)	0.05
Fracturing fluid viscosity (cp)	1.0
Medium permeability (nD)	10.0
Critical damage	0.25
Tensile strength multiplier	0.5
Shear failure coefficient	0.89
Cohesion (psia)	464
Number of elements	200*200
Horizon size ($=\frac{\delta}{\Delta x}$ = 78 ft / 26 ft)	3.0

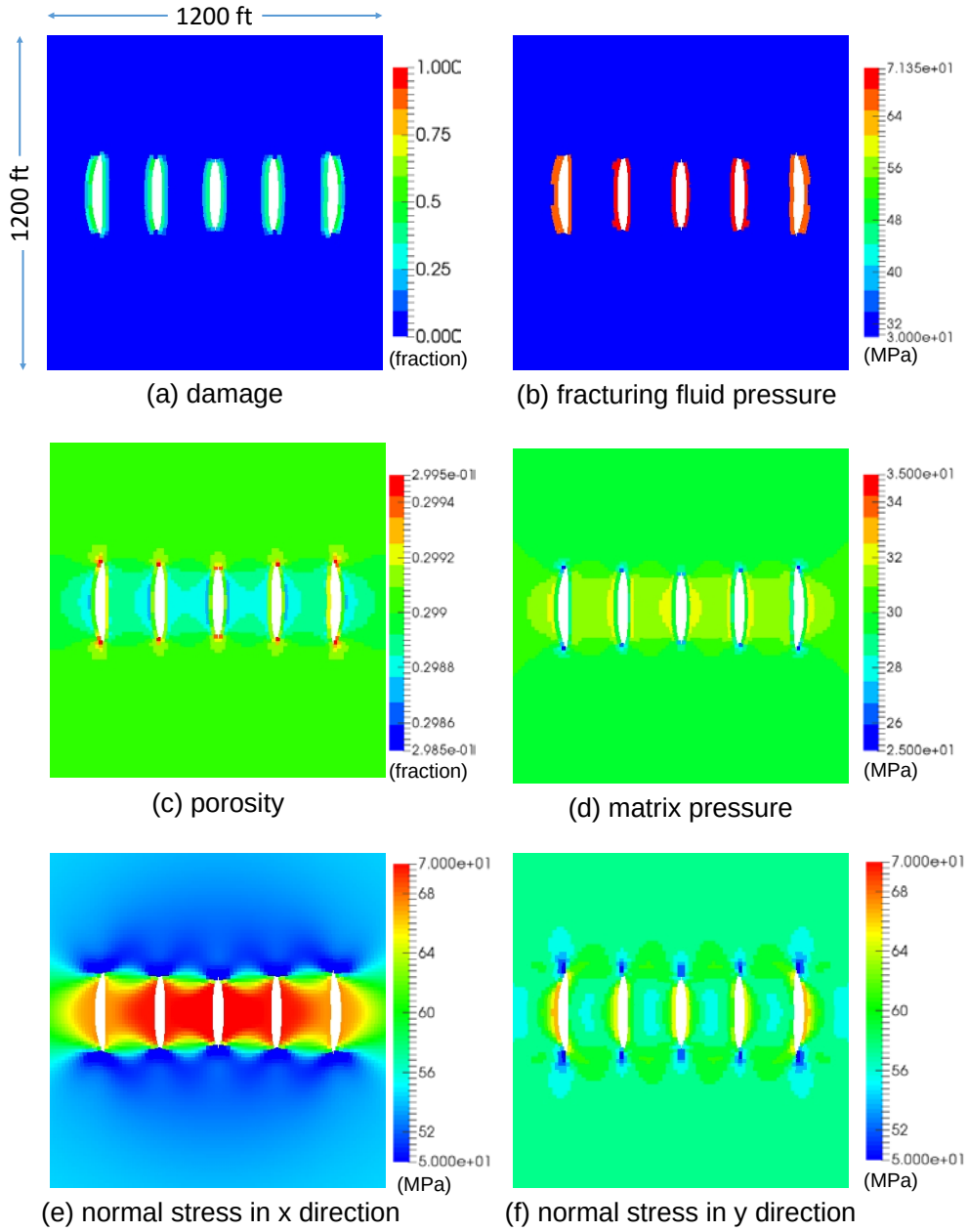

Fig. 5.23 Stresses and reservoir property distribution after 2,000 sec in No-NF case.

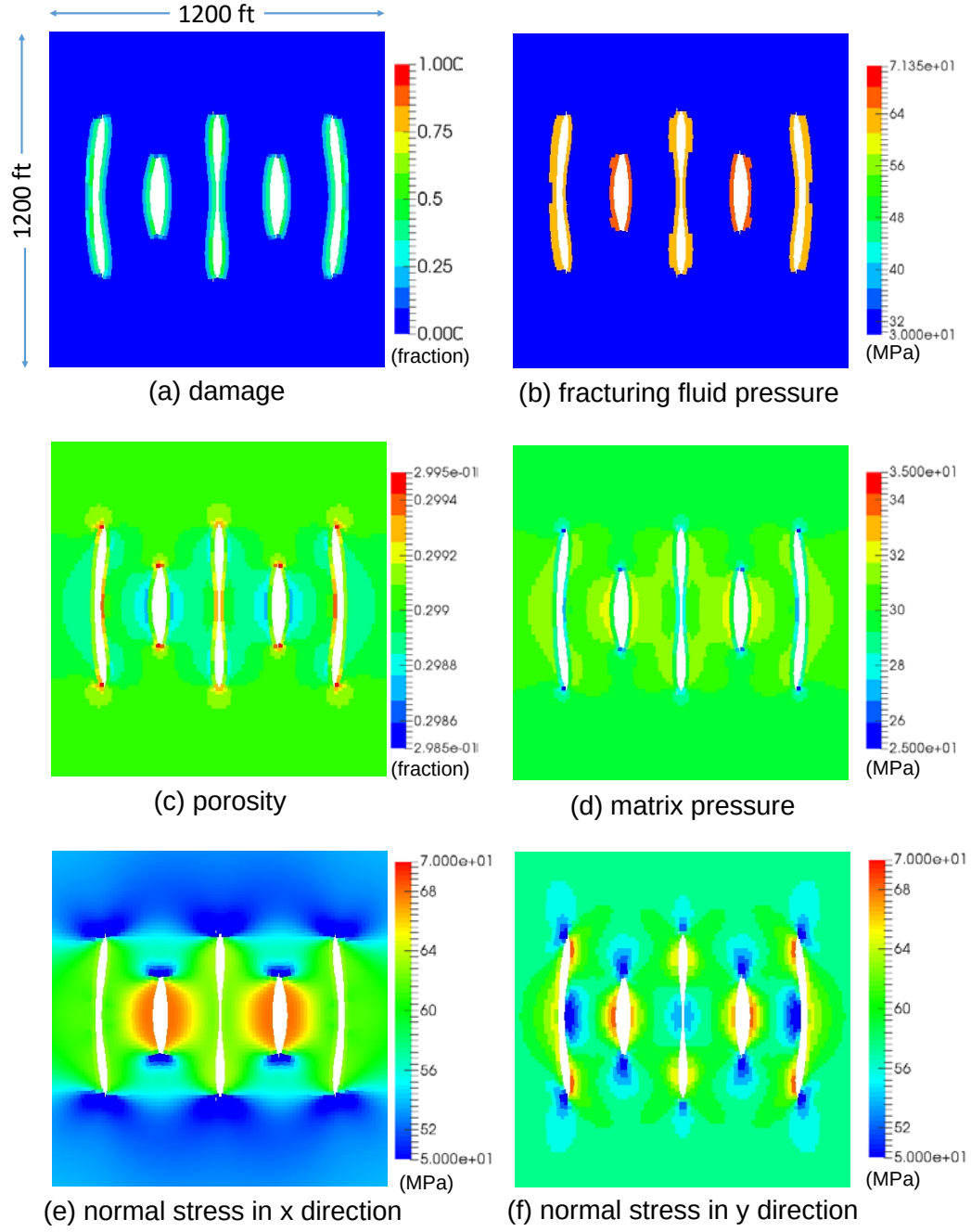

Fig. 5.24 Stresses and reservoir property distribution after 4,000 sec in No-NF case.

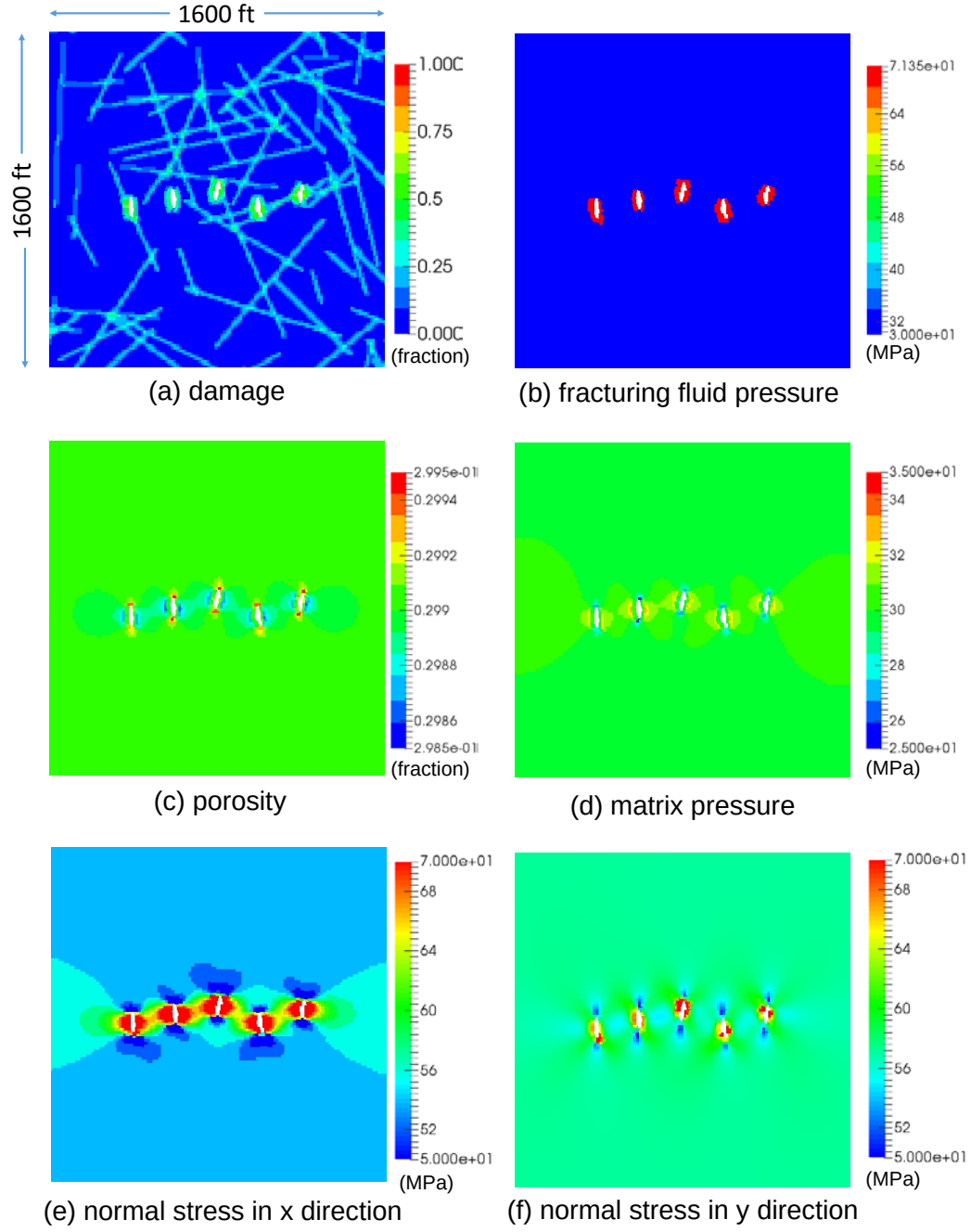

Fig. 5.25 Stresses and reservoir property distribution after 3,000 sec in NF case.

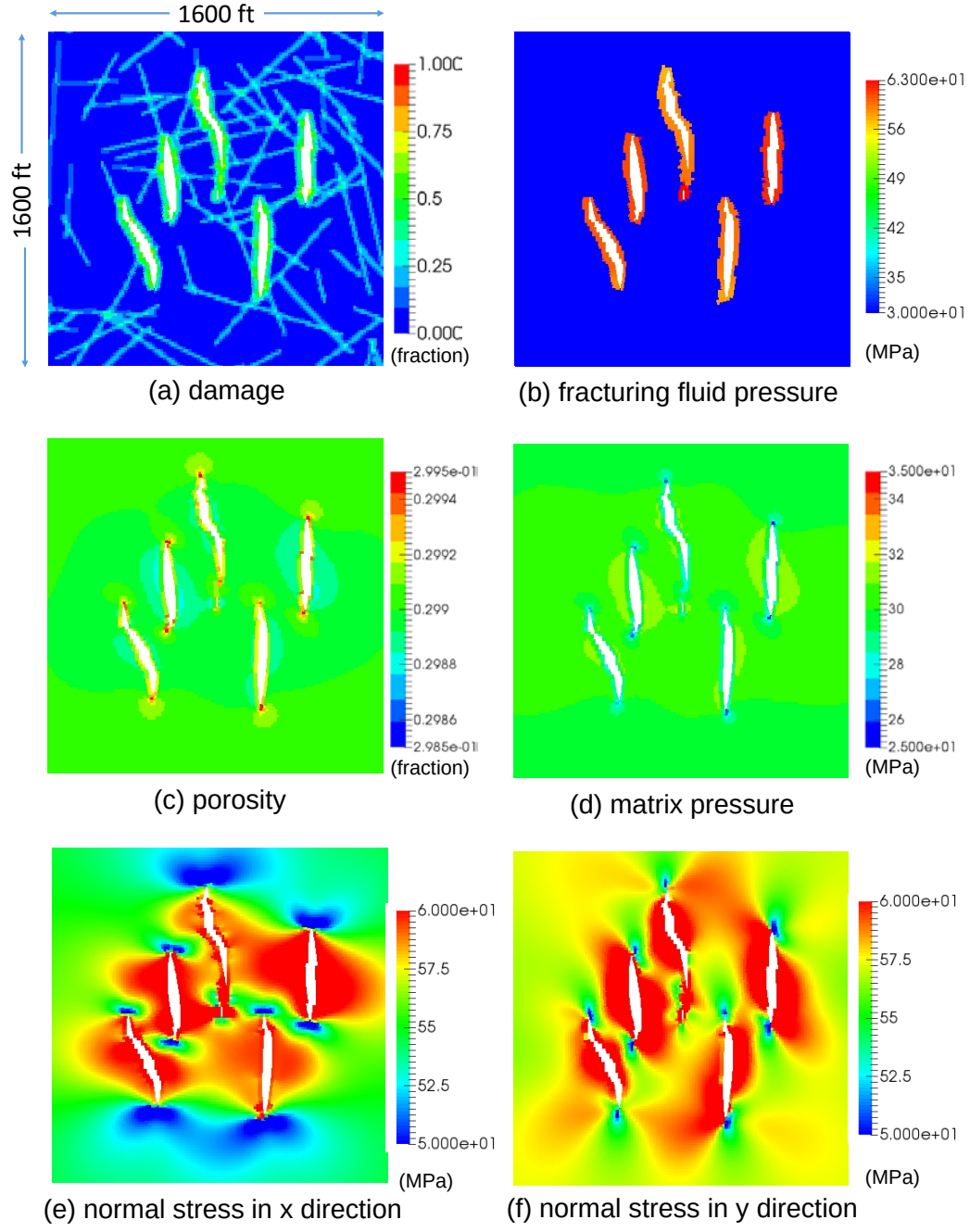

Fig. 5.26 Stresses and reservoir property distribution after 6,000 sec in NF case.

5.6 3-D Interaction between hydraulic fracture and natural fracture

In the previous sections, we show our model's validity by comparing with experimental results, and demonstrate our model's applicability to predict interaction behaviors with HF and NF through two dimensional simulations. As we show in those cases, our model can properly predict the three basic interaction behaviors between HF and NF: crossing, turning (or arresting), and reinitiating a new fracture (Fig. 5.27).

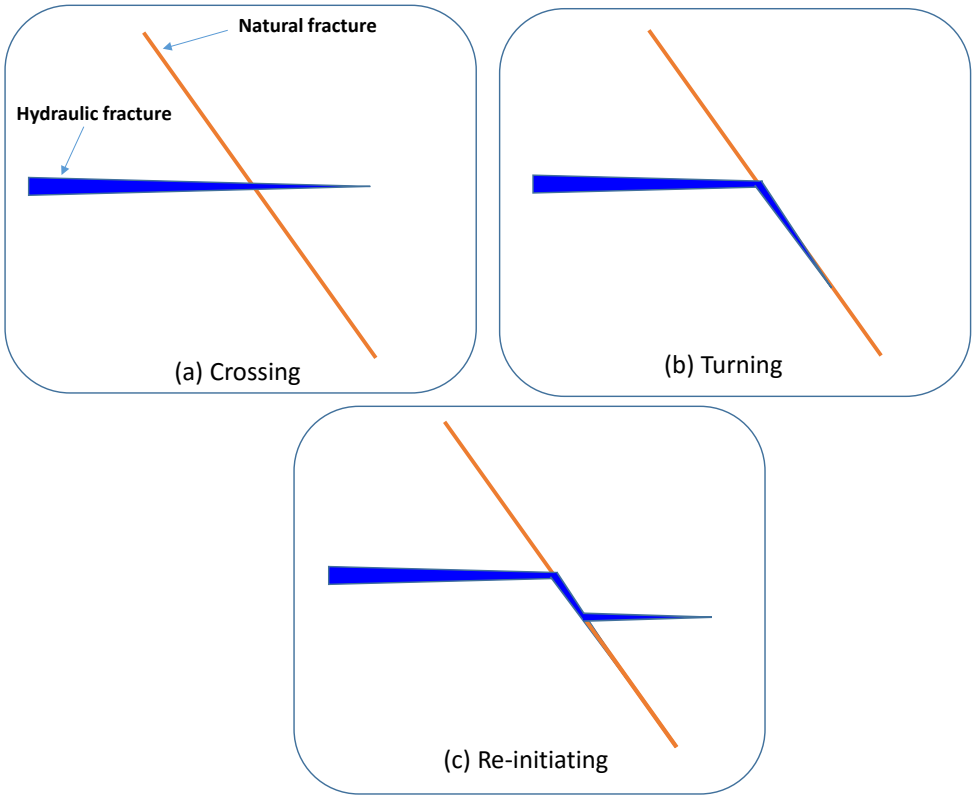

Fig. 5.27 Basic hydraulic fracture interactions with a natural fracture.

However, Bahorich et al. [102] reveal, through their experiments, that when a HF turns along a NF, if the NF does not fill the entire height of the pay-zone, it can display

more complicated behavior as shown in Fig. 5.28 (combination of bypassing NF and turning along NF, or a combination of turning along the NF and diverting propagation along the top and bottom of the NF).

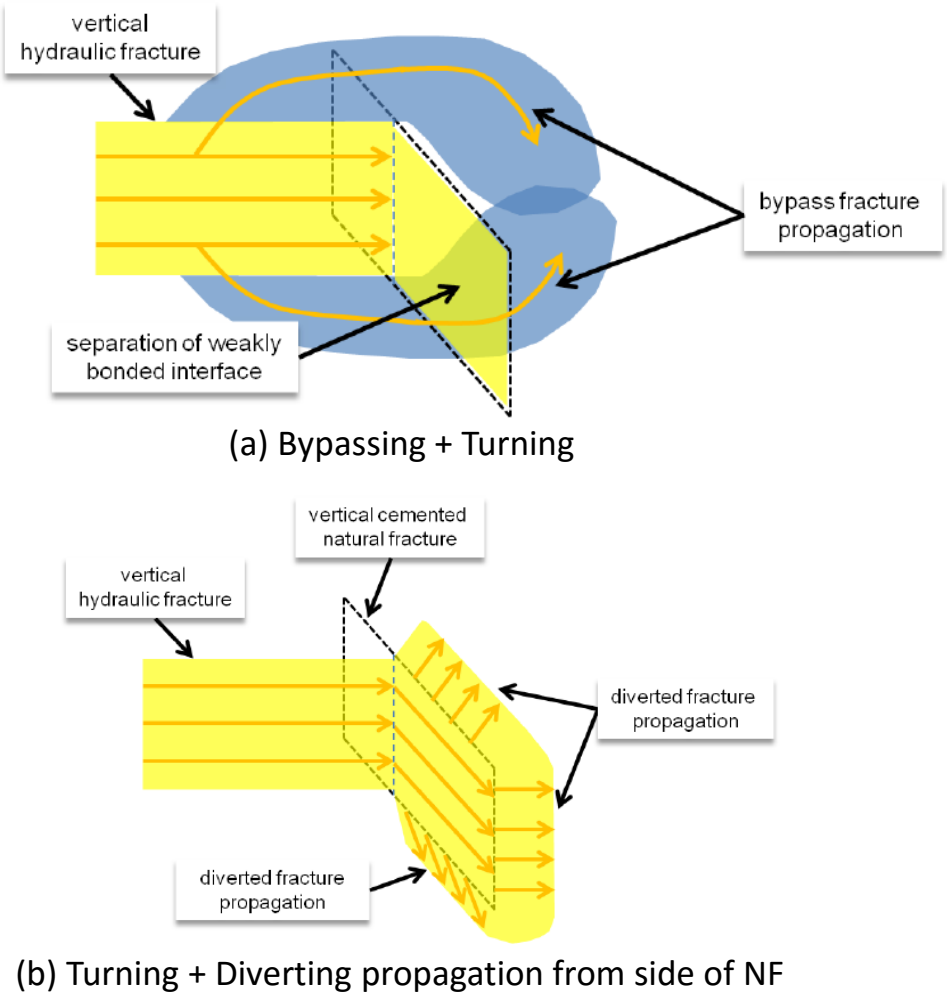

Fig. 5.28 Complicated fracture propagation in 3D **(**Figures are taken from [102]**).**

Predicting this kind of complex interaction behavior requires full 3-D simulations, something that most state-of-the-art simulators cannot do. Two-dimensional interactions between HF and NF shown in Fig. 5.27 cannot simulate this behavior. However, our

peridynamics based hydraulic fracturing model is fully capable of simulating such complicated interaction behavior. In this section, we demonstrate our simulator's applicability to model complex 3-D fracture interaction problems.

As shown in Fig. 5.29, we consider a simulation domain of 1.6 m × 1.6 m × 0.68 m where three different principal stresses (S_x=41 MPa, S_y=40 MPa,S_z=60 MPa) are applied from x, y, and z planes respectively. At the middle of the surface at x = 0, an injection point is defined as an injector. Water is injected from this injection point at the rate of 0.003 kg/s. By changing the height of NF and cohesion parameter, we investigate how HF interacts with NF. Common input parameters for the simulations are summarized in Table 5.6. Parameters particular to cases are summarized in Table 5.7. Note that numerical convergence of the simulations is quite slow in these complicated 3-D interaction problems once the HF interacts with the NF. In order to complete the simulations in a reasonable time, poroelastic effects are neglected. This is a reasonable assumption for nano-Darcy permeability shales and when comparing our results with lab results (where there is very little leakoff). We don't solve pore pressure in these cases (constant initial pore pressure is used for the leak-off calculation and effective stress calculation). In addition, to reduce the calculation time further, instead of simulating bounding layers which have higher stress than the pay-zone, the displacement in the non-local area of the top and bottom boundary elements are fixed for mimicking the bounding layer.

Fig. 5.30 shows the fracturing fluid pressure distribution in Case 1 after 26 seconds. This is the reference case. In this case, since NF fills the entire pay-zone (60 cm) and the horizontal principal stress difference and cohesion of NF surface is low enough ($\Delta S = 1.0\,\text{MPa}$, $cohesion = 0.0\,\text{MPa}$) to cause shear failure along the NF surface, the HF turns along the NF, which is the same behavior as was observed in the 2-D plain strain simulation.

However, as shown in Fig. 5.31, if the NF fills only the lower half of the pay-zone (Case 2, with all other conditions being the same as Case1), the HF does not fully turn along NF but shows a combination of bypassing and turning behavior which is the same as the behavior shown in Fig. 5.28 (a). In this case, as shown in Fig. 5.32 (a), once the tip of the HF reaches the NF, the HF begins to turn along the NF in the lower half of the pay-zone due to shear failure at the point where it hits the NF. However, since NF does not fill in the upper half of the pay-zone, the HF continues to propagate without turning in the upper half of the pay-zone (Fig. 5.32 (b)). Once the HF overcomes the NF in the upper part of the pay-zone, it gradually moves down to the lower part of the pay zone and fills it again (Fig. 5.32 (c)). With the main fracture moving down from the upper part of the pay-zone, fracture propagation in the NF slows down due to the stress interference from the main fracture, and finally it stops before reaching the end of the NF (Fig. 5.32 (d)). This case suggests that the height of the NF (the ratio of NF to the pay-zone) is also one of the important parameters which control the interaction between the HF and the NF.

Case 3 shows different HF propagation behavior from Case 2. In this case, the tensile strength multiplier for the NF is set lower than for Case 2 (all other conditions are the same as Case 2). As shown in Fig. 5.33, in the lower part of the pay-zone, the HF completely turns along the NF, while, in the upper part of the pay-zone, the HF also turns along the NF with some diverting angle from the vertical axis. This is the same propagation behavior as in Fig. 5.28 (b) (turning + diverting). In this case, after the tip of the HF reaches the NF, most of the injected water moves into the NF rather than going straight due to the lower tensile resistance caused by lower tensile strength multiplier than Case2. After water reaches the end of the NF, the HF begins to propagate from the top side of the NF at some diverting angle from the vertical axis. This case shows the degree of resistance to open the NF also affects 3-D interaction behavior between the HF and the NF. The lower opening

resistance of the NF causes more turning and diverting behavior rather than bypassing and turning behavior.

In Case 4, the NF fills half of the pay-zone (same as Case 2), but it is set in the middle of the pay-zone instead of the bottom of the pay-zone. All the other conditions are the same as Case 2. As shown in Fig. 5.34, the fracture propagation behavior in Case 4 is also different from Case 2. It shows (turning + diverting) behavior instead of (bypassing + turning) behavior. In this case, since the tip of the HF shows a circular or elliptic shape, the middle part of the HF propagates faster than the upper and lower parts. When the upper part and lower quarter part of the HF just reach the NF, as shown in Fig. 5.35, a certain amount of water has already moved into the NF and this increase in pore pressure and resulting stress interference prevents the crossing of the NF by the HF. This case suggests that the position of the NF also affects the interaction between the HF and NF. A NF located in the center of pay-zone is more likely to cause HF turning.

In Case 5, the NF has the same shear and tensile strength as Case 3 but the NF fills the lower one-third of the pay-zone. All the other settings except NF height are the same as Case 3. In this case, as shown in Fig. 5.36, the HF bypasses the NF though the tensile strength multiplier is as low as Case 3. The main reason for the bypassing is that the middle part of the HF crosses the NF before the lower part of the HF hits the NF. In addition, even if the NF opens as easily as Case 3, a relatively small amount of water can move into the NF than Case 3 due to the smaller height of the NF, which allows more water / energy to be used for straight fracture propagation.

Table 5.6 Simulation parameters for 3-D fracture propagation cases.

Parameter	Value
Dimension of the 3D domain in X direction L_x (cm)	160.0
Dimension of the 3D domain in Y direction L_y (cm)	160.0
Dimension of the 3D domain in Y direction L_z (cm)	68.0
Boundary stress in x direction $\mathcal{T}_x$ (MPa)	41.0
Boundary stress in y direction $\mathcal{T}_y$ (MPa)	40.0
Boundary stress in y direction $\mathcal{T}_z$ (MPa)	60.0
Young's modulus of the domain (MPa)	30.0
Shear modulus of the domain (MPa)	12.0
Initial pore pressure p_0 (MPa)	30.0
Injection rate (kg/s)	0.003
Fracturing fluid viscosity (cp)	1.0
Medium permeability (nD)	10.0
Critical damage (%)	25.0
Number of elements	80*80*34
Horizon size (= $\frac{\delta}{\Delta x}$)	2.0

Table 5.7 Case settings.

Case	Approaching angle (degree)	Shear failure coefficient	Cohesion (MPa)	tensile strength multiplier	Natural fracture height (cm)
Case1	60.0	0.5	0.0	0.5	60.0 (z=4 – 64 cm)
Case2	60.0	0.5	0.0	0.5	30.0 (z=34 – 64 cm)
Case3	60.0	0.5	0.0	0.0	30.0 (z=34 – 64 cm)
Case4	60.0	0.5	0.0	0.5	30.0 (Z=19 – 49 cm)
Case5	60.0	0.5	0.0	0.0	20.0 (Z=44 – 64 cm)

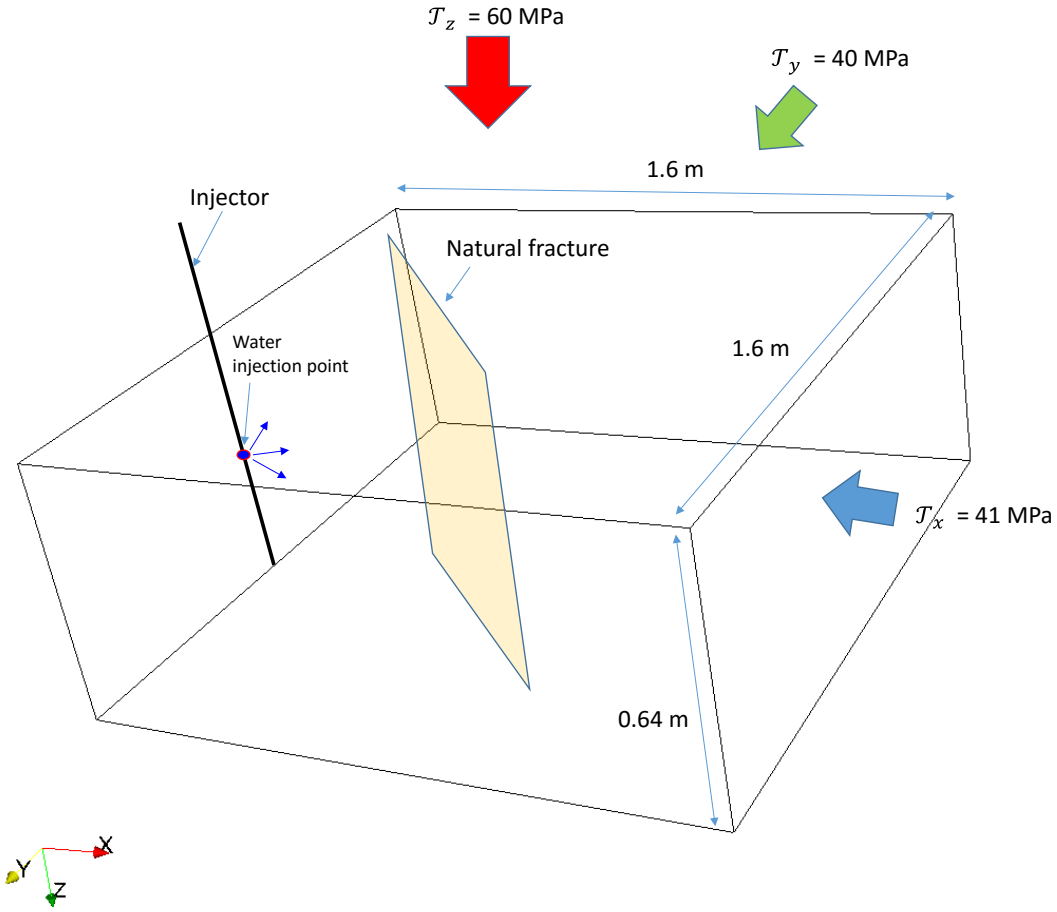

Fig. 5.29 Model description for 3-D interaction problem between HF and NF.

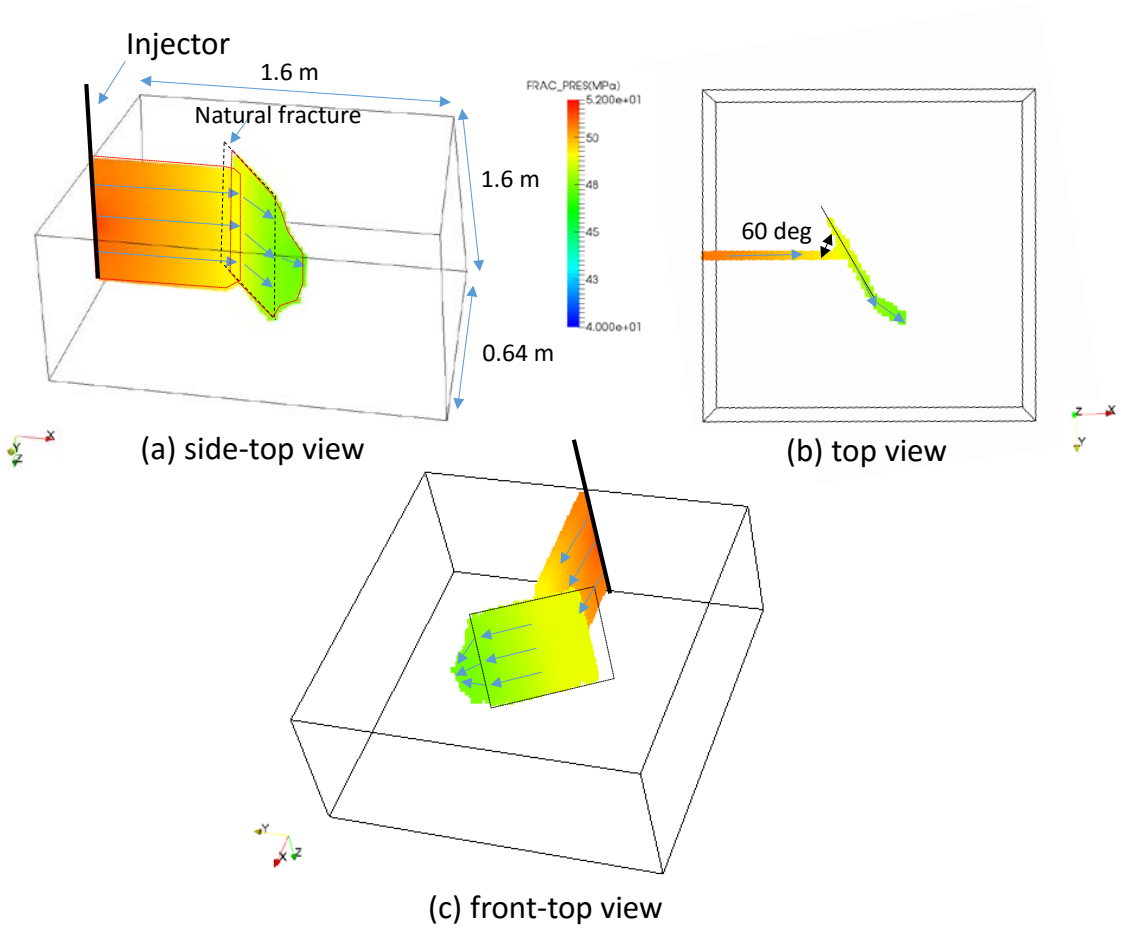

Fig. 5.30 Fracturing fluid pressure distribution (Case1, after 26 sec).

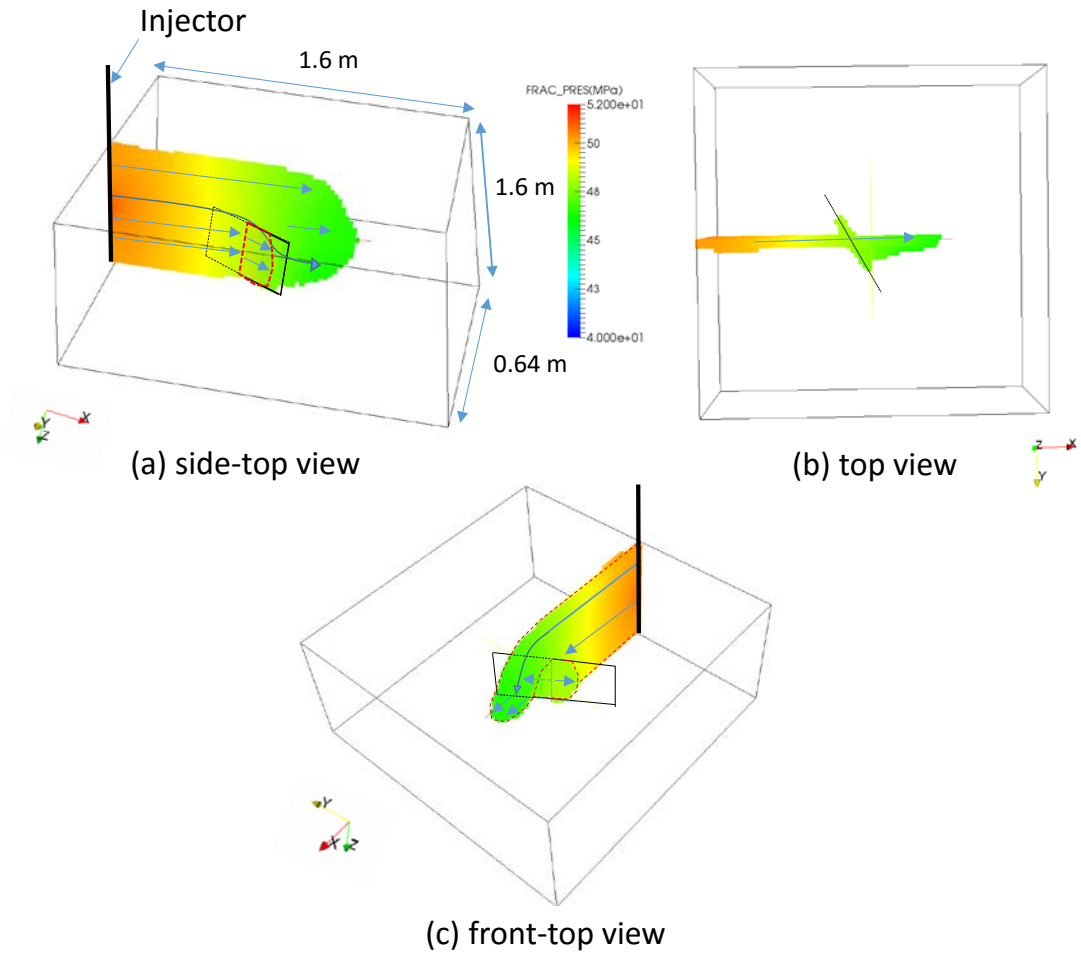

Fig. 5.31 Fracturing fluid pressure distribution (Case 2, after 26 sec).

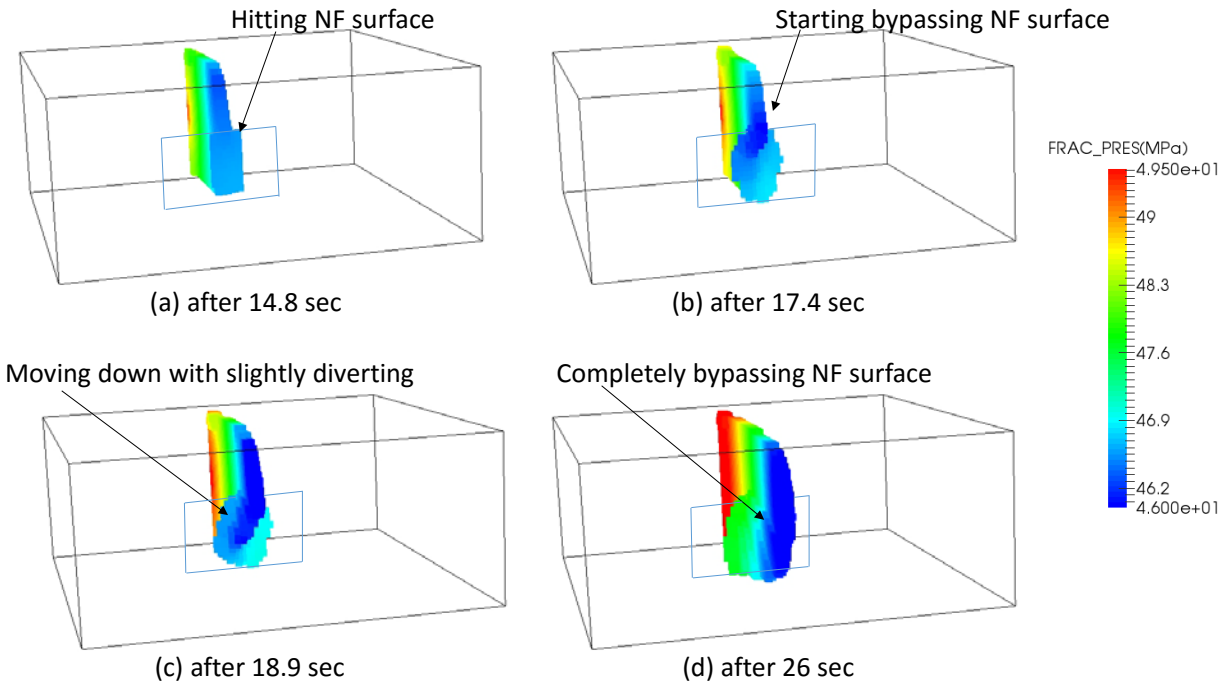

Fig. 5.32 Fracture bypassing (Case 2).

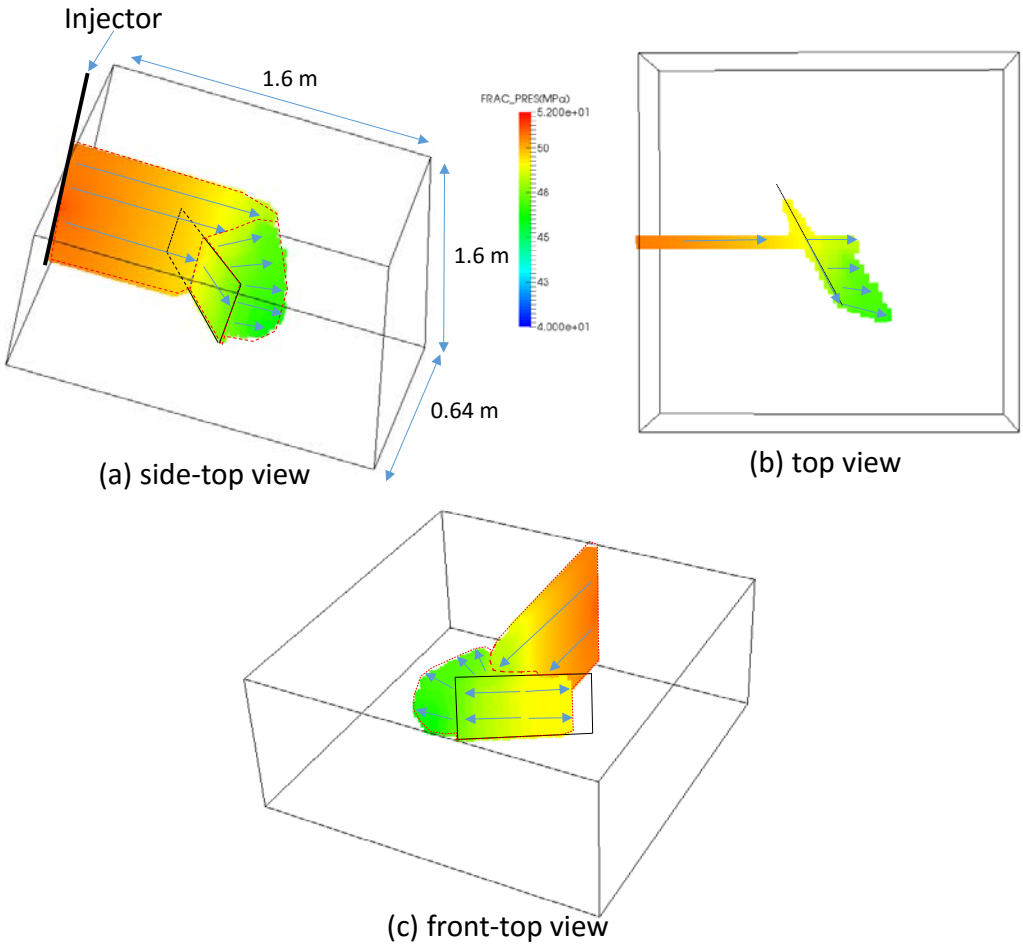

Fig. 5.33 Fracturing fluid pressure distribution (Case 3, after 26 sec).

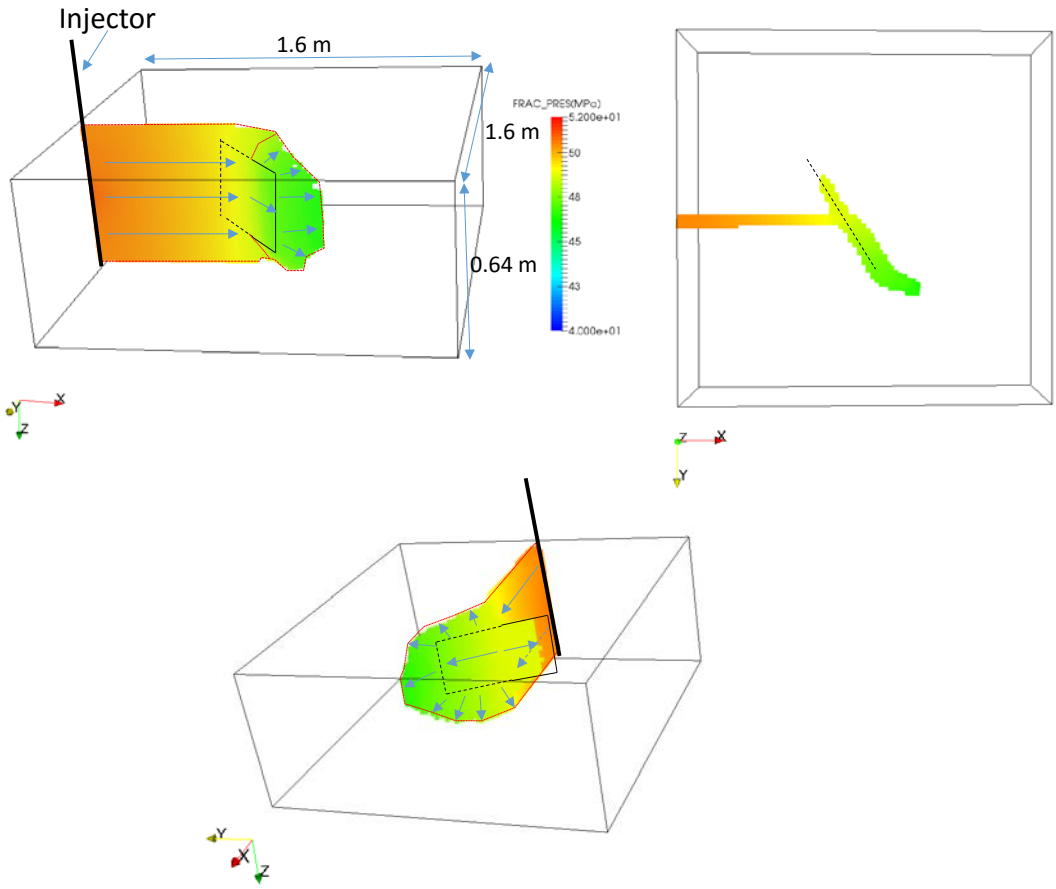

Fig. 5.34 Fracturing fluid pressure distribution (Case 4, after 26 sec).

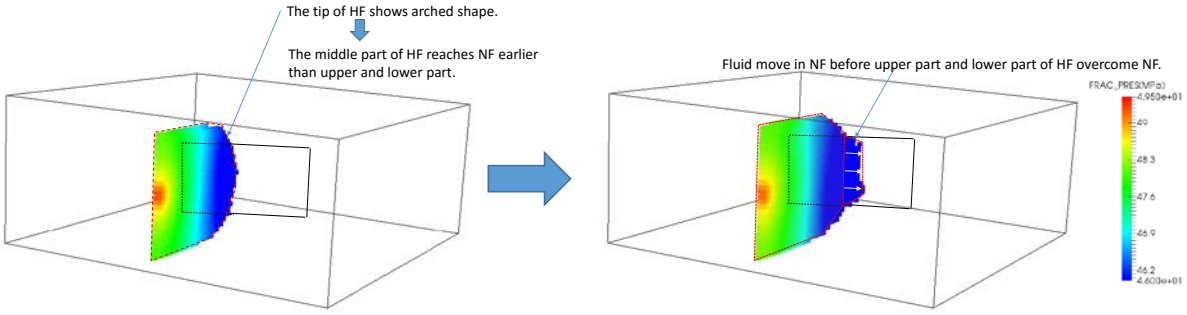

Fig. 5.35 Investigation of fracture propagation behavior in Case 4.

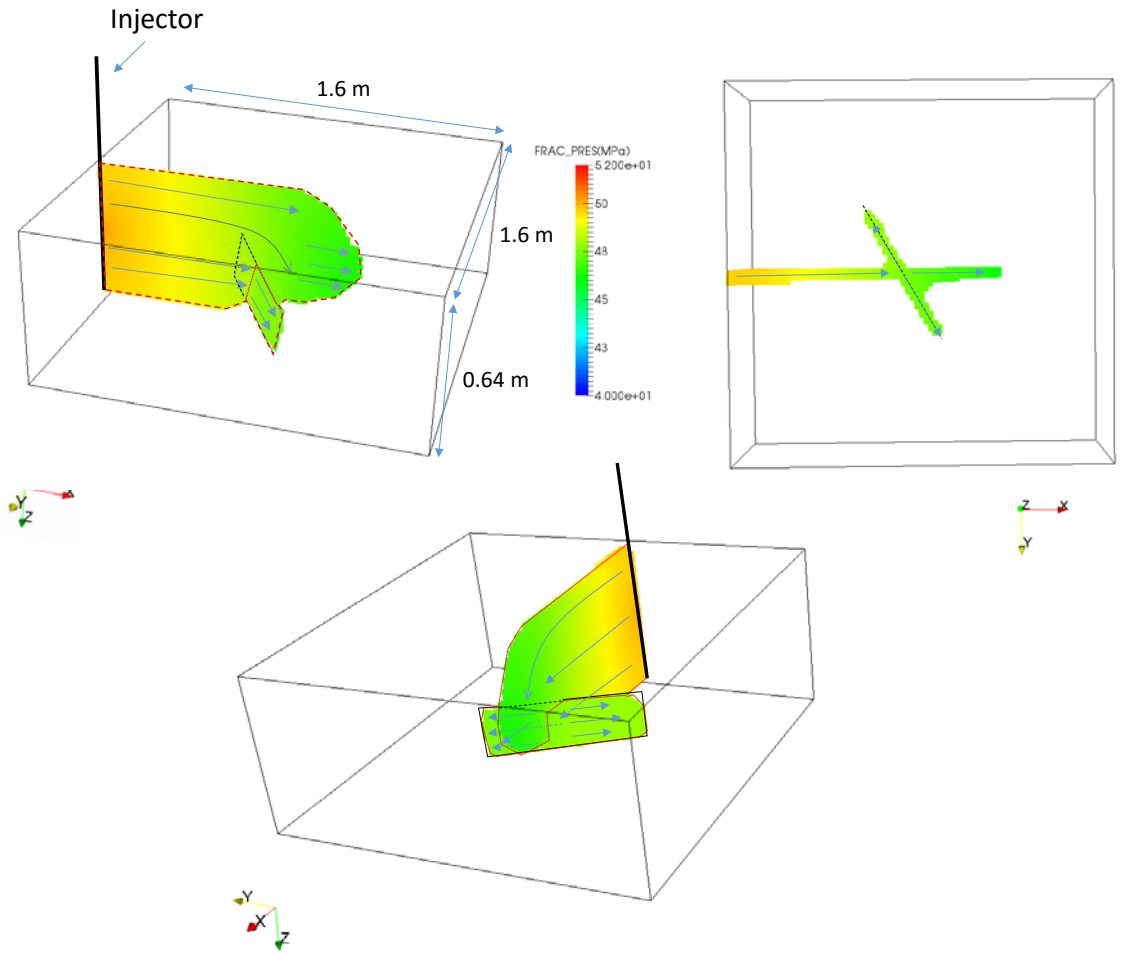

Fig. 5.36 Fracturing flFig_name 1uid pressure distribution (Case 5, after 26 sec).

5.7 Conclusion

Since peridynamics theory has been mainly developed for tensile or unloading conditions, the definition of pre-existing cracks under compressional conditions was not established. In this chapter, we introduce the preliminary definition of pre-existing cracks under compressional conditions, which consists of a preliminary contact model and two different failure criteria (tensile failure criterion and shear failure criterion), into our peridynamics based hydraulic fracturing model in order to simulate the interaction between a HF and a NF. To demonstrate the capability of our model to predict the results of interaction between a HF and a NF, the simulation results are compared with the analytical solution of a one-dimensional compression test and with large block experiments conducted with simulated natural fractures. A sensitivity analysis is conducted by changing the rock mechanical properties, rock permeability, natural fracture permeability, and injection rate to examine the key controlling parameters. We show that poroelastic effects have a large influence on the interaction between HF and NF if leak-off is high. In addition, we also demonstrated that the fracture toughness of the rock, the fracture toughness of the natural fracture, and the shear failure criteria of the natural fracture affect the interaction between HF and NF. In addition, the principal stress contrast and the approach angle have a first order effect. These results are consistent with published experiments. Furthermore, we have demonstrated our simulator's applicability to simulate field scale hydraulic fracturing simulations. Simulation results are presented for the growth of multiple fractures, while taking into account the mechanical stress shadow and pore pressure effects created by the growing fractures. Finally, through three dimensional simulations, we also demonstrate that our peridynamics based hydraulic fracturing model can capture the complicated three dimensional interaction behavior between a HF and a NF shown by

Bahorich et al. [102] (bypassing + turning, and turning + diverting). These simulation results reveal that the height of the NF, the position of the NF, and the opening resistance of the NF have a huge impact on the three-dimensional interaction behavior between a HF and a NF.

CHAPTER6: INVESTIGATION OF THE EFFECT OF RESERVOIR HETEROGENEITY ON FRACTURE PROPAGATION

6.1 Introduction

Shale gas/oil reservoirs inherently contain heterogeneities at multiple length scales [103, 104]. Examples of this include micrometer scale heterogeneities at the grain scale, and meter scale heterogeneities such as bedding planes [105, 106]. All of them may influence hydraulic fracture propagation. However, the effect of these heterogeneities on fracture propagation have not been fully investigated. The effect of layer-scale heterogeneity on fracture propagation was investigated by several authors [107-109]. They studied the effect of such layering on width growth of planar fractures. However, contrasts in mechanical properties and weak interfaces between different layers, not only affects the width of planar fractures, but can also cause complicated fracture propagation. As Fisher et al. [110] point out, fractures can show complicated behavior such as “bending”, “kinking”, and “offsetting” at layer interfaces. When these phenomena occur, fracture height growth is limited when compared with a planar fracture due to the narrower fracture width at the fracture turning point. Moreover, this could cause proppant bridging or screen out [110]. Therefore, understanding the mechanism of fracture propagation near layer interfaces is important from the view point of fracture design. A few authors have tried to investigate such complicated fracture propagation behavior near layer interfaces. Based on an energy analysis and comparisons with experimental results, Wu et al. [111] have shown that hydraulic fractures can turn (bend), kink, and be arrested at the layer boundary when fractures go from a softer layer to a harder layer. Zhang et al. [112] have demonstrated that the magnitude of far field stress acting on a layer interface and the frictional strength of a

layer interface mainly affect the fracture turning along the layer interface. Garcia et al. [113] have shown that the contrast in fracture toughness could also cause different types of complicated fracture propagation behavior ("turning", "kinking", and "offsetting") near the layer interface. However, a comprehensive study of fracture propagation near a layer interface for multi-layered rocks has not been conducted yet. Part of the reason for this has been the inability of past models to simulate fracture propagation without prescribing the fracture propagation direction. Allowing the fracture to propagate in any direction is essential to simulating fracture complexity in heterogeneous rocks.

In order to investigate the effect of vertical heterogeneity on fracture propagation at different scales, we simulate the fracture propagation behavior by using two dimensional models at different scales, in this chapter. In Section 6.2, we systematically investigate how the four types of phenomena ("crossing", "turning (bending)" "kinking", and "branching") take place near the layer interface depending on the contrast in the mechanical properties and layer dip angle by using a two dimensional two layer model. In the subsequent Section (6.3), we analyze how fracture propagation is affected by the relative difference in the mechanical properties near the two different tips of the fracture by using a three-layer, two-dimensional model. In Section 6.4, we investigate the effect of smaller scale, sub-layer heterogeneity on fracture propagation by using a two dimensional sequential-pattern multi-layer model. Finally, in Section 6.5, we investigate how the fracture propagates in a micro-scale domain which is filled with heterogeneities of mechanical properties due to the existence of different mineral grains by using two-dimensional models which are constructed based on an actual micro-scale image of the sample (thin sections or SEM images).

6.2 Investigation of fracture propagation behavior near a layer boundary

6.2.1 MODEL CONSTRUCTION

To investigate the effect of mechanical property contrast and layer dip angle on fracture propagation near a layer boundary, as shown in Fig. 6.1, we constructed a two layer model and conducted a comprehensive parametric study of the model. The model domain (30 cm$\times$15 cm) is divided into 150 x 75 elements. The upper two-thirds of the domain (10 cm from the top) is assigned to Layer 1 and the lower one-third of the domain (5cm from the bottom) is assigned to Layer 2. For fluid flow calculations, a no-flow boundary condition is applied to every boundary (top, bottom, left side, and right side). For mechanical calculations, a normal stress of magnitude σ_V is applied as a maximum principal stress at the top boundary, and a normal stresses of magnitude σ_{H1} (horizontal stress for layer 1) and σ_{H2} (horizontal stress for layer 2) are applied to Layer 1 and Layer 2 respectively. Note that to avoid stress concentration near the layer interface due to different strains in the two different layers, the same stress condition as the far field stresses mentioned above are directly assigned to each element as a background force vector (in the same manner as explained in Section 4.2.2.5). As shown in Fig. 6.1, to simulate fracture propagation, a water injection point is set as "dual injection point" at the bottom of the model and no vertical displacement is allowed at the bottom boundary so that the boundary can only deform in the horizontal direction. By changing the mechanical properties, horizontal stress, and layer dip angle, we investigated the fracture propagation behavior near the layer interface. The parameters we changed in this section are summarized in Table 6.1. Calculation settings are summarized in Table 6.2.

Table 6.1 Parameter list for 2-layer model.

Parameters	Variation
Young's modulus in layer 1 (GPa)	10, 20, 40, 80
Young's modulus in layer 2 (GPa)	10, 20, 40, 80
Fracture toughness in layer 1 (MPa m0.5)	0.25, 0.5, 1.0, 1.4, 2.0, 2.5, 3.0, 5.0
Fracture toughness in layer 2 (MPa m0.5)	0.25, 0.5
Layer dip angle (degree)	0, 15, 30
Vertical stress (MPa)	41, 47, 50, 60
Horizontal stress in layer 1 (MPa)	40, 45, 50

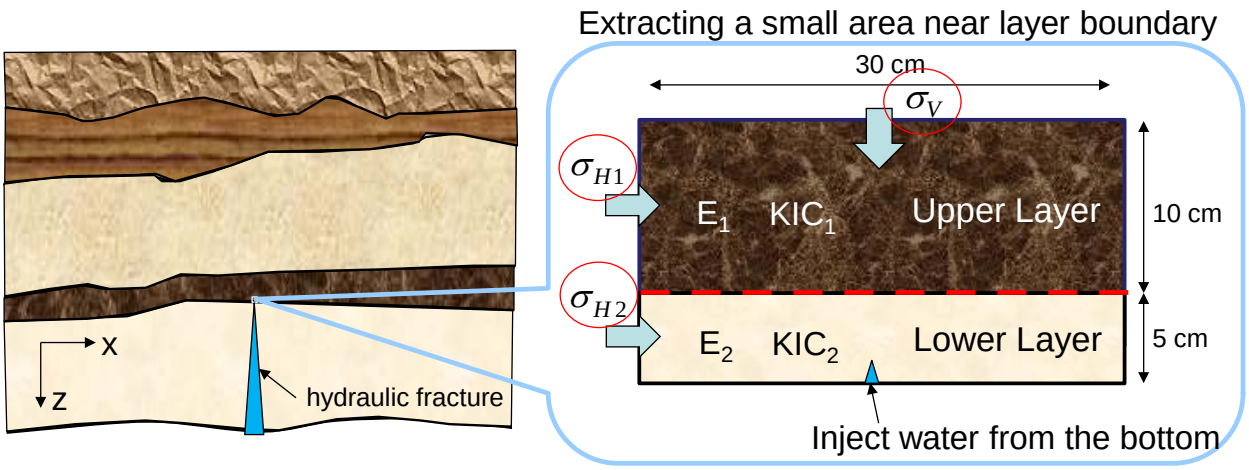

Fig. 6.1 Schematic view of the 2 layer model.

Table 6.2 Calculation settings.

Parameter	Value
Dimension in horizontal direction L_x (cm)	30.0
Dimension in vertical direction L_y (cm)	15.0
Layer 1 thickness (cm)	10.0
Layer 2 thickness (cm)	5.0
Boundary stress in vertical direction σ_V (MPa)	Table 6.1
Boundary stress in layer 1 in horizontal direction σ_{H1} (MPa)	Table 6.1
Boundary stress in layer 2 in horizontal direction σ_{H2} (MPa)	40.0
Young's modulus in layer 1	Table 6.1
Young's modulus in layer 2	Table 6.1
Poisson's ratio	0.25
Initial pore pressure (MPa)	30.0
Injection rate (kg/s)	0.005
Fracturing fluid viscosity (cp)	1.0
Medium permeability (mD)	0.00001
Number of elements	150×75
Horizon size ($=\frac{\delta}{\Delta x}$)	3.0

6.2.2 EFFECT OF YOUNG'S MODULUS, FRACTURE TOUGHNESS, AND HORIZONTAL/VERTICAL STRESS CONTRAST

In this section, we investigated the effect of Young's modulus, fracture toughness contrast, and horizontal/vertical stress difference, which are considered to have primary influence on fracture propagation near the layer interface based on previous studies [111-113]. All other properties are fixed as shown in Table 6.3. The results in these cases are summarized in Fig. 6.2, Fig. 6.3, and Fig. 6.4. Different fracture propagation patterns are observed by changing the stress contrast ($=\sigma_V - \sigma_H$ plotted on the x axis) and fracture toughness of the first layer (plotted on the y axis).

Table 6.3 List of fixed and changed parameters.

Parameters	Condition	Variation
Young's modulus in layer 1 (GPa)	Changed	10, 20, 40, 80
Young's modulus in layer 2 (GPa)	Changed	10, 40, 80
Fracture toughness in layer 1 (MPa $m^{0.5}$)	Changed	0.25, 0.5, 1.0, 1.4, 2.0, 2.5, 3.0, 5.0
Fracture toughness in layer 2 (MPa $m^{0.5}$)	Fixed	0.5
Layer dip angle (degree)	Fixed	0
Vertical stress (MPa)	Changed	41, 47, 50, 60
Horizontal stress in layer 1 (MPa)	Fixed	40
Medium permeability (mD)	Fixed	0.00001

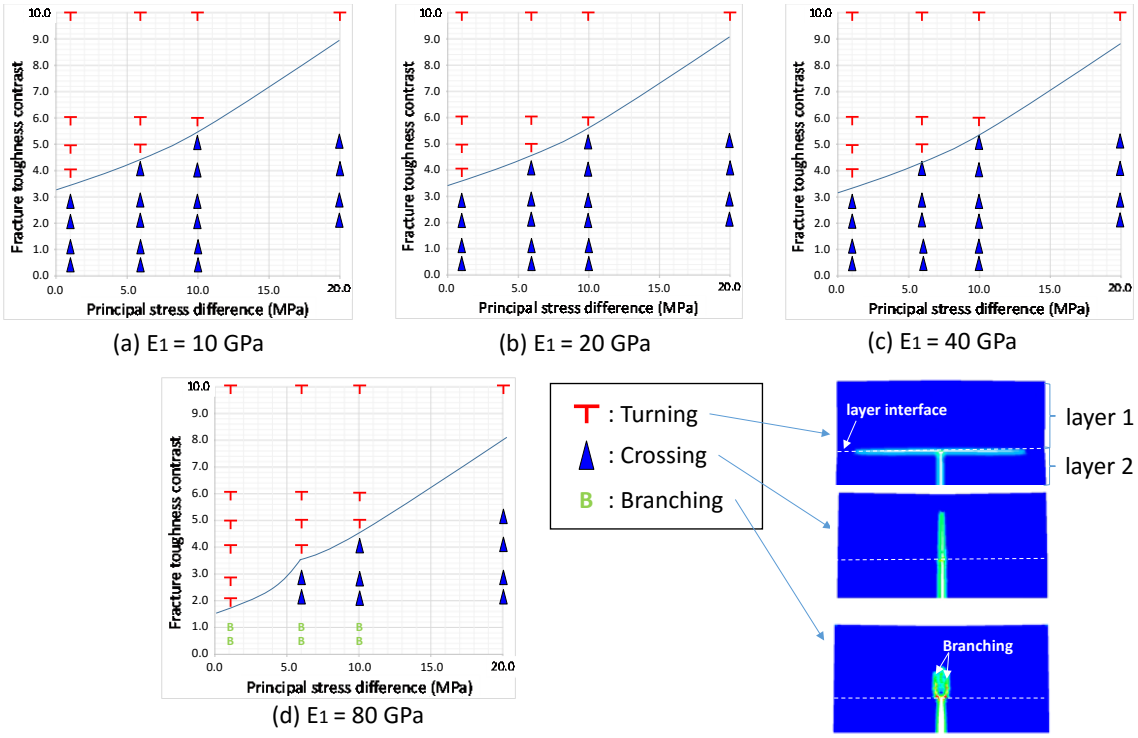

Fig. 6.2 Fracture turning behavior (E_2=10 GPa).

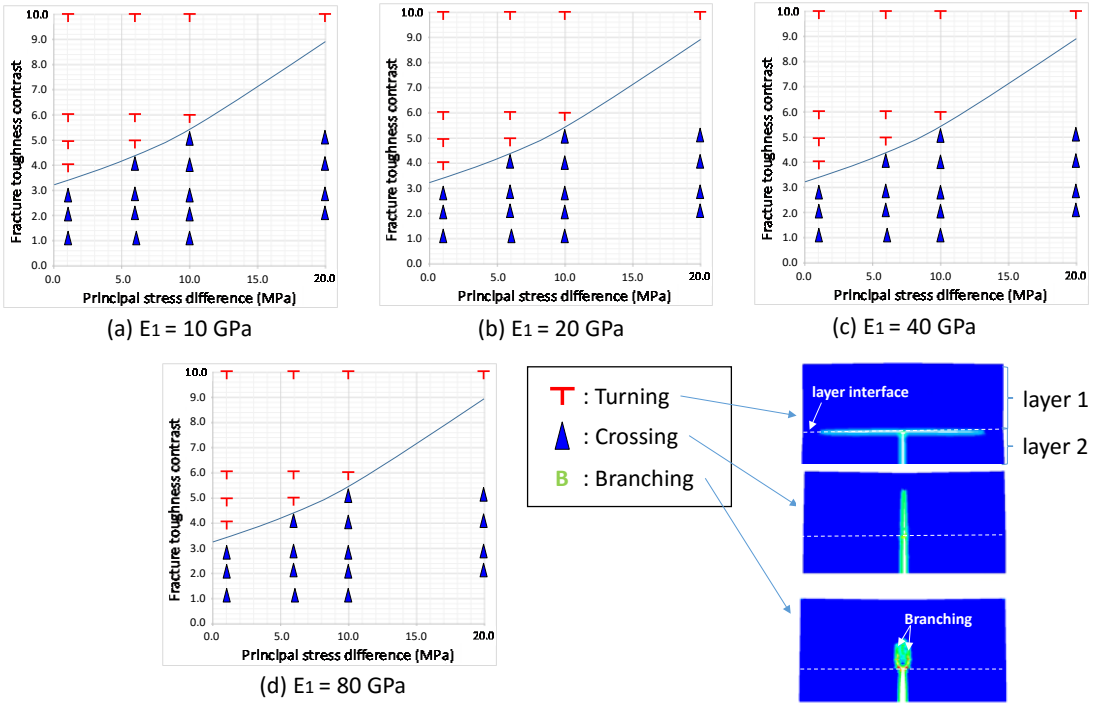

Fig. 6.3 Fracture turning behavior (E_2=40 GPa).

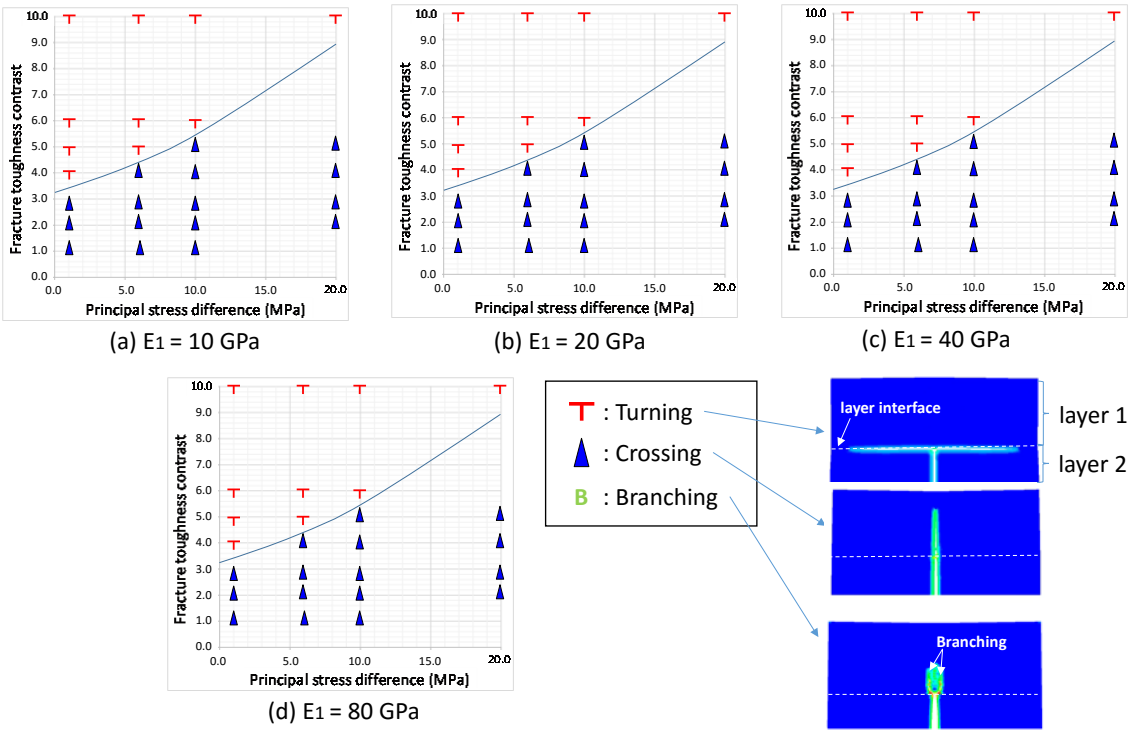

Fig. 6.4 Fracture turning behavior (E_2=80 GPa).

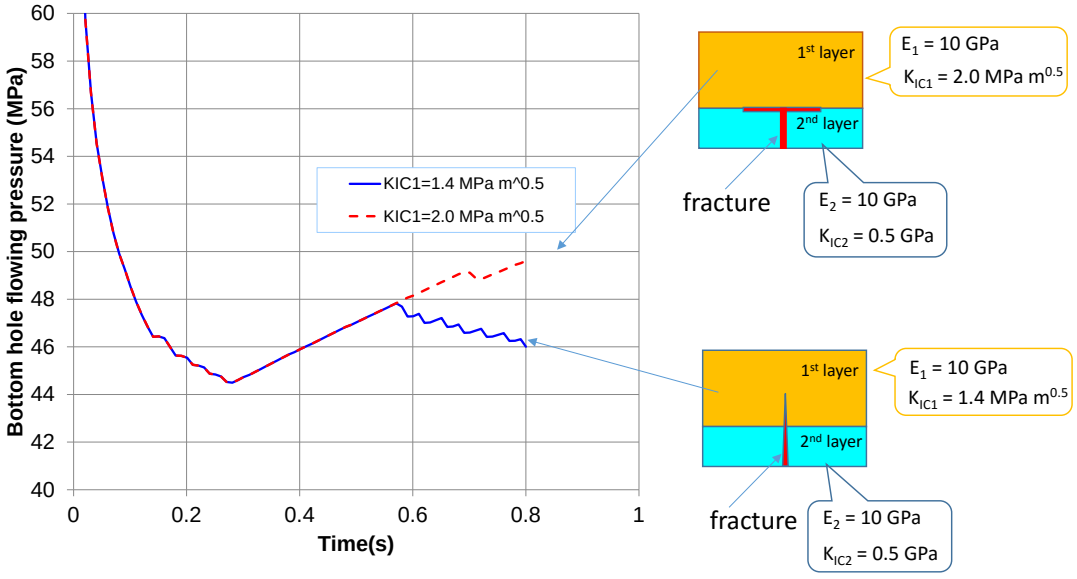

Fig. 6.5 Bottomhole pressure change with time (E2 = 10GPa, principal stress difference = 1 MPa).

6.2.2.1 Basic fracture propagation behavior (crossing, turning, and Branching)

As shown in Fig. 6.2 – Fig. 6.4, three types of fracture propagation behavior near the layer interface are observed: “crossing”, “turning”, and “branching”. We first explain the mechanism leading to these behaviors based the results of some specific cases before discussing the effect of fracture toughness, principal stress difference, and Young’s modulus contrast.

Crossing and turning

As shown in Fig. 6.2 (a), if the Young’s modulus of the first layer and the principal stress difference are fixed as 10 GPa, and 1 MPa respectively, the fracture passes through the layer interface in the case where fracture toughness of the first layer (K_{IC1}) is less than 1.41 MPa $m^{0.5}$ (we call this case the “crossing” case). The fracture turns along the layer interface in the case where the fracture toughness in Layer 1 is higher than 2.0 MPa $m^{0.5}$ (we call this case the “turning” case). Fig. 6.5 shows the bottom-hole pressure (BHP) as it changes with time in these cases. As shown in Fig. 6.5, at the early stage ($t < 0.27$ sec), BHP decreases with time in both cases due to the fracture volume expansion. Then, from ($0.27 \text{ sec} <= t < 0.5 \text{ sec}$), the BHP begins to increase in both cases since the fracture propagation stops at the layer interface due to the higher energy requirement for breaking bonds in the first layer compared to the second layer. During this time, the fracture width continues to increase. As shown in Fig. 6.6, the fracture width expansion causes the bonds to stretch both in the horizontal direction in Layer 1 and in the bonds across the layer interface between Layer 1 and Layer2. If the horizontal bonds in Layer1 shown in Fig. 6.6 break sooner than the bonds across the layer interface, the fracture crosses the layer interface. Conversely, if all the bonds across the layer interface break sooner than the

horizontal bonds in Layer1 due to a shear like displacement along the layer interface, the fracture turns along the layer interface.

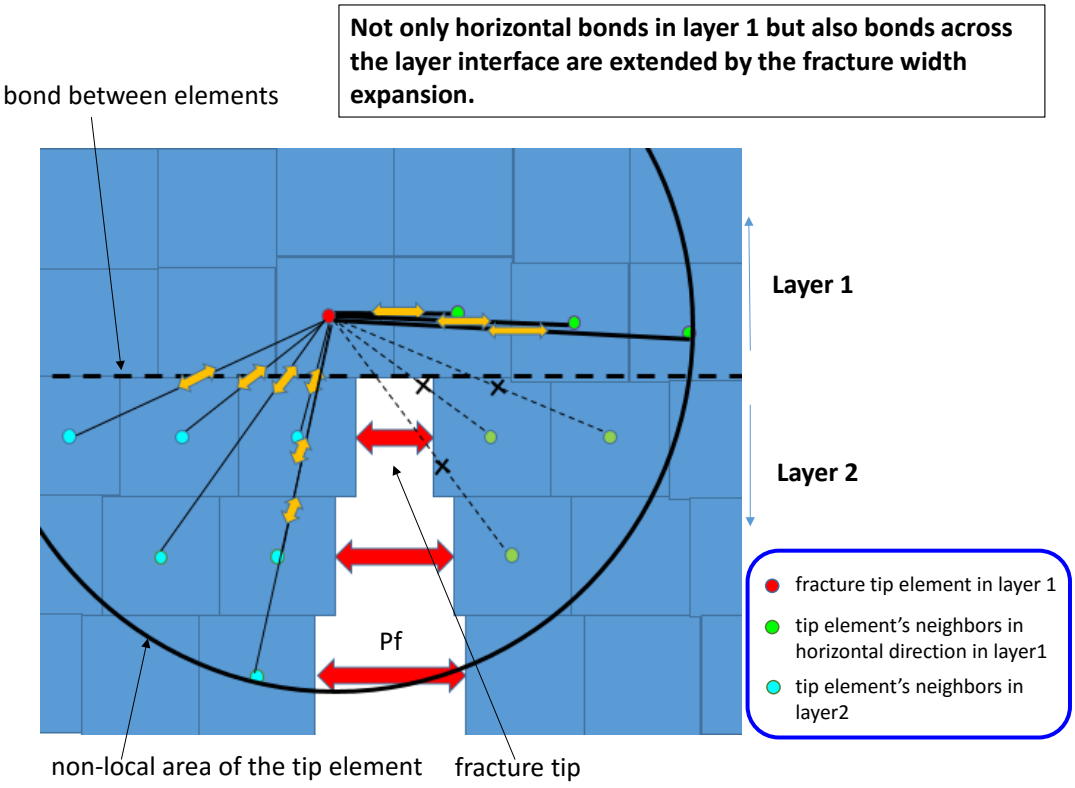

Fig. 6.6 Schematic view of bond extension near layer interface.

Fig. 6.7 and Fig. 6.8 show the normalized stored energy density (= stored energy density of a bond / critical energy density of a bond) in the bonds which connect to the fracture tip element in the "crossing" case and the "turning" case respectively. In these figures, the normalized stored energy density of the bonds between the neighbor elements and the fracture tip element are color coded. For example, if the element color in the figure is blue, it means that energy is not stored in the bond between the element and the fracture tip element. On the other hand, if the element color in the figure is red, it means that the stored energy density of the bond between the element and the fracture tip element reaches

the critical energy density and the bond is broken. As shown in Fig. 6.7 (b), not only horizontal bonds in Layer 1 but also more than half of the bonds across the layer interface are broken even in the "crossing" case (K_{IC1} = 1.4 MPa $m^{0.5}$). Hence, in the "turning" case which has higher fracture toughness in the layer 1 (K_{IC1} = 2.0 MPa $m^{0.5}$) where the critical energy density in bonds in Layer 1 are twice as much as the "crossing" case, all the bonds across the layer interface break before the horizontal bonds in the first layer break, which results in the fracture turning along the layer interface.

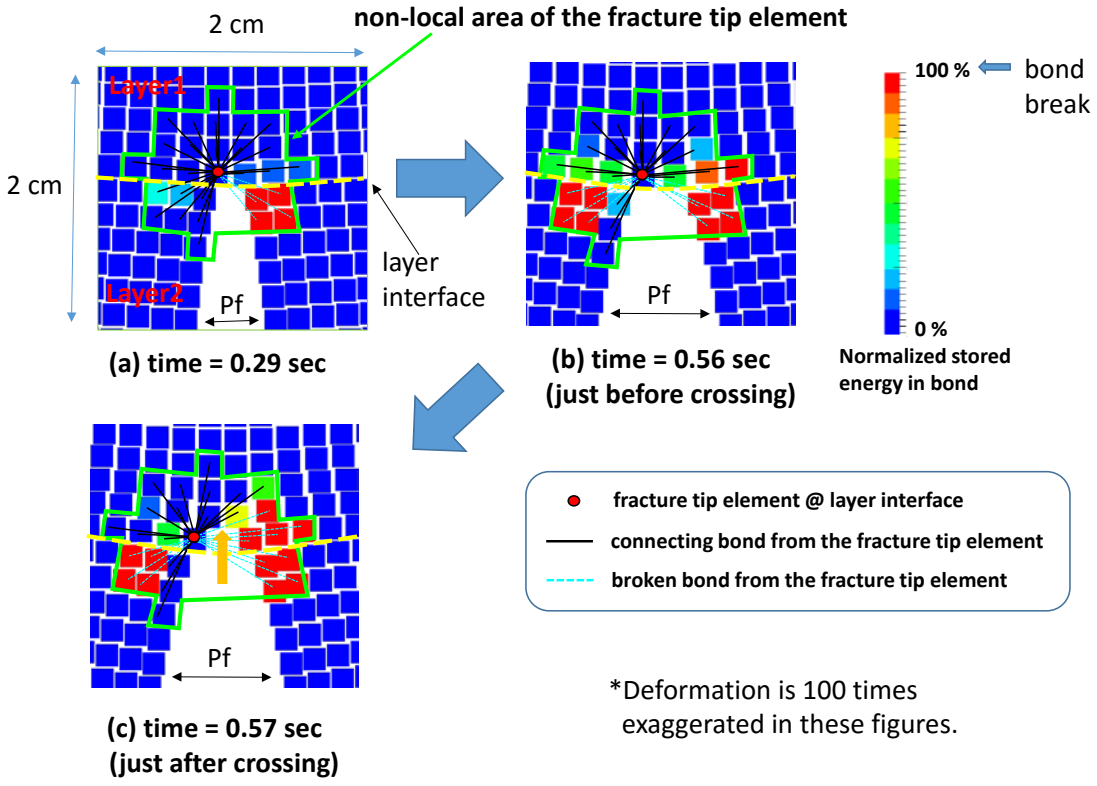

Fig. 6.7 Normalized stored energy density change in bonds at the fracture tip elements ("crossing" case: KIC = 1.4 MPa $m^{0.5}$).

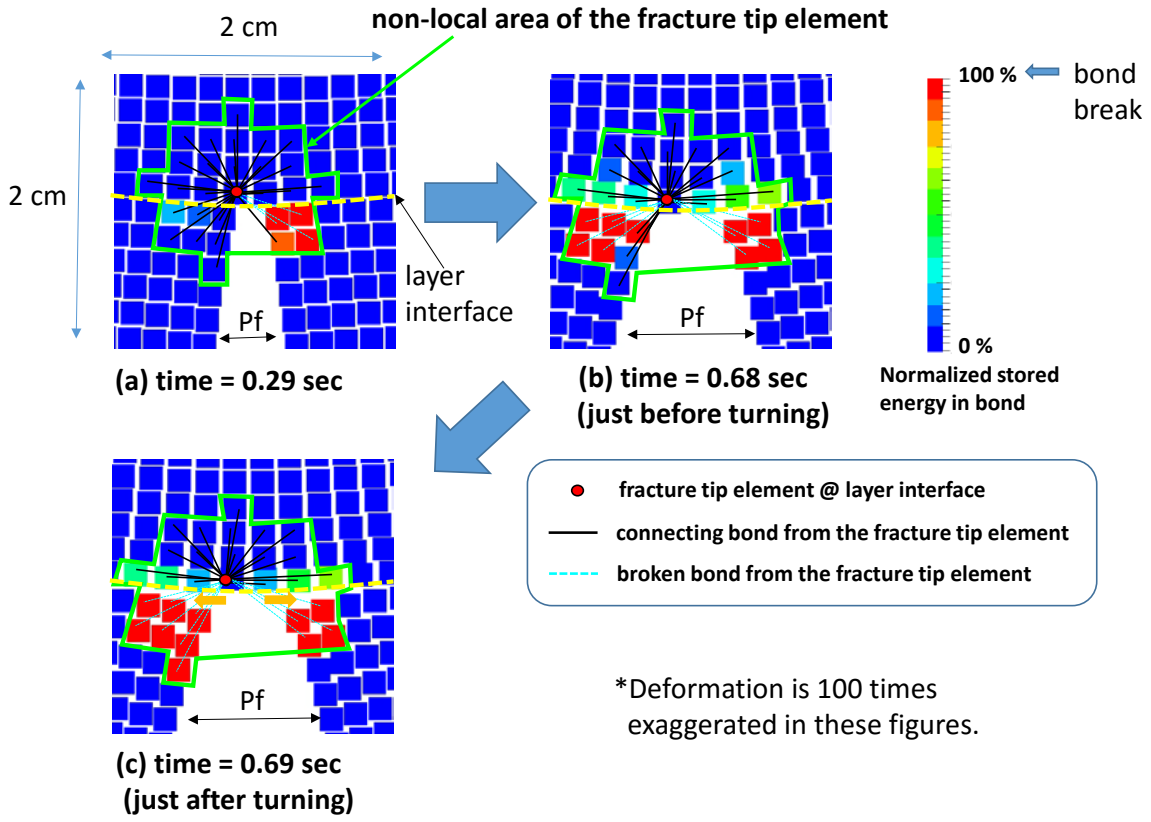

Fig. 6.8 Normalized stored energy density change in bonds of the fracture tip elements at the fracture tip elements ("turning" case: KIC = 2.0 MPa $m^{0.5}$).

These results show that fracture turning along the layer interface is mainly controlled by the contrast of the energy release rate between the two layers since the critical energy density of the bonds are calculated based on the energy release rate and the critical energy density of the bonds across the layer interface are calculated based on the lower energy release rate of the two layers (in this case, Layer 2 has the lower energy release rate). Note that we assume 2-D plane strain condition in these simulations. Therefore, under a constant injection rate condition, the fracture must select crossing or turning along the layer interface due to BHP increase. However, in 3-D, since the fracture can propagate in the third direction (in other words, the fracture can propagate in the weakest direction in three dimensions), the BHP does not increase as rapidly as in the 2-D cases. In such cases,

fracture “arresting” may occur instead of “turning” along the layer interface for most of the “turning” cases in the 2-D simulations.

Branching

As shown in Fig. 6.2 (d), our results show that if the following conditions are satisfied, the fracture branches at the layer interface (first turns along the layer interface and then quickly move into the first layer).

- Fracture propagates from the low Young’s modulus layer to the high Young’s modulus layer
- Young’s modulus contrast between the two layers is high ($E_1 / E_2 \geq 8.0$).
- Fracture toughness contrast is less than 1.0 ($K_{IC1} / K_{IC2} <= 1.0$).

In essence, if the upper layer material is very brittle (High Young’s modulus and Low Fracture toughness), fracture branching will occur. Fig. 6.9 shows the damage distribution near the fracture tip in the branching case where the Young’s modulus contrast, fracture toughness contrast, and principal stress difference are 8 (E_1/E_2= 80GPa/10GPa), 1.0 (=0.5 MPa $m^{0.5}$/0.5 MPa $m^{0.5}$), and 1.0 MPa respectively. As shown in Fig. 6.9, if Layer 1 is much more brittle than Layer 2 as mentioned above, the damage zone begins to grow before the fracture tip reaches the layer interface due to the much smaller energy requirement for the bond breakage in Layer 1 than for Layer2. In this case, the energy required for breaking bonds in Layer 1 is just 12.5 % of the energy required to break bonds in Layer 2. Hence, even small deformations, induced by the fracture propagation in Layer2, which do not break bonds in Layer 2 can break the bonds near the layer interface and in Layer 1. As shown in Fig. 6.9 (c), since Layer 1 has already been damaged when the fracture reaches

the layer interface, the fracture continues to propagate through the pre-damaged zone in Layer 1. Note that the fracture perfectly branches in this example case due to the perfect symmetry of the mechanical properties in front of the fracture tip. However, for most cases, the mechanical properties in front of the fracture tip are not fully symmetric at the layer interface. At such cases, fracture "kinking" may occur (in other words, one side of the branches may grow) instead of "branching" since the fracture always propagates through the weakest path (the easiest open path).

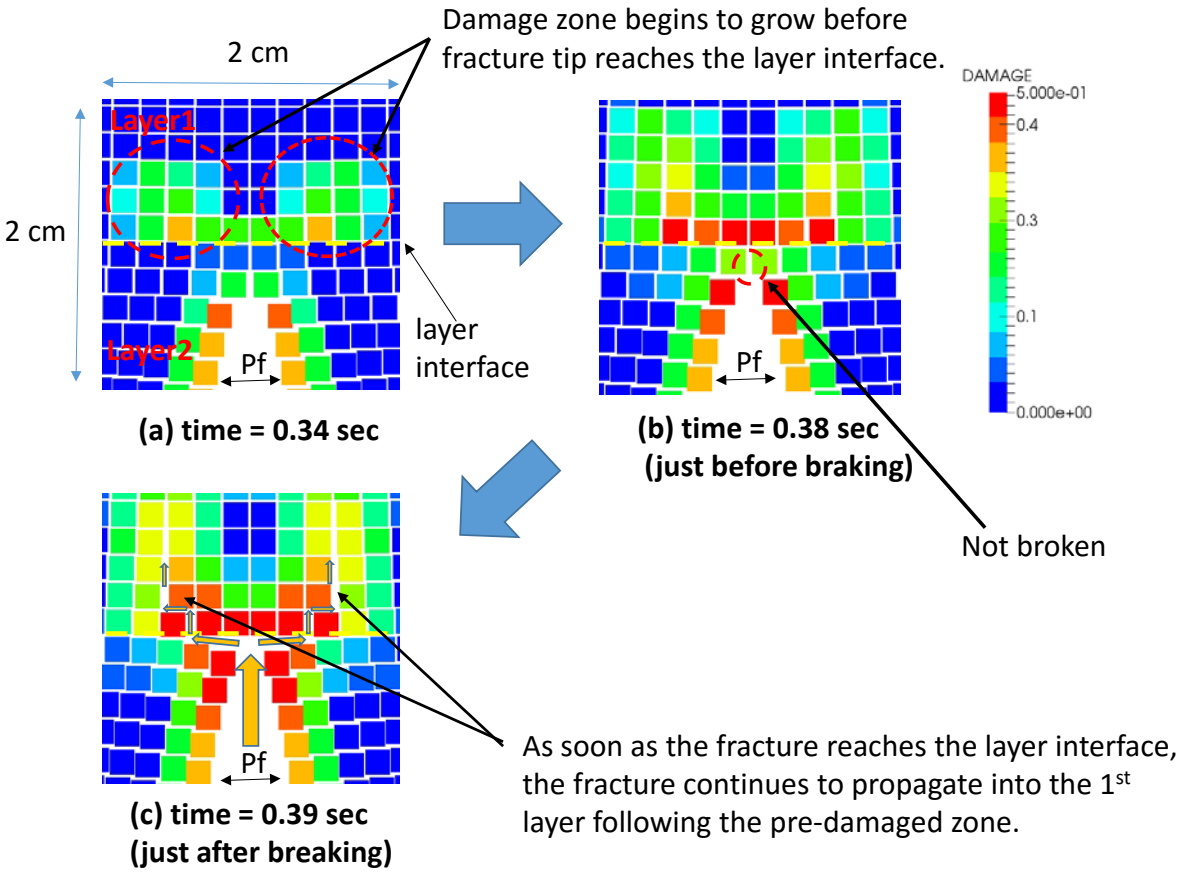

Fig. 6.9 Damage distribution change near the fracture tip ("branching" case).

6.2.2.2 Effect of fracture toughness and principal stress difference

As shown in Fig. 6.2 – Fig. 6.4, fracture propagation is mainly affected by the principal stress difference between vertical and horizontal stresses, and the toughness contrast between the two layers. A hydraulic fracture is more likely to turn along the layer interface for lower principal stress difference and higher fracture toughness contrast. A two to four times fracture toughness contrast ($K_{IC1} / K_{IC2} > 2 \sim 4$) is necessary for the fracture to turn under a low principal stress difference condition ($\Delta\sigma < 1.0\,MPa$), while about eight to ten times fracture toughness contrast is necessary for a high principal stress difference condition ($\Delta\sigma \simeq 20\,MPa$). Since the published values of fracture toughness range is $0.2 \sim 3.0\ MPa\sqrt{m}$ [108, 114, 115], the possible fracture toughness contrast is less than fifteen even in extreme cases. This suggests that fracture turning along a layer interface is unlikely to occur especially in deep reservoirs. This is consistent with field observations by tiltmeter surveys. Almost no horizontal fracture propagation is observed deeper than 4000 ft, whereas a horizontal fracture component begins to appear in measurements made for fractures shallower than 4000 ft, as reported by Fisher et al. [110]. In our model the tendencies related to toughness contrast and principal stress difference are explained by using the formulation for the critical displacement $\|\boldsymbol{\eta}_{crit}\|$ (the bond displacement just before the bond breaks). The critical displacement $\|\boldsymbol{\eta}_{crit}\|$ can be analytically estimated as follows.

Critical displacement

As explained in Chapter 2.2.4, each bond breaks when the stored energy density ω_ξ in the bond exceeds the critical energy density ω_c in the bond. If we consider the effect of background force vector state, which is defined in Section 4.2.2.5, the stored energy density and critical energy density in the plane strain condition are written as follows respectively.

$$\omega_{\xi} = \int_0^{\boldsymbol{\eta}\left(t_{final}\right)} \left\{ \underline{T}^{*}_{back}\left[\mathbf{x},t\right]\left\langle \boldsymbol{\xi} \right\rangle - \underline{T}^{*}_{back}\left[\mathbf{x}',t\right]\left\langle -\boldsymbol{\xi} \right\rangle \right\} \bullet d\boldsymbol{\eta} \tag{4.36}$$

$$\omega_c = \frac{9G_c}{4\delta^3} = \frac{9{K_{IC}}^2\left(1-\nu^2\right)}{4\delta^3 E} \tag{2.27}$$

Where,

$$\begin{aligned} &\underline{T}^{*}_{back}\left[\mathbf{x},t\right]\left\langle \boldsymbol{\xi} \right\rangle - \underline{T}^{*}_{back}\left[\mathbf{x}',t\right]\left\langle -\boldsymbol{\xi} \right\rangle \\ &= \max\left\{ \left(\left(\underline{t}\left[\mathbf{x},t\right]\left\langle \boldsymbol{\xi} \right\rangle - \underline{t}\left[\mathbf{x}',t\right]\left\langle -\boldsymbol{\xi} \right\rangle \right) + \left(T_0\left[\mathbf{x}\right]\left\langle \boldsymbol{\xi} \right\rangle - T_0\left[\mathbf{x}'\right]\left\langle -\boldsymbol{\xi} \right\rangle \right) \cdot \frac{\boldsymbol{\xi}+\boldsymbol{\eta}}{\left\|\boldsymbol{\xi}+\boldsymbol{\eta}\right\|} \right), 0.0 \right\} \frac{\boldsymbol{\xi}+\boldsymbol{\eta}}{\left\|\boldsymbol{\xi}+\boldsymbol{\eta}\right\|} \end{aligned} \tag{4.37}$$

$$\underline{t}\left[\mathbf{x},t\right]\left\langle \boldsymbol{\xi} \right\rangle = \frac{2\left(\left(K - \frac{G}{3} \right)\theta - \alpha P \right)}{m} \underline{\omega}\underline{x}\left\langle \boldsymbol{\xi} \right\rangle + \frac{8G}{m} \underline{\omega}\underline{e}^{d}\left\langle \boldsymbol{\xi} \right\rangle \tag{4.4}$$

$$\underline{T}_0\left[\mathbf{x}\right]\left\langle \boldsymbol{\xi} \right\rangle = \underline{\omega}\boldsymbol{\sigma}_{eff}\mathbf{M}^{-1}\boldsymbol{\xi} \tag{4.32}$$

Here, we consider the critical displacement in the horizontal direction under the condition that the element size is one-third of the horizon size. For the further calculation, we assume that the influence function is given as $\underline{\omega} = 1/r$ (default of the simulator, $0 < r \le \delta$), effective stress tensor is given as $\boldsymbol{\sigma}_{eff} = \begin{pmatrix} \sigma_H & 0 \\ 0 & \sigma_V \end{pmatrix}$, Poisson's ratio = 0.25, Biot's coefficient $\alpha = 0.0$, weighted volume m and shape tensor $\mathbf{M}$ are given by the following analytical forms respectively.

$$m = \int_0^{\delta} \int_0^{2\pi} \underline{\omega} r^2 r d\varphi dr = \frac{2\pi\delta^3}{3} \tag{6.1}$$

$$\mathbf{M} = \int_{H_{\mathbf{x}}} \underline{\omega}\boldsymbol{\xi} \otimes \boldsymbol{\xi} dV_{\mathbf{x}'} = \frac{\pi\delta^3}{3} I \tag{6.2}$$

Based on the assumptions above, Equation (4.4), and Equation (4.32) are written as follows respectively.

$$\begin{aligned}
\underline{t}\left[\mathbf{x},t\right]\langle\boldsymbol{\xi}\rangle &= \frac{2\left(\left(K-\frac{G}{3}\right)\theta - \alpha P\right)}{m}\underline{\omega}\underline{x}\langle\boldsymbol{\xi}\rangle + \frac{8G}{m}\underline{\omega}\underline{e}^{d}\langle\boldsymbol{\xi}\rangle \\
&= \frac{2\left(\left(K-\frac{G}{3}\right)\theta\right)}{m}\underline{\omega}\underline{x}\langle\boldsymbol{\xi}\rangle + \frac{8G}{m}\underline{\omega}\left(\underline{e}\langle\boldsymbol{\xi}\rangle - \frac{\theta}{3}\underline{x}\langle\boldsymbol{\xi}\rangle\right) \qquad (\because \alpha = 0.0) \\
&= \left[\frac{\underline{\omega}}{m}\left\{\frac{2}{3}(3K-5G)\theta + 8G\underline{e}\right\}\right] \\
&= \frac{8\underline{\omega}G\underline{e}}{m} \qquad (\because 3K-5G = 0.0 \; if \; \nu = 0.25) \\
&= \frac{8\left(\frac{1}{r}\right)\left(\frac{2}{5}E\right)\left(\|\boldsymbol{\xi}+\boldsymbol{\eta}\| - \|\boldsymbol{\xi}\|\right)}{\left(\frac{2\pi\delta^3}{3}\right)} \\
&= \frac{24E}{5\pi r\delta^3}\left(\|\boldsymbol{\xi}+\boldsymbol{\eta}\| - \|\boldsymbol{\xi}\|\right)
\end{aligned} \tag{6.3}$$

$$\begin{aligned}
\underline{T}_0\left[\mathbf{x}\right]\langle\boldsymbol{\xi}\rangle &= \underline{\omega}\boldsymbol{\sigma}_{eff}\mathbf{M}^{-1}\boldsymbol{\xi} \\
&= \frac{1}{r}\begin{pmatrix}\sigma_H & 0\\ 0 & \sigma_V\end{pmatrix}\frac{3}{\pi\delta^3}\begin{pmatrix}1 & 0\\ 0 & 1\end{pmatrix}\begin{pmatrix}r\\ 0\end{pmatrix} \\
&= \frac{3\sigma_H}{\pi\delta^3}\begin{pmatrix}1\\ 0\end{pmatrix}
\end{aligned} \tag{6.4}$$

By inserting Equation (6.3) and Equation (6.4) into Equation (4.37), we obtain

$$
\begin{aligned}
&\underline{T}^{*}_{back}\left[\mathbf{x},t\right]\langle\boldsymbol{\xi}\rangle-\underline{T}^{*}_{back}\left[\mathbf{x}',t\right]\langle-\boldsymbol{\xi}\rangle\\
&=\max\left\{\left(\left(\underline{t}\left[\mathbf{x},t\right]\langle\boldsymbol{\xi}\rangle-\underline{t}\left[\mathbf{x}',t\right]\langle-\boldsymbol{\xi}\rangle\right)+\left(T_0\left[\mathbf{x}\right]\langle\boldsymbol{\xi}\rangle-T_0\left[\mathbf{x}'\right]\langle-\boldsymbol{\xi}\rangle\right)\cdot\frac{\boldsymbol{\xi}+\boldsymbol{\eta}}{\left\|\boldsymbol{\xi}+\boldsymbol{\eta}\right\|}\right),0.0\right\}\frac{\boldsymbol{\xi}+\boldsymbol{\eta}}{\left\|\boldsymbol{\xi}+\boldsymbol{\eta}\right\|}\\
&=\max\left\{\frac{48E}{5\pi r\delta^3}\left(\left\|\boldsymbol{\xi}+\boldsymbol{\eta}\right\|-\left\|\boldsymbol{\eta}\right\|\right)-\frac{6\sigma_H}{\pi\delta^3},0.0\right\}\frac{\boldsymbol{\xi}+\boldsymbol{\eta}}{\left\|\boldsymbol{\xi}+\boldsymbol{\eta}\right\|}
\end{aligned}
\tag{6.5}
$$

For simplification, if we assume displacement only occurs in the same direction as the original bond direction ($\boldsymbol{\eta}$ is parallel to $\boldsymbol{\xi}$), from Equation (6.5) and Equation (4.36), we have,

$$
\begin{aligned}
\omega_{\boldsymbol{\xi}} &= \int_0^{\boldsymbol{\eta}\left(t_{final}\right)}\left\{\underline{T}^{*}_{back}\left[\mathbf{x},t\right]\langle\boldsymbol{\xi}\rangle-\underline{T}^{*}_{back}\left[\mathbf{x}',t\right]\langle-\boldsymbol{\xi}\rangle\right\}\bullet d\boldsymbol{\eta}\\
&= \int_0^{\boldsymbol{\eta}\left(t_{final}\right)}\max\left\{\frac{48E}{5\pi r\delta^3}\left(\left\|\boldsymbol{\xi}+\boldsymbol{\eta}\right\|-\left\|\boldsymbol{\eta}\right\|\right)-\frac{6\sigma_H}{\pi\delta^3},0.0\right\}\frac{\boldsymbol{\xi}+\boldsymbol{\eta}}{\left\|\boldsymbol{\xi}+\boldsymbol{\eta}\right\|}\bullet d\boldsymbol{\eta}\\
&\approx \int_0^{\left\|\boldsymbol{\eta}\right\|_{final}}\max\left\{\frac{48E}{5\pi r\delta^3}\left\|\boldsymbol{\eta}\right\|-\frac{6\sigma_H}{\pi\delta^3},0.0\right\}d\left\|\boldsymbol{\eta}\right\|\\
&= \int_{\left\|\boldsymbol{\eta}\right\|^{*}}^{\left\|\boldsymbol{\eta}\right\|_{final}}\frac{48E}{5\pi r\delta^3}\left(\left\|\boldsymbol{\eta}\right\|-\left\|\boldsymbol{\eta}\right\|^{*}\right)d\left\|\boldsymbol{\eta}\right\| \qquad \left(\left\|\boldsymbol{\eta}\right\|^{*}=\frac{5\sigma_H r}{8E}\right)\\
&= \frac{24E}{5\pi r\delta^3}\left(\left\|\boldsymbol{\eta}\right\|-\frac{5\sigma_H r}{8E}\right)^2
\end{aligned}
\tag{6.6}
$$

Finally, by equating Equation (6.6) with Equation (2.27), we obtain the critical displacement for the bonds in the horizontal direction.

$$
\begin{aligned}
&\omega_{\xi} = \omega_c \\
&\Leftrightarrow \frac{24E}{5\pi r\delta^3}\left(\|\boldsymbol{\eta}\|_{crit\_hori} - \frac{5\sigma_H r}{8E}\right)^2 = \frac{9{K_{IC}}^2\left(1-\nu^2\right)}{4\delta^3 E} \\
&\Leftrightarrow \|\boldsymbol{\eta}\|_{crit\_hori} = \sqrt{\frac{15\pi {K_{IC}}^2\left(1-1/16\right)r}{32E^2}} + \frac{5\sigma_H r}{8E} \\
&\Leftrightarrow \|\boldsymbol{\eta}\|_{crit\_hori} = \frac{5\sqrt{r}}{8E}\left(\sqrt{\frac{9\pi}{8}}K_{IC} + \sqrt{r}\sigma_H\right) \qquad \left(0 < r \le \delta\right)
\end{aligned}
\tag{6.7}
$$

From Equation (6.7), the critical displacement for the bonds in the horizontal direction $\|\boldsymbol{\eta}\|_{crit\_hori}$ in Layer 1 is given as follows,

$$
\|\boldsymbol{\eta}\|_{crit\_hori} = \frac{5\sqrt{r}}{8E_1}\left(\sqrt{\frac{9\pi}{8}}K_{IC1} + \sqrt{r}\sigma_H\right) \qquad \left(0 < r \le \delta\right) \tag{6.8}
$$

In the same way, we can also obtain the critical displacement for the bonds in the vertical direction across the layer interface $\|\boldsymbol{\eta}\|_{crit\_vert}$ as follows. Note that the critical energy density for the bond across the layer interface is given as the smaller value of the two critical energy densities (we assume that the critical energy density for the layer 2 is smaller in this case). In addition, the Young's modulus for the bonds across the interface is calculated as the arithmetic average of the values of Young's modulus for both layers.

$$
\begin{aligned}
&\omega_{\xi\_vert} = \omega_{c\_vert} \\
&\Leftrightarrow \frac{24\bar{E}}{5\pi r\delta^3}\left(\|\boldsymbol{\eta}\|_{crit\_vert} - \frac{5\sigma_H r}{8\bar{E}}\right)^2 = \frac{9{K_{IC2}}^2\left(1-{\nu_2}^2\right)}{4\delta^3 E_2} \\
&\Leftrightarrow \|\boldsymbol{\eta}\|_{crit\_vert} = \sqrt{\frac{15\pi {K_{IC2}}^2\left(1-1/16\right)r}{32E_2\bar{E}}} + \frac{5\sigma_V r}{8\bar{E}} \\
&\Leftrightarrow \|\boldsymbol{\eta}\|_{crit\_vert} = \frac{5\sqrt{r}}{8\bar{E}}\left(\sqrt{\frac{9\pi\bar{E}}{8E_2}}K_{IC2} + \sqrt{r}\sigma_V\right) \qquad \left(0 < r \le \delta\right)
\end{aligned}
\tag{6.9}
$$

Where, $\overline{E}$ is the average Young's modulus between Layer 1 and Layer 2 (dimension: [Pa]). Equation (6.7) clearly shows that a higher fracture toughness a higher initial stress requires a higher displacement to break a bond. Hence, as shown in Equation (6.8), if the fracture toughness in Layer 1 is high, fracture propagation in Layer 1 is difficult and it is difficult to cross the layer interface. In addition, as shown in Equation (6.9), if the initial vertical stress is high, it is difficult to break the bonds across the layer interface (difficult to turn along the layer interface).

6.2.2.3 Effect of Young's modulus contrast

As shown in Fig. 6.2 – Fig. 6.4, the effect of Young's modulus contrast on fracture turning is not as significant. In the highest Young's modulus contrast cases (Fig. 6.2(a): $E_2 / E_1 = 80GPa / 10GPa$), the fracture turns at a relatively lower fracture toughness contrast than for the other Young's modulus cases. The fracture turns at around two times toughness contrast ($K_{IC1} / K_{IC2} = 1.0 / 0.5$) in a lower principal stress difference and at around eight times toughness contrast ($K_{IC1} / K_{IC2} = 4.0 / 0.5$) for the higher principal stress difference. However, in the lower Young's modulus contrast cases (Fig. 6.2 (b) (c), Fig. 6.3, Fig. 6.4), no apparent differences are observed among the different Young's modulus contrast cases. In those cases, fracture turns at three to four times fracture toughness contrast (turning fracture toughness contrast $K_{IC1} / K_{IC2} > 3 \sim 4$) in the lower principal stress difference ($\Delta\sigma <= 1.0$ MPa) and at eight to ten fracture toughness contrast in the higher principal stress difference ($\Delta\sigma \simeq 20MPa$).

However, if we consider the contrast of the critical energy densities (in other words, the contrast of energy release rate) between Layer 1 and Layer 2, these results show that the higher Young's modulus contrast requires less critical energy density contrast to make

the fracture turn along the layer interface. As shown in Equation (2.27), the critical energy density (the minimum energy density required for breaking a bond) in 2-D plane strain condition is given by a function which is proportional to the square of the fracture toughness and inversely proportional to the Young's modulus.

$$\omega_c = \frac{9G_c}{4\delta^3} = \frac{9K_{IC}{}^2\left(1-\nu^2\right)}{4\delta^3 E} \tag{2.27}$$

Hence, if the fracture toughness contrast at the turning condition are almost the same ($\frac{K_{IC1}}{K_{IC2}} = \chi$) regardless of Young's modulus contrast, it means that the critical energy density contrast between the layers required for fracture turning is inversely proportional to the Young's modulus contrast (Equation (6.10)).

$$\frac{\omega_{c1}}{\omega_{c2}} = \frac{\dfrac{9K_{IC1}{}^2\left(1-\nu^2\right)}{4\delta^3 E_1}}{\dfrac{9K_{IC1}{}^2\left(1-\nu^2\right)}{4\delta^3 E_2}} = \frac{\dfrac{9\chi^2 K_{IC2}{}^2\left(1-\nu^2\right)}{4\delta^3 E_1}}{\dfrac{9K_{IC1}{}^2\left(1-\nu^2\right)}{4\delta^3 E_2}} = \chi^2 / \frac{E_1}{E_2} \tag{6.10}$$

The tendency that the fracture turning criteria only depends on the fracture toughness contrast is partially explained by using the contrast of the critical force scalar states near the tip between the horizontal bond in the layer 1 and the vertical bond across the layer interface which may be used as the turning criteria.

From Equation (6.3), (6.4), (6.7), and (6.8), the critical force scalar state for the horizontal bonds in Layer 1 and the critical force scalar state for the vertical bonds across the layer interface are approximated as,

$$
\begin{aligned}
\underline{t}^{*}\left[\mathbf{x},t\right]\left\langle\boldsymbol{\xi}\right\rangle_{crit\_hori} &= \underline{t}\left[\mathbf{x},t\right]\left\langle\boldsymbol{\xi}\right\rangle_{crit\_hori} - t_0\left[\mathbf{x}\right]\left\langle\boldsymbol{\xi}\right\rangle_{hori} \\
&= \frac{24E_1}{5\pi r\delta^3}\left\|\boldsymbol{\eta}\right\|_{crit\_hori} - \frac{3\sigma_H}{\pi\delta^3} \\
&= \frac{24E_1}{5\pi r\delta^3}\frac{5\sqrt{r}}{8E_1}\left(\sqrt{\frac{9\pi}{8}}K_{IC1} + \sqrt{r}\sigma_H\right) - \frac{3\sigma_H}{\pi\delta^3} \\
&= \frac{9}{2\sqrt{2\pi r}\delta^3}K_{IC1}
\end{aligned}
\tag{6.11}
$$

$$
\begin{aligned}
\underline{t}^{*}\left[\mathbf{x},t\right]\left\langle\boldsymbol{\xi}\right\rangle_{crit\_vert} &= \underline{t}\left[\mathbf{x},t\right]\left\langle\boldsymbol{\xi}\right\rangle_{crit\_hori} - t_0\left[\mathbf{x}\right]\left\langle\boldsymbol{\xi}\right\rangle_{vert} \\
&= \frac{24\bar{E}}{5\pi r\delta^3}\left\|\boldsymbol{\eta}\right\|_{crit\_vert} - \frac{3\sigma_V}{\pi\delta^3} \\
&= \frac{24\bar{E}}{5\pi r\delta^3}\frac{5\sqrt{r}}{8\bar{E}}\left(\sqrt{\frac{9\pi\bar{E}}{8E_2}}K_{IC2} + \sqrt{r}\sigma_V\right) - \frac{3\sigma_V}{\pi\delta^3} \\
&= \frac{9}{2\sqrt{2\pi r}\delta^3}K_{IC2}\sqrt{\frac{\bar{E}}{E_2}}
\end{aligned}
\tag{6.12}
$$

From Equation (6.11) and (6.12), the ratio of the critical force vector states between horizontal and vertical direction is given as follows (note that we assume bond distance r is the same in both directions),

$$
\underline{t}^{*}\left[\mathbf{x},t\right]\left\langle\boldsymbol{\xi}\right\rangle_{crit\_hori} \,/\, \underline{t}^{*}\left[\mathbf{x},t\right]\left\langle\boldsymbol{\xi}\right\rangle_{crit\_vert} = \frac{K_{IC1}}{K_{IC2}}\sqrt{\frac{E_2}{\bar{E}}} \tag{6.13}
$$

As shown in Equation (6.13), the contrast of the critical force scalar states between the horizontal bond in the layer 1 and the vertical bond across the layer interface is mainly affected by the fracture toughness contrast. The effect of Young's modulus contrast ($\sqrt{\frac{E_2}{\bar{E}}}$) is relatively limited from 0.63 to 1.25 in the ranges where E_1 = 10 – 40 GPa, E_2= 10 – 40 GPa. Hence, the fracture turning behavior is mainly controlled by the fracture toughness contrast.

The reason why the highest Young's contrast cases ($E_2 / E_1 = 80GPa / 10GPa$) show a different tendency from the other Young's modulus contrast cases (Fig. 6.2, Fig. 6.3, and Fig. 6.4) can be explained as follows. Fig. 6.10 shows bottom-hole flowing pressure change with time in different Young's modulus cases. In these cases, only the Young's modulus and fracture toughness in the first layer are changed (parameter range: E= 10 - 40 GPa, KIC = 1.0 - 2.0MPa $m^{0.5}$). Other parameters (Young's modulus in Layer 2, fracture toughness in Layer 2, and principal stress difference) are fixed as 10 GPa, 0.5 MPa $m^{0.5}$ and 1 MPa $m^{0.5}$ respectively.

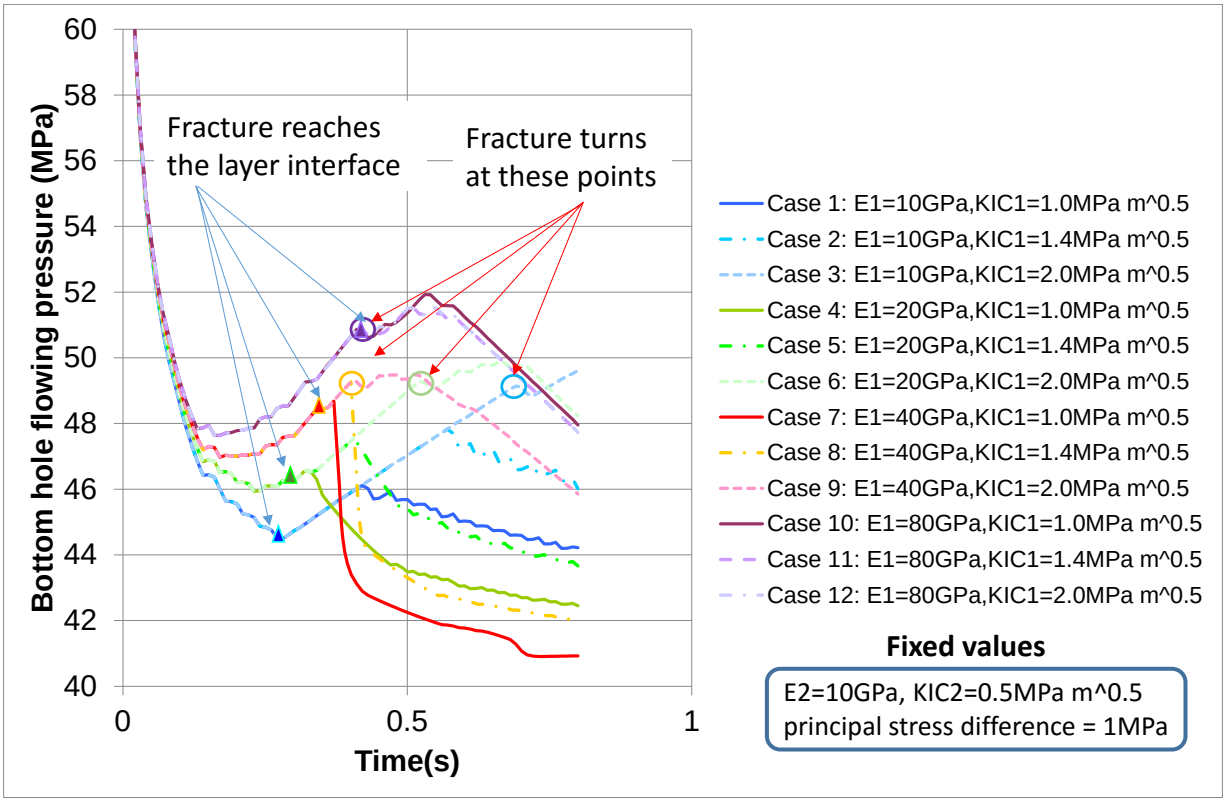

Fig. 6.10 Bottom-hole flowing pressure change with time (different Young's modulus contrast cases).

As shown in Fig. 6.10, in the cases where Young's modulus contrast is 1.0 (Case1-Case3: $E_1 / E_2 = 10GPa / 10GPa$), at time > 0, the BHP continues to decrease until the fracture reaches the layer interface. After the fracture reaches the layer boundary, the BHP increases until the fracture crosses the layer interface (Case 1 and Case 2) or turns along the layer interface (Case 3) depending on the fracture toughness of Layer 1. On the other hand, in the higher Young's modulus contrast cases (Case 4 – Case 12: $E_1 / E_2 > 1$), the BHPs do not continue to decrease until the fractures reach the layer interface. The higher the Young's modulus contrast is, the earlier the BHP begins to increase before it reaches the layer interface. These results suggest that, near the layer interface, the horizontal displacement of Layer 2 (softer layer) is highly constrained by the smaller displacement of Layer 1 (harder layer). In other words, due to the constraints from the harder layer, the softer layer near the layer interface behaves as if it were a barrier to fracture growth which is difficult to penetrate. Therefore, the fracture turns in the highest Young's modulus contrast cases even if the fracture toughness contrast is low. Fig. 6.11 shows the damage distribution near the layer interface in the highest Young's modulus contrast cases. As shown in Fig. 6.12, the fractures turn at the two elements before they reach the layer interface due to the constraints of the horizontal displacement from Layer 1.

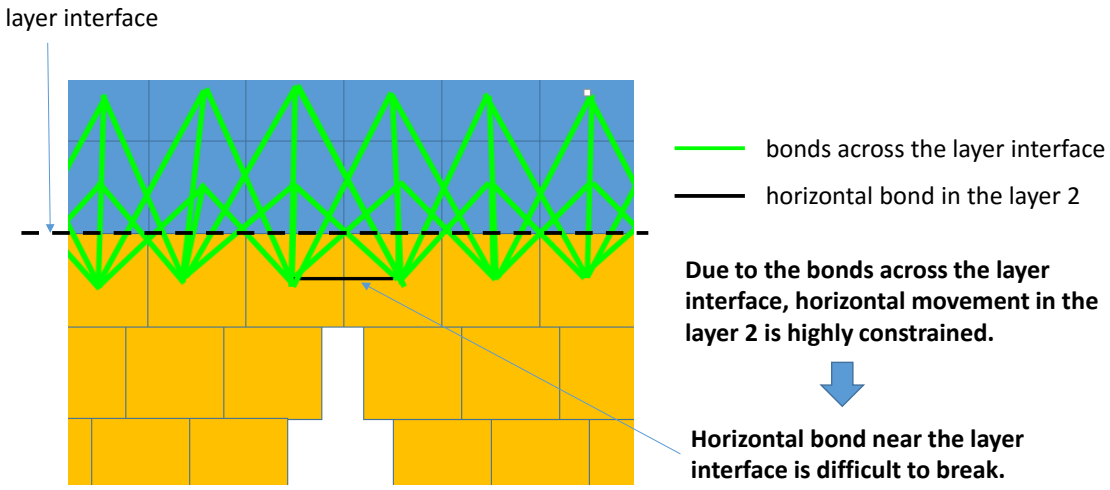

Fig. 6.11 Constraints of the horizontal displacement in the layer 2 from the layer 1.

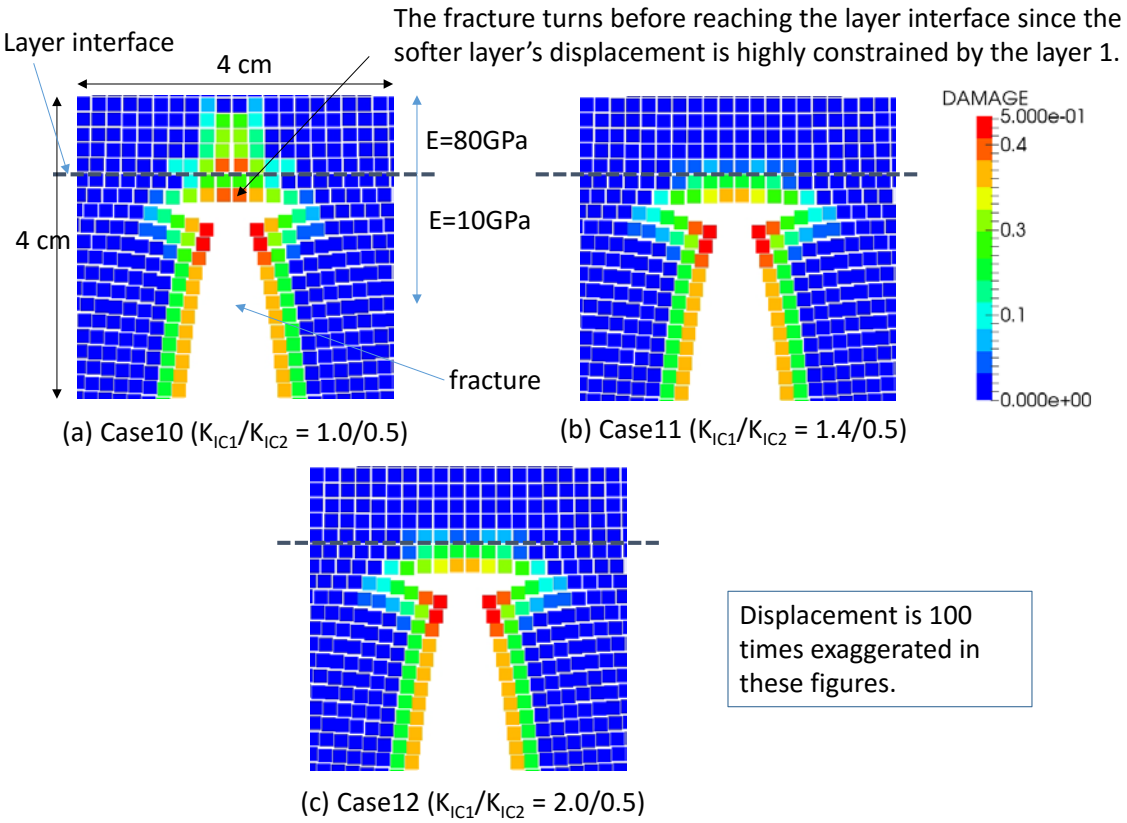

Fig. 6.12 Damage distribution near the layer inteface at t = 0.49 sec (higher Young's modulus contrast cases: Case 10, 11, and 12).

Effect of constitutive law

In the previous section, we explained why the fracture turns in the highest Young's modulus contrast cases even if the contrast of the fracture toughness is low. However, as shown in Fig. 6.12, the results that the fractures turn before they reach the layer interface seem to be unphysical. The effect of Young's modulus contrast may be exaggerated by the constitutive relation in the momentum balance equation. In our model, if we neglect the pore pressure term for simplicity, the force scalar state in a bond in a 2-D plane strain condition is given as follows,

$$t\left[\mathbf{x},t\right]\left\langle\boldsymbol{\xi}\right\rangle - t\left[\mathbf{x}',t\right]\left\langle-\boldsymbol{\xi}\right\rangle = \frac{\omega}{m}\left[\begin{array}{c}\left(\left(2K_i - \frac{10}{3}G_i\right)\theta_i + \left(2K_j - \frac{10}{3}G_j\right)\theta_j\right)\left\|\mathbf{x}_j - \mathbf{x}_i\right\| \\ +8\left(G_i + G_j\right)e_{ij}\end{array}\right] \tag{6.14}$$

In this formulation, the force scalar state is more affected by the higher modulus value of the two ends of the bond rather than the lower modulus value as if the two different materials are connecting in parallel. However, the actual layer connection is not in parallel but in series. The force scalar state should be more affected by the smaller modulus value rather than the higher value. Here, we replace Equation (6.11) with Equation (6.15) (harmonic averaging based force scalar state formulation) and investigate how the constitutive relation of the momentum balance equation affects the fracture propagation behavior near the layer interface by simulating the same cases as shown in Fig. 6.2. List of the modified and unmodified parameters are shown in Table 6.4. Fig. 6.13 shows the summary of fracture propagation behavior with this new constitutive law.

$$t[\mathbf{x},t]\langle\xi\rangle - t[\mathbf{x}',t]\langle-\xi\rangle = \frac{\omega}{m}\left[\left(2\bar{K} - \frac{10}{3}\bar{G}\right)\left(\theta_i + \theta_j\right)\left\|\mathbf{x}_j - \mathbf{x}_i\right\| + 8\bar{G}e_{ij}\right] \quad (6.15)$$

$$\bar{K} = \frac{2K_1K_2}{K_1 + K_2} \quad (6.16)$$

$$\bar{G} = \frac{2G_1G_2}{G_1 + G_2} \quad (6.17)$$

Table 6.4 List of fixed and changed parameters.

Parameters	Condition	Variation
Young's modulus in layer 1 (GPa)	Changed	10, 20, 40, 80
Young's modulus in layer 2 (GPa)	Changed	10
Fracture toughness in layer 1 (MPa $m^{0.5}$)	Changed	0.5, 1.0, 1.4, 2.0, 2.5, 3.0, 5.0
Fracture toughness in layer 2 (MPa $m^{0.5}$)	Fixed	0.5
Vertical stress (MPa)	Changed	41, 47, 50, 60
Horizontal stress in layer 1 (MPa)	Fixed	40
Medium permeability (mD)	Fixed	0.00001

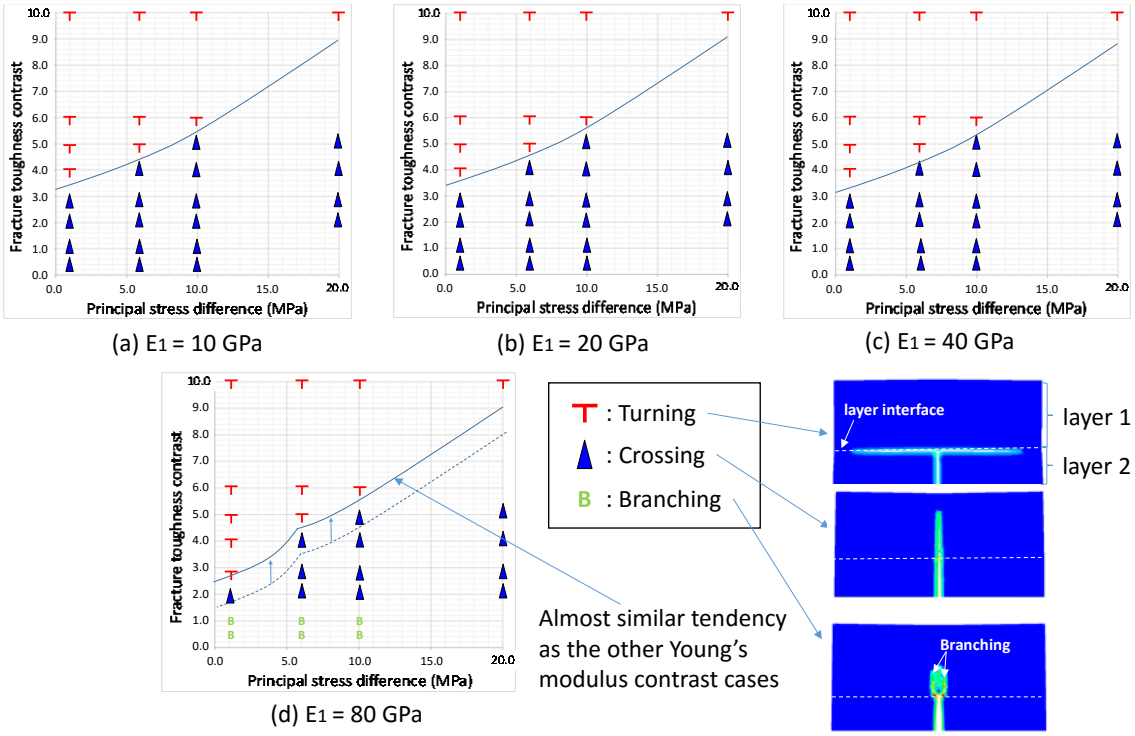

Fig. 6.13 Fracture turning behavior (E_2=10 GPa: harmonic averaging).

As shown in Fig. 6.2 (a) - (c) and Fig. 6.13 (a) - (c), in the lower Young's modulus contrast cases, no apparent differences are observed regardless of the constitutive relations. However, as shown in Fig. 6.2 (d) and Fig. 6.13 (d), in the case of the highest Young's modulus cases, the minimum fracture toughness contrast for fracture turning becomes higher in the cases with Equation (6.15) than the cases with Equation (6.14). The turning criteria in the highest Young's modulus contrast cases becomes almost the same as the other lower Young's modulus contrast cases in the cases where the harmonic mean is used. The Equation (6.15) (harmonic mean) allows the bonds to deform in the horizontal direction in Layer2 more easily than Equation (6.14), which eliminates the un-physical fracture turning region in the lower fracture toughness contrast cases. Fig. 6.14 shows the damage distribution near the layer interface in the highest Young's modulus contrast cases where Equation (6.15) is applied. As shown in Fig. 6.14 (a), (b) and (c), the fracture crosses

the layer interface in the low fracture toughness contrast case and turns at the one element closer point to the layer interface than the original cases in the middle and high fracture toughness contrast cases. Through the simulation studies in this section, we found that Equation (6.15) (the harmonic mean of the two different modulus values) gives us more physically convincing results than Equation (6.14) in the highest Young's modulus contrast cases. Based on these results, we decide to use Equation (6.15) instead of Equation (6.14) in the following part of this study. However, the fractures still turn before the layer interface even if the harmonic mean is applied (softer layer still behaves like a stronger layer even if the harmonic mean is applied). More work is necessary for proving the validity of this constitutive relation.

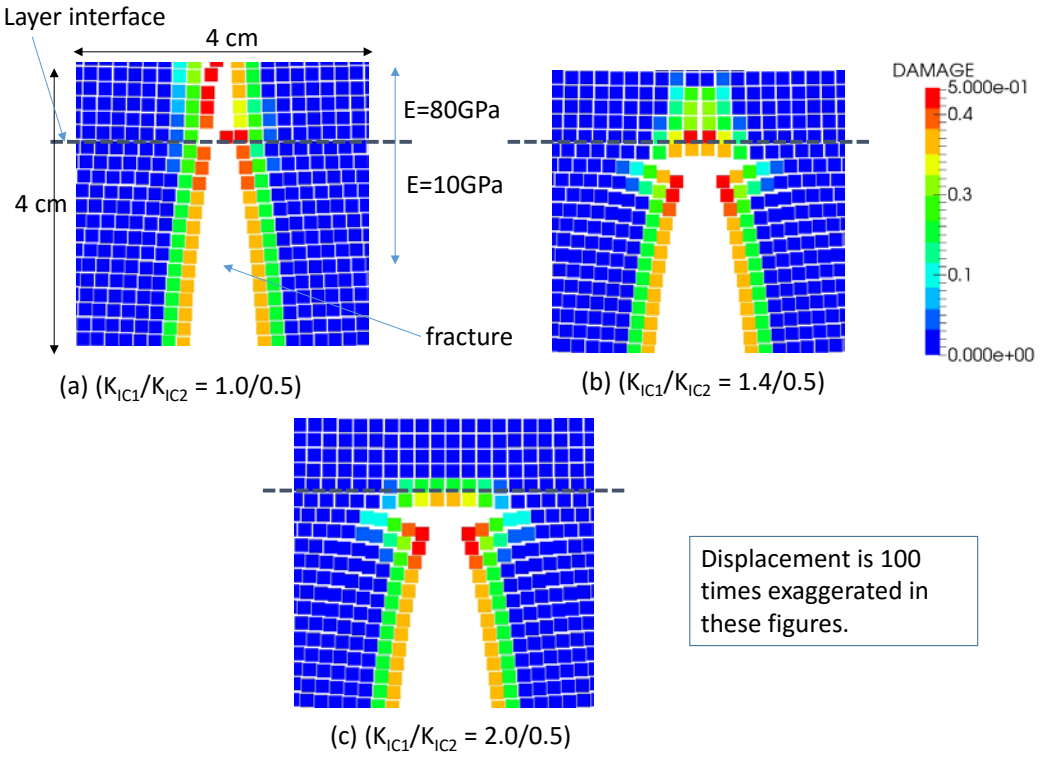

Fig. 6.14 Damage distribution near the fracture tip (E_1=80 GPa, E_2=10 GPa: harmonic averaging).

6.2.3 EFFECT OF LAYER DIP

In this section, we investigated how layer dip angle affects fracture propagation near the layer interface by changing the layer dip angle for different Young's modulus, fracture toughness contrast, and horizontal/vertical stress difference. Parameter ranges are shown in Table 6.5. The results in these cases are summarized in Fig. 6.15 and Fig. 6.16. Note that, in every case after this section, Equation (6.15) is used for the force scalar state calculation instead of the original formulation (Equation (6.14)).

Table 6.5 Parameter ranges.

Parameters	Condition	Variation
Young's modulus in layer 1 (GPa)	Changed	10, 20, 40, 80
Young's modulus in layer 2 (GPa)	Fixed	10
Fracture toughness in layer 1 (MPa $m^{0.5}$)	Changed	0.25, 0.5, 1.0, 1.4, 2.0, 2.5, 3.0, 5.0
Fracture toughness in layer 2 (MPa $m^{0.5}$)	Fixed	0.5
Layer dip angle (degree)	Fixed	15, 30
Vertical stress (MPa)	Changed	41, 47, 50, 60
Horizontal stress in layer 1 (MPa)	Fixed	40
Medium permeability (mD)	Fixed	0.00001

6.2.3.1 Kinking

As shown in Fig. 6.15 and Fig. 6.16, if the layer interface is inclined, the fractures do not go straight but kink before they reach the layer interface in many cases. Here, we explain the basic mechanism of "kinking" and the important parameters that control fracture kinking.

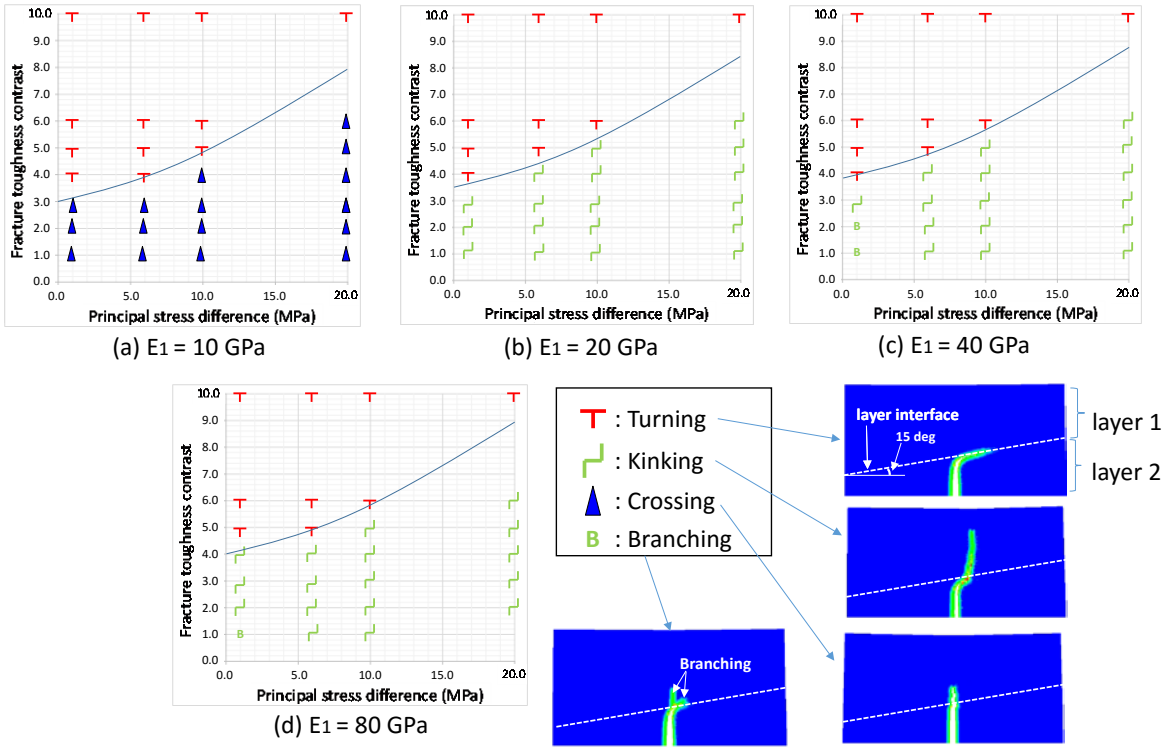

Fig. 6.15 Fracture turning behavior (layer dip angle = 15 degee, E2=10 GPa).

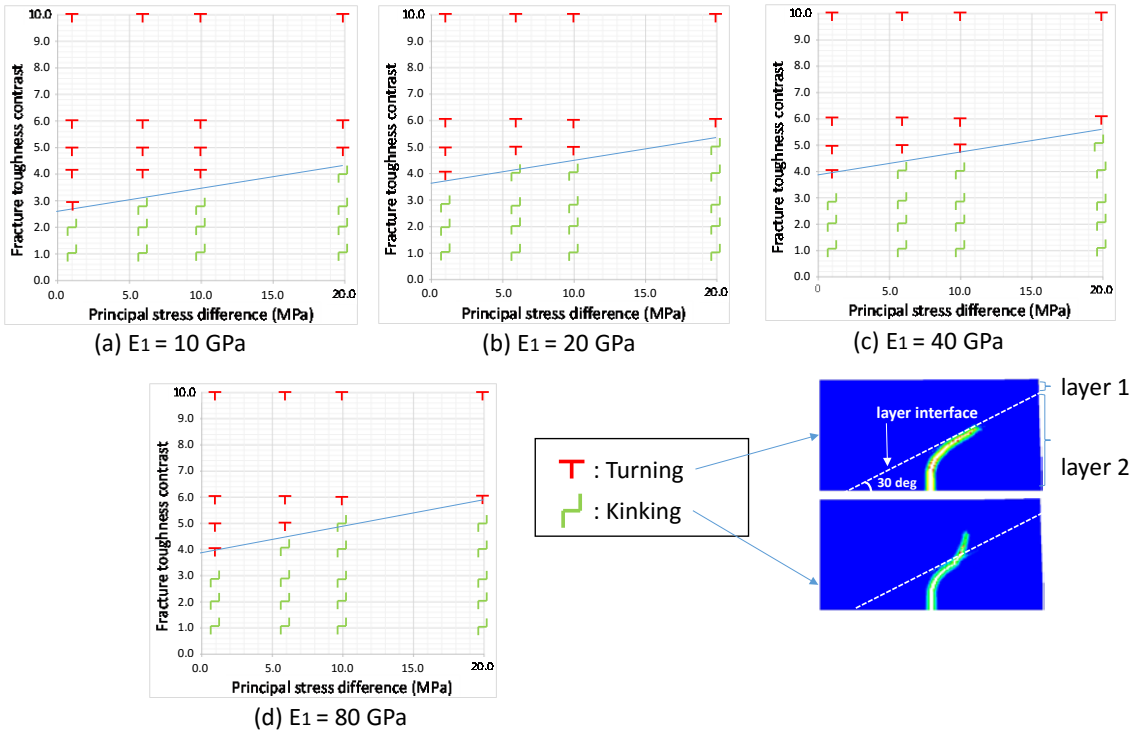

Fig. 6.16 Fracture turning behavior (layer dip angle = 30 degree, E2=10 GPa).

Basic mechanism of kinking caused by layer dip

Fig. 6.17 shows the distribution of horizontal stress and damage at different time steps in the case where the dip angle is 15 degrees, the Young's modulus contrast is 4.0, and the principal stress difference is 1.0 MPa. As shown in Fig. 6.17, if the dip angle is not zero and the Young's modulus contrast is more than 1.0, the fracture turns to the right before it hits the layer interface. Since the displacement of Layer 2 is prevented more by the smaller displacement of Layer 1 to the left of the fracture, the crack propagation becomes relatively difficult on the left side, which results in the fracture turning toward the right. Note that if the fractures propagate from the harder layer to the softer layer, the fracture turns to the left instead of right since the direction perpendicular to the layer

interface is the easiest direction for fracture propagation. These cases are shown in Section 6.4.

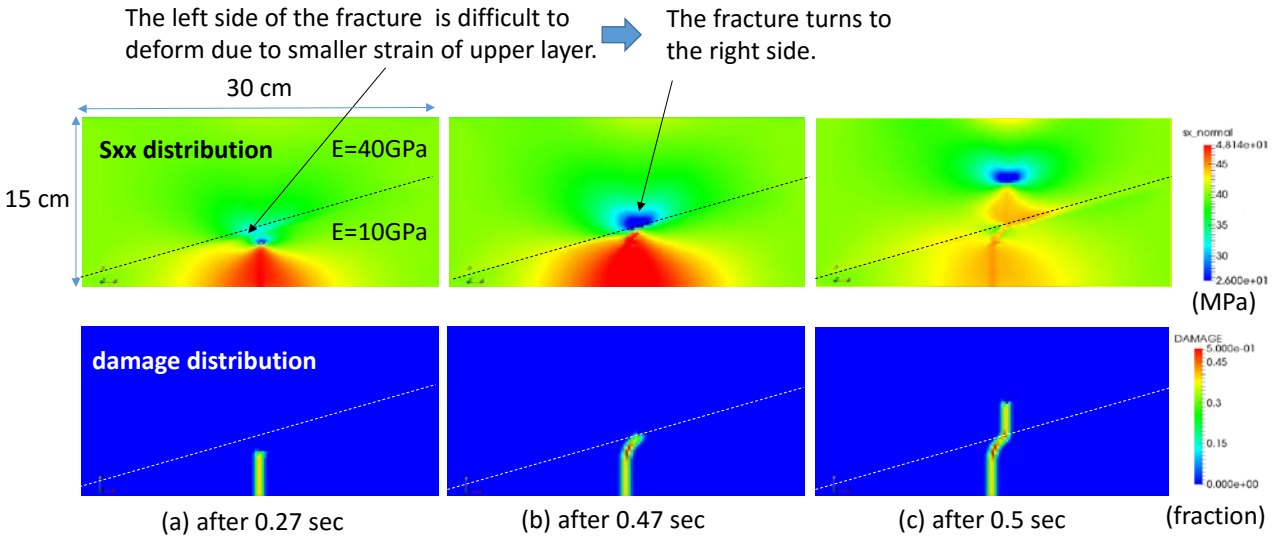

Fig. 6.17 Horizontal stress and damage distribution (layer dip angle = 15 degree, E_1/E_2=40 GPa/10 GPa, K_{IC1}/K_{IC2}=1.41MPa $m^{0.5}$/0.5MPa $m^{0.5}$, principal stress difference = 1.0 MPa).

Effect of Young's modulus contrast on kinking

Fig. 6.18 shows the damage distribution just before crossing the layer interface for the different Young's modulus contrast cases. In these cases, the other parameters are fixed as follows (layer dip angle = 15 degree, the fracture toughness contrast = K_{IC1} / K_{IC2}=1.4 / 0.5, and the principal stress difference = 1.0 MPa). As shown in Fig. 6.18, since the fracture turning is caused by the difference of the displacement between Layer 1 and Layer 2, a higher Young's modulus contrast causes more fracture turning. As shown in Fig. 6.15 (a) and Fig. 6.18 (a), if the fracture toughness contrast is 1.0 and the layer dip angle is 15 degrees, no fracture turning is expected before the fracture reaches the layer interface. However, as shown in Fig. 6.16 (a), if the layer dip angle is 30 degrees, the kinking region

appears even if the fracture toughness contrast is 1.0. There is no kinking before the fracture reaches the layer interface but the kinking occurs along the layer interface due to the fracture toughness contrast.

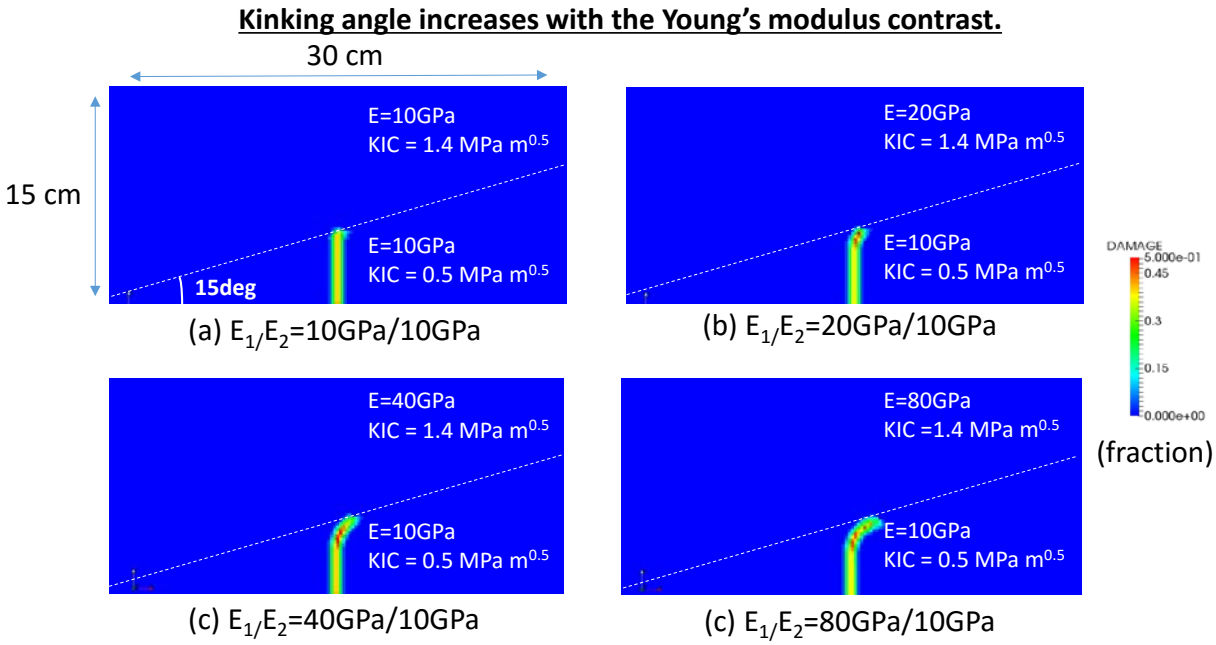

Fig. 6.18 Damage distribution in the different Young's contrast cases (layer dip angle = 15 degree, K_{IC1}/K_{IC2}=1.41MPa $m^{0.5}$/0.5MPa $m^{0.5}$, principal stress difference = 1.0 MPa).

Effect of fracture toughness contrast on kinking

Fig. 6.19 shows the damage distribution just before the fracture crosses the layer interface for the different fracture toughness contrast cases. In these cases, the other parameters are fixed as follows (layer dip angle = 15 degree, the Young's modulus contrast $= E_1 / E_2 = 40/10$, and the principal stress difference = 1.0 MPa). As shown in Fig. 6.19, the degree of fracture kinking (kinking angle) is not different for the different fracture toughness contrast cases. Since the kinking is caused by the displacement difference

between the two layers under compression, the parameters which are not directly related to the compressional displacement such as fracture toughness do not affect the degree of kinking.

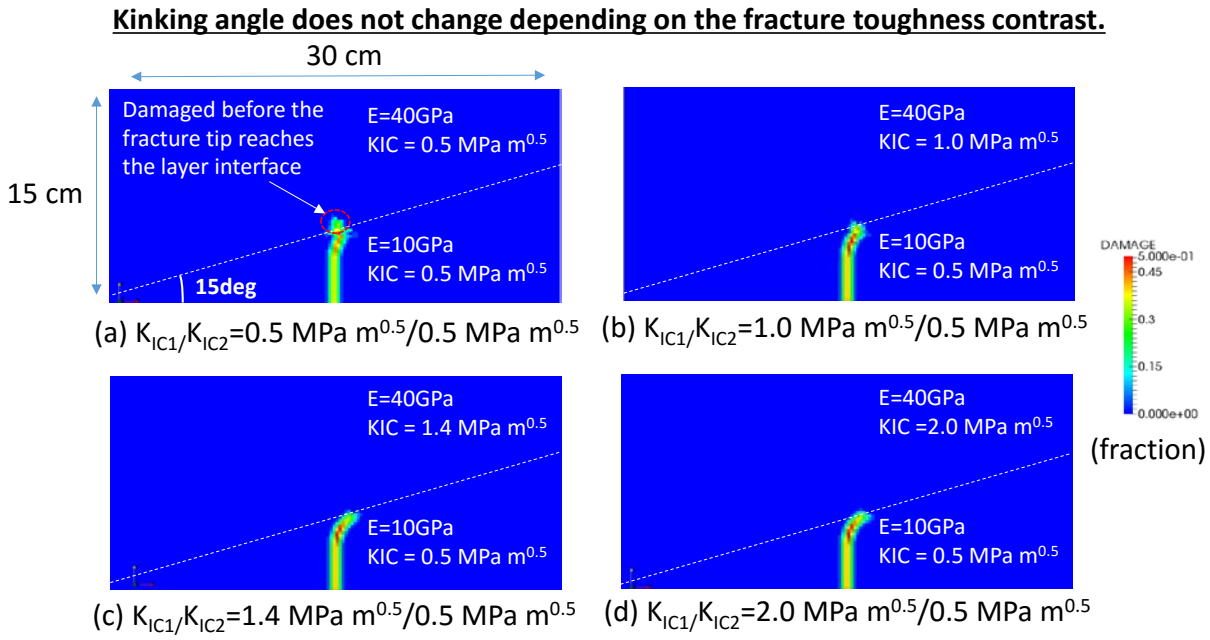

Fig. 6.19 Damage distribution in the different fracture toughness contrast (layer dip angle = 15 degree, E_1/E_2=40 GPa/10 GPa, principal stress difference = 1.0 MPa).

Effect of principal stress difference on kinking

Fig. 6.20 shows the damage distribution just before the fracture crosses the layer interface for the different principal stress difference cases. In these cases, the other parameters are fixed as follows (layer dip angle =15 degree, the Young's modulus contrast $= E_1 / E_2 = 40/10$, and the fracture toughness contrast $= K_{IC1} / K_{IC2} = 1.4/0.5$). As shown in Fig. 6.20, the more the principal stress difference is, the less the fracture turns before it reaches the layer interface. Since the larger vertical stress makes the bonds in the vertical direction have a higher compressional stress than the bonds in the horizontal direction,

breaking the vertical bonds becomes more difficult. Therefore, the fracture turning into the horizontal direction is more difficult in the larger principal stress difference case.

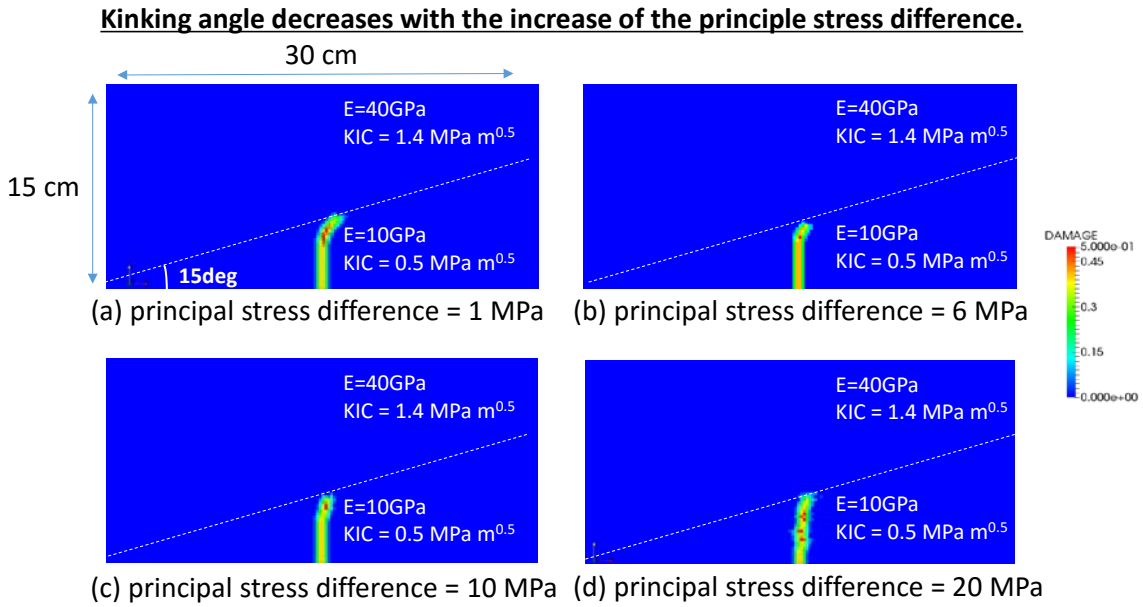

Fig. 6.20 Damage distribution in the different principal stress difference cases (layer dip angle = 15 degree, E_1/E_2=40 GPa/10 GPa, K_{IC1}/K_{IC2}=1.41MPa $m^{0.5}$/0.5MPa.

Effect of layer dip angle on kinking

Fig. 6.21 shows how the fracture turning angle is different depending on the layer dip angle. As shown in Fig. 6.21, the fractures turn more in the cases where the layer dip angle is 30 degrees than the cases where the layer dip angle is 15 degrees. In the larger dip angle cases, since the horizontal displacement in Layer2 is more influenced by Layer 1 at the left of the fracture, the fracture propagates more toward the right.

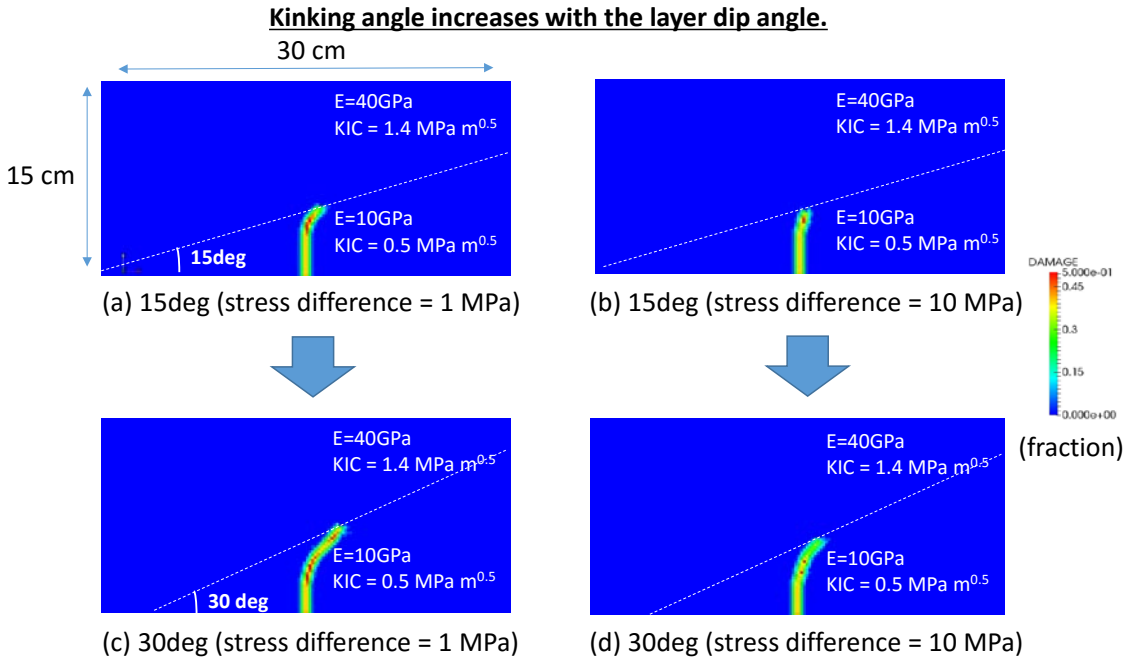

Fig. 6.21 Damage distribution in the different layer dip angle and different principal stress cases (E_1/E_2=40 GPa/10 GPa, K_{IC1}/K_{IC2}=1.41MPa $m^{0.5}$/0.5MPa $m^{0.5}$).

6.2.3.2 Fracture turning in the layer dip angle cases

As shown in Fig. 6.15 and Fig. 6.16, for dipping layers, the minimum fracture toughness contrasts for which fracture turning occurs mainly depends on the principal stress difference. It is not affected much by the Young's modulus contrast. This is the same tendency as the layer dip angle is 0 ("0 degree cases"). The main difference between the 0 degree layer dip cases and the dipping bedding planes is that the fractures only turn to the right along the layer interface in the dip angle cases since the right side is less compressive due to the layer inclination. As shown in Fig. 6.15, in the cases where the layer dip angle is 15 degree ("15 degree cases"), since the initial effective stress acting on the layer interface in the 15 degree cases is almost the same as the 0 degree cases, the fracture turning criterion is almost the same as the 0 degree cases regardless of the Young's modulus

contrast. The minimum fracture toughness contrast for fracture turning is around 3.0 – 4.0 (1.5 MPa $m^{0.5}$/0.5 MPa $m^{0.5}$ – 2.0 MPa $m^{0.5}$/0.5 MPa $m^{0.5}$) in the lower principal stress difference cases ($\Delta\sigma < 1.0$ MPa) and around 8.0 – 10.0 in the high principal stress difference cases ($\Delta\sigma = 20.0$ MPa). As shown in Fig. 6.16, in the cases where the layer dip angle is 30 degrees (30 degree cases), the minimum fracture toughness contrast for fracture turning becomes lower than for the low layer dip angle cases (the 0 degree cases and the 15 degree cases). For a 30 degree layer dip angle, the minimum fracture toughness contrast for fracture turning is around 3.0 – 4.0 (1.5 MPa $m^{0.5}$/0.5 MPa $m^{0.5}$ – 2.0 MPa $m^{0.5}$/0.5 MPa $m^{0.5}$) for a low principal stress difference ($\Delta\sigma < 1.0$ MPa) and around 5.0 – 6.0 for a high principal stress difference condition ($\Delta\sigma = 20.0$ MPa). Since the initial normal effective stress acting on the layer interface in the 30 degree cases is smaller than the 0 degree cases, especially in the high principal stress condition, the fracture propagation along the layer interface is easier than for the low dip angle cases. However, as mentioned in Section 6.2.2, a fracture toughness contrast of the order of 5.0 – 6.0 is still extremely high. Judging from the minimum fracture toughness contrast obtained in this simulation study, no fracture turning is expected in a deep reservoir even if the layer interface is highly inclined. Fracture kinking is expected to be more important than fracture turning in the layer dip cases.

6.2.4 EFFECT OF LAYER THICKNESS

In order to investigate how the layer thickness affects the fracture propagation near the layer interface, as shown in Fig. 6.22, we prepared three different models by changing the 2nd layer thickness for two different layer dip angles (0 degrees and 30 degrees). Then we selected the following reference cases (please see Table 6.6) from the previous cases shown in Fig. 6.2 (c) and Fig. 6.16 (c) and simulated fracture propagation by changing the 2nd layer thickness for each of the reference cases.

Table 6.6 Reference case settings (investigation of the effect of layer thickness).

Case name	layer dip angle (degree)	Principal stress difference (MPa)	Fracture toughness contrast
0degree_1MPa_1	0	1.0	4.0
0degree_1MPa_2	0	1.0	5.0
0degree_1MPa_3	0	1.0	6.0
0degree_1MPa_4	0	1.0	10.0
0degree_10MPa_1	0	10.0	6.0
0degree_10MPa_2	0	10.0	10.0
30degree_1MPa_1	30	1.0	4.0
30degree_1MPa_2	30	1.0	5.0
30degree_1MPa_3	30	1.0	6.0
30degree_1MPa_4	30	1.0	10.0
30degree_10MPa_1	30	10.0	5.0
30degree_10MPa_2	30	10.0	6.0
30degree_10MPa_3	30	10.0	10.0

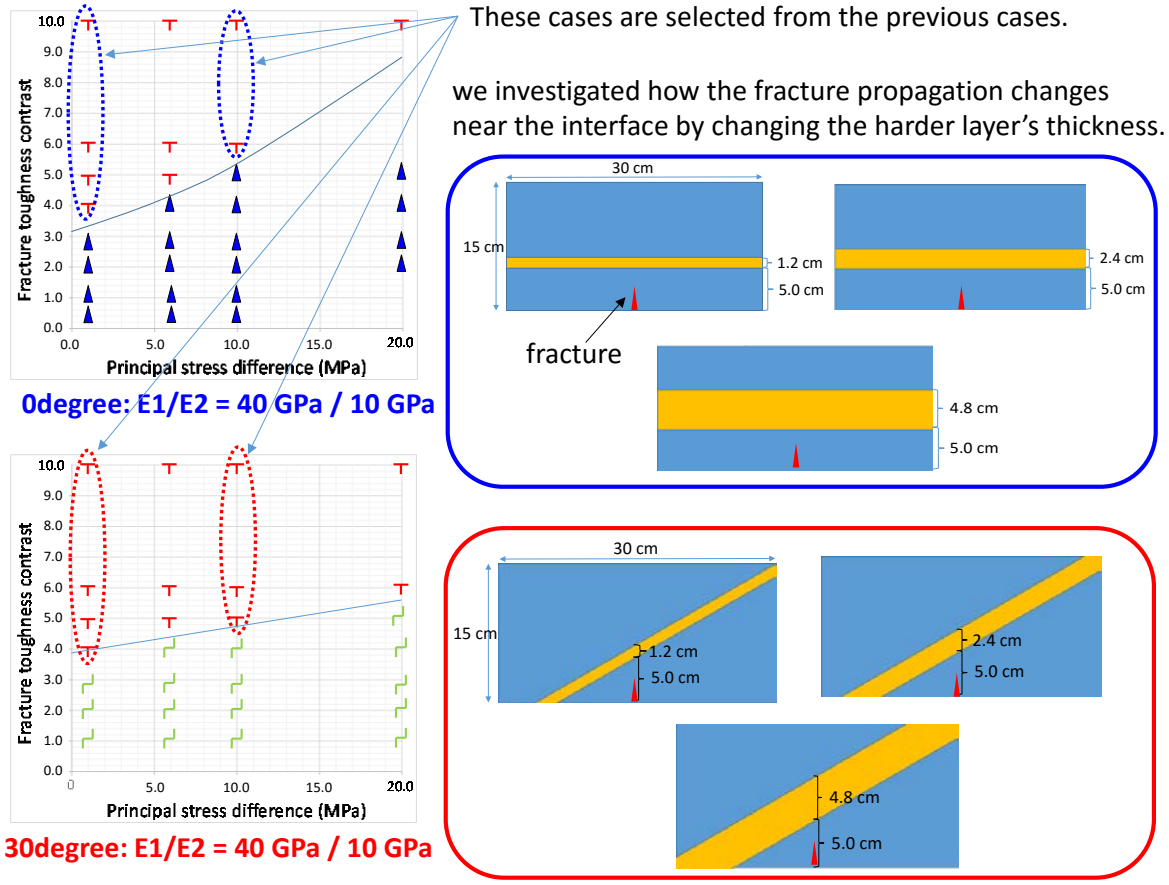

Fig. 6.22 Damage distribution in the different layer dip angle and different principal stress cases (E1/E2=40 GPa/10 GPa, KIC1/KIC2=1.41MPa m0.5/0.5MPa m0.5).

Fig. 6.23 and Fig. 6.24 show the results for fracture propagation for the different layer thickness cases. As shown in Fig. 6.23 and Fig. 6.24, the thinner the 2nd layer thickness is, the higher the minimum fracture toughness contrast needed for fracture turning. Fig. 6.25 shows the horizontal stress difference between the thinnest layer case (l = 1.2 cm) and the reference case (l = 10.0 cm) in the 0 degree case. As shown in Fig. 6.25, if the 2nd layer thickness is thin, since the existence of the softer layer (the 1st layer) makes the displacement of the 2nd layer larger, the stress reduction near the layer interface between

the 2nd layer and the 3rd layer is bigger for the thinnest 2nd layer thickness case than for the reference case. This leads to easier fracture penetration in the 2nd layer in the thinnest layer cases. As shown in Fig. 6.23, in the 0 degree case, if the 2nd layer thickness is more than 4.8 cm, the fracture turning criteria is the same as the reference case regardless of the principal stress difference. However, in the 30 degree case, if the principal stress difference is high, the fracture turning behavior is still different from the reference case even in the case where the 2nd layer thickness is 4.8 cm. On the other hand, if the principal stress is low, the fracture propagation behavior is the same as the reference case in the cases where the layer thickness is more than 2.4 cm. These differences may be caused by the kinking angle difference between the two different cases. Since the fracture has already turned before reaching the layer interface in the low principal stress difference case, the horizontal stress reduction near the fracture tip in the 2nd layer is not as large as in the high principal stress difference case. Therefore, if the principal stress difference is low, the layer thickness difference does not significantly affect the fracture propagation behavior in the 30 degree cases. Note that, in the 30 degree cases, as shown in Fig. 6.24, the fracture turns before the fracture reaches the layer interface even for the thinnest 2nd layer thickness. These results suggest that fractures will frequently kink in most reservoirs which have some degree of bed dipping and vertical heterogeneity in mechanical properties.

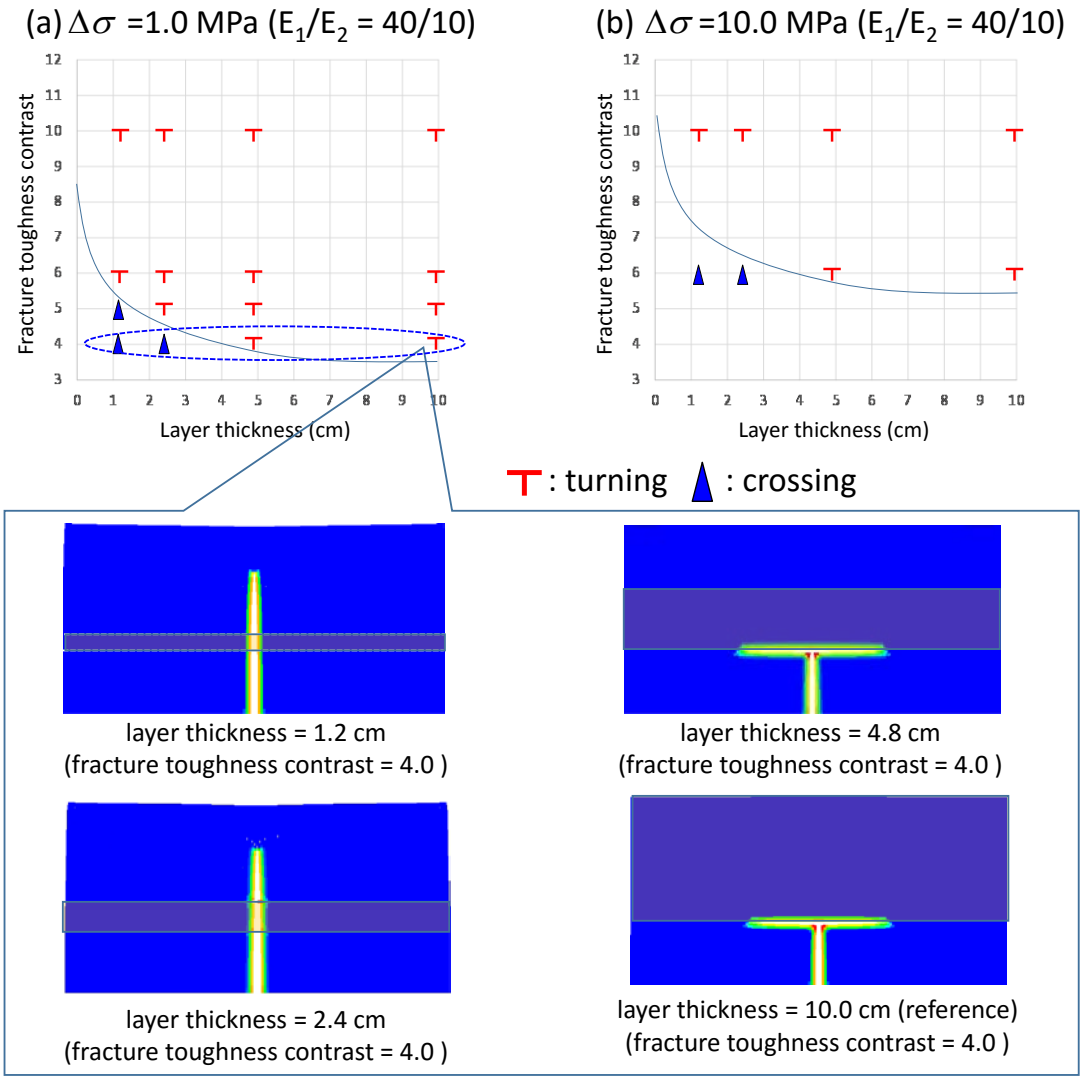

Fig. 6.23 Fracture propagation behavior for the different layer thickness cases (0 degree dip cases).

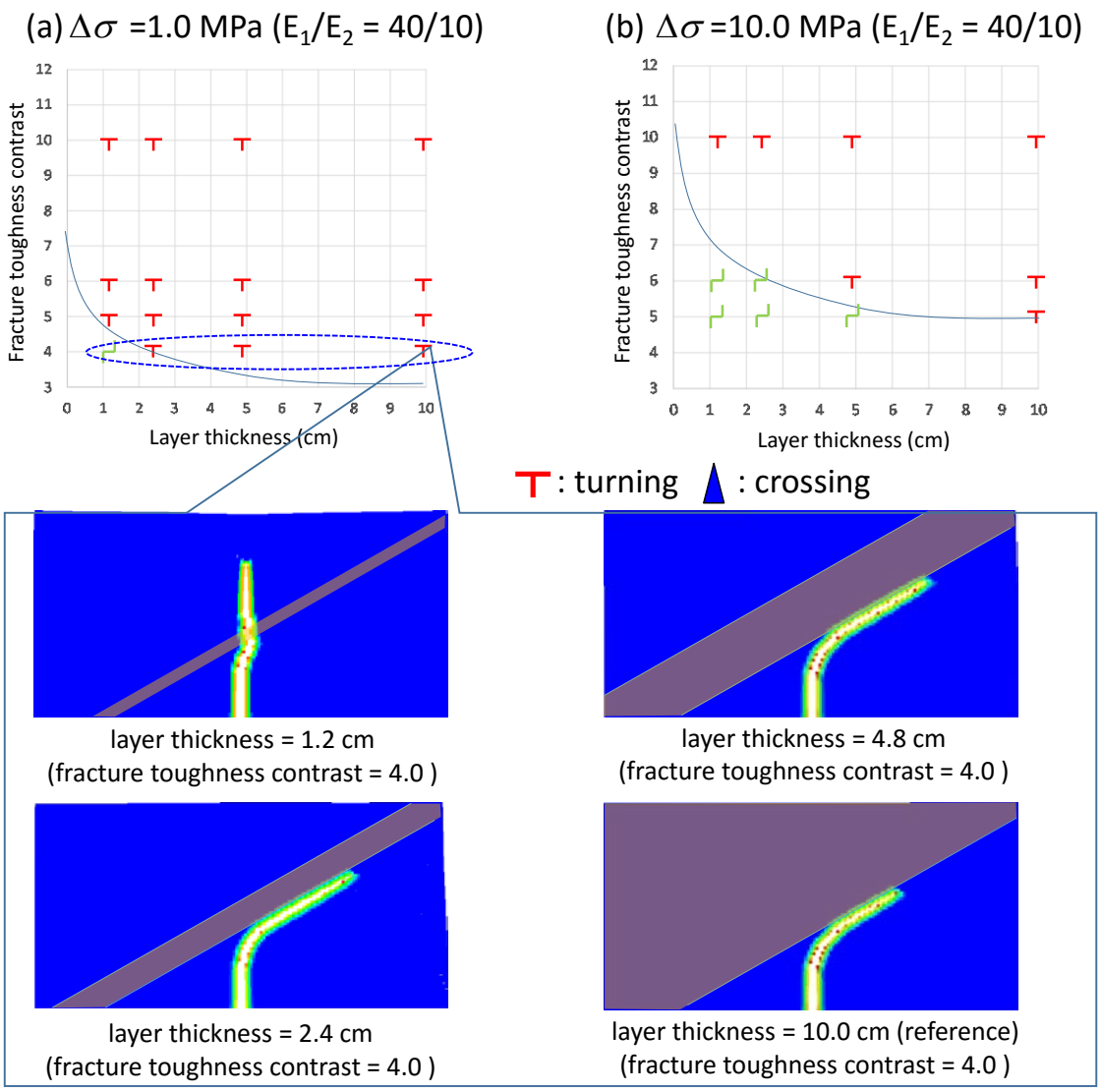

Fig. 6.24 Fracture propagation behavior for the different layer thickness cases (30 degree dip cases).

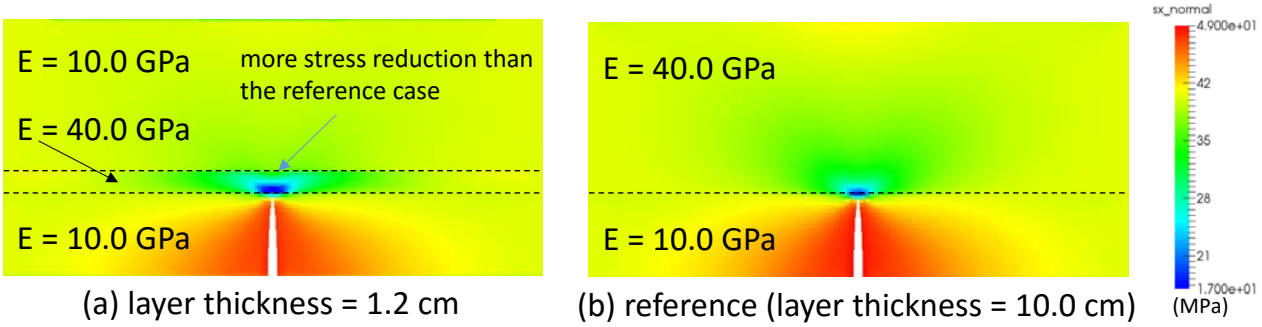

Fig. 6.25 Stress distribution near the layer interface (the thinnest layer case vs. referece case).

6.2.5 EFFECT OF HORIZONTAL STRESS DIFFERENCE

For investigating the effect of horizontal principal stress difference between the layers, we choose the eight reference cases from the previous cases shown in Fig. 6.2 (two cases for each Young's modulus contrast). All these reference cases have the same layer dip angle (θ =0 degree), the same principal stress difference ($\Delta\sigma$ =10 MPa), the same horizontal principal stress both in the layer 1 and the layer2 (σ_H =40.0 MPa), and a smaller fracture toughness contrast than the minimum fracture toughness contrast for fracture turning. As shown in Fig. 6.26, by applying a 5 MPa higher effective horizontal principal stress to Layer 1 than in the reference cases, we simulate how fracture propagation changes as the horizontal stress is increased. Table 6.7 shows the reference cases for the simulations in this section.

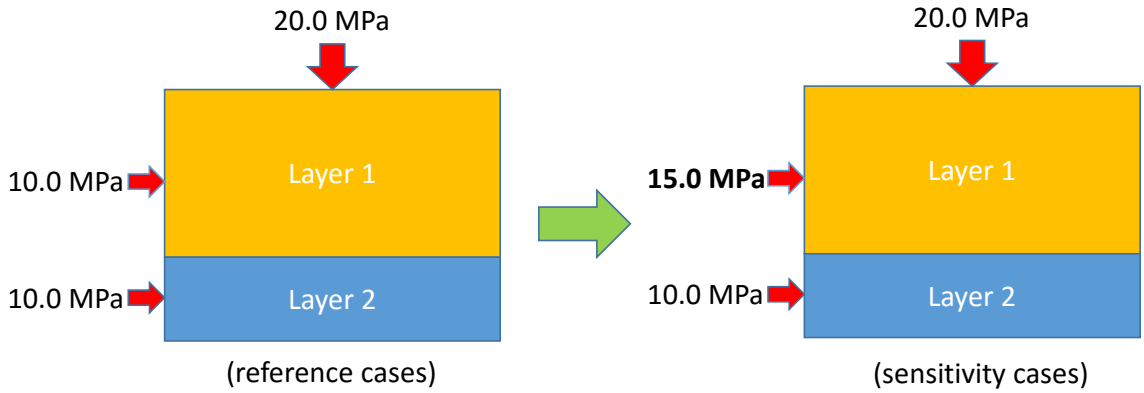

Fig. 6.26 Horizontal stress modification from the referece cases.

Table 6.7 Reference cases for the investigation of the effect of horizontal stress difference.

Case name	Effective horizontal stress (MPa)	Effective vertical stress (MPa)	Young's modulus in the layer 1 (GPa)	Young's modulus in the layer 2 (GPa)	Fracture toughness contrast
Case1_1	10.0	20.0	10.0	10.0	5.0
Case1_2	10.0	20.0	10.0	10.0	4.0
Case2_1	10.0	20.0	20.0	10.0	5.0
Case2_2	10.0	20.0	20.0	10.0	4.0
Case3_1	10.0	20.0	40.0	10.0	5.0
Case3_2	10.0	20.0	40.0	10.0	4.0
Case4_1	10.0	20.0	80.0	10.0	4.0
Case4_2	10.0	20.0	80.0	10.0	2.8

Fig. 6.27 shows a summary of the simulation results in this section. As shown in Fig. 6.27, the fractures turn at a smaller fracture toughness value than the reference cases (in every instance). These results show that increasing the horizontal principal stress difference between layers lowers the minimum fracture toughness contrast for fracture turning. However, when we consider the fact that a large horizontal stress difference is only expected in deep reservoirs where the required fracture toughness contrast for the fracture

turning is around 10, the effect of horizontal principal stress difference (the reduction of the minimum fracture toughness change order of 1.0 – 2.0) may not significantly affect the fracture turning behavior (practically not turning only by horizontal stress difference).

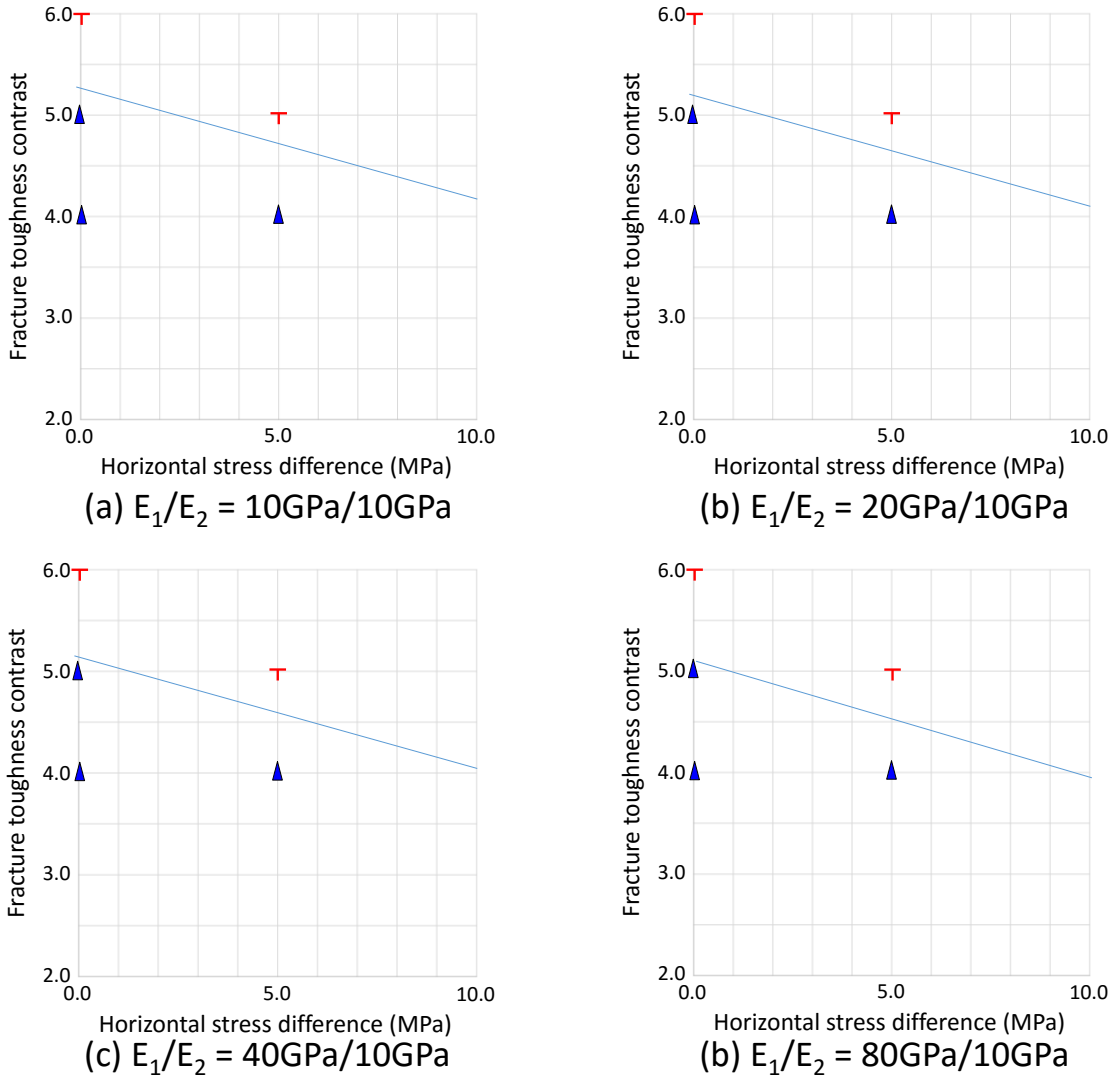

Fig. 6.27 Effect of horizontal stress difference.

6.2.6 EFFECT OF WEAK SURFACE

In the previous sections, we investigated the effect of several mechanical properties based on the assumption that layer interface is fully bonded (in other words, the layer interface is not allowed to be damaged). However, layer interfaces are not always strongly bonded. Sometimes, they can be weakly bonded and easily slip along the layer interface. In order to analyze the effect of a weak layer interface on fracture propagation, we apply the following shear failure parameter (shear coefficient = 0.6, cohesion = 0.0 MPa) to the layer interface in the cases shown in Fig. 6.13, Fig. 6.15, and Fig. 6.16 ("original cases"), and simulate fracture propagation in these cases ("weak surface cases"). Note that, in these cases, all the parameters except the shear failure parameters are the same as the original cases.

Fig. 6.28 - Fig. 6.30 show the fracture propagation behavior near the layer interface for the different layer dip angle cases (0 degree, 15 degree, and 30 degree cases in the weak surface cases respectively). As shown in these figures, the minimum fracture toughness contrasts for fracture turning in the weak surface cases are lower than the original cases for all layer dip angles. However, the degree and the criteria for fracture turning are very different depending on the layer dip angles. As shown in Fig. 6.28, in the 0 degree cases, even if the cohesion of the layer interface is zero, the difference of the minimum fracture toughness contrast for fracture turning between the original cases and the weak surface cases is less than 1.0. Since the initial normal stress acting on the layer interface is equivalent to the maximum principal stress in these cases, shear failure along the layer interface is difficult and unlikely to occur. These results show that fracture turning is not expected in deep reservoirs even if the layer interface is weak. Note that fracture branching is not observed in the low fracture toughness region in the highest Young's modulus case (see Fig. 6.28 (d)) since the harder layer cannot limit the displacement of the softer layer

due to shear slip. Shear slip prevents fracture branching in the highest Young's modulus contrast case.

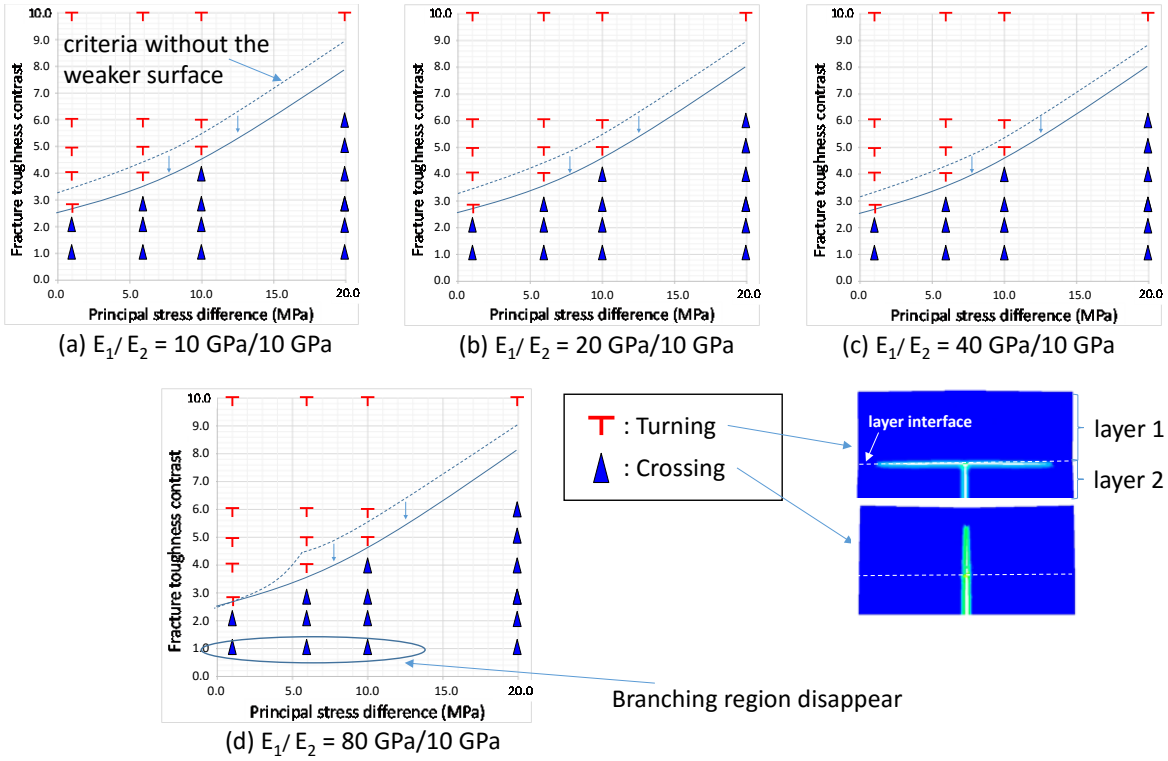

Fig. 6.28 Fracture turning behavior (weak surface cases: layer dip angle = 0 degree).

As shown in Fig. 6.29, in the 15 degree cases, the differences of the minimum fracture toughness contrast for fracture turning between the original cases and the weak surface cases are larger than for the 0 degree cases since shear failure is more likely to occur along the layer interface. A 1.5 to 2.0 reduction in the fracture toughness contrast is observed in these cases. Note that, as shown in Fig. 6.29, the extent of fracture kinking is smaller in the weak surface cases than in the original cases. In these cases, since Layer 2 can slip along the layer interface, the displacement of the layer 2 is not limited by Layer 1, which results in more straight fracture propagation into Layer 2.

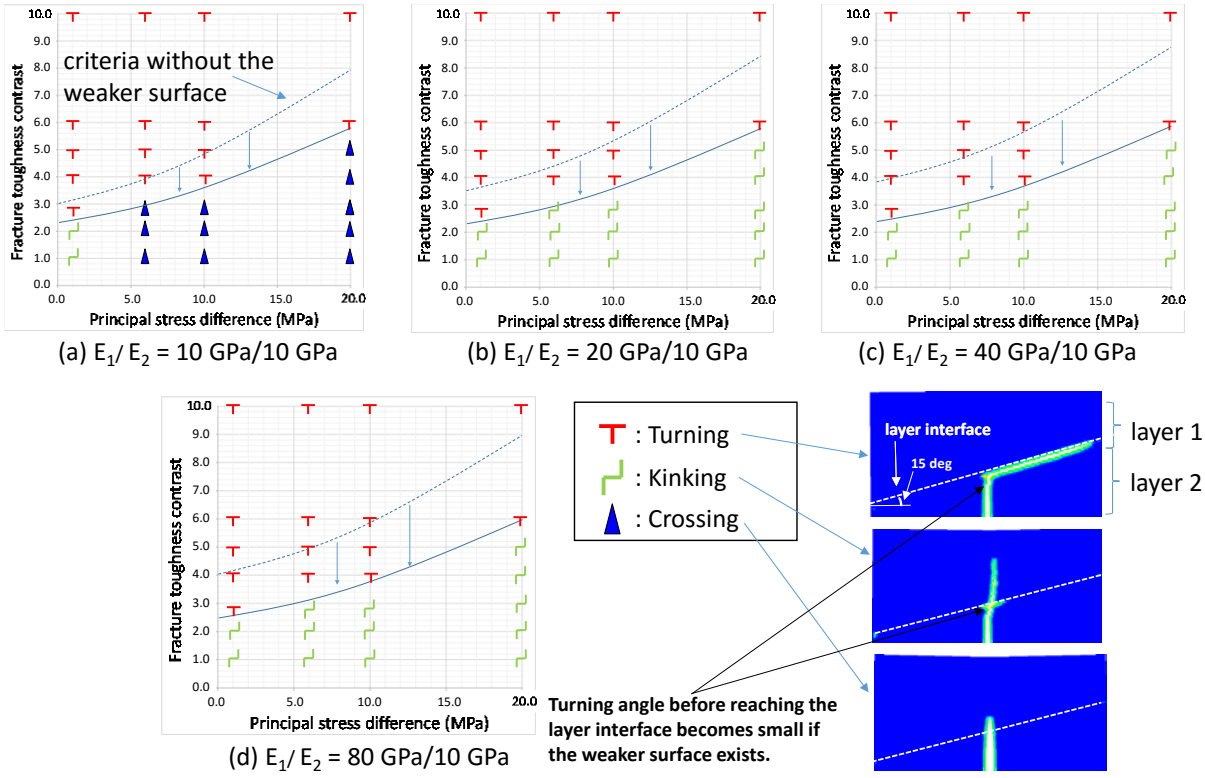

Fig. 6.29 Fracture turning behavior (weak surface cases: layer dip angle = 15 degree).

As shown in Fig. 6.30, in the 30 degree cases, the fractures always turn along the layer interface regardless of the principal stress difference and the fracture toughness contrast since shear failure always occurs along the layer interface. A weak layer interface has a significant influence on fracture turning in high dip angle layers.

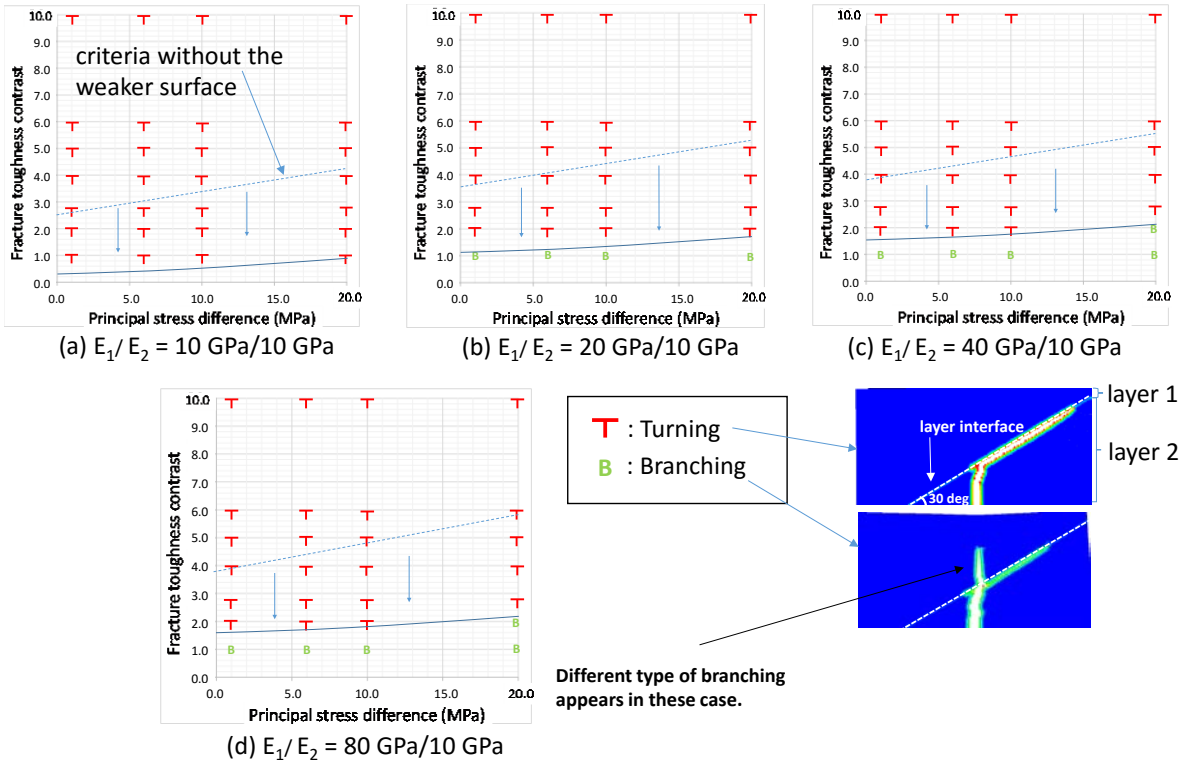

Fig. 6.30 Fracture turning behavior (weak surface cases: layer dip angle = 30 degree).

6.3 Investigation of fracture propagation behavior in three layer cases

In the previous section, we investigated how a fracture propagates near a layer interface by using a two layer model. As shown in the previous section, since we simulate only one wing of the fracture, possible fracture propagation behaviors at the layer interface was limited to "crossing" the layer interface or "turning" along the layer interface. However, it is also interesting to study situations in which both wings of the fracture propagate across layers with different layer properties. At such cases, as shown in Fig. 6.31, it is possible that only one side of the fracture crosses the layer interface while the other side of the fracture stops at the layer interface.

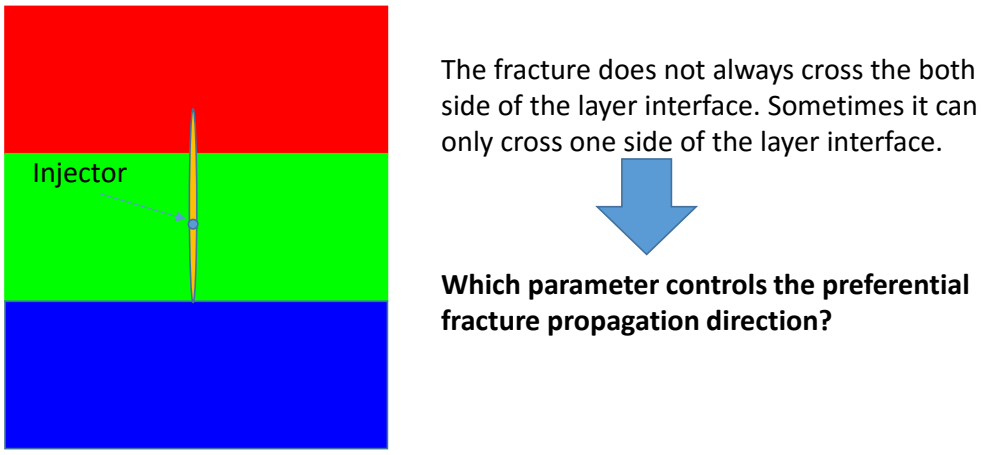

Fig. 6.31 Fracture propagation in multiple layers.

In order to analyze which parameter controls fracture propagation, we simulate fracture propagation in a three layer model which has a 30 cm by 30 cm domain size (Fig. 6.32). In this model, the model domain is divided into 150×150 elements. The upper one-thirds, the middle one-thirds, and the bottom one-thirds of the model domain (30 cm×30 cm each) are assigned to the layers 1, 2 and 3 respectively. For the fluid flow calculation, constant initial pore pressure P is assigned to every element. No flow boundary

conditions are applied to every boundary for the fluid flow calculation. For the mechanical calculations, through the background force vector state method (introduced in Section 4.2.2.5), a constant vertical stress σ_V and different horizontal stresses for each layer (σ_{H1}, σ_{H2}, and σ_{H3}) are applied to each element depending on the layer number as a vertical principal stress and a horizontal principal stress respectively. In addition, from the top and the bottom of the model domain, a normal stress of magnitude σ_V is applied as traction boundary condition. Also, from the left side and the right side of the model domain, the normal stress of magnitude of σ_{H1}, σ_{H2}, and σ_{H3} are applied to Layers1, 2, and 3 respectively as a traction boundary condition.

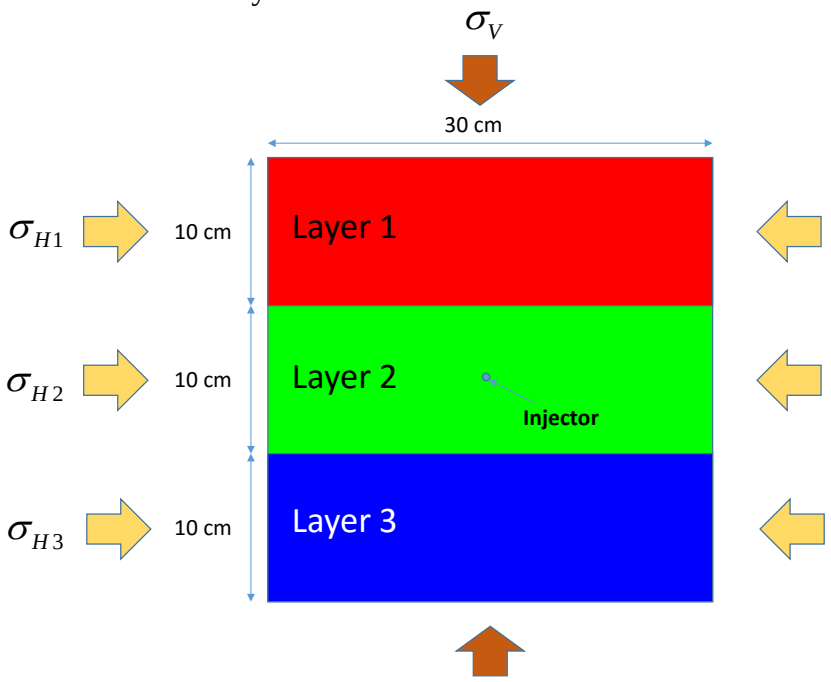

Fig. 6.32 Schematic view of the 3 layer model.

By changing the mechanical property and horizontal principal stress in each layer, we investigated how the preferential fracture propagation direction changes. Table 6.8 shows the common parameter settings for the 3 layer cases. Table 6.9 shows the case settings of

the 3 layer cases. Note that, to simplify the investigation of the results, the Young's modulus of Layer 3 is always lower than Layer 1 in all these cases.

Table 6.8 Common calculation settings (3 layer case).

Parameter	Value
Dimension in horizontal direction L_x (cm)	30.0
Dimension in vertical direction L_y (cm)	30.0
Layer 1 thickness (cm)	10.0
Layer 2 thickness (cm)	10.0
Layer 2 thickness (cm)	10.0
Boundary stress in vertical direction σ_V (MPa)	60.0
Boundary stress in horizontal direction σ_{H1}, σ_{H2}, and σ_{H3} (MPa)	Table 6.9
Young's modulus E_1, E_2, and E_3 (GPa)	Table 6.9
Shear modulus G_1, G_2, and G_3 (GPa)	Table 6.9
Fracture toughness K_{IC1}, K_{IC2}, K_{IC3}	Table 6.9
Initial pore pressure P (MPa)	28.5
Injection rate (kg/s/m)	0.01
Fracturing fluid viscosity (cp)	1.0
Medium permeability (mD)	0.00001
Number of elements	150×150
Horizon size ($= \frac{\delta}{\Delta x}$)	3.0

Table 6.9 Case parameter settings (3 layer case).

Case	Case1	Case2	Case3	Case4	Case5	Case6	Case7	Case8
Young's modulus in layer1 E_1 (GPa)	40	20	40	40	40	40	40	40
Young's modulus in layer2 E_2 (GPa)	20	40	10	12	20	20	20	20
Young's modulus in layer3 E_3(GPa)	10	10	20	10	10	10	10	10
Shear modulus in layer1 G_1(GPa)	16	8	16	16	16	16	16	16
Shear modulus in layer2 G_2(GPa)	8	16	4	4.8	8	8	8	8
Shear modulus in layer3 G_3(GPa)	4	4	8	4	4	4	4	4
Fracture toughness in layer1 K_{IC1} (MPa $m^{0.5}$)	0.707	0.500	0.707	0.707	1.200	1.600	0.707	0.707
Fracture toughness in layer2 K_{IC2} (MPa $m^{0.5}$)	0.500	0.707	0.354	0.500	0.500	0.500	0.500	0.500
Fracture toughness in layer3 K_{IC3} (MPa $m^{0.5}$)	0.354	0.354	0.500	0.354	0.354	0.354	0.354	0.354
Horizontal stress in layer1 (MPa)	40	40	40	40	40	40	45	50
Horizontal stress in layer2 (MPa)	40	40	40	40	40	40	40	40
Horizontal stress in layer3 (MPa)	40	40	40	40	40	40	40	40
Energy release rate in layer 1 G_{e1}(J/m^2)	11.7	11.7	11.7	11.7	23.4	33.8	11.7	11.7
Energy release rate in layer 2 G_{e2}(J/m^2)	11.7	11.7	11.7	19.5	11.7	11.7	11.7	11.7
Energy release rate in layer 3 G_{e3}(J/m^2)	11.7	11.7	11.7	11.7	11.7	11.7	11.7	11.7
K_{IC1}/E_1*1000	0.018	0.025	0.018	0.018	0.030	0.040	0.018	0.018
K_{IC2}/E_2*1000	0.025	0.018	0.035	0.042	0.025	0.025	0.025	0.025
K_{IC3}/E_3*1000	0.035	0.035	0.025	0.035	0.035	0.035	0.035	0.035

Fig. 6.33 – Fig. 6.40 show the calculation results for some of the 3 layer cases. As shown in these figures, the fractures always preferentially propagate toward the layer with the lower Young's modulus due to less constraints on the displacement from the lower Young's modulus layer. However, after the fractures reach the layer interface between the middle layer and the lower Young's modulus layer (the lower interface), the fracture propagation behaviors are mainly categorized into three groups. In the first group (Case1, Case2, and Case 5), as shown in Fig. 6.33, Fig. 6.34, and Fig. 6.37, after the fractures reach the lower interface, they stop at the lower layer interface, and begin to propagate to the harder Young's modulus layer and finally pass through the layer interface between the middle layer and the harder Young's modulus layer (the upper interface). In the second

group (Case 3, and Case4), as shown in Fig. 6.35 and Fig. 6.36, after the fractures reach the lower interface, they cross the lower interface without stopping. In the third group (Case 6, Case 7 and Case 8), as shown in Fig. 6.38, Fig. 6.39, and Fig. 6.40, the fracture propagation behaviors are the same until the fractures reach the upper interface. However, after reaching the upper interface, the lower fracture tip begins to propagate again and crosses the lower interface in these cases. The upper fracture tip movements are different for each case. The fractures stop at the upper interface and begin to propagate in the lower direction again in Case 6 and Case 8. On the other hand, the fracture crosses both the upper and lower interfaces in Case 7.

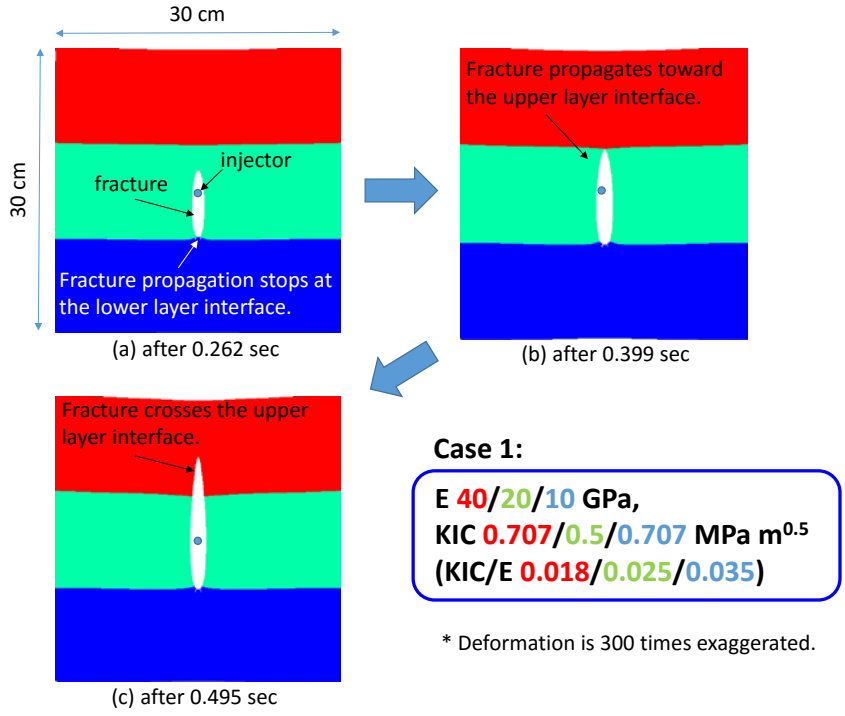

Fig. 6.33 Fracture propagation with time (Case 1).

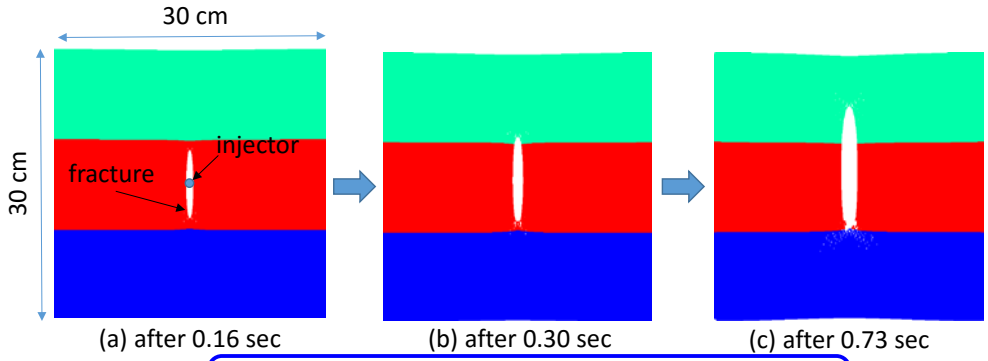

Fig. 6.34 Fracture propagation with time (Case 2).

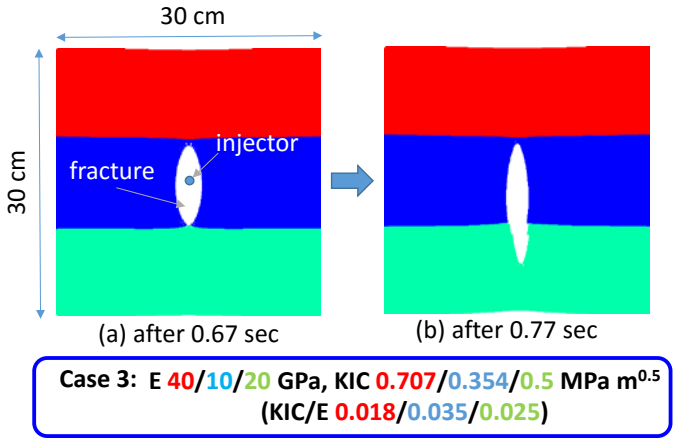

Fig. 6.35 Fracture propagation with time (Case 3).

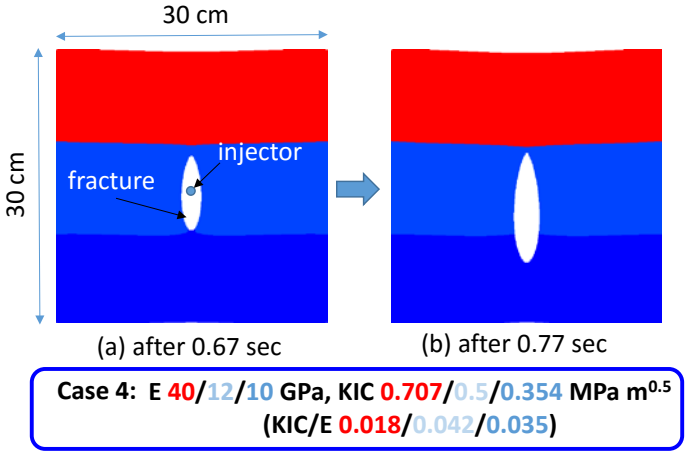

Fig. 6.36 Fracture propagation with time (Case 4).

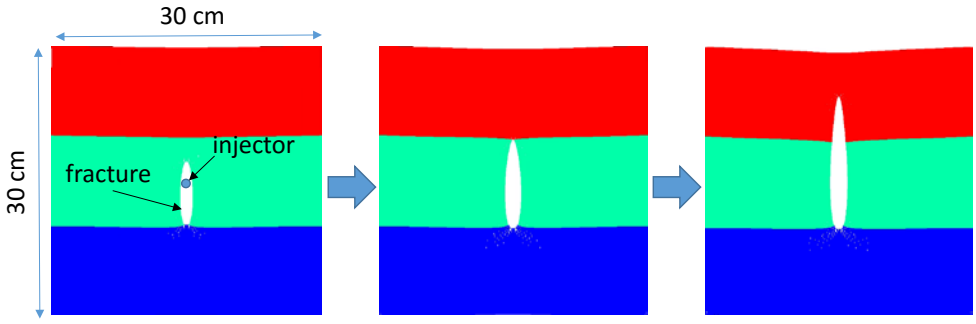

Case 5: E 40/20/10 GPa, KIC 1.2/0.5/0.354 MPa $m^{0.5}$ (KIC/E 0.03/0.025/0.035)

Fig. 6.37 Fracture propagation with time (Case 5).

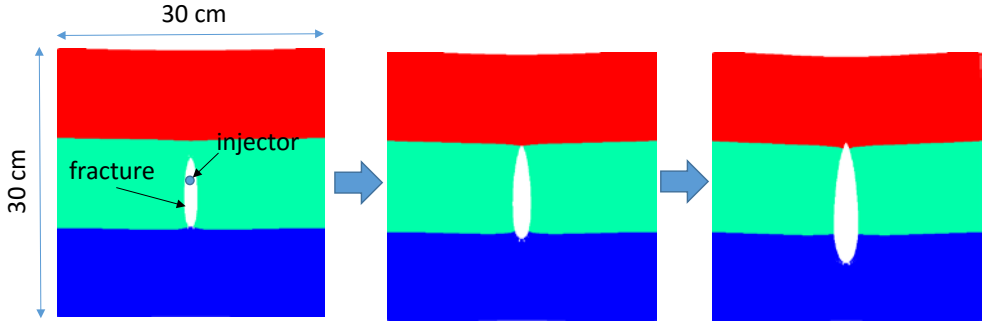

Case 6: E 40/20/10 GPa, KIC 1.6/0.5/0.354 MPa $m^{0.5}$ (KIC/E 0.04/0.025/0.035)

Fig. 6.38 Fracture propagation with time (Case 6).

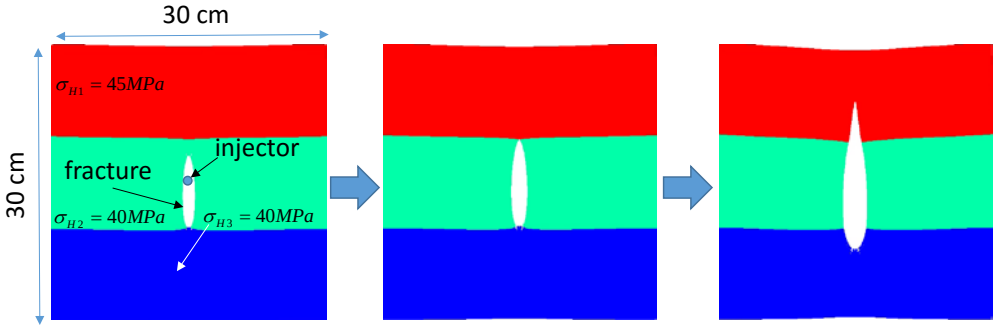

Case 7: E 40/20/10 GPa, KIC 0.707/0.5/0.354 MPa $m^{0.5}$ (KIC/E 0.018/0.025/0.035)

Fig. 6.39 Fracture propagation with time (Case 7).

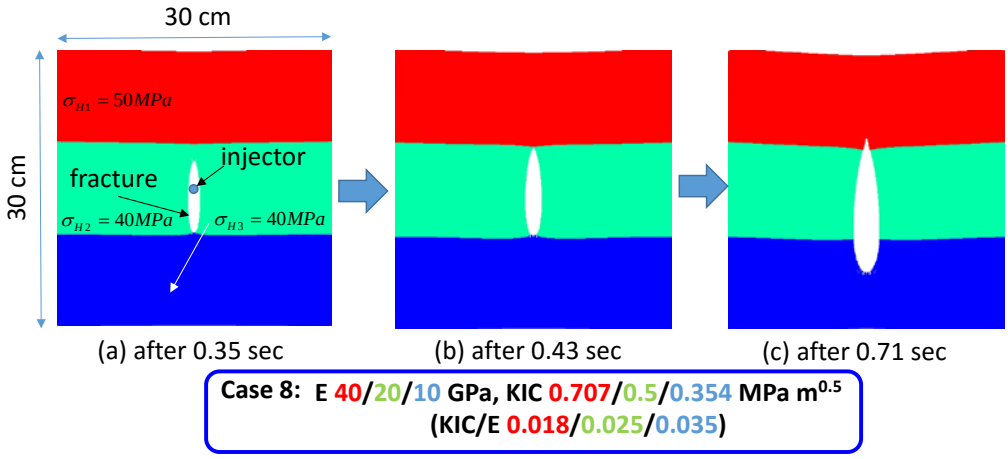

Fig. 6.40 Fracture propagation with time (Case 8).

As clearly shown in these cases, the fracture propagation tendencies cannot be explained by the critical energy release rate in each layer (the fracture propagation directions are different case by case even if the critical energy release rates are the same). However, those tendencies can be explained by the critical displacement shown in Equation (6.8). Here, for simplicity if we neglect the effect of initial far field stress from Equation (6.8) and only consider the critical displacement of the shortest bond (r = δ / 3 when $\delta / \Delta x = 3.0$), the critical displacement of a bond is expressed as follows,

$$\|\boldsymbol{\eta}\|_{crit} = \frac{5}{8}\sqrt{\frac{3\pi\delta}{8}}\frac{K_{IC}}{E} \tag{6.18}$$

As shown in this equation, the critical displacement of the bond in each layer is proportional to the value of the fracture toughness over the Young's modulus. Therefore, as shown in Table 6.9, if we calculate the value of the fracture toughness over the Young's modulus in each layer, we can approximate the relative difference of the critical displacements among the layers. As shown in Table 6.9, in Case 1, Case 2, and Case 5, the following relationships are observed among the critical displacements of the layers.

$$\left\|\boldsymbol{\eta}\right\|_{crit\_layer3(softer\_side)} > \left\|\boldsymbol{\eta}\right\|_{crit\_layer2} \tag{6.19}$$

$$\left\|\boldsymbol{\eta}\right\|_{crit\_layer3(softer\_side)} > \left\|\boldsymbol{\eta}\right\|_{crit\_layer1(harder\_side)} \tag{6.20}$$

Where,

$\left\|\boldsymbol{\eta}\right\|_{crit\_layer1(harder\_side)}$: the critical displacement of Layer 1 [m]

$\left\|\boldsymbol{\eta}\right\|_{crit\_layer2}$: the critical displacement of Layer 2 [m]

$\left\|\boldsymbol{\eta}\right\|_{crit\_layer3(softer\_side)}$: the critical displacement of Layer 3 [m]

In these cases, since the critical displacement of the softer side layer (Layer 3) is higher than the critical displacement of the middle layer (1.4 times difference in Case 1 and Case 5, 1.9 times difference in Case 2), the fracture cannot propagate at the lower interface until the horizontal displacement of Layer 3 reaches the critical displacement. While waiting for the lower side displacement, the fracture propagates toward the upper interface. Since the upper side displacement is constrained by the harder layer, slightly higher bottom hole flowing pressure (BHP) is required for fracture propagation in the upper direction than in the lower direction. However, the required bottom-hole pressure (BHP) change is smaller than the required BHP change for crossing the lower interface in the cases where at least 1.4 times critical displacement contrasts are overcome. Therefore, the fracture reaches the upper interface before the fracture crosses the lower interface in these cases. After the fracture tip reaches the upper layer interface, as shown in Equation (6.20), since the critical displacement of the harder layer (the layer 1) is smaller than the critical displacement of the harder layer (the layer 3), the fractures finally crosses the upper layer interface in Case 1, Case 2, and Case 5. Note that, in Case 5, the fracture crosses the upper interface rather than the lower interface even if the critical energy release rate in Layer 1 is

twice as much as in Layer 3. This result suggests that the critical displacement contrast has a much more dominant effect for preferential fracture propagation among layers than the contrast in energy release rates.

If the following condition is satisfied (the critical displacement of the harder layer is larger than the softer layer) in addition to Equation (6.19) such as in Case 6,

$$\|\boldsymbol{\eta}\|_{crit\_layer3(softer\_side)} < \|\boldsymbol{\eta}\|_{crit\_layer1(harder\_side)} \tag{6.21}$$

the fracture stops at the higher interface and crosses the lower interface since the critical displacement of the lower side is smaller than the upper side.

Not only critical displacement of each layer but also the initial horizontal stress difference in each layer affects the preferential fracture propagation direction. If the initial horizontal stress in the harder layer (Layer 1) is sufficiently higher than the other layers such as in Case 8 (the effective initial horizontal stress in Layer 1 is 10 MPa higher than the other layers), the fracture stops at the harder layer and crosses the lower interface. In this case, as shown in Fig. 6.41, since the BHP is lower than the initial horizontal stress in Layer 1, the fracture cannot deeply move into Layer 1. The upper fracture propagation stops near the upper layer interface in Layer 1, and only the lower side continues to propagate in this case. If the horizontal stress of Layer 1 is not sufficiently higher than the other layers to prevent fracture propagation such as in Case 7 (the effective initial horizontal stress in the layer 1is 5 MPa higher than the other layers), the fracture propagates in both directions. Note that, since the net pressure is high in these simulations due to the small domain size, the effect of horizontal stress is underestimated in these simulations. In actual hydraulic fracturing jobs, the net pressure becomes much smaller than in these

simulations. For such cases the horizontal stress difference may be the most dominant factor for deciding whether the fracture crosses the layer interface or not.

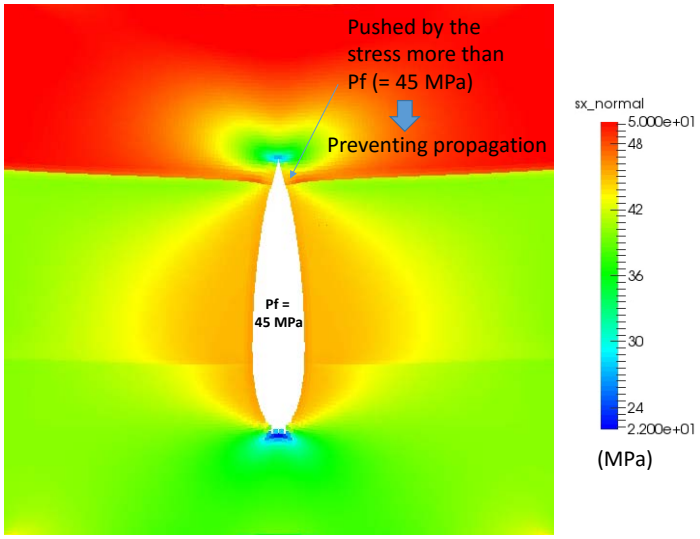

Fig. 6.41 Horizontal stress distribution after 1.0 sec (Case 8).

All the previous cases explained above (Case 1, Case 2, Case 5, Case 6, Case 7 and Case 8) satisfied Equation (6.19) (the critical displacement of Layer 2 is lower than Layer 3). However, if the critical displacement of the middle layer is larger than the critical displacement of the softer layer (in other words, Equation (6.19) is not satisfied) such as in Case 3 and Case 4, the fracture propagation behavior is totally different from the previous cases. In these cases, as shown in Fig. 6.35, Fig. 6.36, since the critical displacement of the middle layer is higher than that of the softer layer, the fractures cross the lower interface without stopping.

6.4 Investigation of the fracture propagation behavior in multiple layer cases (effect of small scale heterogeneity)

In shale gas reservoirs, mechanical property distribution in vertical direction is highly heterogeneous. As Passey et al. [116] point out, mineralogical changes in shale gas reservoirs can be observed at the order of mm and cm scale as well as meter scale (Fig. 6.42).

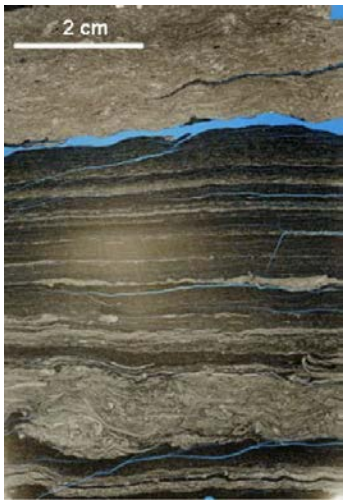

Fig. 6.42 Example of the cm order vertical heterogeneity (taken from [116]).

In this section, we investigated, how fracture propagation is affected if this kind of small scale heterogeneity (cm scale heterogeneity) exists in the reservoir. We prepare the two types of models ("Model 1" and "Model 2") which have a 30 cm×30 cm model domain and consist of 150×150 elements. Both models are divided into multiple layers which have constant thickness (= 2 cm). The layer dip angle of Model 1 is 0 degrees, while the layer dip angle for Model 2 is 30 degrees. As shown in Fig. 6.43, in order to represent small scale vertical heterogeneity, we alternatively assign two different sets of mechanical properties

to each layer in both models. As shown in Fig. 6.44, one of two different stress initialization methods is applied in each case (Initialization 1 or Initialization 2).

- **Initialization 1 (assuming homogeneous stress distribution)**: At time t < 0, a constant horizontal stress (σ_H = 40 MPa) and vertical stress (σ_V = 60 MPa) are assigned to each element through the background stress tensor method.
- **Initialization 2 (assuming zero strain in horizontal direction):** At time t < 0, a roller boundary condition is applied to the side boundaries (no deformation in the horizontal direction) and only a normal traction of magnitude (σ_V = 60MPa) is applied to the top and the bottom boundary. At time t >= 0, the roller boundary condition applied to the side boundaries is replaced by constant traction boundaries which gives the same traction as the roller boundary condition in order to allow horizontal displacement of the side boundaries due to fracture propagation.

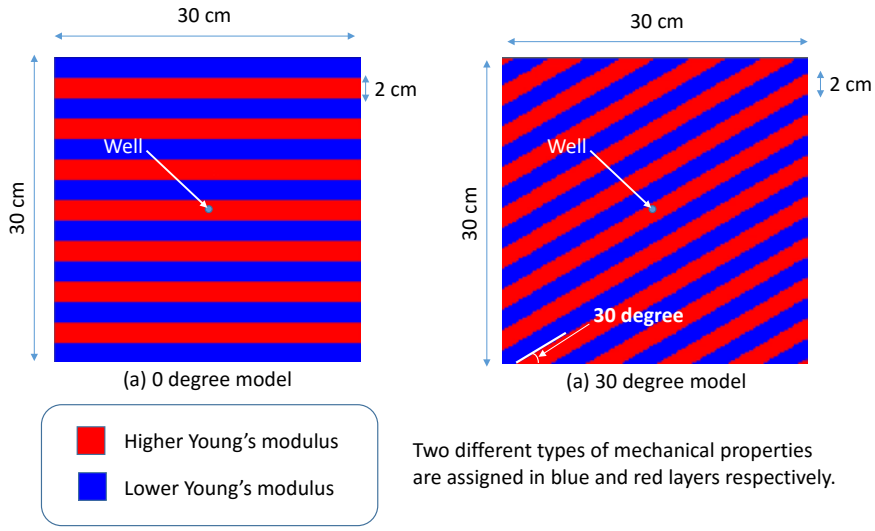

Fig. 6.43 Model description (0 degree and 30 degree dip).

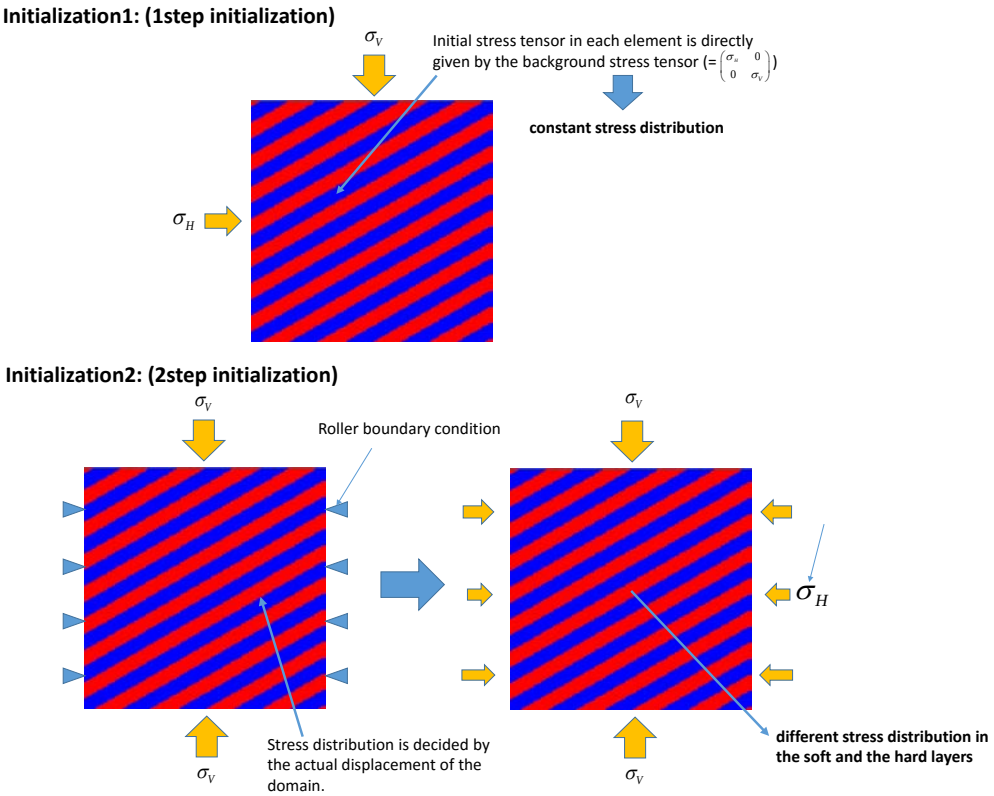

Fig. 6.44 Two different initialization.

After stress initialization (at time t >= 0), water is injected from the "injection dual point" at the center of the model domain at constant rate to propagate a fracture. We investigated the effect of small scale heterogeneity on fracture propagation by changing the contrast in mechanical properties and the initial stress distribution in both models. Table 6.10 shows the case settings. Table 6.11 shows the common calculation settings for these cases. In these cases, we assumed that the energy release rate is the same both in the higher Young's modulus layer and the smaller Young's modulus layer (except in the contrast-high 2 case and contrast-high 2_dip case). Fig. 6.45 shows the initial stress distribution in the cases where the Initialization 2 method is applied. Note that in Model 1 (layer dipping angle = 0), we only apply Initialization1 to all the cases. However, since the Poisson's ratio is the

same (= 0.25) in every layer in these cases, if Initialization 2 is applied, it also gives the same initial stress distribution as Initialization 1.

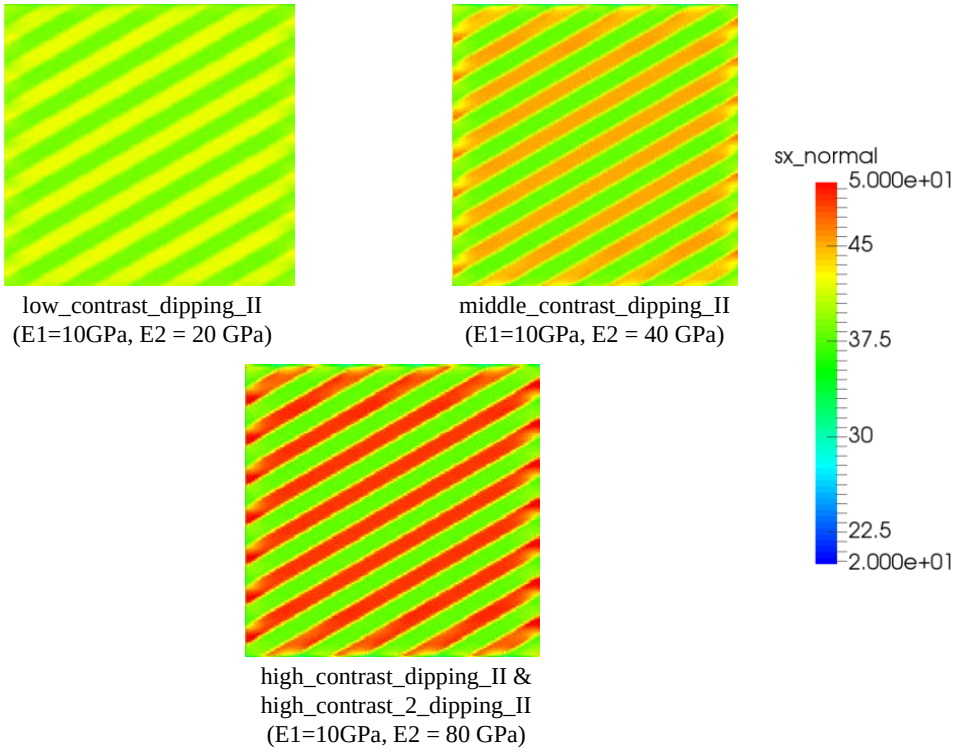

Fig. 6.45 Initial stress distribution (Initialization2 Cases)

Table 6.10 Case settings for multi-layer cases.

Case	Initialization	Young's modulus 1 (GPa)	Young's modulus 2 (GPa)	Fracture toughness 1 (MPa $m^{0.5}$)	Fracture toughness 2 (MPa $m^{0.5}$)	Energy release rate contrast between layers (hard layer/soft layer)	Layer dip angle
low_contrast	1	10	20	0.5	0.707	1.00	0
middle_contrast	1	10	40	0.5	1.000	1.00	0
high_contrast	1	10	80	0.5	1.414	1.00	0
high_contrast_2	1	10	80	0.5	0.707	0.25	0
low_contrast_dipping	1	10	20	0.5	0.707	1.00	30
low_contrast_dipping_II	2	10	20	0.5	0.707	1.00	30
middle_contrast_dipping	1	10	40	0.5	1.000	1.00	30
middle_contrast_dipping_II	2	10	40	0.5	1.000	1.00	30
high_contrast_dipping	1	10	80	0.5	1.414	1.00	30
high_contrast_dipping_II	2	10	80	0.5	1.414	1.00	30
high_contrast_2_dipping	1	10	80	0.5	0.707	0.25	30
high_contrast_2_dipping_II	2	10	80	0.5	0.707	0.25	30

Table 6.11 Common calculation settings for multi-layer cases.

Parameter	Value
Dimension in horizontal direction L_x (cm)	30.0
Dimension in vertical direction L_y (cm)	30.0
Layer thickness (cm)	2.0
Boundary stress in vertical direction σ_V (MPa)	60.0
Boundary stress in horizontal direction σ_H (MPa)	40.0
Young's modulus E_1, E_2 (GPa)	Table 6.10
Poisson's ratio	0.25
Fracture toughness K_{IC1}, K_{IC2}	Table 6.10
Initial pore pressure P (MPa)	28.5
Injection rate (kg/s/m)	0.01
Fracturing fluid viscosity (cp)	1.0
Medium permeability (mD)	0.00001
Number of elements	150×150
Horizon size ($= \frac{\delta}{\Delta x}$)	3.0

Fig. 6.46 - Fig. 6.57 show the mechanical and fluid property distributions after fracture propagation. Note that the displacements are 50 times exaggerated in these figures. As shown in Fig. 6.46 and Fig. 6.47, in the cases where the layer dip angle is zero and the Young's modulus contrast is not very high (less than 4.0), the fractures just propagate in the maximum principal stress direction even if the vertical heterogeneity exists in the reservoir. However, as shown in Fig. 6.48, in the cases where the layer dip angle is zero and the Young's modulus contrast is very high (= 8.0), the fracture propagation is affected by the small scale heterogeneity in the reservoir. In this case, the fracture does not go straight, but branches at the layer interface when it propagates from the lower Young's modulus layer (softer layer) to the higher Young's modulus layer (harder layer) due to the pre-damage zone in the higher Young's modulus layer. As explained in Chapter 6.3, if the Young's modulus between the two layer is highly different, the required displacement for

the fracture propagation in the harder layer is much smaller than the softer layer (in this case, the critical displacement of the softer layer is about one-third of the harder layer). Therefore, the displacement induced by the fracture propagation in the softer layer can cause damage in the harder layer before the fracture tip reaches the layer interface, which finally causes fracture branching. As shown in Fig. 6.49, if the harder layer's energy release rate is smaller than the softer layer (contrast_high2 case: $G_{E\_hard} / G_{E\_soft} = 0.25$), branching is more clearly observed due to the higher critical displacement contrast between the harder layer and the softer layer. These high Young's modulus contrast cases demonstrate that even a thin (order 1 cm) high Young's modulus layer such as a calcite vein can cause fracture branching at the layer interface between the softer layer and the harder layer. When we take into account the published mechanical property of calcite (E = 84.3 GPa, K_{IC} = 0.19 MPa $m^{0.5}$)[117, 118], branching may occur in some reservoirs where calcite veins exist. Note that, due to the difficulty of convergence of the calculation when the fracture tips reach the pre-damage zone in the harder layer, the symmetricity of the fracture propagation is not perfectly kept in these high Young's modulus contrast cases. However, since the pre-damage zone in the harder layer has already existed before the fracture tip reaches the layer interface, branching is not the result of numerical instability.

If the layer has a high dip angle (30 degrees), regardless of the initial stress distribution (Initialization 1, assuming a homogeneous stress distribution) and Initialization 2 (assuming zero strain in the horizontal direction)), the fracture kinks at the layer interface even in the low Young's modulus contrast case ($E_{hard} / E_{soft} = 2.0$) since the fracture propagates in the propagation direction offering the least resistance. As shown in Fig. 6.50 and Fig. 6.51, in the dipping layers, the fracture turns as if avoiding the harder layer and staying in the softer layer. In addition, the fracture also turns towards the softer layer when propagating in the harder layer. Due to the combination of these two types of kinking in

the softer layer and the harder layer, the total kinking angle at the layer interface finally becomes more than 60 degrees in these cases. When the two different stress initializations are compared, Initialization 2 which has a higher horizontal stress contrast between the high Young's modulus layer and the low Young's modulus layer, the fracture is more likely to turn in the "low_contrast_dippingII" case (non-homogeneous stress distribution case) than the "low_contrast_dipping" case (homogeneous stress distribution case). The stress difference caused by mechanical property variations enhances fracture turning. As shown in Fig. 6.52 and Fig. 6.53, in the cases where the Young's modulus contrast is not as large ($E_{hard} / E_{soft} = 4.0$), the kinking angle of the fracture at the layer interface becomes higher (more than 70 – 80 degrees) than the lower Young's modulus contrast cases. The fracture turning angle in the non-homogeneous stress distribution case (middle_contrast_dippingII case) is higher than the homogeneous stress distribution case (middle_contrast_dipping case). In the cases where the Young's modulus contrast is the highest ($E_{hard} / E_{soft} = 8.0$), as shown in Fig. 6.54 and Fig. 6.55, the fracture kinks at around 80 – 90 degrees at the layer interface in both stress distribution cases. These layer dipping cases clearly show the tendency that the higher the Young's modulus contrast, the more local kinking is expected in a dipping layer. When compared with the two different stress initialization cases, the overall fracture propagation direction in the homogeneous initial stress distribution case is about 12 degrees deviated from the maximum principal stress direction (Fig. 6.54) while the overall fracture propagation direction in the non-homogeneous initial stress distribution case is almost parallel to the maximum principal stress direction (Fig. 6.55). As shown in Fig. 6.56 and Fig. 6.57, if the energy release rate in the harder layer is 25 % of the softer layer in the highest Young's modulus contrast cases, the fracture propagation geometries in the different stress initialization cases (high_contrast_2_dipping case and high_contrast_2_dipping case) also show very high turning angle (80 – 90 degrees).

However, the global fracture propagation direction in the uniform initial stress distribution case (high_contrast_2_dipping case) is different from the non-uniform initial stress distribution case (high_contrast_2_dippingII case). In the “high_contrast_2_dipping” case, as shown in Fig. 6.58, one observes the same kind of pre-damaged zone, as in the case where the layer dip angle is zero and the other conditions are the same. However, due to the layer dipping angle, the magnitude of the two pre-damage zones ahead of the fracture tip is not equivalent. One of the pre-damage zones which is closer to the principal stress direction in the softer layer grows more than the other side of the pre-damage zone due to the ease of fracture propagation. Therefore, the fracture preferentially selects the larger pre-damaged zone and the overall fracture propagation direction in this case is different from the “high_contrast_dipping” case. In the non-uniform stress distribution case (high_contrast_2_dippingII case), the pre-damage zones do not appear in the high Young’s modulus layers due to the high stress concentration in the high Young’s modulus layers. Therefore, the global fracture propagation direction is still same as the high_contrast_dipping-II case even if the fracture toughness in the high Young’s modulus layer is low.

These simulation results clearly show that, if the layer interface is inclined, the effect of cm scale sublayers on fracture propagation cannot be neglected. As Fisher et al. point out [110], kinking at the layer interface will affect proppant transport (screen out could occur) due to changes in the fracture width at the kinking point. In addition, the frequent kinking could also have a significant influence on the net pressure (fracturing fluid pressure distribution in the frequently kinked fracture geometry may be totally different from a single planar fracture). Judging from the kinking angle, even if the Young’s modulus contrast is low, inclined sub-layers could be an obstacle to fluid flow and proppant transport.

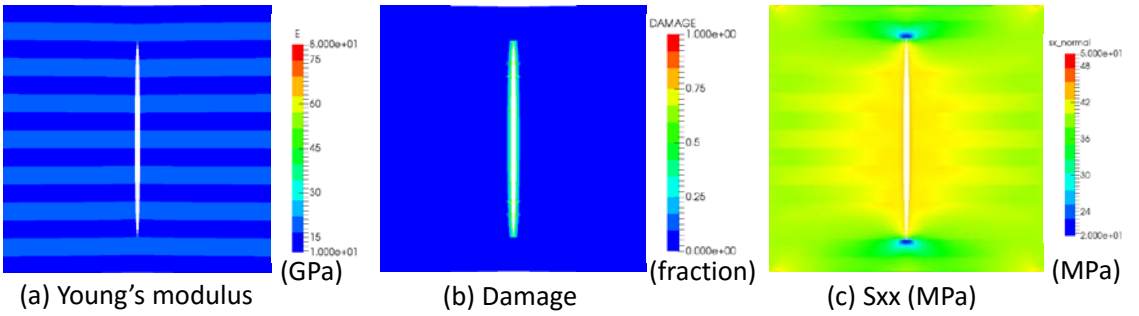

Fig. 6.46 Reservoir property distribution after 2.0 sec (contrast_low case).

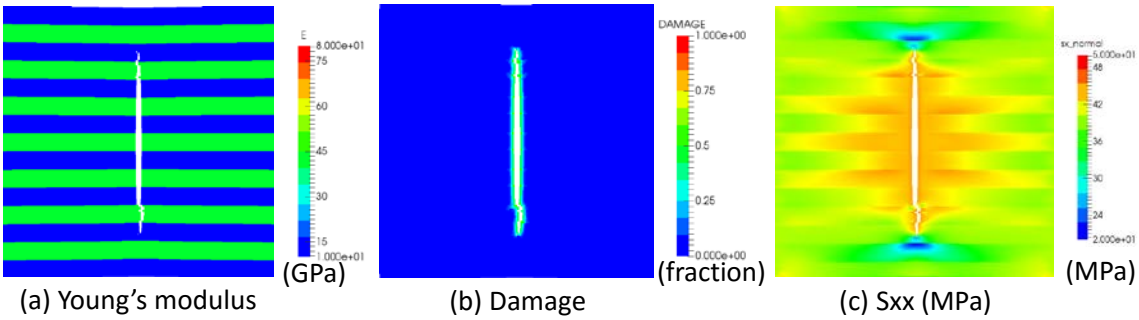

Fig. 6.47 Reservoir property distribution after 2.0 sec (contrast_middle case).

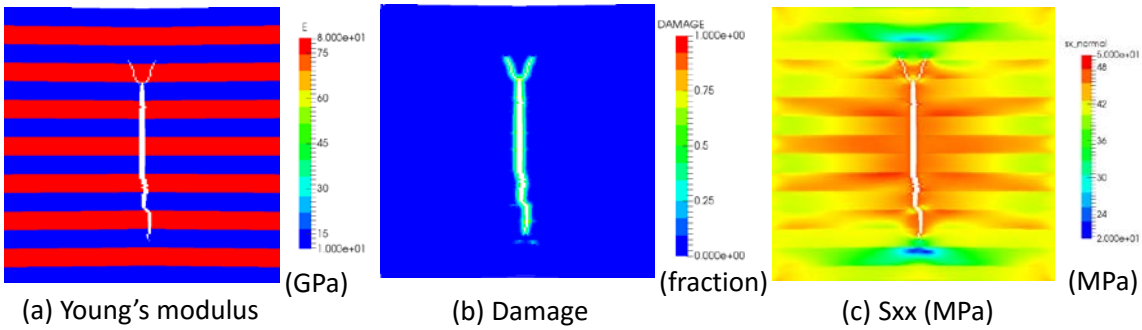

Fig. 6.48 Reservoir property distribution after 2.0 sec (contrast_high case).

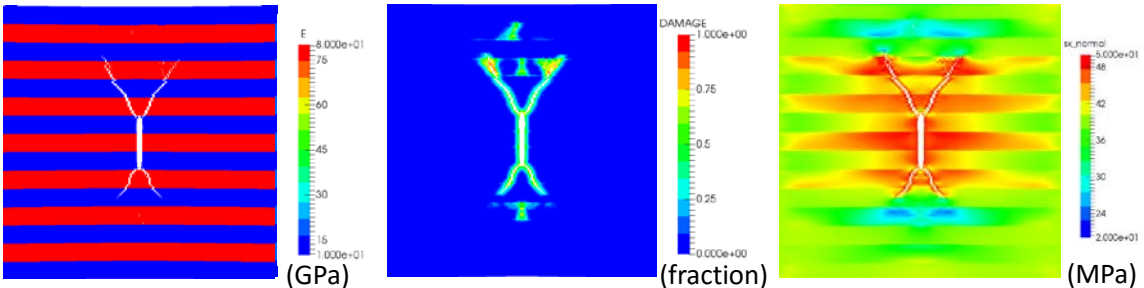

Fig. 6.49 Reservoir property distribution after 1.4 sec (contrast_high2 case).

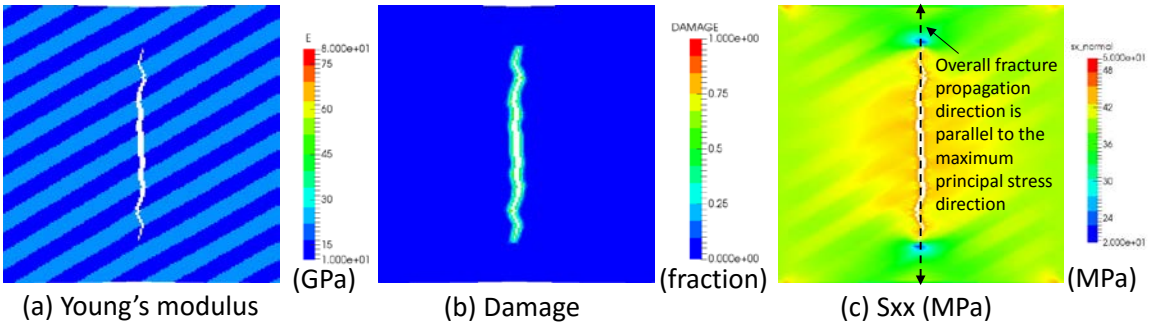

Fig. 6.50 Reservoir property distribution after 2.0 sec (contrast_low_dip case).

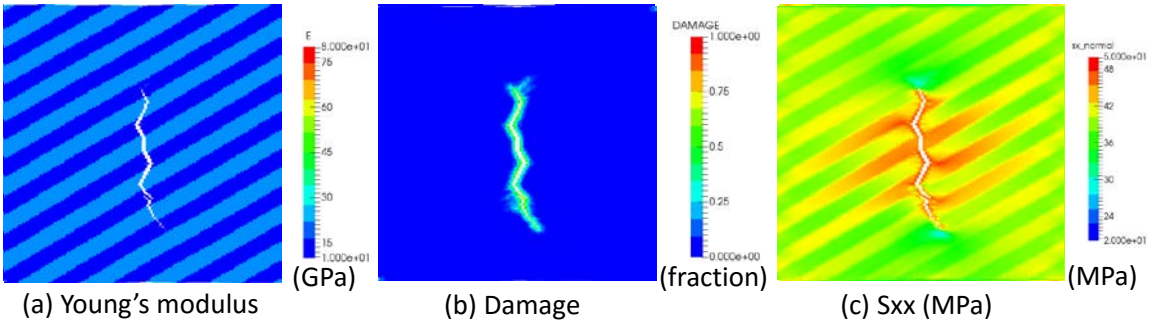

Fig. 6.51 Reservoir property distribution after 1.0 sec (contrast_low_dip caseII).

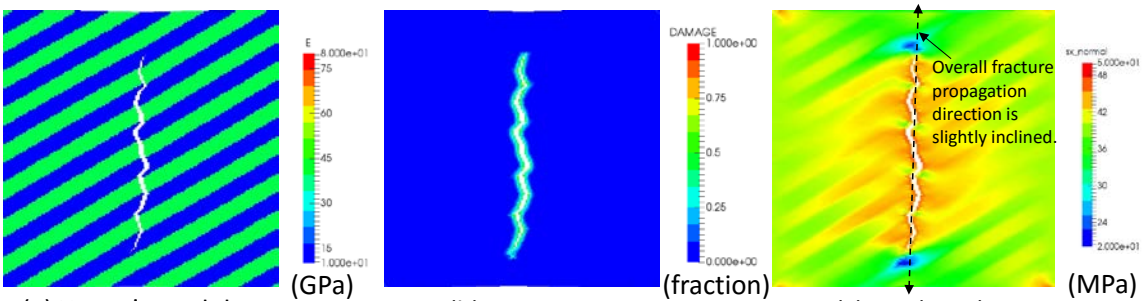

Fig. 6.52 Reservoir property distribution after 2.0 sec (contrast_middle_dip case).

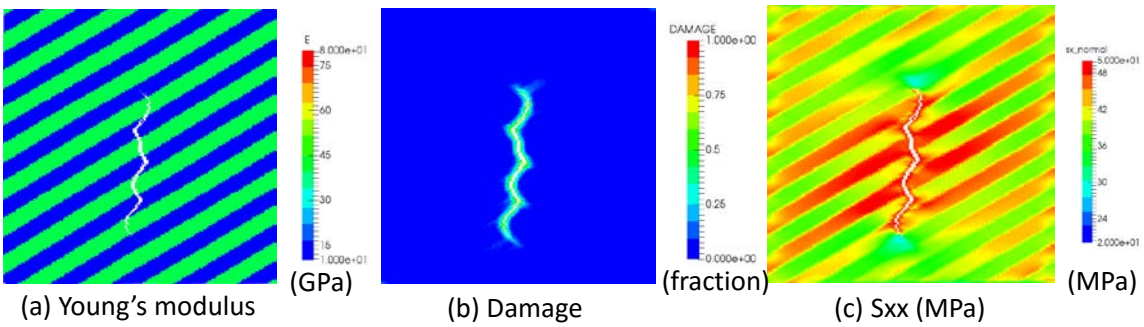

Fig. 6.53 Reservoir property distribution after 1.0 sec (contrast_middle_dip caseII).

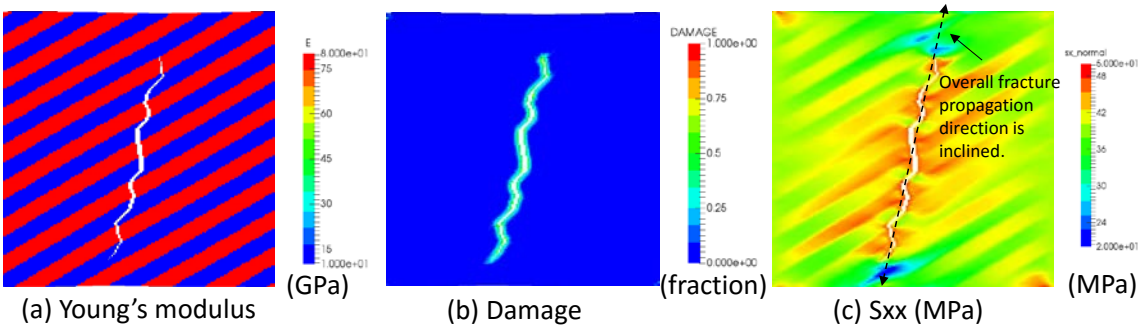

Fig. 6.54 Reservoir property distribution after 2.0 sec (contrast_high_dip case).

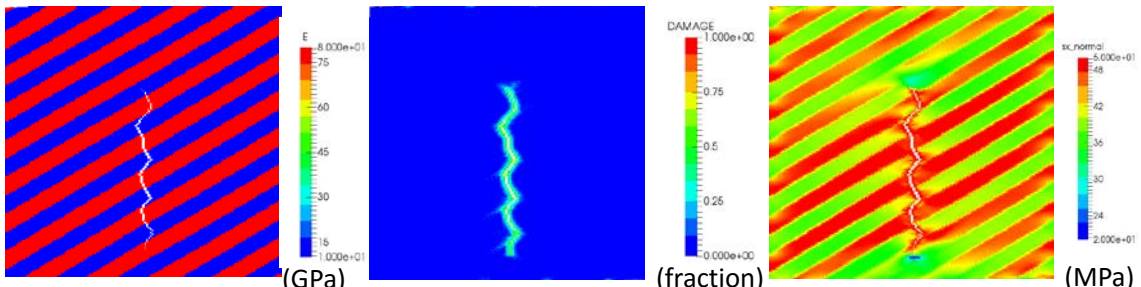

Fig. 6.55 Reservoir property distribution after 1.0 sec (contrast_high_dip caseII).

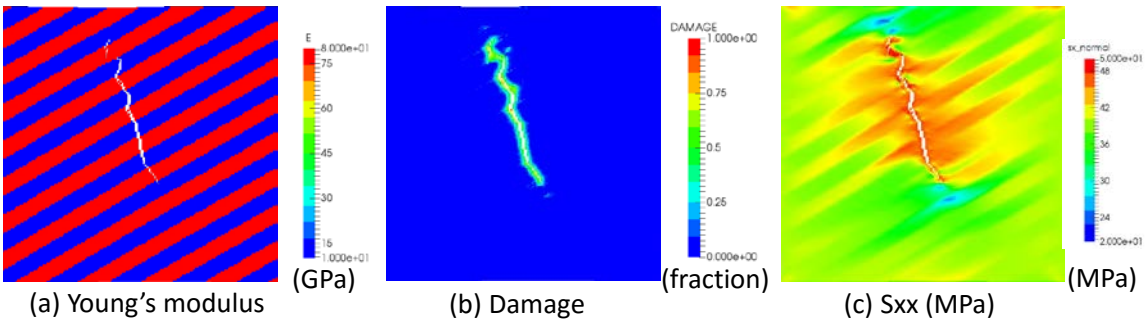

Fig. 6.56 Reservoir property distribution after 1.0 sec (contrast_high2_dip case).

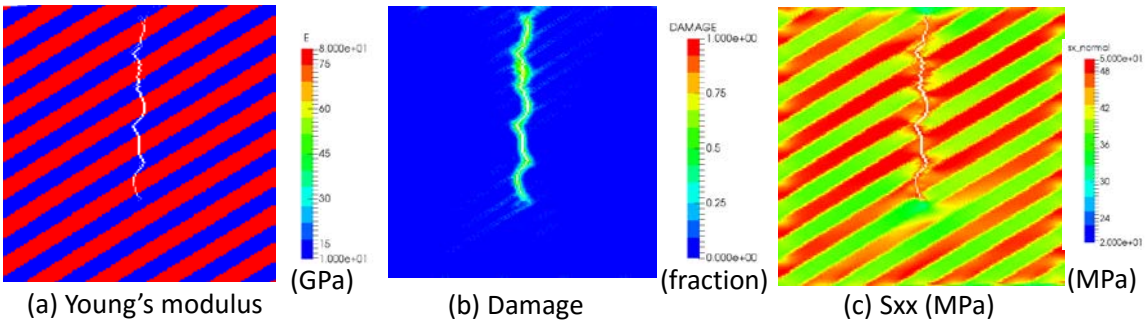

Fig. 6.57 Reservoir property distribution after 1.0 sec (contrast_high2_dip caseII).

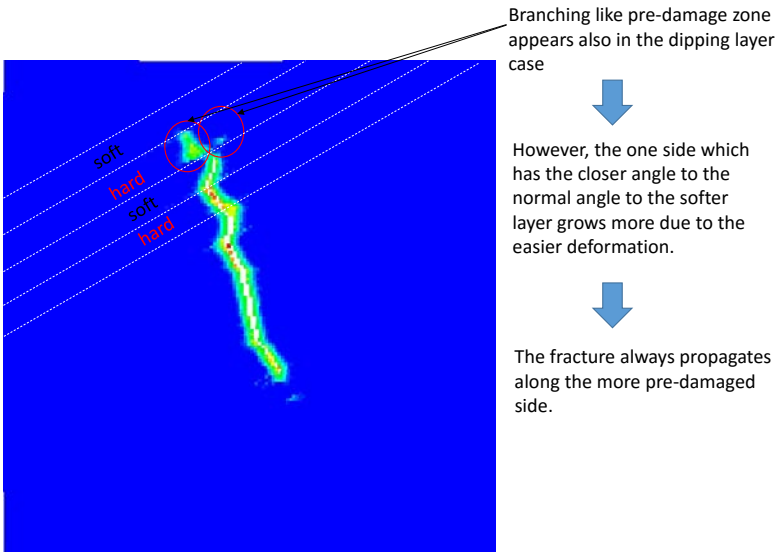

Fig. 6.58 Preferential fracture propagation direction (contrast_high2_dip case).

6.5 Investigation of microscale fracture propagation

In the previous section, we investigated how fracture propagation is affected by small scale heterogeneity (cm scale layer heterogeneity). In those simulations, we assumed that each layer is homogeneous. However, as shown in Fig. 6.53, if we extract a small area, at a mm scale (from a cm scale layer), this small section also displays large heterogeneity due to the existence of different mineral grains at a pore scale.

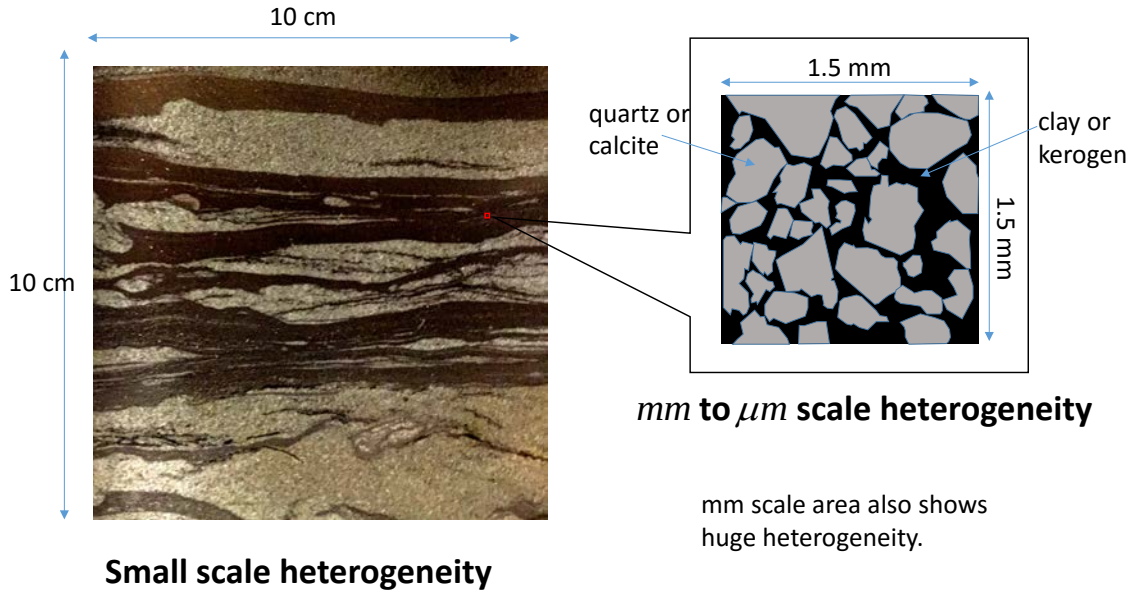

Fig. 6.59 Mm to μm scale heterogneity in oil and gas reservoirs.

In this section, we analyze how the fracture propagates in the small domain filled with mm to μm scale heterogeneity by using the mm scale model described below. We prepare the 2D plain strain model where the model domain ($1.5mm \times 1.5mm$) is divided into 200*200 elements (each element size = 7.5 μm). As shown in Fig. 6.54, the shape of the mineral distribution of the actual small scale rock sample picture [119], we define the three different mineral groups and assign one of the three different mineral groups

(group1, group 2, and group 3) to each element. Note that in our simulations we have only borrowed the shape of mineral grains from the original thin sections of other grain scale images. The mineral type assigned to each mineral group is not always consistent with the mineral types in the original reference. Since each mineral group has entirely different mechanical properties and is randomly distributed, there is a strong possibility that the initial stress distribution is highly heterogeneous both in the horizontal and vertical directions even under the common assumption that strain is almost zero in the horizontal direction (plain strain assumption). In order to initialize the stress distribution in the model, as shown in Fig. 6.55, at time t < 0, based on the plain strain assumption, a roller boundary condition is applied to the side boundaries (no deformation in the horizontal direction) and only normal traction of magnitude σ_V is applied to the top and the bottom boundary. Note that during this period, pore pressure is kept constant ($p = p_0$) due to the drained condition assumption. At time t >= 0, the roller boundary condition applied to the side boundaries are replaced by the traction boundaries in order to allow horizontal displacement of the side boundaries due to fracture propagation. The same magnitude of tractions that elements felt from the side boundaries in the initialization period are applied as a traction boundary condition in addition to the normal traction of magnitude σ_V applied to the top and the bottom boundary. To simulate a half-wing fracture, we set “injection dual points” as a water injector at the bottom of the model domain, and the bottom boundary (y- boundary) is constrained to be unable to deform in the vertical direction (by symmetry arguments). By changing the mineral type assigned to each mineral group, the critical energy density for the bonds across the two different minerals, and the initial stress distribution in the simulation domain, we investigated how the fracture propagation is affected by the type of minerals, their degree of connectivity, and initial stress distribution.

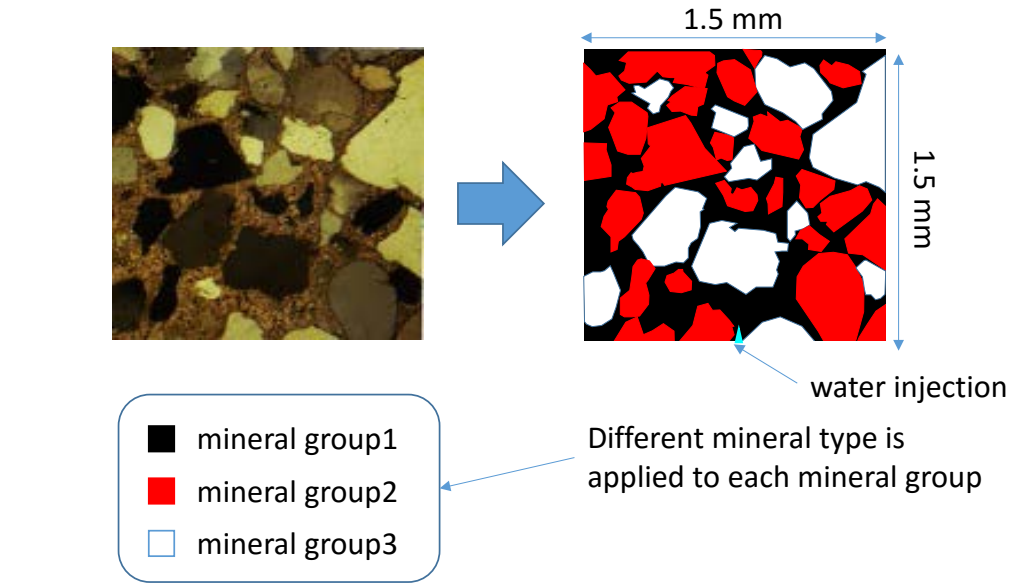

Fig. 6.60 Extraction of the shape and distribution of mineral groups from the actural rock sample picture (the rock sample picture is taken from [119]).

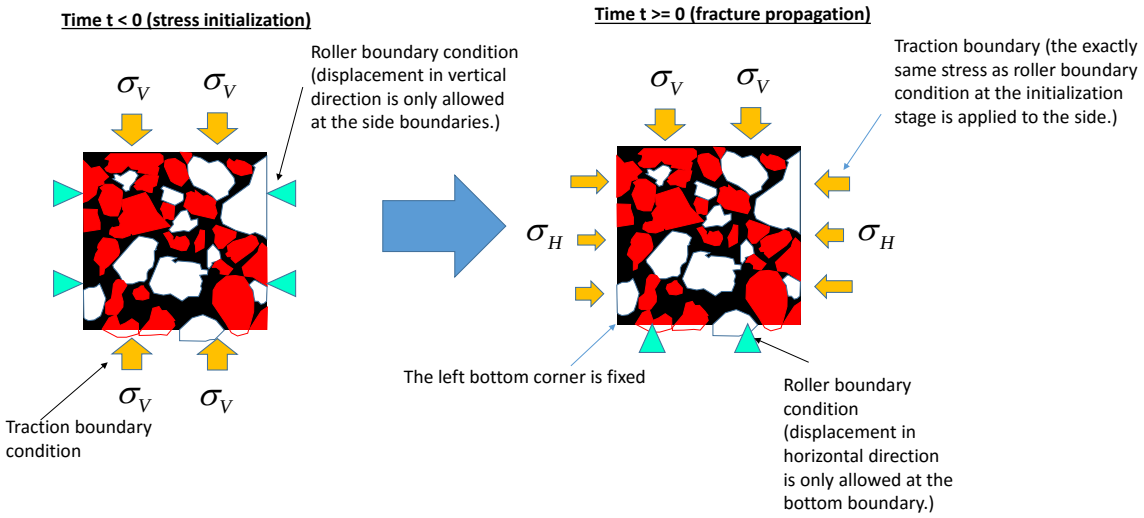

Fig. 6.61 Schematic view of the boundary setting for the stress initialization and fracture propagation.

Table 6.12 shows the mechanical property of the elements. Table 6.13 and Table 6.14 show the case settings and the common calculation settings of these simulations

respectively. Fig. 6.56 and Fig. 6.57 show the initial stress distribution in all simulated cases.

Table 6.12 Mineral mechanical properties ([118, 120]).

Mineral type	Young's modulus (GPa)	Shear modulus (GPa)	Fracture toughness (MPa $m^{0.5}$)
Quartz	**95.6**	**44.3**	**2.40**
Calcite	**83.8**	**32.0**	**0.19**
Clay	**10.0**	**4**	**0.50**

Table 6.13 Case settings (micro scale simulation).

Mineral type	Mineral group1	Mineral group2	Mineral group3	Multiplier for the critical energy density of the bonds across the mineral groups
Case1	**clay**	**quratz**	**quartz**	**1.0**
Case2	**clay**	**quratz**	**quartz**	**0.3**
Case3	**clay**	**quratz**	**calcite**	**1.0**
Case4	**clay**	**quratz**	**calcite**	**0.3**

Table 6.14 Common calculation settings (micro scale simulation).

Parameter	Value
Dimension in horizontal direction L_x (mm)	1.5
Dimension in vertical direction L_y (mm)	1.5
Boundary stress in vertical direction σ_V (MPa)	60.0
Boundary stress in horizontal direction σ_{H1}, σ_{H2}, and σ_{H3} (MPa)	40.0
Young's modulus E_1, E_2, and E_3 (GPa)	Table 6.12
Shear modulus G_1, G_2, and G_3 (GPa)	Table 6.12
Fracture toughness K_{IC1}, K_{IC2}, K_{IC3}	Table 6.12
Initial pore pressure P (MPa)	30.0
Injection rate (kg/s/m)	0.0003
Fracturing fluid viscosity (cp)	1.0
Medium permeability (mD)	0.00001
Number of elements	200×200
Horizon size ($=\frac{\delta}{\Delta x}$)	3.0

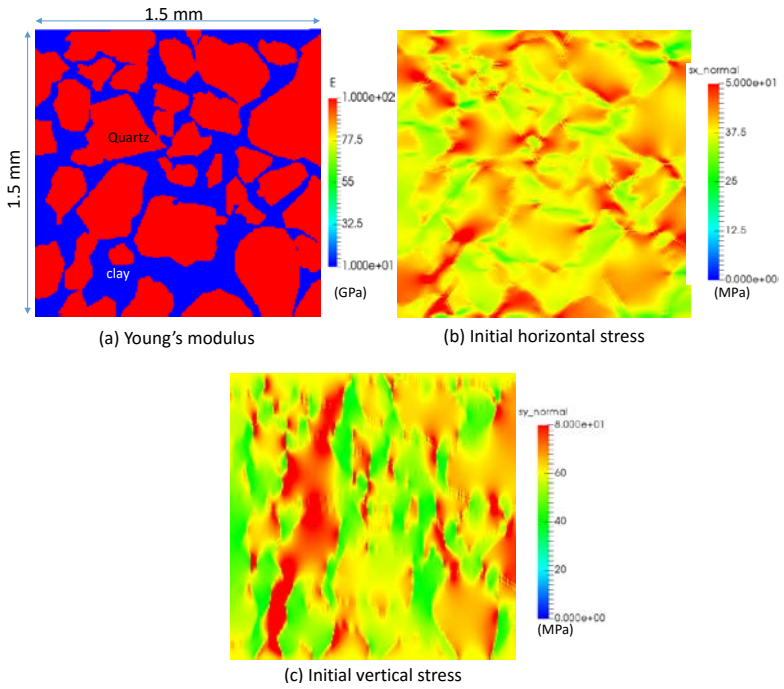

(a) Young's modulus

(b) Initial horizontal stress

(c) Initial vertical stress

Fig. 6.62 Initial stress distribution (Case 1 and Case 2).

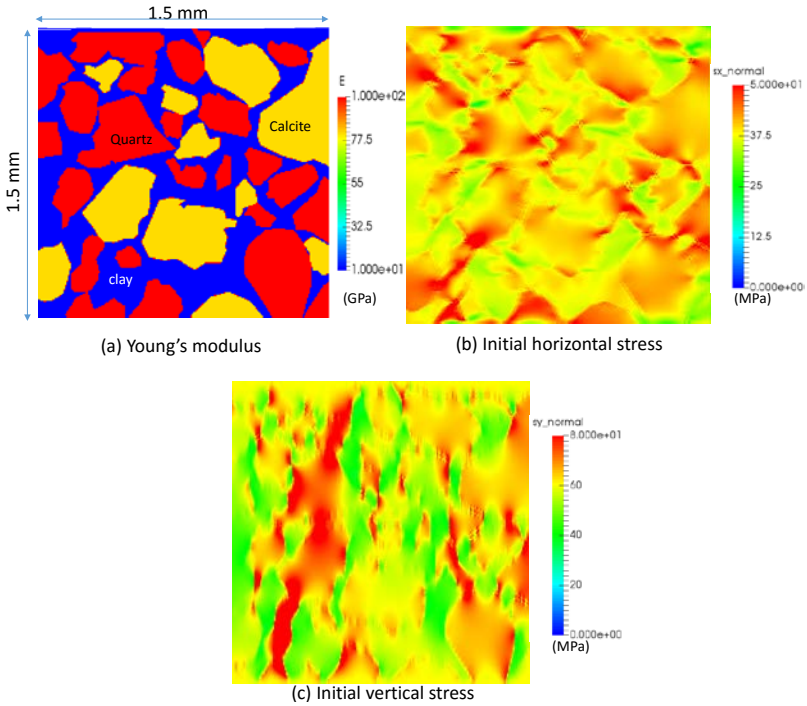

(a) Young's modulus

(b) Initial horizontal stress

(c) Initial vertical stress

Fig. 6.63 Initial stress distribution (Case 3 and Case 4).

Fig. 6.64 - Fig. 6.71 show the mechanical and fluid property distributions after fracture propagation. These results show that the fracture propagation path is highly affected by the type of minerals and the magnitude of the connection between the minerals.

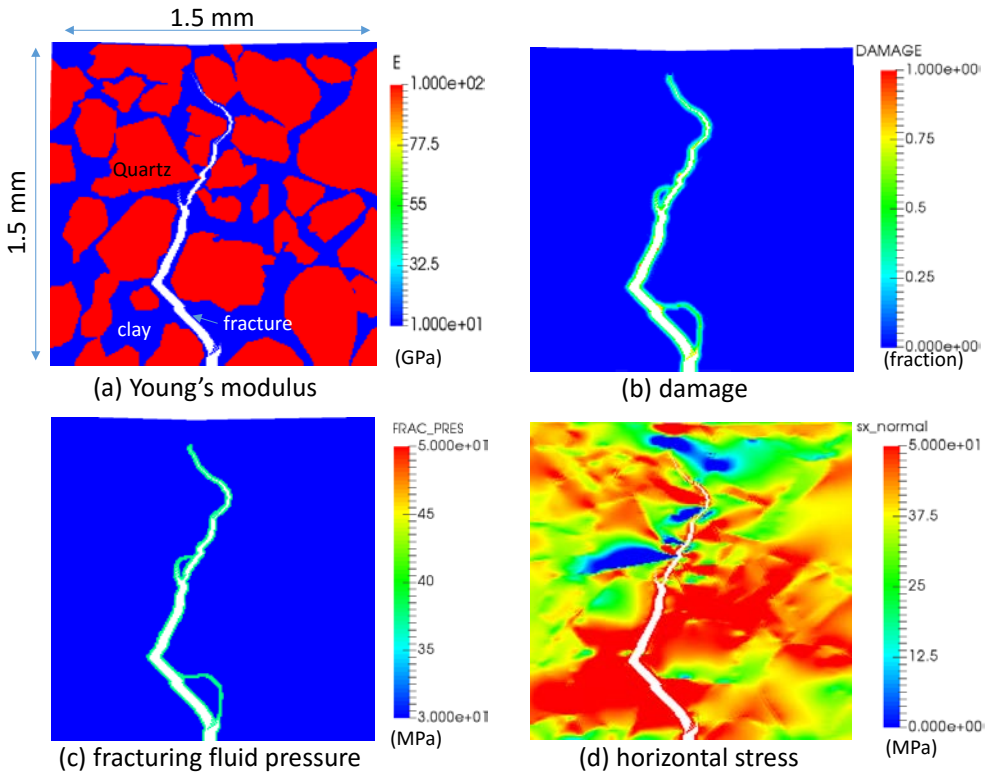

Fig. 6.64 Property distribution after 0.3 sec (Case 1).

As shown in Fig. 6.64, in the case where only two minerals (clay and quartz) exist in the domain and the connection between the minerals is not weak (Case1), the fracture locally turns in the clay as if avoiding the harder mineral (quartz) though it generally propagates toward the maximum principal stress direction. In this case, the Young's modulus of the quartz (95.2 GPa) is about 10 times higher than the clay (10 GPa), which constrains the deformation of the clay near the clay – quartz interface. Moreover, the fracture toughness of the quartz (2.4 MPa $m^{0.5}$) is about five times higher than the clay (0.5

MPa $m^{0.5}$). Therefore, the fracture has a hard time propagating through the quartz and can only propagate in the clay and around the quartz grains. However, as shown in Fig. 6.65, the fracture does not propagate along the shortest path which can avoid the clay–quartz interface from the beginning.

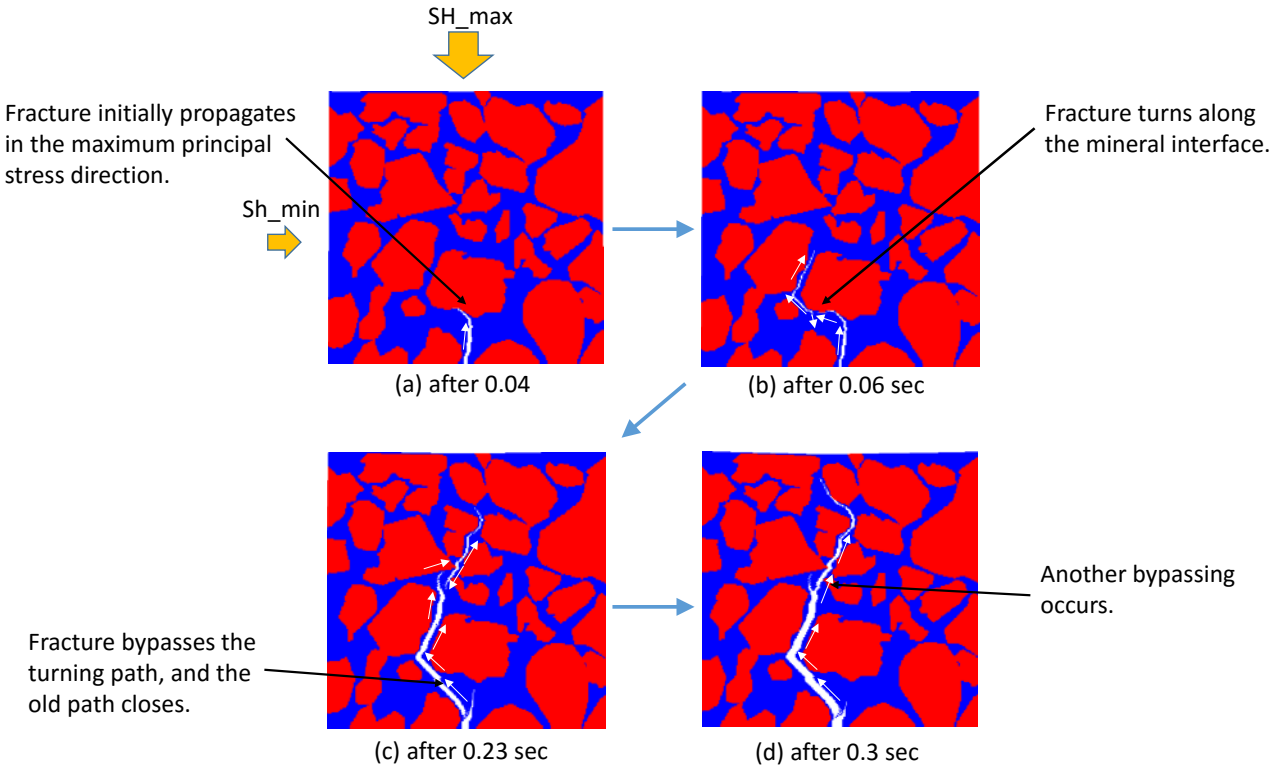

Fig. 6.65 Fracture propagation with time (Case1).

It initially propagates parallel to the maximum principal stress direction until it reaches the clay–quartz interface (Fig. 6.65 (a)) and then turns along the interface (Fig. 6.65 (b)). However, as shown in Fig. 6.65 (c) and (d), due to the fracturing fluid pressure increase caused by the highly turning fracture path, the new fracture branch bypasses the turning path at a later time, which results in the closing of the original turning path. By bypassing the tortuous path, the shortest fracture path which can avoid the clay–quartz interface

always remains as a main path. These results suggest that the initial fracture propagation path can be more tortuous near the fracture tip than the final path depending on the mineral distribution in the rock.

If the connection between the cray and the quartz is weak (Case2: the critical energy density for the bonds across the mineral interface is reduced to 30 % of Case1), as shown in Fig. 6.66, the fracture preferentially propagates along the mineral interface.

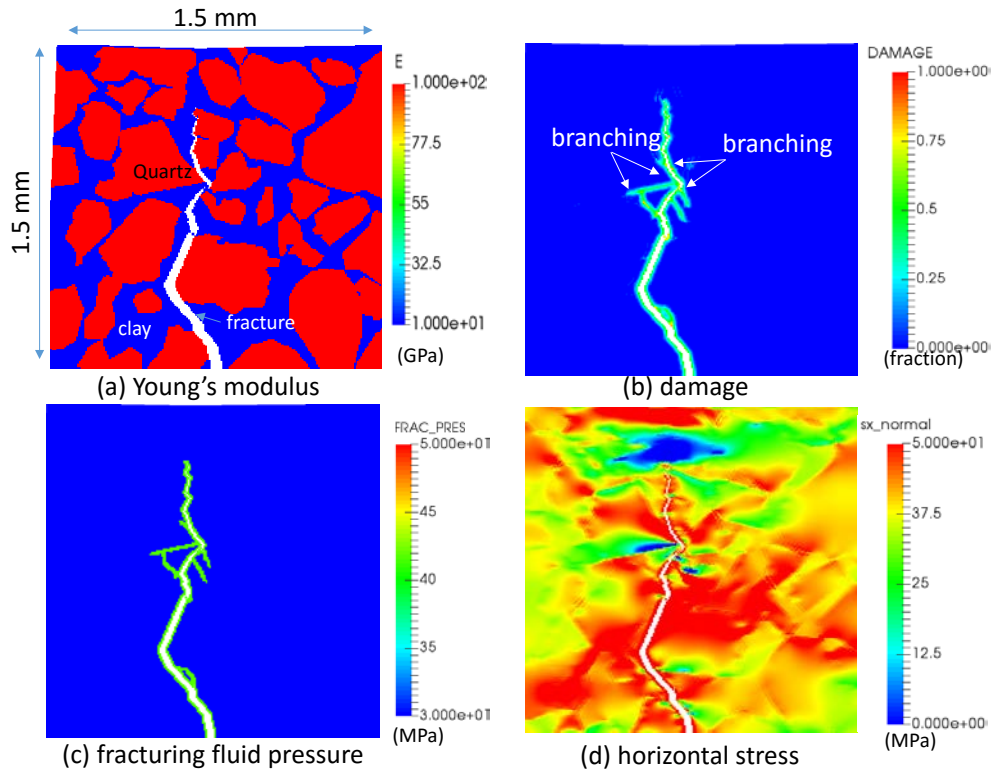

Fig. 6.66 Property distribution after 0.2 sec (Case 2).

In this case, as shown in Fig. 6.67, due to the weak connection between the two different minerals, the bonds across the mineral interface break (pre-damage zone appears) before the fracture tip reaches the interface, and the fracture propagates along the pre-damage zone. Since the energy requirement for breaking bonds across the mineral interface are

lower than Case 1, as shown in Fig. 6.68 (b), more fracture branches grow along the mineral interface in this case. However, as with Case 1, only the shortest path created by bypassing finally remains, and the other branching path closes (Fig. 6.68 (c)).

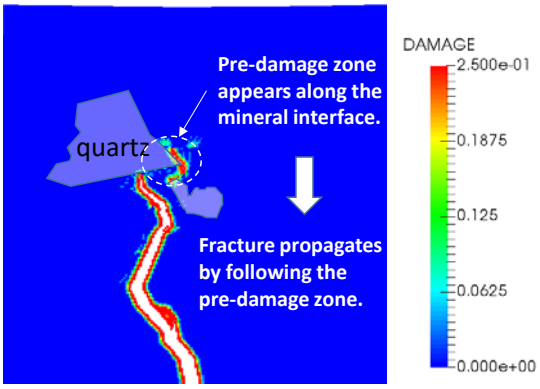

Fig. 6.67 Fracture propagation along the pre-damage zone (Case 1: Damage distribution after 0.16 sec).

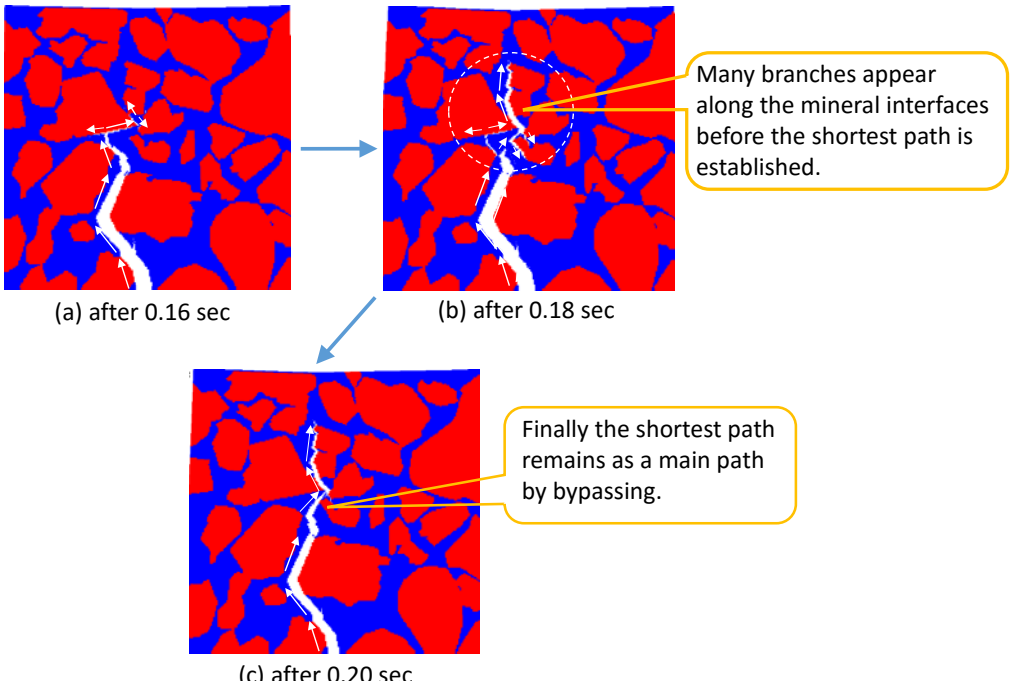

Fig. 6.68 Fracture propagation with time (Case2).

As shown in Fig. 6.69 (Case 3), if the part of the durable mineral (=quartz) in Case 1 are the brittle mineral (= calcite), the fracture propagation behavior is different from Case 1. In this case, the fracture propagates not only in the clay but also in the calcite. Since the fracture toughness of the calcite is low (0.19 MPa $m^{0.5}$) and the Young's modulus of the calcite is high (84.3 GPa) (in other words, the calcite is brittle), as mentioned in Section 6.2.2, even the small deformation in the clay by fracture propagation can cause damage (the bonds' break) in the calcite near the fracture tip before the fracture tip reaches the mineral interface.

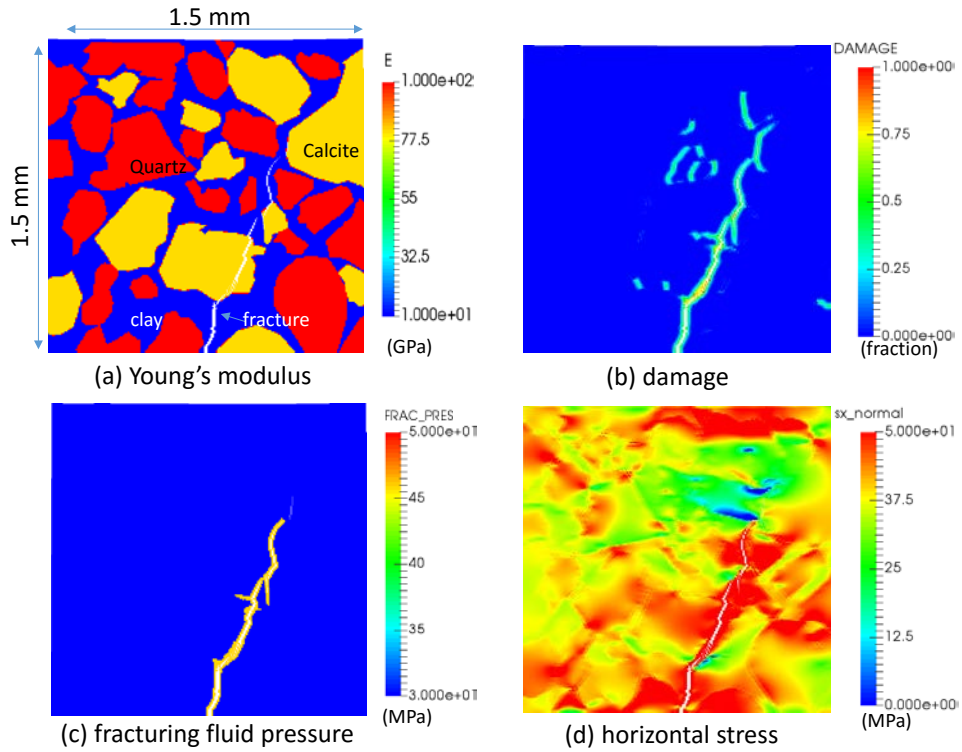

Fig. 6.69 Property distribution after 0.1 sec (Case 3).

As shown in Fig. 6.70 (a) - (d), the fracture continuously propagates by following the pre-damage zone in the calcite. As shown in Fig. 6.70 (a) and (d), pre-damage zone appears inside the calcite before the fracture tip reaches the clay-calcite boundary in the situation

where the fracture approaches the clay-calcite interface at a right angle, while, as shown in Fig. 6.70 (b) and (c), the pre-damage zone appears along the clay-calcite interface in the situation where the fracture approaches the clay-calcite interface at a low angle. This result shows that the fracture propagation path is very much controlled by the distribution of brittle minerals such as calcite.

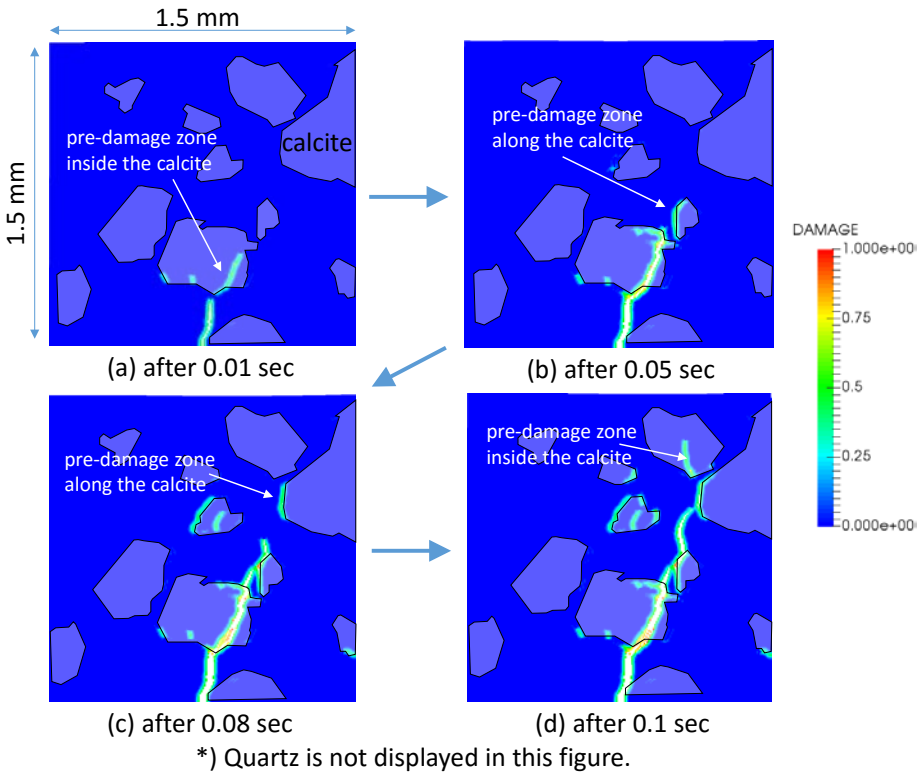

Fig. 6.70 Fracture propagation with time (Case 3: damage distribution).

As shown in Fig. 6.71 (Case 4), if the critical energy density of the bonds across the mineral interface is just 30 % of Case 3, a larger damage zone appears near the clay – calcite interface around the fracture due to the smaller energy requirement for bond breakage. However, most of the damage zones at the clay – calcite interface are parallel to the maximum principal stress direction and are not connected to each other since the

damage zone is difficult to grow in the direction of the minimum principal stress due to the high principal stress contrast. As with Case 3, the fracture generally propagates in the direction of the maximum principal stress direction by following the pre-damage zone near the fracture tip.

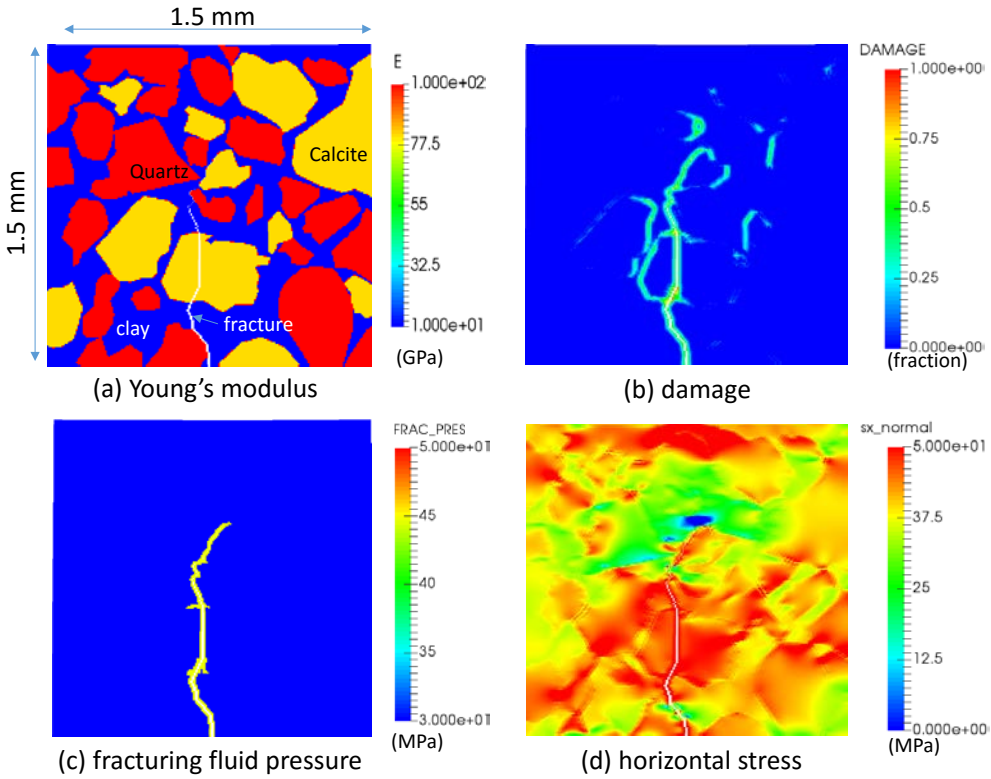

Fig. 6.71 Property distribution after 0.1 sec (Case 4).

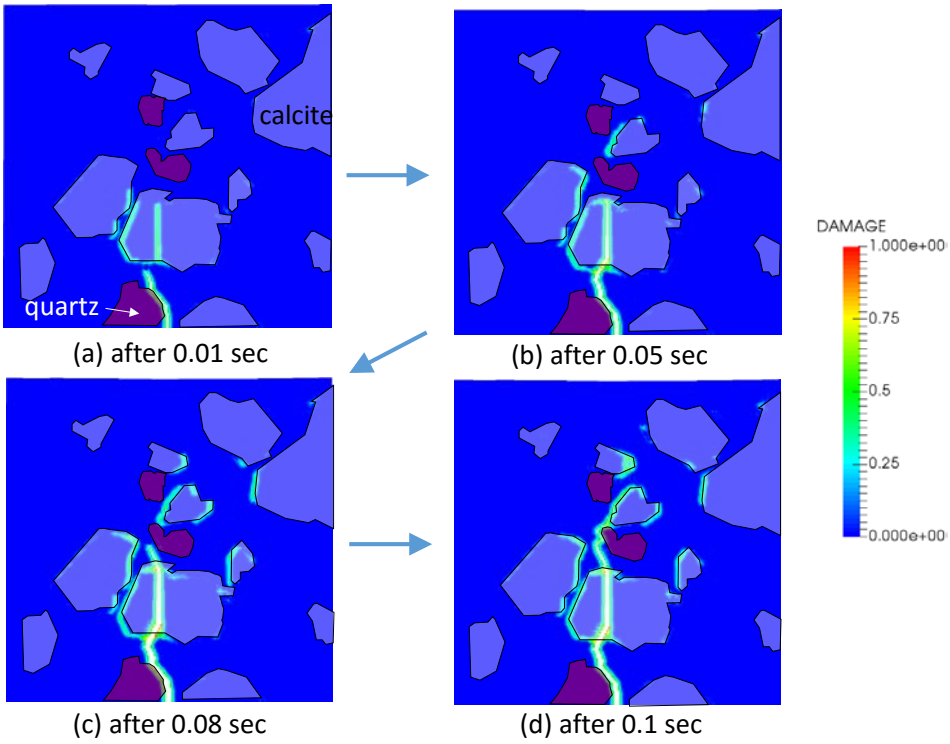

(a) after 0.01 sec (b) after 0.05 sec

(c) after 0.08 sec (d) after 0.1 sec

*) Only the quartz near the fracture is displayed in this figure.

Fig. 6.72 Fracture propagation with time (Case 4: damage distribution).

6.6 Conclusion

In this chapter, we have systematically investigated fracture propagation in heterogeneous reservoirs by using different models (two layer model, three layer model, multi-layer model, and micro scale model). The influence of this heterogeneity was demonstrated by changing multiple parameters such as contrast of mechanical properties between layers, horizontal/vertical principal stress difference, layer dip angle, and existence of weak planes between layers by using our newly developed peridynamics based hydraulic fracturing simulator.

In the two layer model study which focuses on revealing the mechanism of characteristic fracture propagation behaviors near a layer interface such as "turning" (bending along the layer interface), "kinking" and "branching", the following conclusions are obtained.

<u>Turning</u>

- Fracture turning along the layer interface is primarily controlled by fracture toughness contrast and principal stress difference. The effects of Young's modulus contrast, layer dip angle, and horizontal stress contrast between layers are limited. Higher principal stress difference and lower toughness contrast prevent fracture turning along the layer interface.
- If the layer interface is weak, fracture turning along the layer interface is also highly affected by layer dip angle. In the high layer dip angle ($\theta >= 30$ degree) with weak layer interface cases, fracture turns regardless of fracture toughness contrast and principal stress difference. However, for a low layer dip angle ($\theta <= 15$ degree) with

weak layer interface, fracture turning is still primarily controlled by fracture toughness contrast and principal stress difference.

- Layer thickness also affects the fracture turning along the layer interface. The thinner the layer in front of the fracture tip is, the easier it is for the fracture to cross the layer interface.
- Judging from the required fracture toughness contrast, fracture turning at a layer interface is only expected in shallow reservoirs which the principal stress difference is less than 1 MPa. Fracture turning in deep reservoirs can only occur with weak interfaces and some degree of layer dipping.

Kinking

- If a layer interface is inclined, the fracture kinks before it reaches the layer interface. If the fracture propagates from a softer layer to a harder layer, it turns as if avoiding the layer interface. On the other hand, if the fracture propagates from a harder layer to a softer layer, it turns as if trying to cross the layer interface at a right angle.
- The magnitude of the layer kinking is primarily decided by the magnitude of Young's modulus contrast and layer dipping angle. Principal stress difference also plays a role.
- The effects of fracture toughness contrast and layer thickness on fracture kinking are limited, which suggests that if layers are inclined, a fracture can kink at severe angles in reservoirs where significant heterogeneities exist in the vertical direction.

Branching

- If specific conditions are satisfied (Young's modulus contrast is very high (E_1/E_2>=8.0), the fracture toughness contrast is low (K_{IC1} / K_{IC2} <=1.0), and the layer

interface is not inclined), a fracture branches in the harder layer due to the pre-damage in the harder layer.

In the three layer model study which focuses on revealing the mechanism of deciding the preferential fracture propagation direction (fracture sometimes stops at one side of the layer interface and only crosses on the other side of the layer interface), the following conclusions are obtained.

- Preferential fracture propagation direction (upper side propagation only, lower side propagation only) is decided by the relative magnitude of the value of the fracture toughness over the Young's modulus of each layer which is directly related to the critical displacement of bonds in the horizontal direction in each layer.
- If the horizontal critical displacement value of the middle layer is not the largest, the fracture finally crosses the layer interface between the middle layer and the layer which has the smaller horizontal critical displacement.
- If the horizontal critical displacement value of the middle layer is the largest, the fracture simply propagates toward the softer layer and crosses the interface between the middle layer and the softer layer.

In the multi-layer model study which focuses on investigating the effect of cm order sub-layers on fracture propagation, the following conclusions are obtained.

- If the layers are not inclined, the effect of small scale sub-layers on fracture propagation is limited. Only in the case where a small vein which has very high Young's modulus and low fracture toughness contrast exists, a fracture can branch in such a layer.

- If the layers are inclined, the fracture can frequently kink at a high angle in the small scale sub layers even if the Young's modulus contrast is low (<= 2.0) and the principal stress difference is high. This result suggests that if layers are inclined in a vertically heterogeneous reservoir, proppant screen out or bridging may occur.

In the micro-scale fracture propagation study, the following observations are obtained.

- Fracture propagation path is highly affected by the distribution of minerals and the type of minerals. Fractures avoid harder minerals such as quartz, but preferentially penetrate brittle minerals such as calcite.
- If weak points (weak interface or brittle mineral) exist, the damage zone grows at the weak points before the fracture tip reaches the weak points. By following the part of the pre-damage zones at the weak points, the fracture continues to propagate.
- Even if multiple fracture branches appear during fracture propagation, the path which has the lowest turning angle is generated by bypassing and the other paths finally close.

CHAPTER7: CONCLUSIONS AND FUTURE RESEARCH

7.1 Summary and conclusions

The primary objective of this research was to develop a non-local peridynamics model for fracture propagation and to elucidate the complicated fracture propagation patterns in naturally fractured, arbitrarily heterogeneous reservoirs based on such a model. A new peridynamics formulation was derived for fluid flow and coupled with mechanics of the porous medium. This model was then applied to investigate fracture propagation in naturally fractured and other heterogeneous reservoirs. In this chapter, we summarize the conclusions of this research.

7.1.1 DEVELOPMENT OF PERIDYNAMICS-BASED POROUS FLOW MODEL

1. We derived a generalized non-local, state-based peridynamics formulation of the governing mass conservation equation for single-phase flow of slightly compressible fluid thorough a porous medium.
2. We selected the constitutive model proposed by Seleson et. al [80] for the state-based peridynamics fluid flow formulation and computed the non-local constitutive parameters to obtain results consistent with the classical theory in the limit of horizon size going to zero.
3. We validated our formulation against the well-known analytical solution for the 5-spot well pattern. The results showed that our peridynamics fluid flow formulation closely matched the exact local solution if the horizon size was chosen to be small enough with the appropriate volumetric constraints.

4. We also showed that the model can capture heterogeneity in constitutive flow properties (permeability) by implementing harmonic averaging of the properties.

7.1.2 DEVELOPMENT OF PERIDYNAMICS BASED HYDRAULIC FRACTURING MODEL

1. A new peridynamics based hydraulic fracturing model was developed by modifying the existing formulation of solid mechanics for porous media and coupling it with the new peridynamics formulation for fluid flow.
2. A novel approach was developed to impose a non-local traction boundary condition which allows us to apply rigorous stress distribution around the fracture surfaces.
3. This model can simulate non-planar, multiple fracture growth in arbitrarily heterogeneous reservoirs by solving deformation of the reservoir, fracturing fluid pressure and pore pressure simultaneously.
4. The poroelastic deformation is verified by comparing our results against the analytical solution for the 1-D consolidation problem. Our coupled poroelastic formulation produces a close match with the analytical solution to this classical 1-D consolidation problem.
5. Hydraulic fracture propagation is verified under a 2-D plane-strain assumption and in a 3-D setting against the corresponding classical analytical solution obtained from the KGD model and PKN model respectively. In both cases, our model shows a close agreement in both fracture geometry and injection pressure.
6. For the 2-D plane strain problem, the stress distribution around the fracture is also verified by comparing against the Sneddon solution. The calculated stress distribution shows very good agreement with the Sneddon solution, which supports the validity of our newly proposed calculation method to impose traction boundary conditions.

7. This model has been parallelized based on a domain decomposition method using Sandia National Laboratory's Trilinos library. Performance tests for the parallelized model reveal that about 30 times speed up can be obtained by using 128 CPUs.

7.1.3 INTERACTION BETWEEN HYDRAULIC FRACTURES AND NATURAL FRACTURES

1. We defined pre-existing cracks under compressional loading, using a simple contact model and two different failure criteria (tensile failure criterion and shear failure criterion). This new definition allows us to simulate interactions between hydraulic fractures (HF) and natural fractures (NF).
2. The capability of our model to predict interactions between a HF and a NF has been shown through a comparison against the analytical solution to 1-D compression test and against large block experiments conducted with simulated natural fractures.
3. A sensitivity analysis reveals that poroelastic effects have a large influence on the interaction between HF and NF if leak-off is high. In addition, we also demonstrate that the stress contrast, the angle of approach, the fracture toughness of the rock, the fracture toughness of the natural fracture, and shear failure criteria of the natural fracture also affect the interaction between HF and NF. These results are consistent with published experiments.
4. We have demonstrated our simulator's applicability to simulate field scale hydraulic fracturing jobs. Simulation results are presented for the growth of multiple fractures, while taking into account poroelastic effects and mechanical stress shadow effects created by the growing fractures.
5. Through 3-D simulations, we also demonstrate that our hydraulic fracturing model can capture the complicated 3-D interaction between HF and NF shown by Bahorich et al.

[102] (bypassing + turning, and turning + diverting). These simulation results reveal that the height of the NF, the position of the NF, and the resistance to opening of the NF have a huge impact on the 3-D interaction behavior between the HF and the NF.

7.1.4 INVESTIGATION OF THE EFFECT OF RESERVOIR HETEROGENEITY ON FRACTURE PROPAGATION

We systematically investigated fracture propagation in heterogeneous reservoirs by using different models with different types of heterogeneity (two layer model, three layer model, multi-layer model, and arbitrary micro-scale heterogeneity).

1. In the two layer model, we observed three characteristic fracture propagation behavior near the layer interface: “turning”, “kinking”, and “branching”. The following conclusions were drawn from this study.

   Turning

   - If the layer interface is not damaged, fracture turning along the layer interface is primarily controlled by fracture toughness contrast and principal stress difference. Lower principal stress difference and higher toughness contrast facilitates fracture turning along the layer interface. The effect of other parameters (Young’s modulus contrast, layer dip angle, and horizontal stress contrast between layers) on turning is limited.
   - If the layer interface is damaged (weak), the fracture always turns at high interface dip angles ($\theta >= 30$ degree) regardless of the toughness contrast between layers or the principal stress difference. However, if the interface dip angle is low ($\theta <= 15$

degree), fracture turning is primarily controlled by fracture toughness contrast and principal stress difference.

- Layer thickness also affects fracture turning along the layer interface. The thinner the layer in front of the fracture tip, the easier it is for the fracture to cross the layer interface.
- Based on the required fracture toughness contrast, fracture turning along the layer interface is expected only in shallow reservoirs in which the principal stress contrast is less than 1 MPa or in reservoirs which have highly dipping or weak layer interfaces.

Fracture Kinking

- If the layer interface is inclined, the propagating fracture kinks before it reaches the layer interface. If the fracture propagates from a softer layer to a harder layer, it turns as if avoiding the layer interface. On the other hand, if the fracture propagates from a harder layer to a softer layer, it turns as if trying to cross the layer interface at a right angle.
- The magnitude of fracture kinking is primarily controlled by the magnitude of Young's modulus contrast and layer dip angle. The effects of fracture toughness contrast and layer thickness on fracture kinking are limited, which suggests that, if layers are inclined enough, the fracture can kink in reservoirs which contain small scale heterogeneities in Young's modulus (bedding planes in the vertical direction) as are commonly observed in shale reservoirs.

Branching

- If the Young's modulus contrast is very high (E_1/E_2 >= 8.0), fracture toughness contrast is low (K_{IC1} / K_{IC2} <=1.0), and the layer interface is not inclined), a propagating fracture branches in the harder layer due to the damage ahead of the fracture tip in the harder layer.

2. In fracture propagation through 3 geologic layers, we have analyzed which parameter controls the fracture propagation direction (top or bottom).
   - The preferred fracture propagation direction (propagation into the upper / lower layer only, versus propagation into both layers) is decided by the relative magnitude (or the ratio) of fracture toughness to Young's modulus of each layer which is directly related to the critical displacement of bonds in the horizontal direction in each layer.
   - If the ratio of fracture toughness to Young's modulus in the middle layer is not the largest, the fracture finally crosses the layer interface between the middle layer and the layer which has a smaller value of the fracture toughness over the Young's modulus.
   - If the ratio of fracture toughness to Young's modulus for the middle layer is the largest, the fracture propagates toward the smaller Young's modulus layer and crosses the interface between the middle layer and the layer with the smaller Young's modulus.

3. In a multi-layer model, we investigated the effect of many sub-layers or bedding planes on fracture propagation. The following conclusions are obtained.
   - If the layers are not inclined, the effect of small scale heterogeneity (sub layers) on fracture geometry is limited. Only in the case where a small vein which has very

high Young's modulus and low fracture toughness contrast exists, a fracture can branch in such a layer. The fracture propagation pressure increases as the contrast between the Young's moduli and fracture toughness in the layers increases.

- If the layers are inclined, the fracture can frequently kink at a high angle in the small scale sub layers even if the Young's modulus contrast is low (<= 2.0) and the principal stress difference is high. This result suggests that proppant screen out or proppant bridging is likely to happen in a highly inclined, vertically heterogeneous reservoir.

4. Heterogeneities at the micro scale are also shown to impact fracture propagation. The following observations are obtained.
   - The fracture propagation path is highly affected by the distribution and the type of minerals. The fracture avoids minerals with high tensile strength such as quartz but penetrates weaker, brittle minerals such as calcite.
   - If weak interfaces between mineral grains exist, the damage zone grows into the weak points before the fracture tip propagates through the weak points. This can often lead to complex fracture geometries at the grain / pore scale.
   - Even if multiple fracture branches appear, the branch which has the lowest turning angle propagates, bypassing the others.

7.2 Future work

7.2.1 IMPROVEMENT OF THE CALCULATION EFFICIENCY

Peridynamics, being a non-local method, is numerically more expensive than local methods such as finite volume and finite element methods. This is due to the large number of neighbors in the horizon that need to be considered. To simulate 3-D hydraulic fracture propagation in our peridynamics based hydraulic fracturing model, further improvements of the calculation efficiency are necessary. The following tasks should be considered for future work.

1. Co-existence of the different sizes of horizon (static/adaptive mesh refinement)

One of the limitations of the state-based peridynamics theory is that the elements must be equally spaced to avoid the "ghost force issue". Due to this limitation, the same size of fine elements as the fracture front have to be prepared even in the area far from the fracture propagation front where less displacement of elements is expected. This limitation significantly increases the computation time for field scale 3-D fracture propagation simulations. In recent years, several authors [121, 122] proposed new theoretical frameworks to overcome the limitation of horizon size. Incorporating one of their theories into our model deserves consideration to improve the numerical efficiency of our model.

2. Coupled with local fluid flow models

In the current model, porous fluid flow and fracture fluid flow are solved using the peridynamics theory to keep theoretical consistency between the mechanics part and the fluid flow part. However, non-locality does not play an important role in fluid flow in most hydraulic fracturing simulations. It is worth considering replacing the peridynamics fluid

flow formulation with a local fluid flow formulation based on a finite difference method as one of the calculation options. This will help to reduce the calculation times due to the reduction in non-zero elements in the Jacobian matrix.

3. Introduction of more efficient pre-conditioner for the parallel linear solver

In our model, solving the Jacobian matrix by the linear solver is the most time consuming part (more than 90 % of the calculation time is spent for the linear solution part). Therefore, solving the matrix more efficiently is the key to improving our calculation efficiency. Incorporating a state of the art pre-conditioner such as "Algebraic Multi-Grid Method" [123] instead of the current pre-conditioner ("incomplete LU decomposition") may be one of the promising ways to improve the calculation efficiency.

7.2.2 MODEL EXTENSION TO SIMULATE PROPPANT TRANSPORT, NON-NEWTONIAN FLUID FLOW, AND MULTI-PHASE FLOW

1. Non-Newtonian fluid

The peridynamics fluid flow formulation that we proposed in Chapter 3 is currently limited to slightly compressible single phase fluid. However, this theory can be extended to non-Newtonian fluid and multi-phase flow. Since non-Newtonian fluids are used in fracturing jobs, extending the current fluid flow formulation to non-Newtonian fluid and incorporating it into our model will be useful.

2. Proppant transport

The prediction of proppant distribution in complex fracture networks is also an important topic. Moreover, the prediction of the fracture propagation path itself is

important since the unpropped fractures may not keep their transmissibility during production and flowback. Incorporating proppant transport into our model including the effect of fracture geometry is challenging. However, incorporating an ordinary proppant transport formulation for solving proppant concentration, which allows us to consider the change in fluid density and viscosity, is also worth trying. It will give us more insight to be able to accurately predict the fracture length and fracture width.

7.2.3 SHEAR FAILURE MODELING OF NATURAL FRACTURES / WEAK SURFACES

1. Modification of shear failure criteria

In Chapter 5, we introduce a preliminary shear failure model, which successfully captures the first order effect of shear failure on the interaction of HF and NF. However, this model explicitly decides the shear failure of bonds based on the previous time step's stress condition using a Mohr-Coulomb type failure criterion that is independent of the energy stored in the bonds (in other words, it is not based on the energy based bond failure criteria). A more rigorous theoretical framework which is consistent with the energy based bond failure criteria is required for further improvement of the model.

2. Introducing fracture conductivity by shear failure

In our current model, fracture conductivity is estimated based only on the approximated fracture width (equal to the current displacement between the nearest elements – the critical displacement between the nearest elements.) Therefore, even after a shear failure occurs in a natural fracture, fracturing fluid cannot directly flow into a natural fracture without undergoing a subsequent tensile failure. However, as Barton et. al [124] show, even if rock surfaces are in contact, the joint has some degree of conductivity and it

changes with shear displacement. Incorporating this kind of fracture conductivity by shear displacements will improve the accuracy of prediction of fracture propagation behavior in naturally fractured reservoirs.

APPENDIX

Appendix A.1: Derivation of the peridynamic equation of motion

The peridynamic equation of motion is derived from the Hamilton's principle states. Based on the principle, a motion of a body is expressed as follows,

$$\int_{t_1}^{t_2} \left(\delta \left(T - U \right) + \delta W \right) dt = 0 \qquad \text{(A-1)}$$

Where,

t	:	time	[s]
T	:	kinetic energy	[J]
U	:	potential energy	[J]
W	:	virtual work	

In the above equation, the kinetic energy T is given by the following formulation.

$$T = \int_{\mathrm{B}} \frac{1}{2} \rho \dot{\mathbf{u}} \cdot \dot{\mathbf{u}} dV \qquad \text{(A-2)}$$

$$\dot{\mathbf{u}} = \frac{\partial \left\{ \mathbf{y}\left(\mathbf{x}, t \right) - \mathbf{x} \right\}}{\partial t} \qquad \text{(A-3)}$$

Where,

$\dot{\mathbf{u}}$	:	velocity of a point $\mathbf{x}$	[m/s]
V	:	volume	[m^3]
$\mathbf{x}$	:	reference configuration	[m]
$\mathbf{y}$	:	current configuration	[m]
ρ	:	density	[kg/m^3]

The first term of the Equation (A-1) can be rewritten as follows,

$$\begin{aligned}\int_{t_1}^{t_2}\delta T dt &= \int_{t_1}^{t_2}\frac{\partial T}{\partial \dot{\mathbf{u}}}\cdot\delta\dot{\mathbf{u}}dt \\ &= \left[\frac{\partial T}{\partial \dot{\mathbf{u}}}\cdot\delta\mathbf{u}\right]_{t_1}^{t_2} - \int_{t_1}^{t_2}\frac{d}{dt}\left(\frac{\partial T}{\partial \dot{\mathbf{u}}}\right)\cdot\delta\mathbf{u}dt \\ &= -\int_{t_1}^{t_2}\frac{d}{dt}\left(\frac{\partial T}{\partial \dot{\mathbf{u}}}\right)\cdot\delta\mathbf{u}dt\end{aligned} \tag{A-4}$$

Where, $\delta\mathbf{u}(t_1)=\delta\mathbf{u}(t_2)=0$. Inserting Equation (A-2) into Equation (A-4) gives,

$$\int_{t_1}^{t_2}\delta T dt = -\int_{t_1}^{t_2}\int_{\mathrm{B}} p\ddot{\mathbf{u}}\cdot\delta\mathbf{u}dVdt \tag{A-5}$$

The third term of Equation (A-1) (the virtual work term) is given by the following formulation.

$$\int_{t_1}^{t_2}\delta W dt = \int_{t_1}^{t_2}\int_{\mathrm{B}}\rho\mathbf{b}\cdot\delta\mathbf{u}dV_{\mathbf{x}}dt \tag{A-6}$$

Here, to express the second term of Equation (A-1), we introduce a strain energy density Ψ as a function of deformation vector state $\underline{\mathbf{Y}}\langle\boldsymbol{\xi}\rangle$ as follows,

$$\Psi = \Psi\left(\underline{\mathbf{Y}}\langle\boldsymbol{\xi}\rangle\right) \tag{A-7}$$

$$\underline{\mathbf{Y}}\langle\boldsymbol{\xi}\rangle = \mathbf{y}(\mathbf{x}') - \mathbf{y}(\mathbf{x}) = \mathbf{x}' - \mathbf{x} + \mathbf{u}(\mathbf{x}') - \mathbf{u}(\mathbf{x}) = \boldsymbol{\xi} + \boldsymbol{\eta} \tag{A-8}$$

Where,

$\mathbf{x}'$	:	material point inside the horizon of $\mathbf{x}$	[m]
$\mathbf{u}$	:	displacement vector field	[m]
$\boldsymbol{\xi}$	:	bond vector $(=\mathbf{x}'-\mathbf{x})$	[m]
$\boldsymbol{\eta}$	:	relative displacement $(=\mathbf{u}(\mathbf{x}')-\mathbf{u}(\mathbf{x}))$	[m]
Ψ	:	strain energy density	[J/m^3]

The potential energy U is given as a function of the strain energy density as follows,

$$U = \int_{\mathrm{B}} \Psi\left(\underline{\mathbf{Y}}\left(\mathbf{x}\right)\langle\xi\rangle\right) dV_{\mathbf{x}} \tag{A-9}$$

Therefore, the second term in Equation (A-1) is

$$\int_{t_1}^{t_2} \delta U dt = \int_{t_1}^{t_2} \int_{\mathrm{B}} \delta\Psi\left(\underline{\mathbf{Y}}\left(\mathbf{x}\right)\langle\xi\rangle\right) dV_{\mathbf{x}} dt \tag{A-10}$$

Applying the following Frechet derivative of the strain energy density to Equation (A-10)

$$\begin{aligned} &\delta\Psi\left(\underline{\mathbf{Y}}\left(\mathbf{x}\right)\langle\xi\rangle\right) = \Psi\left(\underline{\mathbf{Y}}\left(\mathbf{x}\right)\langle\xi\rangle + \Delta\underline{\mathbf{Y}}\left(\mathbf{x}\right)\langle\xi\rangle\right) - \Psi\left(\underline{\mathbf{Y}}\left(\mathbf{x}\right)\langle\xi\rangle\right) \\ &= \int_{\mathrm{B}} \underline{\nabla}\Psi\left(\underline{\mathbf{Y}}\left(\mathbf{x}\right)\langle\xi\rangle\right) \cdot \Delta\underline{\mathbf{Y}}\left(\mathbf{x}\right)\langle\xi\rangle \, dV_{\xi} + O\left(\left|\Delta\underline{\mathbf{Y}}\left(\mathbf{x}\right)\langle\xi\rangle\right|^2\right) \end{aligned} \tag{A-11}$$

Equation (A-10) becomes,

$$\begin{aligned} \int_{t_1}^{t_2} \delta U dt &= \int_{t_1}^{t_2} \int_{\mathrm{B}} \int_{\mathrm{B}} \underline{\nabla}\Psi\left(\underline{\mathbf{Y}}\left(\mathbf{x}\right)\langle\xi\rangle\right) \cdot \Delta\underline{\mathbf{Y}}\left(\mathbf{x}\right)\langle\xi\rangle \, dV_{\mathbf{x}'} dV_{\mathbf{x}} dt \\ &= \int_{t_1}^{t_2} \int_{\mathrm{B}} \int_{\mathrm{B}} \underline{\nabla}\Psi\left(\underline{\mathbf{Y}}\left(\mathbf{x}\right)\langle\xi\rangle\right) \cdot \left(\delta\mathbf{u}\left(\mathbf{x}'\right) - \delta\mathbf{u}\left(\mathbf{x}\right)\right) dV_{\mathbf{x}'} dV_{\mathbf{x}} dt \\ &= \int_{t_1}^{t_2} \left\{ \int_{\mathrm{B}} \int_{\mathrm{B}} \underline{\nabla}\Psi\left(\underline{\mathbf{Y}}\left(\mathbf{x}\right)\langle\xi\rangle\right) \cdot \delta\mathbf{u}\left(\mathbf{x}'\right) dV_{\mathbf{x}'} dV_{\mathbf{x}} - \int_{\mathrm{B}} \int_{\mathrm{B}} \underline{\nabla}\Psi\left(\underline{\mathbf{Y}}\left(\mathbf{x}\right)\langle\xi\rangle\right) \cdot \delta\mathbf{u}\left(\mathbf{x}\right) dV_{\mathbf{x}'} dV_{\mathbf{x}} \right\} dt \end{aligned} \tag{A-12}$$

In Equation (A-12), by exchange the variable $\mathbf{x} \leftrightarrow \mathbf{x}'$ and the order of integration in the first term, we obtain,

$$\begin{aligned} \int_{t_1}^{t_2} \delta U dt &= \int_{t_1}^{t_2} \left\{ \int_{\mathrm{B}} \int_{\mathrm{B}} \underline{\nabla}\Psi\left(\underline{\mathbf{Y}}\left(\mathbf{x}'\right)\langle -\xi\rangle\right) \cdot \delta\mathbf{u}\left(\mathbf{x}\right) dV_{\mathbf{x}} dV_{\mathbf{x}'} - \int_{\mathrm{B}} \int_{\mathrm{B}} \underline{\nabla}\Psi\left(\underline{\mathbf{Y}}\left(\mathbf{x}\right)\langle\xi\rangle\right) \cdot \delta\mathbf{u}\left(\mathbf{x}\right) dV_{\mathbf{x}'} dV_{\mathbf{x}} \right\} dt \\ &= \int_{t_1}^{t_2} \left[\int_{\mathrm{B}} \left\{ \left(\int_{\mathrm{B}} \left(\underline{\nabla}\Psi\left(\underline{\mathbf{Y}}\left(\mathbf{x}'\right)\langle -\xi\rangle\right) - \underline{\nabla}\Psi\left(\underline{\mathbf{Y}}\left(\mathbf{x}\right)\langle\xi\rangle\right) \right) dV_{\mathbf{x}'} \right) \cdot \delta\mathbf{u}\left(\mathbf{x}\right) \right\} dV_{\mathbf{x}} \right] dt \end{aligned} \tag{A-13}$$

By substituting Equation (A-5), (A-6), (A-13) into Equation (A-1), we obtain,

$$\int_{t_1}^{t_2} \left(\int_{\mathrm{B}} \left(-p\ddot{\mathbf{u}} - \left(\int_{\mathrm{B}} \left(\underline{\nabla}\Psi\left(\underline{\mathbf{Y}}\left(\mathbf{x}'\right)\langle -\xi\rangle\right) - \underline{\nabla}\Psi\left(\underline{\mathbf{Y}}\left(\mathbf{x}\right)\langle\xi\rangle\right) \right) dV_{\mathbf{x}'} + \rho\mathbf{b} \right) \right) \cdot \delta\mathbf{u} dV \right) dt = 0 \tag{A-14}$$

Finding the stationary value to satisfy Equation (A-14) and defining Equation (A-15), we have the constitutive relationship of the peridynamic equation of motion (Equation (A-16)).

$$\underline{T}\left(\mathbf{x}\right)\left\langle \xi \right\rangle = \underline{t}\,\frac{\left(\underline{\mathbf{Y}}\left(\mathbf{x}\right)\left\langle \xi \right\rangle\right)}{\sqrt{\left(\underline{\mathbf{Y}}\left(\mathbf{x}\right)\left\langle \xi \right\rangle\right)\cdot\left(\underline{\mathbf{Y}}\left(\mathbf{x}\right)\left\langle \xi \right\rangle\right)}} = t\underline{\mathbf{M}} = \underline{\nabla}\Psi\left(\underline{\mathbf{Y}}\left(\mathbf{x}\right)\left\langle \xi \right\rangle\right) \tag{A-15}$$

$$p\ddot{\mathbf{u}} = \int_{\mathrm{B}}\left(\underline{T}\left(\mathbf{x}\right)\left\langle \xi \right\rangle - \underline{T}\left(\mathbf{x}'\right)\left\langle -\xi \right\rangle\right)dV_{\mathbf{x}'} + \rho\mathbf{b} \tag{A-16}$$

Appendix A.2: Derivation of the constitutive relation

The constitutive relation of the linear peridynamic isotropic solid is derived from the analogous to the strain energy density in the classical theory. The strain energy density in the classical theory is given as follows,

$$\begin{aligned}
\Psi &= \frac{1}{2} K\, trac(\boldsymbol{\tau}\boldsymbol{\varepsilon}) \\
&= \frac{\lambda}{2}\varepsilon_v{}^2 + G\left\{\varepsilon_{ij}{}^2\right\} \\
&= \frac{1}{2}\left(K - \frac{2}{3}\right)\varepsilon_v{}^2 + G\left\{\varepsilon_{ij}{}^2\right\} \\
&= \frac{1}{2}K\varepsilon_v{}^2 + G\left\{\varepsilon_{ij}{}^2 - \frac{2}{3}\varepsilon_v{}^2 + \frac{3}{9}\varepsilon_v{}^2\right\} \\
&= \frac{1}{2}K\varepsilon_v{}^2 + G\left\{\left(\varepsilon_{11} - \frac{\varepsilon_v}{3}\right)^2 + \left(\varepsilon_{22} - \frac{\varepsilon_v}{3}\right)^2 + \left(\varepsilon_{33} - \frac{\varepsilon_v}{3}\right)^2 + \varepsilon_{12}{}^2 + \varepsilon_{13}{}^2 + \varepsilon_{21}{}^2 + \varepsilon_{23}{}^2 + \varepsilon_{31}{}^2 + \varepsilon_{32}{}^2\right\} \\
&= \frac{1}{2}K\left(\varepsilon_{kk}\right)^2 + G\left(\varepsilon_{ij}^d\right)^2
\end{aligned} \tag{A-17}$$

Where,

K	:	bulk modulus	[Pa]
G	:	shear modulus	[Pa]
$\boldsymbol{\varepsilon}$	:	strain tensor	
$\boldsymbol{\varepsilon}^d$	:	deviatoric strain tensor	
λ	:	lame constant	[Pa]
$\boldsymbol{\tau}$	:	stress tensor	[Pa]

In the same way, the strain energy density for the linear peridynamic isotropic solid is given as follows,

$$\Psi = \frac{1}{2}k\theta^2 + \frac{\alpha}{2}\left(\underline{\omega}\underline{e}^d\right) \bullet \underline{e}^d \tag{A-18}$$

$$e^d = e\langle\boldsymbol{\xi}\rangle - \frac{\theta}{3}\underline{x}\langle\boldsymbol{\xi}\rangle \tag{A-19}$$

$$\theta = \frac{3}{m}\underline{\omega x} \bullet \underline{e} = \frac{3}{m}\int_{H_x} \underline{\omega x}\langle\boldsymbol{\xi}\rangle e\langle\boldsymbol{\xi}\rangle dV_{\mathbf{x}'} \tag{A-20}$$

$$\underline{e} = \mathbf{y} - \mathbf{x} = \boldsymbol{\xi} \cdot \boldsymbol{\varepsilon} \cdot \frac{\boldsymbol{\xi}}{\|\boldsymbol{\xi}\|} \tag{A-21}$$

$$m = \int_{H_x} \underline{\omega x} \cdot \underline{x} dV_{\mathbf{x}'} \tag{A-22}$$

Where,

e : elongation scalar state

e^d : deviatoric scalar state

k : material property representing the resistance to compression/expansion [Pa]

m : weighted volume [m^5]

$\underline{x}$: reference scalar state (=$\|\boldsymbol{\xi}\|$)

α : material property representing the resistance to shearing [Pa/m^5]

θ : dilatation

In the spherical coordinate, $\boldsymbol{\xi}$ and $dV_{\mathbf{x}'}$ are expressed as follows respectively,

$$\boldsymbol{\xi} = \begin{pmatrix} \xi_1 \\ \xi_2 \\ \xi_3 \end{pmatrix} = \begin{pmatrix} r\sin\phi\cos\theta \\ r\sin\phi\sin\theta \\ r\cos\phi \end{pmatrix} \tag{A-23}$$

$$dV_{\mathbf{x}'} = r^2 \sin\phi d\phi d\theta dr \tag{A-24}$$

By inserting Equation (A-23) and (A-24) into Equation (A-20) and (A-22), we have,

$$\begin{aligned} m &= \int_{H_x} \underline{\omega x} \cdot \underline{x} dV_{\mathbf{x}'} \\ &= \int_0^{\delta}\int_0^{\pi}\int_0^{2\pi} \underline{\omega} r^2 \left(r^2 \sin\phi d\theta d\phi dr \right) \\ &= \int_0^{\delta} 4\pi \underline{\omega} r^4 dr \end{aligned} \tag{A-25}$$

$$\begin{aligned} \theta &= \frac{3}{m}\int_{H_x} \underline{\omega x} \langle \boldsymbol{\xi} \rangle e \langle \boldsymbol{\xi} \rangle dV_{\mathbf{x}'} \\ &= \frac{3}{m}\int_0^{\delta}\int_0^{\pi}\int_0^{2\pi} \underline{\omega} r \frac{\boldsymbol{\xi}\cdot\boldsymbol{\varepsilon}\cdot\boldsymbol{\xi}}{r} r^2 \sin\phi d\theta d\phi dr \\ &= \frac{3}{m}\int_0^{\delta}\int_0^{\pi}\int_0^{2\pi} \underline{\omega} \varepsilon_{ij}\xi_i\xi_j r^2 \sin\phi d\theta d\phi dr \\ &= \frac{3}{m}\int_0^{\delta}\int_0^{\pi}\int_0^{2\pi} \underline{\omega} r^4 \left(\varepsilon_{11}\sin^2\phi\cos^2\theta + \varepsilon_{22}\sin^2\phi\sin^2\theta + \varepsilon_{33}\cos^2\phi \right) \sin\phi d\theta d\phi dr \\ &= \frac{3}{m}\varepsilon_{kk}\int_0^{\delta} 4\pi \underline{\omega} r^4 dr \\ &= \frac{3}{m}\varepsilon_{kk} m \\ &= \varepsilon_{kk} \end{aligned} \tag{A-26}$$

In Equation (A-26), the following relations are used in the derivation from the third line to the fourth line.

$$\int_0^{2\pi} \sin\theta d\theta = \int_0^{2\pi} \cos\theta d\theta = \int_0^{2\pi} \cos\theta \sin\theta d\theta = 0 \tag{A-27}$$

By inserting Equation (A-23) and (A-24) into the second term in Equation (A-18), we obtain,

$$
\begin{aligned}
\frac{\alpha}{2}\left(\underline{\underline{\omega}}\underline{e}^d\right)\bullet\underline{e}^d &= \frac{\alpha}{2}\int_{H_x}\underline{\omega}\left(\frac{\boldsymbol{\xi}\cdot\boldsymbol{\varepsilon}^d\cdot\boldsymbol{\xi}}{\|\boldsymbol{\xi}\|}\right)\left(\frac{\boldsymbol{\xi}\cdot\boldsymbol{\varepsilon}^d\cdot\boldsymbol{\xi}}{\|\boldsymbol{\xi}\|}\right)dV_{\mathbf{x}'} \\
&= \frac{\alpha}{2}\int_{H_x}\underline{\omega}\frac{\varepsilon_{ij}^d\varepsilon_{kl}^d\xi_i\xi_j\xi_k\xi_l}{\|\boldsymbol{\xi}\|^2}dV_{\mathbf{x}'} \\
&= \frac{\alpha}{2}\int_0^{\delta}\int_0^{\pi}\int_0^{2\pi}\underline{\omega}\frac{\varepsilon_{ij}^d\varepsilon_{kl}^d\xi_i\xi_j\xi_k\xi_l}{r^2}r^2\sin\phi d\theta d\phi dr \\
&= \frac{\alpha}{2}\frac{\left\{\begin{array}{l}3\left(\left(\varepsilon_{11}^d\right)^2+\left(\varepsilon_{22}^d\right)^2+\left(\varepsilon_3^d\right)^2\right) \\ +\left(\varepsilon_{12}+\varepsilon_{21}\right)^2+\left(\varepsilon_{13}+\varepsilon_{31}\right)^2+\left(\varepsilon_{23}+\varepsilon_{32}\right)^2 \\ +2\left(\varepsilon_{11}^d\varepsilon_{22}^d+\varepsilon_{22}^d\varepsilon_{33}^d+\varepsilon_{33}^d\varepsilon_{11}^d\right)\end{array}\right\}}{15}\int_0^{\delta}\frac{4\pi\underline{\omega}r^4}{3}dr \\
&= \frac{\alpha m}{2}\frac{\left\{\begin{array}{l}2\left(\left(\varepsilon_{11}^d\right)^2+\left(\varepsilon_{22}^d\right)^2+\left(\varepsilon_3^d\right)^2\right) \\ +\left(\varepsilon_{12}+\varepsilon_{21}\right)^2+\left(\varepsilon_{13}+\varepsilon_{31}\right)^2+\left(\varepsilon_{23}+\varepsilon_{32}\right)^2 \\ +2\left(\varepsilon_{11}^d+\varepsilon_{22}^d+\varepsilon_{33}^d\right)^2\end{array}\right\}}{15} \\
&= \alpha\frac{m\left(\varepsilon_{ij}^d\right)^2}{15}
\end{aligned}
\tag{A-28}
$$

In the above derivation, we used the following relations.

$$
\begin{aligned}
e^d &= e\langle\boldsymbol{\xi}\rangle-\frac{\theta}{3}\underline{x}\langle\boldsymbol{\xi}\rangle=\frac{\boldsymbol{\xi}\cdot\boldsymbol{\varepsilon}\cdot\boldsymbol{\xi}}{\|\boldsymbol{\xi}\|}-\varepsilon_{kk}\|\boldsymbol{\xi}\| \\
&= \frac{\boldsymbol{\xi}\cdot\boldsymbol{\varepsilon}^d\cdot\boldsymbol{\xi}}{\|\boldsymbol{\xi}\|}
\end{aligned}
\tag{A-29}
$$

$$
\varepsilon_{kk}^d = 0 \tag{A-30}
$$

$$
\varepsilon_{ij}^d = \varepsilon_{ji}^d \tag{A-31}
$$

By comparing Equation (A-18), (A-26), (A-28) with Equation (A-17), we have,

$$
k = K \tag{A-32}
$$

$$\alpha = \frac{15G}{m} \tag{A-33}$$

By taking Frechet derivative of the strain energy density (Equation (A-17)), we have,

$$\begin{aligned}
\Delta\Psi\left(\underline{\mathbf{Y}}(\mathbf{x})\langle\underline{\xi}\rangle\right) &= \Psi\left(\underline{\mathbf{Y}}(\mathbf{x})\langle\underline{\xi}\rangle + \Delta\underline{\mathbf{Y}}(\mathbf{x})\langle\underline{\xi}\rangle\right) - \Psi\left(\underline{\mathbf{Y}}(\mathbf{x})\langle\underline{\xi}\rangle\right) \quad \left(\simeq \underline{\nabla}\Psi\left(\underline{\mathbf{Y}}(\mathbf{x})\langle\underline{\xi}\rangle\right) \bullet \Delta\underline{\mathbf{Y}}(\mathbf{x})\right) \\
&= \Delta\left\{\frac{1}{2}K\theta^2 + \frac{15G}{2m}\left(\underline{\omega}\underline{e}^d\right)\underline{\mathbf{M}} \bullet \underline{e}^d\underline{\mathbf{M}}\right\} \\
&\simeq K\theta\underline{\nabla}\theta \bullet \Delta\underline{e}\underline{\mathbf{M}} + \frac{15G}{m}\underline{\omega}\underline{e}^d\underline{\mathbf{M}} \bullet \Delta\underline{e}^d\underline{\mathbf{M}} \\
&= K\theta\underline{\nabla}\theta \bullet \Delta\underline{e}\underline{\mathbf{M}} + \frac{15G}{m}\underline{\omega}\underline{e}^d\underline{\mathbf{M}} \bullet \left(\Delta\underline{e}\underline{\mathbf{M}} - \frac{\underline{\underline{x}}}{3}\underline{\nabla}\theta \bullet \Delta\underline{e}\underline{\mathbf{M}}\right) \\
&= \left\{\left(K\theta - \frac{15G}{m}\underline{\omega}\underline{e}^d \bullet \frac{\underline{\underline{x}}}{3}\right)\underline{\nabla}\theta + \frac{15G}{m}\underline{\omega}\underline{e}^d\underline{\mathbf{M}}\right\} \bullet \Delta e\underline{\mathbf{M}} \\
&= \left\{\left(K\theta - \frac{15G}{m}\underline{\omega}\left(\underline{e} - \frac{\theta}{3}\underline{x}\right) \bullet \frac{\underline{\underline{x}}}{3}\right)\frac{3\underline{\underline{\omega x}}}{m}\underline{\mathbf{M}} + \frac{15G}{m}\underline{\omega}\underline{e}^d\underline{\mathbf{M}}\right\} \bullet \Delta\underline{\mathbf{Y}}(\mathbf{x}) \\
&= \left\{\left(K\theta - \frac{5G}{m}\left(\frac{m}{3}\frac{3}{m}\underline{\omega}\underline{e} \bullet \underline{x} - \frac{\theta}{3}\underline{\omega}\underline{x} \bullet \underline{x}\right)\right)\frac{3\underline{\underline{\omega x}}}{m}\underline{\mathbf{M}} + \frac{15G}{m}\underline{\omega}\underline{e}^d\underline{\mathbf{M}}\right\} \bullet \Delta\underline{\mathbf{Y}}(\mathbf{x}) \\
&= \left\{\left(K\theta - \frac{5G}{m}\left(\frac{m}{3}\theta - \frac{\theta}{3}m\right)\right)\frac{3\underline{\underline{\omega x}}}{m} + \frac{15G}{m}\underline{\omega}\underline{e}^d\right\}\underline{\mathbf{M}} \bullet \Delta\underline{\mathbf{Y}}(\mathbf{x}) \\
&= \left\{\frac{3K\theta\underline{\underline{\omega x}}}{m} + \frac{15G}{m}\underline{\omega}\underline{e}^d\right\}\underline{\mathbf{M}} \bullet \Delta\underline{\mathbf{Y}}(\mathbf{x})
\end{aligned} \tag{A-34}$$

From Equation (A-15) and Equation (A-34), we obtain the constitutive relation of the peridynamic linear solid as follows,

$$\underline{T}\left(\mathbf{x}\right)\langle\underline{\xi}\rangle = t\underline{\mathbf{M}} = \left\{\frac{3K\theta\underline{\underline{\omega x}}}{m} + \frac{15G}{m}\underline{\omega}\underline{e}^d\right\}\underline{\mathbf{M}} \tag{A-35}$$

REFERENCES

1. Silling, S.A. and E. Askari, *A meshfree method based on the peridynamic model of solid mechanics.* Computers & Structures, 2005. **83**(17-18): p. 1526-1535.
2. Silling, S.A., et al., *Peridynamic States and Constitutive Modeling.* Journal of Elasticity, 2007. **88**(2): p. 151-184.
3. Silling, S.A. and R.B. Lehoucq, *Peridynamic Theory of Solid Mechanics.* 2010. **44**: p. 73-168.
4. Silling, S.a. and F. Bobaru, *Peridynamic modeling of membranes and fibers.* International Journal of Non-Linear Mechanics, 2005. **40**: p. 395-409.
5. Askari, E., J. Xu, and S. Silling, *Peridynamic Analysis of Damage and Failure in Composites*, in *44th AIAA Aerospace Sciences Meeting and Exhibit*. 2006, American Institute of Aeronautics and Astronautics: Reston, Virigina. p. 1-12.
6. Bobaru, F., *Influence of van der Waals forces on increasing the strength and toughness in dynamic fracture of nanofibre networks: a peridynamic approach.* Modelling and Simulation in Materials Science and Engineering, 2007. **15**: p. 397-417.
7. Xu, J., et al., *Damage and Failure Analysis of Composite Laminates under Biaxial Loads*, in *48th AIAA/ASME/ASCE/AHS/ASC Structures, Structural Dynamics, and Materials Conference*. 2007, American Institute of Aeronautics and Astronautics: Reston, Virigina. p. 1-9.
8. Askari, E., et al., *Peridynamics for multiscale materials modeling.* Journal of Physics: Conference Series, 2008. **125**: p. 012078.
9. Silling, S.A., et al., *Crack nucleation in a peridynamic solid.* International Journal of Fracture, 2010. **162**(1-2): p. 219-227.
10. Gandossi, L., *An overview of hydraulic fracturing and other formation stimulation technologies for shale gas production*. 2013.
11. Khristianovic, S.A. and Y.P. Zheltov, *Formation of Vertical Fractures by Means of Highly Viscous Liquid*, in *4th World Petroleum Congress*. 1955, World Petroleum Congress: Rome, Italy.
12. Geertsma, J. and F. De Klerk, *A Rapid Method of Predicting Width and Extent of Hydraulically Induced Fractures.* Journal of Petroleum Technology, 1969. **21(12)**: p. 1571-1581.
13. Perkins, T.K. and L.R. Kern, *Widths of Hydraulic Fractures.* 1961.
14. Nordgren, R.P., *Propagation of a Vertical Hydraulic Fracture.* 1972.
15. Simonson, E.R., A.S. Abou-Sayed, and R.J. Clifton, *Containment of Massive Hydraulic Fractures.*
16. Settari, A. and M.P. Cleary, *Three-Dimensional Simulation of Hydraulic Fracturing.* Journal of Petroleum Technology, 1984. **36**: p. 1177-1190.
17. Fung, R.L., S. Vilayakumar, and D.E. Cormack, *Calculation of Vertical Fracture Containment in Layered Formations.*

18. Cleary, M.P., M. Kavvadas, and K.Y. Lam, *Development of a Fully Three-Dimensional Simulator for Analysis and Design of Hydraulic Fracturing*. 1983, Society of Petroleum Engineers.
19. Meyer, B.R., *Three-Dimensional Hydraulic Fracturing Simulation on Personal Computers: Theory and Comparison Studies*. 1989, Society of Petroleum Engineers.
20. Adachi, J., et al., *Computer simulation of hydraulic fractures.* International Journal of Rock Mechanics and Mining Sciences, 2007. **44**(5): p. 739-757.
21. Clifton, R.J. and A.S. Abou-Sayed, *A Variational Approach To The Prediction Of The Three-Dimensional Geometry Of Hydraulic Fractures*, in *SPE/DOE Low Permeability Gas Reservoirs Symposium*. 1981, Society of Petroleum Engineers.
22. Bui, H.D., *An integral equations method for solving the problem of a plane crack of arbitrary shape.* Journal of the Mechanics and Physics of Solids, 1977. **25**(1): p. 29-39.
23. Gu, H., *A Study of Propagation of Hydraulically Induced Fractures*. 1987: UMI.
24. Yew, C.H., *Mechanics of Hydraulic Fracturing*, in *Mechanics of Hydraulic Fracturing*, C.H. Yew, Editor. 1997, Gulf Professional Publishing: Houston. p. 1-29.
25. Morita, N., D.L. Whitfill, and H.A. Wahl, *Stress-Intensity Factor and Fracture Cross-Sectional Shape Predictions From a Three-Dimensional Model for Hydraulically Induced Fractures.* Journal of Petroleum Technology, 1988. **40**: p. 1329-1342.
26. Dahi Taleghani, A. and J.E. Olson, *How Natural Fractures Could Affect Hydraulic-Fracture Geometry.* SPE Journal, 2014. **19**: p. 161-171.
27. Warpinski, N.R. and L.W. Teufel, *Influence of Geologic Discontinuities on Hydraulic Fracture Propagation (includes associated papers 17011 and 17074).* Journal of Petroleum Technology, 1987. **39**: p. 209-220.
28. Fisher, M.K., et al. *Integrating fracture mapping technologies to optimize stimulations in the Barnett Shale*. in *SPE Annual Technical Conference and Exhibition*. 2002. Society of Petroleum Engineers.
29. Warpinski, N.R., et al., *Examination of a Cored Hydraulic Fracture in a Deep Gas Well (includes associated papers 26302 and 26946).*
30. Fast, R.E., A.S. Murer, and R.S. Timmer, *Description and Analysis of Cored Hydraulic Fractures, Lost Hills Field, Kern County, California.*
31. Gale, J.F.W., R.M. Reed, and J. Holder, *Natural fractures in the Barnett Shale and their importance for hydraulic fracture treatments.* AAPG Bulletin, 2007. **91**: p. 603-622.
32. Hossain, M.M. and M.K. Rahman, *Numerical simulation of complex fracture growth during tight reservoir stimulation by hydraulic fracturing.* Journal of Petroleum Science and Engineering, 2008. **60**(2): p. 86-104.
33. Olson, J.E., *Multi-fracture propagation modeling: Applications to hydraulic fracturing in shales and tight gas sands*, in *The 42nd U.S. Rock Mechanics Symposium (USRMS)*. 2008, American Rock Mechanics Association: San Francisco, California.

34. Olson, J., *Predicting fracture swarms--the influence of subcritical crack growth and the crack-tip process zone on joint spacing in rock.* Geological Society of London Special Publications, 2004. **231**: p. 73-88.
35. Sesetty, V., Ghassemi, A., *Simulation of Hydraulic Fractures and their Interactions with Natural Fractures.* 2012.
36. McClure, M.W., *Modeling and Characterization of Hydraulic Stimulation and Induced Seismicity in Geothermal and Shale Gas Reservoirs*. 2012, Stanford University.
37. Weng, X., et al., *Modeling of Hydraulic Fracture Network Propagation in a Naturally Fractured Formation.* Proceedings of SPE Hydraulic Fracturing Technology Conference, 2011. **i**.
38. Wu, K., *Numerical Modeling of Complex Hydraulic Fracture Development in Unconventional Reservoirs.* (Ph.D dissertation), 2014(the University of Texas at Austion).
39. Zhao, X.P. and R. Young, *Numerical Simulation of Seismicity Induced by Hydraulic Fracturing in Naturally Fractured Reservoirs*, in *SPE Annual Technical Conference and Exhibition*. 2009, Society of Petroleum Engineers.
40. Shimizu, H., et al., *The Distinct Element Analysis for Hydraulic Fracturing in Unconsolidated Sand Considering Fluid Viscosity*, in *ISRM Regional Symposium - 7th Asian Rock Mechanics Symposium*. 2012, International Society for Rock Mechanics: Seoul, Korea.
41. Yao, Y., et al., *Cohesive Fracture Mechanics Based Analysis to Model Ductile Rock Fracture*, in *44th U.S. Rock Mechanics Symposium and 5th U.S.-Canada Rock Mechanics Symposium*. 2010, American Rock Mechanics Association: Salt Lake City, Utah.
42. Shin, D.H. and M.M. Sharma, *Factors Controlling the Simultaneous Propagation of Multiple Competing Fractures in a Horizontal Well*, in *SPE Hydraulic Fracturing Technology Conference*. 2014, Society of Petroleum Engineers.
43. Ripudaman Manchanda, *A General Poro-Elastic Model for Pad-Scale Fracturing of Horizontal Wells*, in *Petroleum and Geosystems Engineering*. 2015, The University of Texas at Austin.
44. Keshavarzi, R. and S. Mohammadi, *A New Approach for Numerical Modeling of Hydraulic Fracture Propagation in Naturally Fractured Reservoirs*, in *SPE/EAGE European Unconventional Resources Conference and Exhibition*. 2012, Society of Petroleum Engineers.
45. Haddad, M. and K. Sepehrnoori. *Integration of XFEM and CZM to Model 3D Multiple-Stage Hydraulic Fracturing in Quasi-brittle Shale Formations: Solution-Dependent Propagation Direction*. in *Proceedings of the AADE National Technical Conference and Exhibition, AADE2015, San Antonio, Texas, 8-9 April 2015*. 2015.
46. Warpinski, N., et al. *Comparison of single-and dual-array microseismic mapping techniques in the Barnett shale*. in *SPE Annual Technical Conference and Exhibition*. 2005. Society of Petroleum Engineers.

47. Jiu, K., et al., *Fractures of lacustrine shale reservoirs, the Zhanhua Depression in the Bohai Bay Basin, eastern China.* Marine and Petroleum Geology, 2013. **48**: p. 113-123.
48. Blanton, T.L. *Propagation of Hydraulically and Dynamically Induced Fractures in Naturally Fractured Reservoirs*.
49. Zhou, J., et al., *Analysis of fracture propagation behavior and fracture geometry using a tri-axial fracturing system in naturally fractured reservoirs.* International Journal of Rock Mechanics and Mining Sciences, 2008. **45**(7): p. 1143-1152.
50. Renshaw, C.E. and D.D. Pollard, *An experimentally verified criterion for propagation across unbounded frictional interfaces in brittle, linear elastic materials.* International Journal of Rock Mechanics and Mining Sciences and Geomechanics Abstracts, 1995. **32**(3): p. 237-249.
51. Gu, H. and X. Weng, *Criterion For Fractures Crossing Frictional Interfaces At Non-orthogonal Angles*, in *44th U.S. Rock Mechanics Symposium and 5th U.S.-Canada Rock Mechanics Symposium*. 2010, American Rock Mechanics Association: Salt Lake City, Utah.
52. Gu, H., et al., *Hydraulic Fracture Crossing Natural Fracture at Nonorthogonal Angles: A Criterion and Its Validation.* SPE Production & Operations, 2012. **27**: p. 20-26.
53. Chuprakov, D., O. Melchaeva, and R. Prioul, *Injection-Sensitive Mechanics of Hydraulic Fracture Interaction with Discontinuities.* Rock Mechanics and Rock Engineering, 2014. **47**(5): p. 1625-1640.
54. Zhang, X. and R.G. Jeffrey, *The role of friction and secondary flaws on deflection and re‐initiation of hydraulic fractures at orthogonal pre‐existing fractures.* Geophysical Journal International, 2006. **166**(3): p. 1454-1465.
55. Zhang, X., M. Thiercelin, and R. Jeffrey. *Effects of Frictional Geological Discontinuities on Hydraulic Fracture Propagation*. 2007.
56. Zhang, X., R.G. Jeffrey, and M. Thiercelin, *Mechanics of fluid-driven fracture growth in naturally fractured reservoirs with simple network geometries.* Journal of Geophysical Research, 2009. **114**(B12).
57. Dahi-Taleghani, A. and J.E. Olson, *Numerical Modeling of Multistranded-Hydraulic-Fracture Propagation: Accounting for the Interaction Between Induced and Natural Fractures.* Spe Journal, 2011. **16**(3): p. 575-581.
58. Olson, J.E. and A.D. Taleghani, *Modeling simultaneous growth of multiple hydraulic fractures and their interaction with natural fractures*. 2009, Society of Petroleum Engineers.
59. Olson, J.E., *Predicting fracture swarms -- the influence of subcritical crack growth and the crack-tip process zone on joint spacing in rock.* Geological Society, London, Special Publications, 2004. **231**(1): p. 73-88.
60. McClure, M.W., et al., *Fully Coupled Hydromechanical Simulation of Hydraulic Fracturing in 3D Discrete-Fracture Networks.* 2016.
61. Silling, S.a., *Reformulation of elasticity theory for discontinuities and long-range forces.* Journal of the Mechanics and Physics of Solids, 2000. **48**: p. 175-209.

62. Hu, W., Y.D. Ha, and F. Bobaru, *Modeling Dynamic Fracture and Damage in a Fiber-Reinforced Composite Lamina With Peridynamics.* International Journal for Multiscale Computational Engineering, 2011. **9**: p. 707-726.
63. Bobaru, F., Y.D. Ha, and W. Hu, *Damage progression from impact in layered glass modeled with peridynamics.* Central European Journal of Engineering, 2012. **2**: p. 551-561.
64. Foster, J.T., S.A. Silling, and W.N. Chen, *An Energy Based Failure Criterion for Use with Peridynamic States.* International Journal for Multiscale Computational Engineering, 2011. **9**(6): p. 675-687.
65. Pickens, J.F. and G.E. Grisak, *Scale-dependent dispersion in a stratified granular aquifer.* Water Resources Research, 1981. **17**(4): p. 1191-1211.
66. Serrano, S.E., *Forecasting scale-dependent dispersion from spills in heterogeneous aquifers.* Journal of Hydrology, 1995. **169**(1): p. 151-169.
67. Bouchaud, J.P. and A. Georges, *Anomalous diffusion in disordered media: statistical mechanisms, models and physical applications.* Physics reports, 1990. **195**(4): p. 127-293.
68. Klafter, J., A. Blumen, and M.F. Shlesinger, *Stochastic pathway to anomalous diffusion.* Physical Review A, 1987. **35**(7): p. 3081-3081.
69. Metzler, R. and J. Klafter, *The random walk's guide to anomalous diffusion: a fractional dynamics approach.* Physics reports, 2000. **339**(1): p. 1-77.
70. Bobaru, F. and M. Duangpanya, *The peridynamic formulation for transient heat conduction.* International Journal of Heat and Mass Transfer, 2010. **53**(19): p. 4047-4059.
71. Bobaru, F. and M. Duangpanya, *A peridynamic formulation for transient heat conduction in bodies with evolving discontinuities.* Journal of Computational Physics, 2012. **231**(7): p. 2764-2785.
72. Du, Q., et al., *Analysis and approximation of nonlocal diffusion problems with volume constraints.* SIAM Review, 2012. **54**(4): p. 667-696.
73. DU, Q., et al., *A NONLOCAL VECTOR CALCULUS, NONLOCAL VOLUME-CONSTRAINED PROBLEMS, AND NONLOCAL BALANCE LAWS.* Mathematical Models and Methods in Applied Sciences, 2013. **23**(03): p. 493-540.
74. Du, Q., et al., *A new approach for a nonlocal, nonlinear conservation law.* SIAM Journal on Applied Mathematics, 2012. **72**(1): p. 464-487.
75. Seleson, P., M. Gunzburger, and M.L. Parks, *Interface problems in nonlocal diffusion and sharp transitions between local and nonlocal domains.* Computer Methods in Applied Mechanics and Engineering, 2013. **266**: p. 185-204.
76. Reddy, J.N., *An Introduction to the Finite Element Method, 2nd ed.* 1993: McGraw-Hill Education.
77. Katiyar, A., et al., *A peridynamic formulation of pressure driven convective fluid transport in porous media.* Journal of Computational Physics, 2014. **261**: p. 209-229.

78. Seleson, P.D., *Multiscale Models for the Mechanics of Materials: Constitutive Relations, Upscaling from Atomistic Systems, and Interface Problems.* 2010, The Florida State University.
79. Gunzburger, M. and R. Lehoucq, *A Nonlocal Vector Calculus with Application to Nonlocal Boundary Value Problems.* Multiscale Modeling & Simulation, 2010. **8**(5): p. 1581-1598.
80. Seleson , P. and M. Parks, *On the role of influence function in the peridynamic theory.* 2011. **9**(6): p. 689-706.
81. Ansari, R.Z. and R.T. Johns, *Steady-State Coning Solutions With Multiple Wells and Reservoir Boundaries*. Society of Petroleum Engineers.
82. Bobaru, F., et al., *Convergence, adaptive refinement, and scaling in 1D peridynamics.* International Journal for Numerical Methods in Engineering, 2009. **77**: p. 852-877.
83. Silling, S.A. and R.B. Lehoucq, *Convergence of Peridynamics to Classical Elasticity Theory.* Journal of Elasticity, 2008. **93**(1): p. 13-37.
84. Turner, D.Z., *A Non-Local Model for Fluid-Structure Interaction with Applications in Hydraulic Fracturing.* International Journal for Computational Methods in Engineering Science and Mechanics, 2013. **14**(5): p. 391-400.
85. K. R. Rajagopal, L.T., *Mechanics of mixtures*. Series on Advances in Mathematics for Applied Sciences. 2015: World Scientific Pub Co Inc.
86. Truesdell C, T.R., *The classical field theories* Principles of Classical Mechanics and Field Theory / Prinzipien der Klassischen Mechanik und Feldtheorie, ed. S. Flügge. 1960: Springer Berlin Heidelberg.
87. Epstein, M., *The Elements of Continuum Biomechanics*. 2012: Wiley.
88. Sneddon, I.N., *The Distribution of Stress in the Neighbourhood of a Crack in an Elastic Solid.* Proceedings of the Royal Society of London. Series A. Mathematical and Physical Sciences, 1946. **187**(1009): p. 229-260.
89. Le, Q.V., W.K. Chan, and J. Schwartz, *A two-dimensional ordinary , state-based peridynamic model for linearly elastic solids.* 2014: p. 547-561.
90. Tran, D., A. Settari, and L. Nghiem, *New Iterative Coupling Between a Reservoir Simulator and a Geomechanics Module.* SPE Journal, 2004. **9**: p. 362-369.
91. Ouchi, H., et al., *A Peridynamics Model for the Propagation of Hydraulic Fractures in Heterogeneous, Naturally Fractured Reservoirs*. 2015, Society of Petroleum Engineers.
92. Ha, Y.D. and F. Bobaru, *Traction boundary conditions in peridynamics: a convergence study, technical report*. 2009, Department of Engineering Mechanics, University of Nebraska-Lincoln: Lincoln, NE.
93. Willenbring, J.M. and M.A. Heroux, *Trilinos users guide*. 2003. p. Medium: ED; Size: 29 p. in various pagings.
94. Jaeger, J.C., N.G.W. Cook, and R. Zimmerman, *Fundamentals of Rock Mechanics*. 2007: Wiley.
95. Ouchi, H., et al., *A fully coupled porous flow and geomechanics model for fluid driven cracks: a peridynamics approach.* Computational Mechanics, 2015. **55**(3): p. 561-576.

96. Blanton, T.L., *An Experimental Study of Interaction Between Hydraulically Induced and Pre-Existing Fractures*, in *SPE Unconventional Gas Recovery Symposium*. 1982, Society of Petroleum Engineers.
97. Dimitry Chuprakov, O.M.a.R.P., *Hydraulic Fracture Propagation Across a Weak Discontinuity Controlled by Fluid Injection, Effective and Sustainable Hydraulic Fracturing*, ed. D.R. Jeffrey. 2013.
98. Kresse, O., et al., *Numerical Modeling of Hydraulic Fractures Interaction in Complex Naturally Fractured Formations.* Rock Mechanics and Rock Engineering, 2013. **46**: p. 555-568.
99. Donath, F.A., *Experimental study of shear failure in anisotropic rock.* Bulletin of Geological Soc. America, 1966. **72**: p. 985-990.
100. Jaeger, J.C.a.C., N. G. W., *Fundamentals of Rock Mechanics, 2nd edn*. 1979, New York: Chapman and Hall.
101. Agarwal, K. and M.M. Sharma, *A New Approach to Modeling Fracture Growth in Unconsolidated Sands*. Society of Petroleum Engineers.
102. Bahorich, B., J.E. Olson, and J. Holder, *Examining the Effect of Cemented Natural Fractures on Hydraulic Fracture Propagation in Hydrostone Block Experiments*. Society of Petroleum Engineers.
103. Mokhtari, M., et al., *Acoustical and Geomechanical Characterization of Eagle Ford Shale -Anisotropy, Heterogeneity and Measurement Scale*. 2014, Society of Petroleum Engineers.
104. Filder, L.J., *Natural Fracture Characterization of the New Albany Shale*, in *Geological Science*. 2011, The University of Texas at Austin.
105. Walton, I. and J. McLennan, *The Role of Natural Fractures in Shale Gas Production*. 2013, International Society for Rock Mechanics.
106. Maxwell, S.C., et al., *Fault Activation During Hydraulic Fracturing*. 2009, Society of Exploration Geophysicists.
107. Gu, H. and E. Siebrits, *Effect of Formation Modulus Contrast on Hydraulic Fracture Height Containment.* 2008.
108. Thiercelin, M., R.G. Jeffrey, and K.B. Naceur, *Influence of Fracture Toughness on the Geometry of Hydraulic Fractures.* 1989.
109. van Eekelen, H.A.M., *Hydraulic Fracture Geometry: Fracture Containment in Layered Formations.* 1982.
110. Fisher, M.K. and N.R. Warpinski, *Hydraulic-Fracture-Height Growth: Real Data.* 2012.
111. Wu, H., et al., *A Map Of Fracture Behavior In The Vicinity Of An Interface*. 2004, American Rock Mechanics Association.
112. Zhang, X., R.G. Jeffrey, and M. Thiercelin, *Deflection and propagation of fluid-driven fractures at frictional bedding interfaces: A numerical investigation.* Journal of Structural Geology, 2007. **29**(3): p. 396-410.
113. Garcia, X., et al., *Revisiting Vertical Hydraulic Fracture Propagation Through Layered Formations – A Numerical Evaluation*. 2013, American Rock Mechanics Association.

114. Rijken, P. and M.L. Cooke, *Role of shale thickness on vertical connectivity of fractures: application of crack-bridging theory to the Austin Chalk, Texas.* Tectonophysics, 2001. **337**(1–2): p. 117-133.
115. Senseny, P.E. and T.W. Pfeifle, *Fracture Toughness Of Sandstones And Shales*. 1984, American Rock Mechanics Association.
116. Passey, Q.R., et al., *From Oil-Prone Source Rock to Gas-Producing Shale Reservoir - Geologic and Petrophysical Characterization of Unconventional Shale Gas Reservoirs*. 2010, Society of Petroleum Engineers.
117. Gray Mavko, T.M., Jack Dvokin, *The rock physics handbook: Tools for seismic analysis of porous media*. 2009: Cambridge university press.
118. Atkinson, B.K., *Fracture mechanics of rock*. 1987: Academic Press.
119. Carozzi, A.V., *Sedimentary petrography*. 1993: PTR Prentice Hall.
120. Mavko, G., T. Mukerji, and J. Dvorkin, *The rock physics handbook: Tools for seismic analysis of porous media*. 2009: Cambridge university press.
121. Ren, H., et al., *Dual-horizon Peridynamics.* arXiv preprint arXiv:1506.05146, 2015.
122. Silling, S., D. Littlewood, and P. Seleson, *Variable horizon in a peridynamic medium.* Journal of Mechanics of Materials and Structures, 2015. **10**(5): p. 591-612.
123. Stuben, K., *An introduction to algebraic multigrid.* Multigrid, 2001: p. 413-532.
124. Barton, N., S. Bandis, and K. Bakhtar. *Strength, deformation and conductivity coupling of rock joints*. in *International Journal of Rock Mechanics and Mining Sciences & Geomechanics Abstracts*. 1985. Elsevier.